HAL open science

Modeling of pulsating heat pipes

Xiaolong Zhang

To cite this version:

Xiaolong Zhang. Modeling of pulsating heat pipes. Fluid mechanics [physics.class-ph]. Université Paris-Saclay, 2022. English. NNT : 2022UPASP149 . tel-03953103

HAL Id: tel-03953103

https://theses.hal.science/tel-03953103v1

Submitted on 23 Jan 2023

HAL is a multi-disciplinary open access archive for the deposit and dissemination of scientific research documents, whether they are published or not. The documents may come from teaching and research institutions in France or abroad, or from public or private research centers.

L'archive ouverte pluridisciplinaire **HAL**, est destinée au dépôt et à la diffusion de documents scientifiques de niveau recherche, publiés ou non, émanant des établissements d'enseignement et de recherche français ou étrangers, des laboratoires publics ou privés.

université PARIS-SACLAY

Modeling of pulsating heat pipes

Modélisation de caloduc oscillant

Thèse de doctorat de l'université Paris-Saclay

École doctorale n° 564, Physique en Île-de-France (PIF)
Spécialité de doctorat : Physique
Graduate School : Physique. Référent : Université Paris-Saclay

Thèse préparée dans l'unité de recherche **SPEC** (Université Paris-Saclay, CEA, CNRS)
sous la direction de **Vadim NIKOLAYEV**, directeur de recherche

Thèse soutenue à Paris-Saclay, le 14 Décembre 2022, par

Xiaolong ZHANG

Composition du Jury

Membres du jury avec voix délibérative

Bertrand BAUDOUY Directeur de recherche, CEA Paris-Saclay	Président
Michaël BAUDOIN Professeur, Université de Lille	Rapporteur & Examinateur
Fréderic LEFEVRE Professeur, INSA Lyon	Rapporteur & Examinateur
Marie-Christine DULUC Maître de conférences, CNAM Paris	Examinatrice
Vincent AYEL Maître de conférences, ISAE-ENSMA Poitiers	Examinateur

THESE DE DOCTORAT

NNT : 2022UPASP149

ÉCOLE DOCTORALE
Physique en Île-de-France (PIF)

Titre : Modélisation de caloduc oscillant

Mots clés : caloduc oscillant, films liquides, lignes de contact triphasées, modèle OFT (Oscillating Film Thickness), transfert de chaleur, microcanaux.

Résumé : Le caloduc oscillant (Pulsating Heat Pipe-PHP, en anglais) est une alternative prometteuse aux caloducs conventionnels pour répondre aux demandes croissantes de l'industrie du refroidissement de l'électronique. Il s'agit d'un dispositif de transfert de chaleur innovant aux performances exceptionnelles. Cependant, en raison de la complexité des phénomènes physiques impliqués, une théorie complète pour la modélisation du PHP reste en cours de développement. Les PHPs contiennent un tube capillaire chargé d'un fluide pure diphasique. En raison de la capillarité, des bouchons de liquide et des bulles de vapeur se forment naturellement à l'intérieur. Le changement de phase sur les films liquides créés par le retrait des bouchons de liquide est le principal mécanisme de transfert d'énergie. Le développement d'un modèle numérique nécessite une bonne compréhension du comportement de films liquides. Par conséquent, la thèse aborde la dynamique des films liquides au niveau d'un seul ménisque, ce qui inclut le dépôt d'un film par un bouchon oscillant et le retrait de la ligne de contact triple lors de l'évaporation. Notre étude théorique est en accord avec d'observations expérimentales et peut être utilisée pour de nombreuses applications qui impliquent des phénomènes de changement de phase sur de films liquides. A titre d'exemple, l'analyse a été employée pour élucider la formation et l'évolution de la microcouche liquide formant sous une bulle lors de l'ébullition nucléée. Un modèle numérique unidimensionnel de films liquides de PHP, appelé modèle OFT (Oscillating Film Thickness en anglais), est développé. D'une part, le nouveau modèle est efficace du point de vue de calcul numérique. D'autre part, parce qu'il se base sur la compréhension de la dynamique des films liquides, le nouveau modèle reflète le comportement physique des films liquides dans les canaux de PHP. Les simulations de PHP à une branche unique par le modèle OFT ont montré un bon accord avec les données expérimentales. Une extension pour le PHP multi-branches est proposée. Le modèle OFT fournit un outil de simulation fiable pour la conception des PHP futures.

Title : Modeling of pulsating heat pipes

Keywords : Pulsating Heat Pipes (PHP), liquid films, triple-phase contact lines, Oscillating Film Thickness (OFT) model, heat transfer, microchannels.

Abstract : Pulsating Heat Pipe (PHP) is a promising alternative to conventional heat pipes to satisfy the increasing demand of the electronics cooling industry. It is an innovative heat transfer device with outstanding performance. However, due to the complex physical phenomena involved, a comprehensive theory for PHP modeling remains under development. Conceptually, the PHP contains a capillary tube charged with a pure two-phase fluid. Because of capillarity, liquid plugs and vapor bubbles naturally form inside. Phase change over liquid films created by receding liquid plugs is the principal mechanism for energy transfer. Developing a numerical model requires a good understanding of the liquid film behavior. Therefore, the thesis first addresses liquid film dynamics in capillary tubes, which includes film deposition by oscillating plug and the receding of the triple contact line at evaporation. Our theoretical study agrees with experimental observations and can be applied to many applications that involve phase change phenomena on liquid films. For example, the analysis was employed to elucidate the formation and evolution of microlayer liquid under vapor bubbles in nucleate boiling. A one-dimensional numerical model of liquid films in PHPs, called the Oscillating Film Thickness (OFT) model, is developed. On the one hand, the new model is computationally efficient; on the other hand, because it is based on the acquired understanding of liquid film dynamics, the new model reflects the physical behavior of liquid films in PHP's fluid channel. The simulations of single-branch PHPs using the OFT model have shown good agreement with experimental data. An extension for multi-branch PHPs is proposed. OFT model provides a reliable simulation tool for designing future PHP prototypes.

Ponyo on Sōsuke's pulsating-heat-pipe powered boat.
From *Ponyo*, directed by Hayao Miyazaki (宮崎 駿)
Studio Ghibli 2008

Acknowledgments

Salutations to those who have opened this file and decided to read a 120-page report. I hope you wouldn't find it a piece of meaningless drivel.

Well, it's official, 26 years of school education have come to an end. I have to say it was a bumpy road over the past 3 years. About 2 months after I started working at French Alternative Energies and Atomic Energy Commission (abbreviated from the French *Commissariat à l'énergie atomique et aux énergies alternatives*) (CEA) as a Ph.D. candidate, Covid-19 was first identified in Wuhan. The pandemic overlapped practically with the course of my doctoral studies and has disrupted many of my original plans. I was intimidated by the widespread rumor that doing a Ph.D. is fraught with frustration and complications. But who could have thought that not dying from a global pandemic was a side project I had to carry on. Fortunately, in the end, things worked out just fine.

I consider the report you are reading as a collaborative work by me and my thesis supervisor Dr. Vadim NIKOLAYEV. It sounds like a cliché saying that "it would not be possible without the tremendous support from the thesis supervisor," but it's 100 % true in my case. He is a practicing humanitarian and an absolute expert in his scientific fields. He introduced me to heat pipes research and constantly inspired passion in me. I particularly appreciated his encouragement when I felt disheartened and fell into self-questioning. I tend to overthink and get lost in trivial details, but he always pulls me back on the right track. I really appreciate his patience because I can be quite a character sometimes. Altogether, I am greatly indebted to him for his insightful guidance in completing this doctoral project and for his help.

I would also like to take this opportunity to thank colleagues in the research group of SPEC/SPHYNX at CEA for their hospitality and being genuinely friendly. I really appreciate the working environment here and the well-defined boundary between personal and professional lives. Three years at CEA have been quite enjoyable. Revision of the defense committee is well appreciated.

Big thanks go to my friends, old and new, near and far, for sharing many movie nights, exploring a bit of Europe, spending wonderful summer days in the south of France, and simply having a cup of coffee. I'll keep enjoying the serendipity that brought you to me. I would also like to thank my parents. I regret that I wasn't able to go home to visit my family during my doctoral studies because of the self-deluding anti-epidemic policy. I hope to make up for that in the future. I don't recall where I have read this French pun: a piece of chocolate could turn "life is pain" to "life is pain au chocolat". I hope you will find that piece of chocolate and Bon courage!

张晓龙 (ZHANG Xiaolong)
CEA Paris-Saclay Center, France, 11/2022

Contents

Introduction 1

1 Basics and modeling of PHP liquid films 7

1.1 Hydrodynamic theory of thin liquid films . . . 7

1.1.1 Formulation: one-sided model . . . 8

1.1.2 Film edges: triple contact line dynamics . . . 11

1.1.3 Film thickness 1: deposition by liquid plugs . . . 15

1.1.4 Film thickness 2: impact of phase change . . . 16

1.2 One-dimensional PHP models . . . 16

1.2.1 "Superheated vapor" models . . . 16

1.2.2 Film Evaporation-Condensation (FEC) model . . . 19

1.2.3 Discrete volume models . . . 23

1.3 Conclusions . . . 26

I Liquid Film Dynamics 27

2 Liquid films attached to oscillatory menisci 29

2.1 Problem description . . . 30

2.2 Isothermal problem with infinite film . . . 30

2.2.1 Steady solutions . . . 31

2.2.2 Film relaxation . . . 33

2.3 Forced meniscus oscillation from pinned contact lines . . . 34

2.3.1 Relaxing the pressure divergence by the Kelvin effect . . . 35

2.3.2 Oscillation problem statement . . . 36

2.3.3 Determination of the meniscus curvature . . . 36

2.3.4 Initial conditions and solution periodicity . . . 37

2.3.5 Numerical implementation . . . 38

2.3.6 Results and discussion . . . 38

2.4 Combined effects of oscillation and evaporation . . . 46

2.4.1 Multiscale approach . . . 46

2.4.2 Numerical approach . . . 48

2.4.3 Paradox and its solution . . . 49

2.5 Conclusions . . . 50

3 Contact line receding at evaporation 51

3.1 Problem description . . . 52

3.1.1 Generalized lubrication theory . . . 52

3.1.2 Boundary conditions and contact line receding speed . . . 56

3.1.3 Numerical solution . . . 57

3.2 Adiabatic dewetting . . . 57

3.3 Dewetting at evaporation . . . 59

3.3.1 Comparison to multiscale theory . . . 60

3.3.2 Voinov length approximation . . . 62

3.3.3 Comparison with experiment . . . 64
3.4 Time-averaged approach . . . 65
3.5 Conclusions . . . 67
4 Microlayer in nucleate boiling 69
4.1 Problem formation . . . 70
4.1.1 Experiment setup . . . 70
4.1.2 Physical model . . . 70
4.2 Results and discussion . . . 71
4.2.1 Experimental observation . . . 71
4.2.2 Numerical results . . . 72
4.3 Conclusions . . . 75

II Oscillating Film Thickness (OFT) model 77
5 New liquid film model 79
5.1 Single branch PHP configuration . . . 80
5.2 Liquid plug . . . 81
5.3 Vapor phase . . . 82
5.3.1 Vapor thermodynamic state . . . 82
5.3.2 Vapor energy equation . . . 83
5.4 Liquid film . . . 84
5.4.1 Length variation . . . 84
5.4.2 Mass variation 1: liquid deposition and collection . . . 85
5.4.3 Mass variation 2: phase exchange . . . 86
5.5 Singularity analysis . . . 92
5.5.1 Onset of film deposition . . . 92
5.5.2 End of film collection . . . 93
5.6 Boundary conditions . . . 93
5.7 Results and discussion . . . 94
5.7.1 Comparison with FEC model . . . 94
5.7.2 Comparison with vertically orientated PHP . . . 95
5.7.3 Comparison with horizontally oriented PHP . . . 97
5.8 Conclusions . . . 98
6 Extension to multi-branch PHPs 101
6.1 General configuration . . . 101
6.1.1 Numbering system of liquid films . . . 102
6.2 Liquid films . . . 103
6.2.1 Effective film thickness . . . 103
6.2.2 Length variation . . . 103
6.2.3 Mass variation . . . 105
6.2.4 Meniscus velocity . . . 109
6.3 Conclusions . . . 110
Conclusions 111

III Appendices 115
A Nanoscale effects 117
A.1 Kelvin effect . . . 117
A.2 Interfacial thermal resistance . . . 118
A.3 Stokes problem of the straight wedge . . . 120
A.3.1 Pinned contact line and varying angle . . . 120

A.3.2 Conventional lubrication approach to straight wedge flow 121
A.3.3 Moving Contact line 122
A.3.4 Localized evaporation 122
A.4 Characteristic length scales of nanoscale effects 123
B Numerical scheme 125
B.1 Non-dimensionalization 126
B.2 Discretized equations 126
C Résumé substantiel en français 129
C.1 Introduction 129
C.2 Motivations 130
C.3 Structure de la thèse 131
C.4 Conclusions 132
D Abstract in Chinese 135

Nomenclature 137

Bibliography 141

Acronyms

ANN Artificial Neural Networks

CASCO Advanced code for simulation of pulsating heat pipes (abbreviated from the French *Code Avancé de Simulation de Caloduc Oscillant*)

CEA French Alternative Energies and Atomic Energy Commission (abbreviated from the French *Commissariat à l'énergie atomique et aux énergies alternatives*)

CNES French National Center for Space Studies (abbreviated from the French *Centre national d'études spatiales*)

DNS Direct Numerical Simulation

ESA European Space Agency

FEC Film Evaporation Condensation

ISS International Space Station

OFT Oscillating Film Thickness

OHP Oscillating Heat Pipe

PHP Pulsating Heat Pipe

Introduction

In the early 1990s, Pulsating Heat Pipe (PHP), also known as Oscillating Heat Pipe (OHP), was conceived by Hisateru Akachi (Akachi, 1993), and quickly became a promising alternative to conventional heat pipes. As an emerging heat transfer device, PHPs combine principles of thermal conductivity and phase transition. Neither wicking structures nor gravitational force is necessary for its functioning.

Conceptually, the energy transfer in PHPs is realized in a capillary fluid channel, which connects energy reception (referred to as **evaporators**) and dissipation (referred to as **condensers**) sections. Optional adiabatic sections may separate evaporators from condensers. This fluid channel is typically arranged into a serpentine pattern forming a bundle. The channel must be sufficiently narrow. Consecutive sections of liquid plugs and vapor bubbles naturally form when the channel is partially charged with a working fluid. Fluid stratification shall not occur. Most of these bubbles are noticeably longer than the channel diameter.

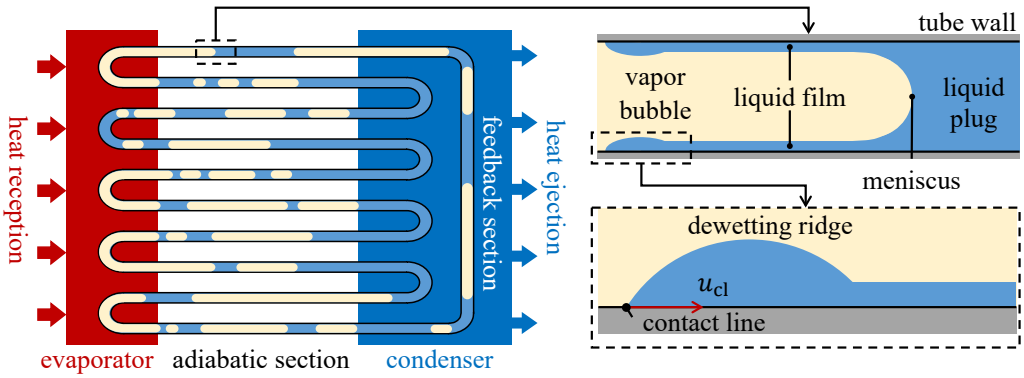

Figure 1: Schematic of a closed-loop 10-branch PHP with an evaporator, a condenser, and an adiabatic section; details of a fluid channel are demonstrated: liquid plug, meniscus, liquid film, contact line, and vapor bubble.

Fig. 1 illustrates one of the most popular PHP designs, where the fluid channel is joined end-to-end by a feedback section in the condenser. This type of design is called the Closed-loop PHP, which many researchers recognize as the most efficient (Nikolayev, 2021).

Describing the configuration of a PHP requires knowing certain terminology. The number of turns N_p refers to the number of U-bends in the evaporator. Branches are the tube section connecting a U-bend in the evaporator to another in the condenser. The number of branches is twice the number of turns. For instance, Fig. 1 illustrates a PHP with 5 turns / 10 branches. From the point of view of how the fluid channel is manufactured, there are two common types of the device: (1) Tubular PHPs, where a simple capillary tube (of circular cross-section) with spatial configuration acts as the fluid channel; (2) Flat-Plate PHPs, where the fluid channel is engraved on a solid metal plate and has a cross-section that is usually rectangular.

In a functioning PHP, the persistent liquid evaporation and vapor recondensation generate a non-equilibrium pressure field that pumps the bubble-plug system. Because the fluid channels are interconnected, the motion of liquid plugs in one branch will displace the

bubbles and plugs in adjacent branches, which leads to a self-sustained pulsating flow, as the name suggests. When menisci recede, they lay down thin liquid films of thickness approximately $10 - 100\ \mu\mathrm{m}$ on the tube wall. Although these liquid films only occupy a tiny fraction of the fluid channel, the amount of latent heat exchange could be substantial because of the low thermal resistance. Additionally, liquid evaporation may lead to film rupture. Dry patches and triple-phase contact lines appear on the tube wall. As a result of capillary action, contact lines recede towards the liquid side, forming liquid ridges, shown in Fig. 1.

Another heat transfer mechanism through phase change is the creation of new bubbles in liquid plugs when the local superheating, with reference to the saturation temperature, exceeds a certain nucleation barrier. Sensible heat transfer in bubbles and heat convection in plugs also play a role, albeit less significant. The latter can be enhanced by pulsating motion. Nonetheless, the latent heat transfer via liquid films remains the principal mechanism responsible for PHP functioning (Nikolayev, 2021).

In a fully activated PHP, a vigorous two-phase flow motion can be observed, and two operation regimes are distinguished: (i) oscillation regime, where the average velocity of fluid flows is close to zero; (ii) circulation regime, the fluid flows at a preferential direction. The latter is believed to have better thermal performance, but it is observed only under particular conditions.

Compared with conventional heat pipes, PHPs possess unique features :

- Simplicity and reliability

Unlike conventional heat pipes, PHPs can operate without capillary (grooves, porous wicks, screen meshes, etc.) or mechanical (pumps and valves) structures, which reduces manufacturing cost and device weight. Equipment operation is also independent of gravity and can be deployed under micro-gravitational working environments, for instance, in space. Various forms and sizes are available depending on the application scenario, and the device can be better integrated with other components of the overall system that require heat exchange. Thanks to the passive heat transfer process, the system reliability is improved.

- High heat transfer coefficient

Liquid films deposited by receding plugs have low thermal resistance, through which the heat transfer by evaporation or condensation is highly efficient. In addition to the latent heat transfer, the pulsating flow significantly enhances heat convection in plugs, resulting in high Nusselt numbers at moderate Reynolds numbers.

- High critical heat flux

Ultimate functioning limits (the maximum heat flux) of two-phase heat transfer systems are often related to dry-out phenomena. When a heated solid surface is no longer wetted by liquid, the heat transfer efficiency plummets sharply, which potentially leads to the burnout of materials of the heated surface. In PHPs, oscillating plugs rewet dry patches on the inner tube wall and thus postpone the occurrence of a persistent dry-out at a particular spot. Therefore, the device can endure higher heat fluxes.

As a simple and promising cooling device, a great number of industrial fields have shown increasing interest in employing PHPs as a means of energy exchange, such as in thermal management of fuel cells and batteries, electronic cooling, cryogenics, and especially in space systems, thanks to its capacity of operating without gravitational force. Many researchers have conducted zero-gravity experiments to reveal and examine certain operation regimes that are unachievable on the ground. One of the experimental projects supported

by the European Space Agency (ESA) aims to test a new concept of large diameter PHP on the International Space Station (ISS) (Abela et al., 2022). The bigger fluid channel reduces viscous losses and increases the heat load capability, whereas it can only operate under microgravity conditions.

Motivations

Although the function principles have been investigated by many researchers, due to the complexity of internal heat and mass transport phenomena, a comprehensive theory of PHP operation and performance prediction remains in development (Ma, 2015; Marengo et al., 2018; Nikolayev et al., 2018b). The lack of a reliable design tool hinders the industrial applications of this device. The unique internal mechanism exhibited in PHPs requests a novel research outlook. With dozens of scientific articles published each year, the PHP modeling is an active field of research.

Researchers have attempted to establish empirical correlations to predict the device's thermal performance. However, describing the configuration of a specific device requires a large number of parameters. To mention a few examples, the physical quantities, including properties of the working fluid and solid material; the device design: PHP topology (open-loop or closed-end), size (lengths and radii), and cross-section of the fluid channel, the number of branches, and the number of heat and cold sources. Additionally, operation conditions impact performance: the device positioning (vertical or horizontal), methods and power of heat reception, and ejection and liquid filling ratio. Inevitably, particular studies omitted certain parameters that are hard to quantify, limiting the empirical correlations to only the range of variables they investigated. Because of the insufficient understanding of operating mechanisms, it is difficult to justify which parameters are indispensable and which can be safely excluded. This issue also appears in the approaches using Artificial Neural Networks (ANN).

The most promising way of achieving a computational tool for PHP design and optimization seems to be the thermo-hydrodynamic modeling (Nikolayev, 2021). The physical behavior of components in the narrow fluid channel: vapor bubbles, liquid plugs and films, and solid tube wall, should be investigated.

Direct Numerical Simulation (DNS) is one of the techniques widely employed in which the Navier–Stokes equations are numerically solved. PHP simulations using DNS, usually in two- and three-dimensional, undoubtedly can illustrate fluid behavior in great detail. However, tremendous programming efforts and computational resources are required to track free liquid-vapor interfaces. Interfacial phase change models often involve artificial parameters that induce uncertainty in results. Liquid films essential to correctly reveal the device functioning are often not resolved in DNS calculations (Nikolayev, 2021).

For these difficulties, one-dimensional modeling (assuming the axisymmetry of fluid behavior in circular channels) is the most pragmatic approach. This approach is capable of generally reproducing the physical phenomena without largely comprising the accuracy. Simulations (Nikolayev, 2011a) and experimental studies (Kamijima et al., 2020; Francom et al., 2021) have confirmed that liquid films make up 70-80% of the total energy transfer in this device. Thus adequate modeling of liquid films becomes the top priority.

The Advanced code for simulation of pulsating heat pipes (abbreviated from the French *Code Avancé de Simulation de Caloduc Oscillant*) (CASCO) has been developed at CEA. It is a 1D simulation code based on the Film Evaporation Condensation (FEC) model (detailed in Subsec. 1.2.2). The geometry of liquid films is simplified. A constant and uniform thickness (a preset value, detailed in Subsec. 1.2.2) represents all liquid films, but their lengths vary

individually, responding to the phase change over films. Thanks to the simple 1D geometry, CASCO is able to cut down a prodigious amount of calculation time. For instance, the 2D simulation of an industrially relevant PHP topology can take up 4-6 weeks per run (Mucci et al., 2021). In contrast, the simulation of the same configuration by CASCO can be completed within an hour (Nikolayev, 2021). This simple 1D approach can produce thermal performance and oscillation behavior that are in agreement with experimental observations (Bae et al., 2017; Abela et al., 2022).

Nevertheless, in terms of realistic representation of liquid film behavior during oscillations, there is still room for improvements in FEC model. The pre-determined, constant-film-thickness assumption should be discarded. The dynamics of triple contact lines, namely the dewetting phenomenon at phase exchange, has not been adequately modeled. A new advanced physical model that does not rely on the external input for film thickness calculation and can reflect contact line receding is desired for the next version of CASCO code. This is the general motivation and objective for the research in this thesis. Developing such a model requires thorough studies of liquid film dynamics, which is why the liquid film theory should be undertaken as the starting point for the thesis.

Thesis structure

The main body of this thesis consists of two parts: the theoretical studies and the computational model development.

After a short introduction, Chap. 1 recapitulates theories on the liquid film dynamics in circular capillary tubes and compares several existing numerical models of PHPs. Chap. 2 details a theoretical analysis of the liquid film dynamics during the meniscus oscillation. Using the theory of Taylor bubbles, the dynamic profile of deposited liquid film is described within the lubrication approximation accounting for the presence of a contact line. The latter is assumed to be pinned on a surface defect and thus immobile; the contact angle is allowed to vary. The fluid flow effects (inertial effects) on the curvature in the central part of the meniscus are neglected; therefore, the meniscus is spherical. This curvature varies in time and is determined as a part of the solution. First, the oscillation under adiabatic conditions is considered. Then, the combined effect of oscillation and evaporation on liquid film behavior is examined.

Chap. 3 continues the studies and deals with the phenomenon that is unmentioned in Chap. 2: the contact line receding in the presence of phase change in capillary tubes. The primary objective is to obtain a simple approach, which is employable in PHP modeling, to describe the contact line dynamics. Our analysis takes the analogy: the contact line dynamics can be comprehended by solving the dewetting problem in the presence of liquid evaporation driven by substrate superheating.

A case study on the microlayer beneath vapor bubbles in nucleate boiling to verify our liquid film theory is presented in Chap. 4. The theory is applied to elucidate the formation of the microlayer and the expansion of the dry nucleation site that highly resembles dewetting of liquid film at evaporation. A comparison with an experiment is made.

Part II centers on developing a novel 1D numerical model of liquid films in PHP simulations, named the Oscillating Film Thickness (OFT) model. On the one hand, the objective is to maintain the advantage of the 1D model of being computationally efficient, and on the other, to incorporate the previous theoretical studies that the physical processes of liquid films are better reflected. Three essential phenomena are emphasized: (1) the film deposition by oscillatory liquid plugs from dry patches (detailed in Chap. 3); (2) the ensuing temporal evolution in film thickness due to mass exchange over films; (3) the contact line dynamics

(discussed in Chap. 3) that shortens film lengths. To evaluate the new model, it is employed in Chap. 5 to simulate the simplest PHP geometry, the single branch PHP, for which detailed experimental data is available. Comparison between simulation results and experimental observation can be performed thoroughly. Eventually, an extension of the new liquid film model for simulating multi-branch PHPs is proposed in Chap. 6. The extension will be integrated into the next version of CASCO and is expected to improve the simulation reliability.

Mathematical details, the numerical scheme, and abstracts of the thesis in French and Chinese are bundled in Part III, the appendices. In summary, the thesis investigates the liquid film dynamics in capillary tubes, on which a 1D computational model is developed.

C'est parti!

Chapter 1

Basics and modeling of PHP liquid films

The working mechanism of PHPs is generally different from that of conventional heat pipes, where physical phenomena are largely steady. Transient, even chaotic fluid flows play a significant role in PHP functioning. Before developing a numerical model, we have to start with understanding fluid behavior and energy transfer of three components in the device channel: vapor bubbles, liquid plugs, and especially liquid films. The physics of liquid films is our top propriety. Then this chapter provides a brief review of existing one-dimensional computational models with the accentuation of examining and comparing how these models reflect the physical phenomena of liquid films.

1.1 Hydrodynamic theory of thin liquid films

In the incipient stage of PHP studies, many researchers mistook that the heat exchange of liquid films (latent heat) is only a marginal factor in the overall energy transfer, and the heat advection via liquid plug motion is stronger than the latent heat exchange. For this reason, early simulation approaches (Zhang et al., 2002; Holley et al., 2005; Mameli et al., 2012; Ma, 2015) based on Shafii et al. (2001) work have not included the liquid film dynamics in their computational models. However, the first film-based simulations by Nikolayev (2011a) have disproved the misinterpretation that the latent heat exchange through liquid films is actually the major contribution. More recent in-situ experiments and simulations (Jo et al., 2019; Kamijima et al., 2020; Francom et al., 2021) have supported this argument as well. Because mass exchange controls the oscillation dynamics, the adequate modeling of liquid films has added significance.

Liquid films in PHPs are different from their counterparts in capillary heat pipes, in which liquid films appear as wetting films due to intermolecular attraction forces that are often described in terms of the disjoining pressure. While the typical thickness of wetting films is merely 10-100 nm, the PHP films can be as thick as 10-100 $\mu\mathrm{m}$. Films in PHP channels are of purely hydrodynamic origin and are created as a result of liquid deposition from receding plugs. This section recapitulates the basics of the hydrodynamic theory of these liquid films.

1.1.1 *Formulation: one-sided model*

In a practical manner, liquid-vapor interfaces are commonly assumed axially symmetric (Fig. 1). The problem is thus formulated in the two-dimensional cross-section that passes through the tube axis (Bretherton, 1961). Liquid films are bounded above by the vapor and below by a heated tube wall.

Since the vapor density ρ_v, viscosity, and thermal conductivity are all smaller compared to the liquid, Burelbach et al. (1988) have proposed the "one-sided" model, where the vapor-side hydrodynamic stress and heat fluxes into vapor at interfaces are neglected in comparison with those on the liquid side. Therefore, p_v is assumed spatially homogeneous.

The configuration is shown in Fig. 2, where the Cartesian coordinates describe the system. The free interface is located at $y = h(x,t)$, where y is the radial coordinate, and the liquid thickness h is a function of axial coordinate x and time t. $\Phi(x,t)$ denotes the liquid volume flux in the film. The unit vectors $\boldsymbol{n}$ and $\boldsymbol{t}$ are the inward normal and tangent vectors, respectively. $J(x,t)$ is the mass flux at the interface, which is positive for evaporation and negative for condensation. The liquid is assumed to evaporate in a direction normal to the interface. The inner tube wall is located at $y = 0$. Here, the problem is formulated for general cases where the tube wall can be superheated or subcooled with respect to the saturation temperature T_sat, corresponding to p_v. For the tube made of highly conductive materials, the tube wall temperature can be regarded uniform: $T_\mathrm{w} = T_\mathrm{sat} + \Delta T$, with ΔT being the superheating. $T^\mathrm{i}(x,t)$ is the temperature of interface. The triple contact line recedes towards the liquid side at speed u_cl.

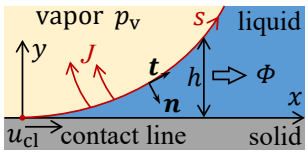

Figure 2: Two-dimensional geometry of the liquid-vapor interface in capillary tubes, including contact line receding towards liquid side at speed u_cl.

1.1.1.1 *Stokes equations*

Liquid films are thin enough that inertial effects are unimportant compared to viscous forces, i. e. $Re = \rho u h/\mu \ll 1$. Here, ρ, u, and μ are liquid density, shear viscosity, and velocity, respectively. Unless otherwise indicated, all quantities mentioned hereafter refer to the liquid phase. The reduced Stokes equations can describe the conservation of momentum and mass in liquid films,

$$\boldsymbol{\nabla p} - \mu \nabla^2 \boldsymbol{u} = \boldsymbol{0}, \tag{1.1a}$$

$$\boldsymbol{\nabla} \cdot \boldsymbol{u} = 0, \tag{1.1b}$$

which are written in the vectorized form for incompressible Newtonian fluids without applied body forces. Here, $\boldsymbol{u} = (u_x, u_y)$, and $\boldsymbol{p}$ denotes pressure in the liquid.

Boundary conditions at interface

At the free interface, $y = h(x,t)$, the normal-stress boundary condition is,

$$J(\boldsymbol{u} - \boldsymbol{u}_\mathrm{v}) \cdot \boldsymbol{n} - (\boldsymbol{T} - \boldsymbol{T}_\mathrm{v}) \cdot \boldsymbol{n} \cdot \boldsymbol{n} = 2\kappa\sigma, \tag{1.2}$$

where $\boldsymbol{T}$ and $\boldsymbol{T}_\mathrm{v}$ are the stress tensors of liquid and vapor, respectively; κ is the interface curvature, and σ is surface tension. Instead of being constant, the value of σ is represented by a liner equation of state as a function of interface temperature T^i,

$$\sigma = \sigma_0 - \gamma(T^\mathrm{i} - T_0), \tag{1.3}$$

where σ_0 is the surface tension at the reference temperature T_0. This temperature dependence is called the **Marangoni effect**, or the thermo-capillary convection. For most common liquids, $\gamma = -\mathrm{d}\sigma/\mathrm{d}T$ is positive.

The shear-stress boundary condition is written as,

$$J(\boldsymbol{u} - \boldsymbol{u}_\mathrm{v}) \cdot \boldsymbol{t} - (\boldsymbol{T} - \boldsymbol{T}_\mathrm{v}) \cdot \boldsymbol{n} \cdot \boldsymbol{t} = -\boldsymbol{\nabla}\sigma \cdot \boldsymbol{t}, \tag{1.4}$$

No slip at the interface between vapor and liquid is assumed,

$$(\boldsymbol{u} - \boldsymbol{u}_\mathrm{v}) \cdot \boldsymbol{t} = 0. \tag{1.5}$$

Mass balance at the interface (Delhaye, 1974) is

$$J = \rho(\boldsymbol{u} - \boldsymbol{u}^\mathrm{i}) \cdot \boldsymbol{n}, \tag{1.6}$$

where $\boldsymbol{u}^\mathrm{i}$ is the velocity of interface.

1.1.1.2 *Conventional lubrication theory*

Within the thin liquid film geometry, the thickness (along y, see Fig. 2) is significantly smaller than the length (along x). Eq. 1.1 can be further simplified by the lubrication approximation (Oron et al., 1997; Shao et al., 2011), where liquid is supposed to move primarily in $x-$direction, i. e. $u_y \ll u_x$. Additionally, the u_x variation across the liquid layer is assumed to be larger than that along the tube axis: $\partial u_x/\partial x \ll \partial u_x/\partial y$. The Stokes equation (1.1a) then reads,

$$\frac{\partial p}{\partial x} = \mu \frac{\partial^2 u_x}{\partial y^2}, \quad \frac{\partial p}{\partial y} = 0. \tag{1.7 a,b}$$

At the vapor-liquid interface $y = h(x,t)$, we impose the shear-stress boundary condition, a simplified form of Eq. 1.4,

$$\mu \left.\frac{\partial u_x}{\partial y}\right|_{y=h(x)} = \frac{\partial \sigma}{\partial x}, \tag{1.8}$$

where the gradient of σ is represented by T^i variation along x, cf. Eq. 1.3 (Nikolayev, 2010):

$$\frac{\partial \sigma}{\partial x} \simeq -\gamma \frac{\partial T^\mathrm{i}}{\partial x}. \tag{1.9}$$

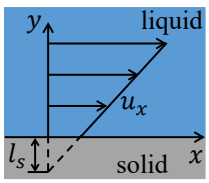

At the solid boundary, $y = 0$, the hydrodynamic slip condition is applied to the tangential component of liquid velocity u_x, and the no-penetration condition is applied to the normal component, u_y,

$$u_x = l_\mathrm{s} \frac{\partial u_x}{\partial y}, \quad u_y = 0, \tag{1.10 a,b}$$

where l_s is the slip length introduced to quantify the boundary slip phenomenon, which is defined as the distance from the liquid-solid interface where the linear extrapolation of $u_x(y)$ vanishes; see the marginal illustration. The value of l_s is usually of several nanometers. Depending on the roughness and wettability, l_s can be one order of value larger for non-wettable surfaces (Lauga et al., 2007).

Using conditions Eq. 1.8 and Eq. 1.10, the solution of Eq. 1.7 is obtained as

$$u_x = cy^2 + by + a, \tag{1.11}$$

where

$$c = \frac{1}{2\mu}\frac{\partial p}{\partial x}, \quad b = \frac{1}{\mu}\left(\frac{\partial \sigma}{\partial x} - h\frac{\partial p}{\partial x}\right), \quad a = l_s b.$$

Integrating $u_x(y)$ from $y = 0$ to $y = h$, the liquid volume flux Φ in the film at a given position x is found as

$$\Phi = \int_0^h u_x(y)dy. \tag{1.12}$$

Mass balance at interface

Near the free interface, liquid velocity in the direction $\boldsymbol{n}$ is $u_\mathrm{n} = \boldsymbol{u} \cdot \boldsymbol{n}$.

Within the small slope approximation, the interface velocity parallel to $\boldsymbol{n}$ is denoted as $u^\mathrm{i} \simeq |\boldsymbol{u}^i|$, positive for pointing into the liquid. We can then reduce Eq. 1.6 to (Nikolayev, 2010),

$$(u^\mathrm{i} - u_\mathrm{n})\rho = J. \tag{1.13}$$

The liquid volume flux Φ at a given location can also be expressed as a function of u_n,

$$\Phi = \int_0^s u_\mathrm{n}(s)\mathrm{d}s \simeq \int_0^x u_\mathrm{n}(x)\mathrm{d}x, \tag{1.14}$$

where s is the curvilinear coordinate that runs along the free interface with $s = 0$ at the contact line. Taking the derivative of Eq. 1.14 yields

$$u_\mathrm{n} = \frac{\partial \Phi}{\partial x}. \tag{1.15}$$

The value of u^i is approximated by

$$u^\mathrm{i} = -\frac{\partial h}{\partial t}\left[1 + \left(\frac{\partial h}{\partial x}\right)^2\right]^{-1/2} \simeq -\frac{\partial h}{\partial t}. \tag{1.16}$$

Substituting Eq. 1.15 and Eq. 1.16 into Eq. 1.13, mass balance at the interface reads,

$$\frac{\partial h}{\partial t} + \frac{\partial \Phi}{\partial x} = -\frac{J}{\rho}. \tag{1.17}$$

Phase exchange

Assuming a stationary and linear temperature distribution across the liquid film and neglecting the heat flux into vapor, the interface energy balance is written as (Nikolayev, 2010),

$$J = \frac{k(T_\mathrm{w} - T^\mathrm{i})}{h\mathcal{L}}, \tag{1.18}$$

where k is the liquid thermal conductivity; $\mathcal{L}$ is the latent heat.

Eq. 1.18 states that only heat conduction exists in liquid films and is used to vaporize the liquid, which is at saturation. In the case of poorly conductive tubes (plastic or glass), T_w may not be constant, and a transient temperature distribution has to be considered. Here, we consider solid tubes made of highly conductive materials, therefore, T_w is uniform. For pure vapor, T^i is close to the saturation temperature, corresponding to the vapor pressure.

Governing equation and pressure jump

Combining the results from the conservation of momentum Eq. 1.12 and Eq. 1.17, we establish the governing equation that describes the interface dynamics (Nikolayev, 2022),

$$\frac{\partial h}{\partial t} + \frac{\partial}{\partial x}\left\{\frac{1}{\mu}\left[\frac{h}{2}(h+2l_\mathrm{s})\frac{\partial \sigma}{\partial x} + \frac{h^2}{3}(h+3l_\mathrm{s})\frac{\partial \Delta p}{\partial x}\right] - u_\mathrm{cl}h\right\} = -\frac{J}{\rho}, \tag{1.19}$$

in which the pressure jump across the interface is $\Delta p \equiv p_\mathrm{v} - p$. This equation is written in the frame of reference of the contact line receding at speed u_cl with respect to the tube wall. A big advantage of Eq. 1.19 over conventional hydrodynamics equations is that the free interface h is an explicit variable.

In the tube geometry, Δp is linked to the local curvature of the interface via the Laplace pressure,

$$\Delta p = \sigma\kappa = \sigma\left(K + \frac{1}{R-h}\right), \tag{1.20}$$

where κ is the interface curvature in 3D; R is the inner radius of tube; K is the local curvature in the 2D axial plane. Within the small slope approximation, $K \simeq \partial^2 h/\partial x^2$.

Liquid flows in thin films are characterized by high hydraulic resistance. In general, axial flows hardly exist in most parts of a liquid film, except in regions of intense variation in interfacial curvature, i. e. near contact lines and the transition from liquid films to menisci. The value of T^i is (nearly) equal to T_sat corresponding to p_v for pure fluids. Conversely, this simple assumption results in the mass flux divergence $\sim h^{-1}$ in Eq. 1.18, as $h \to 0$. This singularity is addressed in Subsec. 1.1.2.

1.1.2 *Film edges: triple contact line dynamics*

A conventional approach to the contact line problem in the presence of evaporation was proposed by Potash et al. (1972). They argued that attractive intermolecular forces generate a continuous wetting film of nanometric thickness, which stretches out from the contact line region and covers the solid surface entirely for any wetting conditions. The intermolecular forces were introduced through the disjoining pressure proportional to h^{-3}, where h is the thickness of the liquid. Vapor is not in direct contact with solid, and triple vapor-liquid-solid contact lines are non-existent; see the marginal illustration. However, Rednikov et al. (2011) contended that when the solid substrate is heated, and the solid superheating surpasses a threshold, this wetting film can dry out and give birth to a triple contact line. The threshold is typical of several K for complete wetting and zero under partial wetting conditions. Therefore, our discussions will neglect wetting films and assume three phases meet at the contact line with a microscopic contact angle on the solid surface, cf. Fig. 3a.

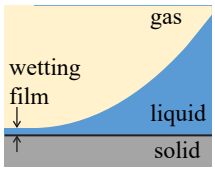

The free interface is a meniscus when liquid films are absent in capillary tubes. Contact lines can advance over or recede from dry patches at the same speed as the meniscus (Snoeijer et al., 2013). In another scenario, when the contact line is the edge of a long liquid film, its motion is decoupled from the meniscus. Due to capillary action, contact lines can only recede towards the liquid side, shortening film lengths (Snoeijer et al., 2010). This phenomenon is similar to the classical dewetting problem, whereas, in PHP channels, phase change often co-occurs (Zhang et al., 2022a). This section briefly discusses the dynamics of triple contact lines and several nanoscale effects, emphasizing the singularities due to contact line movement and phase change. The multiscale analysis of the dewetting phenomenon is also introduced.

1.1.2.1 *Relaxing the singularity at contact line*

Even for the adiabatic case (i. e. for $\Delta T = 0$), the conventional hydrodynamic description of moving contact lines (no-slip condition on the solid surface) leads to the divergence of viscous dissipation at the contact line where $h \to 0$ (deGennes, 1985), refer to Subsec. A.3.3 for details. Introducing the hydrodynamic slip condition of Eq. 1.10 to the liquid-solid boundary (Hocking, 1983) can avoid this singularity. As we approach the contact line, the liquid pressure diverges logarithmically, albeit remaining integrable, which suggests that the measurable hydrodynamic stress is finite and the singularity is relaxed.

Interfacial thermal resistance

The interfacial thermal resistance R^{i} is of importance for preventing evaporation rate J (Eq. 1.18) from diverging at contact line (Nikolayev, 2022). When J is high, the corresponding vapor escape speed is comparable with the thermal velocity of molecules (Nikolayev, 2022). The interfacial thermal resistance reads (see Sec. A.2 for details)

$$R^{\mathrm{i}} = \frac{T_{\mathrm{sat}}\sqrt{2\pi R_{\mathrm{g}} T_{\mathrm{sat}}/M}(\rho - \rho_{\mathrm{v}})}{2\mathcal{L}^2 \rho_{\mathrm{v}} \rho}, \tag{1.21}$$

where R_{g} is the universal gas constant, and M is the molar mass. R^{i} provides a correction term to T^{i} (Palmer, 1976):

$$T^{\mathrm{i}} = T_{\mathrm{sat}} + R^{\mathrm{i}} J \mathcal{L}. \tag{1.22}$$

In order to understand the physical meaning of R^{i}, substituting Eq. 1.22 into Eq. 1.18 yields,

$$J = \frac{\Delta T}{\mathcal{L}(h + kR^{\mathrm{i}})}. \tag{1.23}$$

From this equation, evidently, the length kR^{i} could be regarded as the thickness of an additional liquid layer, which has the same thermal resistance as the rest of the film. When a liquid film becomes very thin, i. e. $h \ll kR^{\mathrm{i}}$, the interfacial thermal resistance considerably curbs liquid evaporation. Thus, the length kR^{i} could be deemed as a characteristic scale, below which this local phenomenon dominates mass and heat transfer. Usually, the value of kR^{i} is of the order of $10\,\mathrm{nm}$, e. g. $kR^{\mathrm{i}} \simeq 20$ nm for n-pentane at $100\,\mathrm{kPa}$.

Kelvin effect

The account of R^{i} and l_{s} provides a finite J and a logarithmically divergent but integrable p at the contact line. However, Janeček et al. (2012) have demonstrated that the Kelvin effect alone can avert the singularity in J and result in a finite pressure at the contact line, which is more reasonable from the physical point of view and more pragmatic for numerical calculations where a pressure boundary condition can be imposed, instead of using the numerical matching to an asymptotic solution.

Wayner (1993) was the first to hypothesize that the moving contact line singularity could be relaxed for volatile fluids through evaporation/condensation when it matches contact line displacement. Rather than sliding over the solid, the contact line recedes because the liquid on it evaporates or advances by liquid condensation. It turns out to be possible thanks to the Kelvin effect, which provides the variation of T^{i} along with the interface that follows local curvature (see Sec. A.1 for the derivation):

$$T^{\mathrm{i}} = T_{\mathrm{sat}}\left(1 + \frac{\Delta p}{\mathcal{L}\rho}\right). \tag{1.24}$$

Janeček et al. (2013) and Rednikov et al. (2013) used the asymptotic matching to show that the Kelvin effect is sufficient to describe the contact line motion for volatile fluids. The interface is strongly curved near the contact line to agree with the phase change rate, which, in turn, is regulated by the contact line motion.

Vapor recoil

Though Janeček et al. (2012) have proved that the vapor recoil cannot relax contact-line singularities, it has a non-negligible impact on interface curvature (Janeček, 2012). The recoil pressure p_r (Nikolayev et al., 1999) is created at liquid-vapor interfaces by the fluid molecules escaping liquid towards vapor:

$$p_\mathrm{r} = J^2 \left(\frac{1}{\rho_\mathrm{v}} - \frac{1}{\rho} \right). \tag{1.25}$$

Because the vapor recoil modifies the pressure jump Δp,

$$\Delta p = \sigma\kappa - p_\mathrm{r}, \tag{1.26}$$

this effect appears in the expression of T^i via the Kelvin effect Eq. 1.24.

Together with the Kelvin effect and R^i, T^i differs from T_sat (Anderson et al., 2007):

$$T^\mathrm{i} = T_\mathrm{sat} \left[1 + \frac{\Delta p}{\mathcal{L}\rho} + \frac{J^2}{2\mathcal{L}} \left(\frac{1}{\rho_\mathrm{v}^2} - \frac{1}{\rho^2} \right) \right] + R^\mathrm{i} J \mathcal{L}. \tag{1.27}$$

Another nanoscale effect relevant to our discussion is the Marangoni effect, introduced in Eq. 1.3. Similar to the vapor recoil, it cannot relax the singularities either. Still, it is commonly included in problem formulation for its impact on interface curvature, especially over the region where the temperature gradient is large, for instance, near the contact line.

In conclusion, the theoretical studies of moving contact lines with phase change should account for the physical effects discussed before to relax the singularities and faithfully represent the phenomena in the narrow vicinity of contact lines down to the nanoscale.

1.1.2.2 *Multiscale analysis*

The analysis of moving contact lines with liquid evaporation is more complex than static scenarios. However, thanks to significant scale differences, the physical effects that govern the dynamics in one scale could be neglected in another (Snoeijer et al., 2013). In general, three scales are identified based on distance from contact lines; see Fig. 3 illustrated for the dewetting of a liquid film under partial wetting conditions (Janeček et al., 2013).

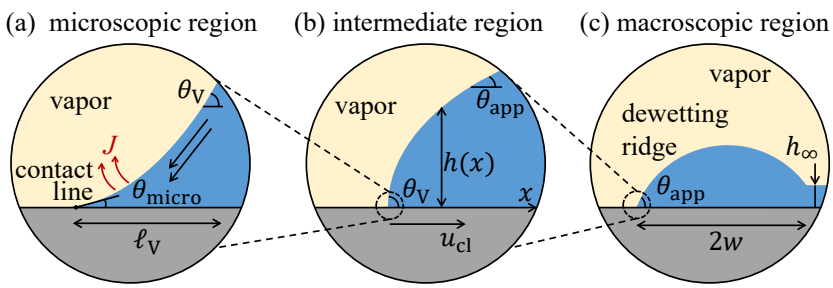

Figure 3: Length scale hierarchy in the case of a moving contact line: the dewetting of a liquid film. Three scales are depicted.

Microregion

The smallest scale is referred to as the microregion, in which the nanoscale effects introduced above significantly impact fluid behavior. The typical size of this region $\ell_{\mathrm{V}} \sim 100\,\mathrm{nm}$ is called hereafter the **Voinov length**. In Fig. 3a, the microregion is illustrated for a partial wetting case with microscopic contact angle θ_{micro}, which is the actual contact angle at triple phase contact line. Because phase change is the predominant phenomenon within this region, the impact of contact line motion is negligible, and the transient and u_{cl} terms thus can also be neglected in Eq. 1.19. At the right-hand boundary of the microregion (far from the contact line), the interface slope saturates to a value that is called the **Voinov angle** θ_{V}, which depends on θ_{micro} and ΔT (Janeček et al., 2012). Intense evaporation induces strong liquid flows towards contact lines, which, together with the vapor recoil, leads to highly curved interfaces in this region (Nikolayev, 2022). As a consequence, $\theta_{\mathrm{V}} > \theta_{\mathrm{micro}}$. The opposite tendency takes place at condensation. If the phase change is absent, $\theta_{\mathrm{V}} = \theta_{\mathrm{micro}}$.

Intermediate region

The intermediate region (typically between $100\,\mathrm{nm}$ and $100\,\mu\mathrm{m}$ from the contact line) is dominated by the flow induced by the contact line motion. The terms responsible for evaporation-induced flow (and discussed above microscopic effects) can all be neglected together with the transient term in Eq. 1.19. The interfacial shape is a result of the balance of surface tension and viscous forces. Many researchers have considered such a problem. Voinov (1976) and Cox (1986) have proposed an asymptotic law that predicts the interface slope ϕ as a function of u_{cl}:

$$\phi^3 = \theta_{\mathrm{V}}^3 - 9Ca \ln \frac{x}{\ell_{\mathrm{V}}}, \tag{1.28}$$

where the dimensionless dewetting speed (the capillary number) is $Ca = \mu u_{\mathrm{cl}}/\sigma$, positive for receding and negative for advancing over a dry patch. Considering the corresponding Stokes problem, Cox (1986) has indicated that its solution could be approximated with Eq. 1.28. The approximation remains accurate until interfacial slopes as high as $150°$ (Snoeijer et al., 2013). Two parameters, ℓ_{V} and θ_{V}, which appear as integration constants within the intermediate region problem, stem from the asymptotic matching to microregion solution.

Macroregion

One of the main objectives of problems involving the contact line is to calculate the apparent contact angle θ_{app}, i.e., the angle obtained at the macroscopic scale (an experimentally observable quantity). In Fig. 3c, θ_{app} is depicted for the dewetting problem, whose value corresponds to the size of the dewetting ridge (Snoeijer et al., 2010). The corresponding region is often called the macroregion. Such a problem is defined by the balance of the transient and surface tension terms in Eq. 1.19.

Snoeijer et al. (2010) considered the adiabatic dewetting problem. They have revealed that the macroscopic ridge shape is defined mainly by surface tension after initial transients. It means that θ_{app} can be obtained by fitting the ridge shape to a circle (Fig. 3c). With the singularity relaxation model based on the slip length, Snoeijer et al. (2010) performed the asymptotic matching between the contact line region, the macroscopic liquid ridge, and the flat film of thickness h_∞ in the adiabatic case. One of their central results is

$$\theta_{\mathrm{app}}^3 = \theta_{\mathrm{V}}^3 - 9Ca \ln \frac{2w}{e\ell_{\mathrm{V}}}, \tag{1.29}$$

where w is the ridge half-width (Fig. 3c) and $e \simeq 2.71$ is the Euler number. The problem solved by Snoeijer et al. (2010) is adiabatic; their ℓ_{V} is thus equal to

$$\ell_{\mathrm{Vsa}} = \frac{3l_{\mathrm{s}}}{e\theta_{\mathrm{micro}}}. \tag{1.30}$$

The central result of Snoeijer et al. (2010) is the asymptotic expression for the dewetting speed,

$$Ca = \frac{\theta_{\mathrm{V}}^3}{9}\left[\ln\left(\frac{4a}{e^2}Ca^{1/3}\frac{w^2}{\ell_{\mathrm{V}}h_\infty}\right)\right]^{-1}. \tag{1.31}$$

where $a \simeq 1.094$.

Though Snoeijer et al. (2010) used the slip length to relax the singularity, Fourgeaud et al. (2016) argued that Eq. 1.29 could be generalized to any microregion models because of the scale separation. In the case of phase change, if only the Kelvin effect is included, then we find a general expression for the Voinov length (Janeček et al., 2013),

$$\ell_{\mathrm{VK}} \simeq f(\varepsilon)\frac{\sqrt{3\mu kT_{\mathrm{sat}}}}{\theta_{\mathrm{V}}^2\rho\mathcal{L}}, \tag{1.32}$$

where

$$\varepsilon = \frac{\sqrt{3\mu kT_{\mathrm{sat}}}}{\sigma\theta_{\mathrm{V}}^3}\frac{\Delta T}{T_{\mathrm{sat}}}, \tag{1.33}$$

and $f(\varepsilon)$ is an increasing function shown in Figure 3(b) of Janeček et al. (2013); for positive ΔT, it varies between $f(0) \simeq 1.31$ and $f(\varepsilon_{\mathrm{c}}) \simeq 3.02$. Note that for large ΔT, ε saturates to a critical value $\varepsilon_{\mathrm{c}} \simeq 0.3$, which results in $\theta_{\mathrm{V}} \sim \Delta T^{1/3}$.

For stationary contact lines, $\theta_{\mathrm{app}} = \theta_{\mathrm{V}}$.

Theoretically, all three regions can be obtained by solving one equation, Eq. 1.19. This, however, requires a heterogeneous adaptive grid, which often causes numerical instabilities in solving nonlinear differential equations. The multiscale approach presented above permits separating the problem and dealing with simpler equations at different scales. Coupling the results using the asymptotic matching technique produces the full solution (Snoeijer et al., 2010; Janeček et al., 2016).

1.1.3 *Film thickness 1: deposition by liquid plugs*

Landau et al. (1942) have first theoretically investigated the deposition of liquid film on a plate vertically withdrawn from a liquid reservoir. Later, Bretherton (1961) examined the liquid deposition of Taylor bubbles (i. e. , bubbles of lengths much larger than their diameters) in capillary tubes. They have considered adiabatic $(J = 0)$ scenarios and the deposition of a meniscus receding at constant speed u_{m}.

Liquid films appear on solid surfaces as a result of competition between viscous and capillary forces in the transition region adjacent to liquid menisci where curvature gradients exist. The viscous friction tends to immobilize the fluid near the tube wall and thus increase the thickness. In contrast, the surface tension tends to minimize the meniscus area and reduce curvature, which consequently makes the film thinner. This competition is characterized by the meniscus capillary number $Ca_{\mathrm{m}} = \mu u_{\mathrm{m}}/\sigma$. Bretherton (1961) has proposed a theoretical formula for predicting the thickness of deposited liquid films δ_{dep}, under the condition that Ca_{m} is small, below $\sim 10^{-2}$. The formula was extended to moderate Ca_{m} up to 2 by Klaseboer et al. (2014). Based on experimental measurements, a dozen of empirical correlations have also been proposed (Aussillous et al., 2000; Han et al., 2010; Youn et al., 2016; Youn et al., 2018; Cheng et al., 2020). Some of them account for inertia effects during

the constant acceleration and deceleration of u_{m} that distorts the spherical shape of menisci. An example of these empirical correlations (Aussillous et al., 2000) is shown here,

$$\delta_{\mathrm{dep}} = \frac{0.67 d Ca_{\mathrm{m}}^{2/3}}{1 + 3.35 Ca_{\mathrm{m}}^{2/3}}. \tag{1.34}$$

However, in modeling PHPs, the liquid film behavior during meniscus oscillations (u_{m} a function of time) is of greater interest.

1.1.4 *Film thickness 2: impact of phase change*

Phase change at the contact line vicinity has been addressed in Subsec. 1.1.2. Here, we evaluate the phase change impact on interface profiles of the nearly flat portion of films.

Consider a liquid film deposited by a meniscus receding at a constant speed. The initial thickness can be approximated by Eq. 1.34. Neglecting the flow along film in Eq. 1.19, which is reasonable due to weak pressure gradient, the thickness variation in time due to phase change is

$$\rho \frac{\mathrm{d}h}{\mathrm{d}t} = -J, \tag{1.35}$$

where J is defined in Eq. 1.18, with $T^{\mathrm{i}} = T_{\mathrm{sat}}$. The free interface is inclined because the film deposited earlier is subject to evaporation or condensation.

For evaporating cases, the film interface slope was first introduced by Thome et al. (2004) for the flow boiling description and applied later to PHP modeling. Combining Eq. 1.18 and Eq. 1.35 and assuming a constant $\Delta T = T_{\mathrm{w}} - T_{\mathrm{sat}}$, we obtain

$$h(x,t) = \sqrt{\delta_{\mathrm{dep}}^2 - 2\frac{k\Delta T}{\mathcal{L}\rho}[t - t_0(x)]}, \tag{1.36}$$

where $t_0(x)$ is the time moment when the meniscus passes by the point x; the initial thickness δ_{dep} can be given by Eq. 1.34. Eq. 1.36 indicates that the film slope is controlled by the dimensionless parameter $k\Delta T/(\mathcal{L}\rho u_{\mathrm{m}}\delta_{\mathrm{dep}})$. Large wall superheating ΔT intensifies the phase change effect on interface inclination.

To summarize, the thickness of liquid films in PHPs is determined by two dynamic processes. The initial thickness depends on the motion of oscillatory menisci, which varies with time, and the local phase change conditions.

1.2 One-dimensional PHP models

This section recapitulates several existing one-dimensional computational PHP models. Flows in liquid plugs are commonly treated as single-phase flows in tubes. The pressure drop and heat transfer modelings have been well established and differ only on minor points between different sources. Since the energy exchange between vapor bubbles and liquid films dominates the system performance, this section will only compare how these two components are described in the numerical models. At this stage, the discussions focus on fluid behavior; thus, the liquid-solid coupling is not a priority.

1.2.1 *"Superheated vapor" models*

Many one-dimensional PHP models (Holley et al., 2005; Mameli et al., 2012) have been based on the pioneering work of Shafii et al. (2001). Their model employs the lumped-parameter method, where a control volume represents a vapor bubble or a liquid plug, and curved

interfaces are simplified; see Fig. 4. The liquid film drying and the dynamics of contact lines do not appear in their modeling.

Most of the time, Shafii et al.'s model uses the ideal gas law to describe the thermodynamic state of the vapor phase. Occasionally, if the vapor pressure p_v calculated by the ideal gas law is higher than the saturation pressure p_{sat}, corresponding to the vapor temperature T_v, p_v is set to p_{sat} (Shafii et al., 2001).

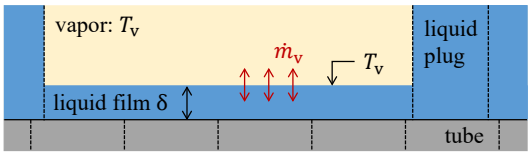

Figure 4: Schematics of "superheated vapor" models with the mass exchange in the vapor phase.

Based on the first law of thermodynamics, the vapor energy equation is written as (Nikolayev, 2011b),

$$c_{vv} m_v \dot{T}_v = R_g T_v \dot{m}_v - p_v \dot{\Omega}_v. \tag{1.37}$$

where c_{vv} is the vapor specific heat at constant volume; m_v and Ω_v are the mass and volume of vapor, respectively; the dot over a variable indicates the time derivative. Eq. 1.37 neglects the sensible heat transfer from tube walls directly to vapor.

The mass exchange rate in a vapor bubble $\dot{m}_v$ is calculated as

$$\dot{m}_v = \frac{\pi d}{\mathcal{L}} \left[U_e L_{ve} (T_e - T_v) + U_c L_{vc} (T_c - T_v) \right], \tag{1.38}$$

where d is the inner diameter of the tubes. Here, U_e, T_e, and L_{ve} are the heat transfer coefficient, tube wall temperature, and length of this bubble in the evaporator, respectively. Correspondingly, the subscript c denotes the quantities in the condenser. The heat transfer coefficient and tube wall temperature are assumed constant and susceptible to adjustment. Different simulations used different values of U_e and U_c. It is hard to justify why a specific value is chosen.

Eq. 1.38 states that the total heat transfer is defined by the temperature difference between the tube wall and T_v and is used to vaporize the liquid. We might interpret Eq. 1.38 equivalent to the energy transfer to a vapor bubble wrapped completely by a flat liquid film of invariable thickness $\delta = k/U_v$, where k is the liquid thermal conductivity, see Fig. 4.

Nikolayev et al. (2018b) constructed a similar model without the mass exchange term $\dot{m}_v$. The energy equation is written as

$$c_{vv} m_v \dot{T}_v = \pi d \left[U_e L_{ve} (T_e - T_v) + U_c L_{vc} (T_c - T_v) \right] - p_v \dot{\Omega}_v, \tag{1.39}$$

which states that pure heat exchange determines the system's behavior.

1.2.1.1 *Start-up analysis of single branch PHPs*

Das et al. (2010) investigated the start-up conditions by applying this model to single branch PHPs, the simplest configuration of this device. A single branch PHP is made of a straight capillary tube. A vapor bubble is confined between the sealed end of the tube and a liquid plug. The other end of the tube remains open and connects the liquid plug to a liquid reservoir, whose pressure is kept constant. Usually, heat is applied to the tube over the vapor section (evaporator) and is brought out from the condenser installed in the plug section. Only one meniscus oscillates in the tube. Fig. 40 shows an example of this configuration.

Das et al. (2010) established the start-up conditions via conventional linear stability analysis. First, they found the equilibrium states by setting the time derivative terms to

zero. The equilibrium-state equations are linearized with respect to a small perturbation that is then introduced to the system. When the perturbation grows with time, it suggests that the equilibrium is unstable, and start-up conditions are found. They also demonstrated the equivalence of the models with and without $\dot{m}_\mathrm{v}$ in determining the start-up criteria.

Das et al. (2010) reported that a single branch PHP described by superheated vapor models (with or without $\dot{m}_\mathrm{v}$) has an infinite number of equilibrium states, in which the meniscus can stay stationary in any section of the tube. Equilibrium positions of the meniscus in the evaporator and the adiabatic section are stable for any system parameters. In contrast to experimental observations, the meniscus is usually placed in these two sections of the tube in order to trigger oscillation (Recklin et al., 2015; Fourgeaud, 2016). Certain combinations of the system parameters satisfy the start-up conditions and can initiate and develop oscillatory behavior. However, the meniscus oscillates only in the condenser without penetrating the evaporator. Liquid evaporation hardly takes place, which is a non-physical behavior.

1.2.1.2 *Simulation of multi-branch PHPs*

Shafii et al. (2001) investigated the effects of tube diameter, filling ratio, and tube wall temperature on the performance of looped and unlooped multi-branch PHPs. However, their conclusion that heat transfer is due mainly to the exchange in liquid plugs (it was called sensible heat in plugs in the original paper) is not in agreement with the later experimental and numerical results (Nikolayev, 2011a; Francom et al., 2021). The value of $U_\mathrm{e} = 150\,\mathrm{W/(m^2{\cdot}K)}$ used in the calculations of Shafii et al. (2001), is equivalent to the heat transfer coefficient of a flat ethanol film of thickness $\delta = k/U_\mathrm{e} \simeq 1.07\,\mathrm{mm}$, where $k \simeq 0.161\,\mathrm{W/(m \cdot K)}$, which is much thicker than typical films encountered in PHPs. This might explain why the latent heat transfer was underestimated.

Sakulchangsatjatai et al. (2004) compared the overall energy transfers resulting from Shafii et al.'s model and existing experimental data and obtained a satisfactory agreement. However, their simulations did not mention the tunable values of heat transfer coefficients U_e and U_c.

Holley et al. (2005) introduced heat conduction in tube wall and liquid-solid thermal coupling, which was a great step forward in developing computational models for PHPs. Therefore, T_w in Eq. 1.38 is not constant. They replaced the heat transfer coefficient in Eq. 1.38 with the heat transfer coefficient for boiling flow. However, the vapor energy equation was not correctly used. Later, in their simulations, Mameli et al. (2012) included the pressure loss at tube bends.

Yoon et al. (2017) implemented Shafii et al.'s model on simulations of a 5-turn micro-PHP, which was charged with ethanol and vertically orientated with a heat source applied at the bottom. They obtained small-amplitude oscillation, similar to their experimental observation.

More recently, Bae et al. (2017) compared the experimental data with the simulation results of a 30-branch PHP. For vertical orientation, Shafii et al.'s model is capable of producing similar oscillatory behavior. However, for horizontally positioned cases, the model fails to initiate oscillation for any reasonable values of U_e and U_c.

1.2.1.3 *Comments on Shafii et al.'s model*

In summary, choosing the appropriate values for U_e and U_c impacts results greatly. In many calculations, the value of U_e differs from U_c. Given the same heat transfer conditions over the device, this assumption can hardly be justified.

Simulations produced by this model show a steady oscillation regime after a transient stage, during which the number of liquid plugs drops from the initially imposed large value to the number of turns in PHP. The system oscillation is periodical, nearly sinusoidal, at a small amplitude. In other words, the device functions as an assembly of oscillating liquid clots coupled through vapor bubble springs (Nikolayev, 2021).

Simplicity is the most significant advantage of this model, whereas the liquid film, the most unique and central player for PHP functioning, is underrepresented. The contact lines' dynamics is neglected completely, and the model cannot describe partially dried tube walls. Consequently, the simulation results rely essentially on vapor bubble behavior. Therefore, this type of modeling is referred to as the *Superheated vapor* models by Das et al. (2010), in contrast to the models in ensuing subsections, which include dynamic liquid films.

1.2.2 *Film Evaporation-Condensation (FEC) model*

Das et al. (2010) developed the FEC model that introduces dry patches on tube wall. They adopted the lumped meniscus geometry; see Fig. 5, and simplified the description of spatially distributed fluid behavior in the radial direction. All liquid films are of constant thickness δ, but their lengths vary individually with time, responding to mass exchange over the film. This subsection summarizes features of the FEC model, mainly on how phase exchange is described over liquid films and how the contact line dynamics is modeled.

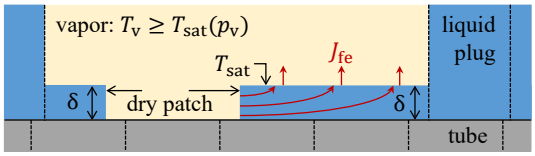

Figure 5: Schematics of Film Evaporation-Condensation model developed by Das et al. (2010).

Vapor phase

Similar to the previous model, the thermodynamic state of the vapor phase is described by the ideal gas law, which suggests that the vapor phase is superheated most of the time. Occasionally, if the vapor pressure p_v calculated by the ideal gas law is higher than the saturation pressure p_{sat} corresponding to the vapor temperature T_v, p_v is set to p_{sat}.

Based on the first law of thermodynamics, the vapor energy equation that includes mass exchange, work done by volume expansion, and sensible heat transfer is written as (Shafii et al., 2001;Nikolayev, 2011b),

$$m_v c_{vv} \dot{T}_v = R_g T_v \dot{m}_v - p_v \dot{\Omega}_v + \pi d U_{sens} \int_{L_v} [T_w(x) - T_v] \mathrm{d}x, \tag{1.40}$$

where U_{sens} is the coefficient of sensible heat transfer, and L_v is the length of dry patch on tube wall. The temperature of tube wall $T_w(x)$ varies along the tube axis x. The total mass exchange $\dot{m}_v$ consists of two contributions, from the liquid film $\dot{m}_f$ and from the meniscus $\dot{m}_m$:

$$\dot{m}_v = \dot{m}_f + \dot{m}_m, \tag{1.41}$$

which is positive for net mass transfer to the vapor phase.

Film description

Neglecting the heat transfer from interface to vapor, the total mass exchange rate $\dot{m}_\mathrm{f}$ is the sum of evaporation mass flux J_fe and condensation flux J_fc,

$$\dot{m}_\mathrm{f} = J_\mathrm{fe} + J_\mathrm{fc}, \tag{1.42}$$

where

$$J_\mathrm{fe} = \frac{U_\mathrm{f}\pi d}{\mathcal{L}} \int_{L_\mathrm{fe}} [T_\mathrm{w}(x) - T_\mathrm{sat}]\mathrm{d}x, \quad J_\mathrm{fc} = \frac{U_\mathrm{f}\pi d}{\mathcal{L}} \int_{L_\mathrm{fc}} [T_\mathrm{w}(x) - T_\mathrm{sat}]\mathrm{d}x, \tag{1.43 a,b}$$

where the heat transfer coefficient of liquid films $U_\mathrm{f} = \varsigma k/\delta$, with the form factor ς (detailed in Subsec. 5.4.3); L_fe and L_fc are the portion of a liquid film where the tube wall temperature $T_\mathrm{w}(x)$ is higher and lower than T_sat, respectively. Remarkably, rather than being proportional to $T_\mathrm{w} - T_\mathrm{v}$ in Shafii et al.'s model, $\dot{m}_\mathrm{f}$ is proportional to the temperature difference between T_w and T_sat, in agreement with Eq. 1.23. The interface has the temperature T_sat.

Similarly, the meniscus contribution $\dot{m}_\mathrm{m}$ is calculated as,

$$\dot{m}_\mathrm{m} = \frac{\pi d U_\mathrm{m} L_\mathrm{m}}{\mathcal{L}} \left[T_\mathrm{w}(x_\mathrm{m}) - T_\mathrm{sat}\right], \tag{1.44}$$

where U_m is the heat transfer coefficient and L_m is the size of meniscus that participates in mass exchange; $T_\mathrm{w}(x_\mathrm{m})$ is the wall temperature at the meniscus.

Introducing drying liquid films (the contact line dynamics) is a huge progress compared to the previous model. The velocity of a liquid film edge u_cl is calculated as

$$u_\mathrm{cl} = J_\mathrm{fe}/\rho S_\mathrm{f}, \tag{1.45}$$

where $S_\mathrm{f} = \pi\delta(d - \delta)$ is the film cross-section. This equation states that to conserve the mass loss J_fe, the film edge recedes, shortening the length. The reason u_cl responds to J_fe rather than $\dot{m}_\mathrm{f}$ is to avoid non-physical film expansion that might occur when the amount of condensed mass $|J_\mathrm{fc}|$ surpasses J_fe, for instance, when $L_\mathrm{fe} \ll L_\mathrm{fc}$. In that case, the liquid film has to extend towards the dry patch, prolonging the film length. However, contact lines can only recede in reality, as discussed in Subsec. 1.1.2. The condensed mass $|J_\mathrm{fc}|$ is conserved by reassigning it to the adjacent liquid plugs.

Now the question is how to determine the fixed *a priori* value of δ. Nekrashevych et al. (2017, 2019) have resolved this issue by an iteration algorithm. The first round of simulation uses a tentative value of δ. Then the results are used to find the root mean square of plug velocity $u_\mathrm{m,RMS}$. Eq. 1.34 can predict the thickness of deposited liquid film δ' corresponding to $u_\mathrm{m,RMS}$. The next round of simulation uses δ'. This process is repeated until convergence between δ and δ' is achieved.

1.2.2.1 *Modified FEC model*

Rao et al. (2017) employed a modified version of the original FEC model. They have introduced two improvements. First, liquid films remain spatially homogeneous, but the thickness is not constant. The time variation of film thickness $\delta(t)$ is defined as

$$\dot{\delta} = -\frac{J_\mathrm{fe}}{\rho\pi d L_\mathrm{fe}}, \tag{1.46}$$

where J_fe is given by Eq. 1.43 with a constant U_f.

Secondly, evaporation flux at the contact line J_cl determines the receding speed. Eq. 1.45 is modified as

$$u_\mathrm{cl} = J_\mathrm{cl}/\rho\pi d\delta(t) \tag{1.47}$$

where

$$J_{\mathrm{cl}} = \begin{cases} \dfrac{U_{\mathrm{cl}}}{\mathcal{L}} \pi d \delta(t)(T_{\mathrm{w,cl}} - T_{\mathrm{sat}}), & \text{if } T_{\mathrm{w,cl}} > T_{\mathrm{sat}}, \quad (1.48a) \\ 0, & \text{otherwise}, \quad (1.48b) \end{cases}$$

Here, U_{cl} and $T_{\mathrm{w,cl}}$ are the heat transfer coefficient and wall temperature at the contact line, respectively. Because the value of U_{cl} is obtained experimentally, this model is not universal.

In contrast to the original FEC model, Eq. 1.47 states that the contact line recedes due to local evaporation rather than the total evaporation over a film. Therefore, liquid flows along the film are averted, in agreement with the thin liquid film theory. For this reason, the extended model is deemed an improved version of the original version. Using the extend FEC model, Rao et al. (2017) have found that the thickness variation over an oscillation period is weak, compared to the value of δ. This supports the constant-thickness assumption in the original FEC model. However, an additional parameter U_{cl} is required to be determined experimentally.

1.2.2.2 *Simulation of single branch PHPs*

Das et al. (2010) performed simulations of a single branch PHP using the original FEC model. The working fluid was n-pentane, and the temperature of the inner tube wall in the evaporator (T_{e}) and in the condenser (T_{c}) were imposed constant (liquid-solid coupling was not considered). Given different values of T_{e} and T_{c}, their numerical results predicted two oscillation regimes that were observed experimentally (Gully et al., 2014; Recklin et al., 2015; Fourgeaud et al., 2017; Tessier-Poirier et al., 2019). In the first regime, the meniscus oscillation is quasi-sinusoidal (Fig.6b of Das et al., 2010). A large amount of phase change can produce large oscillation amplitude, resulting in fast variation in film length, cf. Eq. 1.47. In the second regime, the amplitudes of two consecutive strokes of the meniscus are different (cf. Fig.6a of Das et al., 2010), and the oscillation period doubles. Rao et al. (2017) also obtained similar behavior in their simulations using the extended FEC model. The working fluid was FC-72 (more precisely, n-perfluorohexane), and the values of T_{e} and T_{c} were also imposed constant. Because phase exchange is less intense, the system has to accumulate more evaporated mass to provide a fierce pulse that enables the meniscus to penetrate the evaporator. Comparisons of the numerical results and the experimental data exhibit a good quantitative agreement in oscillation amplitude and vapor pressure (Das et al., 2010; Rao et al., 2017).

Nikolayev (2016) investigated the impact of fluid-solid coupling on determining the start-up criteria of single branch PHPs. The study compared two configurations, which (i) imposed constant values of T_{e} and T_{c} (Nikolayev, 2013); (ii) imposed heat power P_{e} to the evaporator and constant T_{c}. Heat conduction in the tube wall and fluid-solid heat exchange occur in the evaporator and adiabatic section. Therefore, T_{w} varies along the two sections of the tube. In the second configuration, the system processes only a unique equilibrium state, in which the liquid film is absent, and the meniscus situates at the position where $T_{\mathrm{w}} = T_{\mathrm{sat}}$. Any deviation from this equilibrium state would cause a net mass exchange and, consequently, a meniscus displacement that grows with time.

The stability analysis has established a start-up criterion, which is proven independent of liquid film thickness δ (Nikolayev, 2016). This contrasts the imposed temperature case, where oscillations can develop only under a specific range of δ (Nikolayev, 2013). Moreover, since the liquid film description to system start-up is noncontingent, the mass exchange at meniscus Eq. 1.44 plays a crucial role in initiating oscillation. This feature is also contrary to the imposed temperature case, where the mass exchange over liquid film is sufficient to

set off meniscus oscillation. The difference signifies the importance of temperature gradient in the tube wall (in the evaporator) for correctly understanding system start-up.

In summary, the start-up threshold given by the FEC model can be easily interpreted and is more realistic than the threshold given by Shafii et al.'s model (Nikolayev, 2021). A single branch PHP can begin to oscillate when phase change is sufficiently large, and the power injected to evaporator P_e exceeds energy dissipation, which consists of the heat losses due to vapor-tube exchange and the liquid viscous dissipation.

1.2.2.3 *Simulation of multi-branch PHP*

Nikolayev (2011a) first extended the FEC model to simulate multi-branch PHPs with an arbitrary length of the adiabatic section and constant inner wall temperatures as boundary conditions for the system. The computational software that implements the FEC model has been developed at CEA and is named CASCO, abbreviated from the French *Code Avancé de Simulation de Caloduc Oscillant*: Advanced code for simulation of pulsating heat pipes. Over the years, new features have been progressively included in CASCO, which enables the code to reflect more physical processes, such as fluid-solid interaction, heat conduction in the solid tube wall, bubble and plug coalescence, nucleate boiling (generating new bubbles) in plugs, the feedback section and local pressure drop at tube turns (see Fig. 1).

CASCO can simulate PHPs of various structures, particularly those equipped with multiple heat sources or heat sinks. The heat is injected uniformly into the tube wall in evaporators, while the temperature of the inner tube wall in condensers is imposed constant. Liquid film rupture is considered, and more than one dry patch may exist in a single bubble. Conservation of energy and mass in the system and the mesh grid independence have been meticulously verified in CASCO (Nekrashevych et al., 2019).

Abela et al. (2019) compared experimental data and simulation results by CASCO of a closed-loop tubular PHP. The device contains a 14-turn fluid channel and has two condensers and an evaporator that are separated by three adiabatic sections. The working fluid is FC-72 with a filling rate of $50\,\%$. The experiment was conducted under microgravity conditions during a parabolic flight. Because of the large tube diameter ($3\,\mathrm{mm}$), the device cannot operate under the Earth's gravity. Unfortunately, the microgravity condition was maintained roughly $20\,\mathrm{s}$, which was too short to achieve a stable operation regime. Therefore, the simulations show transient behavior that depends on the initial conditions. Abela et al. (2019) have assumed that prior to the microgravity condition, the liquid plugs gather on the evaporator side, and the internal wall is covered completely by liquid films. The comparisons include the tube temperature and plug velocity at several measurements. A good agreement has been archived.

To evaluate the role that liquid film dynamics plays in the device functioning, a comparative study by Bae et al. (2017) has employed the FEC model to simulate multi-branch PHPs of various system parameters. Only one dry patch was considered per bubble. Instead of using the iteration method of Nekrashevych et al. (2017) to determine δ, the simulations set different δ in the same configuration to examine its impact on results. They have concluded that properly choosing δ enables the FEC model to produce the thermal performance and oscillation behavior that are in satisfactory agreement with experimental observation. However, the results depend heavily on the value of δ.

1.2.2.4 *Comments on the FEC model*

As described in Eq. 1.47, the mass loss of a film leads to an instantaneous receding of film edge, which implies a fast hydrodynamic flow along the film, depicted in Fig. 5. However, the

assumption can barely be justified from a physical point of view since the strong viscous shear would prevent liquid from flowing within these thin films. cf. the hydrodynamic description in Subsec. 1.1.1. On the other hand, free contact lines recede spontaneously after liquid film deposition. It is a local phenomenon that should be determined by local parameters, such as the wetting properties (contact angle) and the superheating at contact lines, rather than the overall mass conservation on liquid film, as discussed in Subsec. 1.1.2.

1.2.3 *Discrete volume models*

The discrete volume model was first developed by Senjaya et al. (2013). Later it was adapted and improved by several research groups (Bae et al., 2017; Noh et al., 2020; Rouaze et al., 2021). The tube and fluid channel are discretized into control volumes containing tube walls, vapor bubbles, and liquid films, or liquid plugs; see Fig. 6. The thermal coupling of fluid and solid and new bubble generation in liquid plugs (nucleation) are often considered (Senjaya et al., 2014; Bae et al., 2017; Rouaze et al., 2021). Conservation equations for mass, momentum, and energy must be established in each control volume (only energy equation for solid tube).

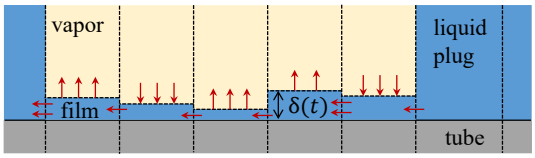

Figure 6: Schematic of a discrete volume model.

The computational meshes of liquid films are consecutive liquid rings with a flat interface as shown Fig. 6. In a control volume, a liquid film completely covers the tube's inner wall, and the thickness $\delta(t)$ evolves individually as a result of a mass exchange with neighbor volumes (or with plugs) and phase change at interface $\dot{m}_{\mathrm{v}}$. Bubble movements entrain liquid into films at the front meniscus, which triggers the mass exchange among the consecutive control volumes of liquid films. Eventually, liquid leaves films at the rear meniscus. Such a description treats the flow inside a film control volume as a uniform flow in annular tubes. This conflicts with the liquid film dynamics, cf. Eq. 1.19, which suggests that the flows should be induced by the gradient in interface curvature.

The momentum equations in liquid control volumes (films and plugs) used the 1D Navier-Stokes equation for incompressible flows, with only minor differences in source term (Senjaya et al., 2013, 2014; Bae et al., 2017; Rouaze et al., 2021). For liquid films, the source terms principally include friction forces on vapor-liquid interfaces and the inner tube walls and gravity force. Bae et al. (2017) considered the momentum loss due to the mass exchange with the vapor phase. For control volumes of liquid plugs, the source term excludes the interface friction.

Similarly, the energy conservation in liquid control volumes is based on the 1D energy equation for incompressible flows, with a source term representing heat exchange with the tube. An additional term for heat exchange with vapor is required for liquid films. The exact form of this term differs from one model to another.

1.2.3.1 *Vapor bubbles and phase exchange*

Senjaya et al. (2013, 2014) employed the ideal gas law to describe the thermodynamic state of the vapor phase. The heat flux in liquid films Q_f is calculated as

$$Q_\mathrm{f} = \frac{k}{\delta}(T_\mathrm{w} - T^\mathrm{i}), \tag{1.49}$$

where the interface temperature $T^\mathrm{i} = 2T_\mathrm{f} - T_\mathrm{w}$. Here, T_f is the film temperature determined by the energy equation. However, the phase change rate $\dot{m}_\mathrm{v}$ in a control volume is independent of Q_f. Instead, it is calculated as follows:

$$\dot{m}_\mathrm{v} = \alpha[p_\mathrm{sat}(T^\mathrm{i}) - p_\mathrm{v}].$$

where the constant $\alpha = 5.4 \times 10^{14}\,\mathrm{kg/(Pa \cdot s)}$, and $p_\mathrm{sat}(T^\mathrm{i})$ is the saturation pressure corresponding to T^i.

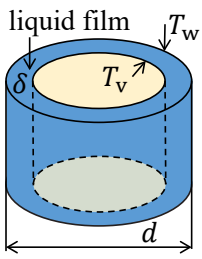

Aubin et al. (2019) and Rouaze et al. (2021) assumed that the vapor phase does not stray far away from the saturation state. Therefore, the phase change rate is determined by the difference between the saturation temperature and the temperature of the inner tube wall. Rouaze et al. (2021) mended the heat exchange description in their previous studies (d'Entremont et al., 2015; Aubin et al., 2019), where the heat transfer in liquid films is calculated as the heat conduction through a thin flat plate. Rouaze et al. (2021) argued that the heat flux through films could be better represented by the heat equation of a hollow cylinder for conduction in the radial direction; see the marginal illustration. The phase change rate per unit of length in the tube axis direction is

$$\dot{m}_\mathrm{v} = \left(\frac{1}{2\pi k}\ln\frac{d}{d-2\delta}\right)^{-1}\frac{T_\mathrm{w} - T_\mathrm{v}}{\mathcal{L}}, \tag{1.50}$$

where $T_\mathrm{v} = T_\mathrm{sat}$.

Bae et al. (2017) and Noh et al. (2020) employed the van der Waals equation to describe the vapor thermodynamic state. They postulated that the difference in the amount of heat transferred from the tube to films Q_f and from the interface to vapor Q^i is used to vaporize the liquid. Therefore, the phase change rate per unit of length channel is

$$\dot{m}_\mathrm{v} = \pi(d - 2\delta)\frac{Q_\mathrm{f} - Q^\mathrm{i}}{\mathcal{L}},$$

where

$$Q_\mathrm{f} = \frac{k}{\delta/2}(T_\mathrm{f} - T_\mathrm{sat}), \tag{1.51}$$

in which T_f is the temperature of liquid film, determined by energy balance.

1.2.3.2 *Liquid dryout*

The description of liquid dry-out is a unique feature of discrete volume models. As $\delta(t)$ might drop to an extremely low value, preventing the mass flux from diverging cf. Eq. 1.49, Eq. 1.50 and Eq. 1.51, requires introducing a critical value δ_cr that limits the heat conduction through liquid films. Following the practice of the three-zone model (Thome et al., 2004), Bae et al. (2017) and Rouaze et al. (2021) used the mean surface roughness as the value of δ_cr, at which the calculations put a halt to phase change and mass exchange with neighbor control volumes, and it is regarded as the occurrence of film dry out.

1.2.3.3 *Simulation results*

Bae et al. (2017) conducted simulations of PHPs with various configurations employed in previous experimental studies, including the different numbers of branches, working fluids, filling ratios, operation temperatures, and orientations. Numerical results exhibited good agreement with experimental data in thermal performance and oscillation behavior. They have concluded that the liquid film dynamics is indispensable for theoretically predicting plug oscillation in horizontally-oriented PHPs. For vertical PHPs, the film dynamics is less significant because the circulation can be driven by buoyancy. In the following study, using a similar computational model, Noh et al. (2020) investigated the number of branches and the inner diameter of the tube that would maximize the thermal performance of a closed-loop PHP in the vertical orientation under the constraint of fixed space.

Rouaze et al. (2021) validated their computational model by comparing simulation results and experimental data of a closed-loop PHP prototype with 20 branches. The working fluid was R1233zd(E), and the filling ratio was 70%. Horizontal and vertical orientations were considered. A heat load up to 230 W was applied to the evaporator, and a thermal bath chilled the condenser with water at 20°C. The comparisons mainly concerned the tube wall temperature at measurement points spreading over the device. They also obtained the oscillation and circulation regimes under normal operation. In the oscillation regime, the average velocity of liquid plugs $\langle u_{\mathrm{m}} \rangle$ is close to zero, whereas $\langle u_{\mathrm{m}} \rangle$ is non-zero in the circulation regime, which indicates the fluid has a preferential moving direction.

1.2.3.4 *Comments on discrete volume models*

Discrete volume models are based on phenomenological considerations rather than the fundamental physical processes leading to liquid film evolution. The spatial variation of film interfaces is represented better than Shafii et al. (2001) and the FEC models. The liquid flows in individual control volumes of the film are assimilated as flows in annular channels. However, in reality, as discussed in Sec. 1.1, liquid flows are induced by the curvature gradient over interfaces. The variation in film length that should rely on the contact line dynamics is not considered.

Discrete volume models include marginal effects such as shear stress at the vapor-liquid interface and pressure gradients within vapor bubbles. Those effects increase the complexity of modeling and numerical implementation, whereas they only have inconsequential contributions to the system behavior.

The conservation equations are resolved at each time step in all four domains (liquid films, plugs, vapor bubbles, and solid tubes). To obtain results independent of the mesh grid, the size of control volumes is in the order of $\sim 1\,\mathrm{mm}$ (Noh et al., 2020). It would significantly increase the number of control volumes for PHPs with a large number of branches, which is necessary to produce mesh-independent results. A considerably more computational resource is required than the FEC model.

Bae et al. (2017) compared the simulation results produced by their discrete volume model and by the FEC model. Both models can reasonably predict the plug oscillation and overall thermal performance observed in experiments. Since the primary objective for PHP simulation is to predict the device operation regimes, the detailed information on fluid behavior produced by discrete volume models seems less desirable (Nikolayev, 2021).

1.3 Conclusions

This chapter has been dedicated to introducing liquid film dynamics in capillary tubes and demonstrates its importance in PHP functioning. The Stokes equations and lubrication approximation have been employed in formulating the governing equations that describe the dynamic profile of the 2D free interface, which later will be used in Chap. 2. Although some of the existing 1D numerical models can produce results comparable to experimental data, they rely on adjustable phenomenological parameters, and the physical processes of liquid films are inadequately represented. Shafii et al.'s model neglects the dynamics of contact lines. The FEC model relies on the preset constant value of film thickness as input and implicitly introduces large flows along liquid films, which is a non-physical assumption. Discrete volume approaches have been based on phenomenological considerations instead of on the hydrodynamic theory of thin films.

Given that latent heat transfer through liquid films is the dominant mechanism for this device, a reliable computational model should reflect the physical behavior of liquid films in PHPs. Some of the processes are unique and have been less studied in the past. New theoretical studies are necessary to answer questions, such as how liquid films respond to oscillatory menisci and how contact lines recede in fluid channels in the presence of liquid evaporation.

Part I

Liquid Film Dynamics

Chapter 2

Liquid films attached to oscillatory menisci

As the first part of our theoretical studies, this chapter deals with liquid film behavior during the oscillation of a meniscus. [1]

Apart from occurring in PHPs, the oscillatory motion of menisci in thin capillaries is important for many applications. To cite a few, the liquid plugs that obstruct the airways in living organisms for certain pathologies (Baudoin et al., 2013), the distribution of fluids in microfluidics (Angeli et al., 2008), and the oscillations caused by the vapor-liquid mass exchange in many types of heat pipes. In capillary pumped loops (Zhang et al., 1998) or loop heat pipes, pressure oscillations are observed (Launay et al., 2007) and impact the menisci in capillary structures.

Hydrodynamics of liquid films deposited by receding menisci has been extensively studied since the seminal articles of Landau et al. (1942), Taylor (1961) and Bretherton (1961). Since their works, a substantial effort has been invested in understanding the dynamics of the Taylor bubbles, i. e. bubbles of a length larger than their diameter. Initially, the hydrodynamics of such a process was described theoretically within the creeping flow approximation (i. e. for vanishingly small Reynolds numbers) by using the lubrication approach for the liquid film description. The inertial effects have been accounted for by direct numerical simulation (Talimi et al., 2012).

Previous studies have focused on the uniform motion of bubbles that deposit liquid films of constant thickness. The films were considered continuous, with no dry patches on the tube wall. However, oscillatory menisci are of greater interest for modeling PHPs (Fourgeaud et al., 2017; Marengo et al., 2018; Nikolayev, 2021), because liquid films provide the primary channel of heat and mass transfer and behave differently under the non-uniform motion of menisci. Moreover, the liquid evaporation rate is defined by local film thickness; adequate modeling requires knowing film profiles. As liquid films might be partially dried out, triple contact lines also need to be accounted for in our studies.

In this chapter, the objectives are twofold: (i) to study the liquid films created by meniscus oscillation; (ii) and to examine the impact of film edges, i. e. , of triple contact lines, for the simplest case where contact lines are pinned at surface defects and are thus immobile.

1 This chapter is based on the article (Zhang et al., 2021).

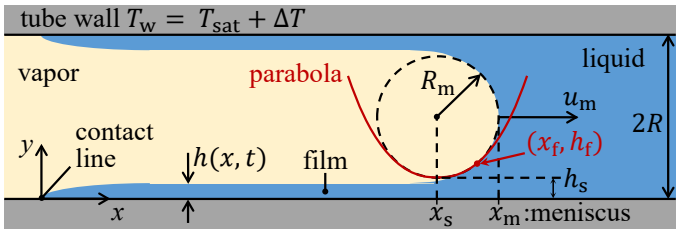

Figure 7: Sketch of the axial cross-section of a cylindrical capillary tube with the liquid film deposited by the receding meniscus. At $x = x_f$, the film profile solution matches the right branch of the parabola (solid red line), which is a small-slope approximation of the circular meniscus shape (dashed line).

2.1 Problem description

Consider a cylindrical capillary tube of an inner radius R, containing a liquid and its vapor. The vapor-liquid interface is assumed to be axially symmetric (Fig. 7).

For sufficiently thin tubes, the gravity force can be neglected. Following the classical approach (Bretherton, 1961), the vapor-liquid interface can be divided into the film and the meniscus regions. The liquid-vapor interface slope in the film region is believed to be small; therefore, the film can be described with the conventional lubrication theory briefly restated in Subsec. 1.1.1.2. The meniscus region is assumed to be controlled by the surface tension only, thus being of constant curvature (shown in Fig. 7 with a circle of radius R_m).

The lubrication theory is applicable within the assumption $|\partial h/\partial x| \ll 1$, where $h = h(x,t)$ is the local film thickness. The pressure jump $\Delta p = p_v - p$ across the interface obeys the normal jump condition Eq. 1.20 without the vapor recoil term,

$$\Delta p = \sigma \left(K + \frac{1}{R-h} \right) \simeq \sigma \left(\frac{\partial^2 h}{\partial x^2} + \frac{1}{R_m} \right), \tag{2.1}$$

where σ is the surface tension, K is the two-dimensional interface curvature in the axial cross-section shown in Fig. 7; in the small-slope approximation, $K \simeq \partial^2 h/\partial x^2$. Because of this limitation, such a film region theory is hardly suitable to describe the meniscus region. The radial contribution to the curvature R_m^{-1} is assumed to be independent of x in the film region (where h remains much smaller than R). At a large x, the interface approaching the tube axis results in an increasingly larger h, where the viscous forces vanish, and the surface tension controls the interface; its curvature $\partial^2 h/\partial x^2$ thus becomes constant. Such a condition corresponds to a parabolic shape in the axial plane. This parabola needs to be joined to the circular meniscus, which results in the condition

$$\partial^2 h/\partial x^2|_{x=x_f} = R_m^{-1}. \tag{2.2}$$

defined at the ending point $(x_f,\ h_f)$ of the film region.

2.2 Isothermal problem with infinite film

To begin with, we would like to recall the theory for cases with no phase change ($J = 0$), and contact lines are not considered, meaning that the film is infinitely long. In this case, it is pragmatic to choose the frame of reference linked to the moving meniscus where the axial coordinate becomes $x' = x - u_m t$. The velocity of the axial meniscus center (assumed positive for a receding meniscus according to the x-axis direction choice) is denoted u_m. Since $J = 0$, we take the minimal complexity of Eq. 1.19: non-slip condition on the inner

tube wall $l_s = 0$ and non-tangential-stress at the free interface. The governing equation becomes

$$\frac{\partial h}{\partial t} + \frac{\partial}{\partial x'}\left(\frac{\sigma}{3\mu}h^3\frac{\partial^3 h}{\partial x'^3} - u_m h\right) = 0, \tag{2.3}$$

which is used in the rest of this section.

2.2.1 *Steady solutions*

The steady version of Eq. 2.3 for the case of a constant positive velocity ($u_m = u_r$) is the Landau-Levich equation (Landau et al., 1942) describing the infinite flat film being deposited by a receding meniscus. Note that the film in a cylindrical capillary (Bretherton, 1961) is described by the same equation because of the approximation, Eq. 2.1.

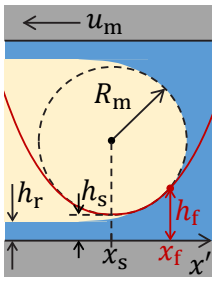

The boundary conditions at $x' \to -\infty$ describe flat films of yet unknown thickness h_r,

$$h = h_r,\ \partial h/\partial x' = 0. \tag{2.4}$$

The scaling of this problem (Tab. 1) is based on h_r. The characteristic axial length scale involves the capillary number $Ca_r = \mu u_r/\sigma$ and is chosen in such a way that rends the steady version of Eq. 2.3 dimensionless

$$\frac{\partial}{\partial \tilde{x}'}\left(\frac{\tilde{h}^3}{3}\frac{\partial^3 \tilde{h}}{\partial \tilde{x}'^3} - \tilde{h}\right) = 0, \tag{2.5}$$

which does not contain any parameters; the tilde means hereafter the corresponding dimensionless variable hereafter.

Integrating Eq. 2.5 from $-\infty$ to $\tilde{x}'$ and using the conditions (2.4) (in the dimensionless form, $\tilde{h}(\tilde{x}' \to -\infty) = 1$), we obtain

$$\frac{\partial^3 \tilde{h}}{\partial \tilde{x}'^3} = 3\frac{\tilde{h} - 1}{\tilde{h}^3}, \tag{2.6}$$

which is equivalent to the Bretherton equation within a factor 3 that we leave in the equation instead of bundling inside the scaling parameters of Tab. 1. This helps us to avoid it in many formulas used below.

Consider now the behavior at large $\tilde{x}'$. Eq. 2.6 remains valid until the transition region (between the film and the meniscus), in which $1 \ll \tilde{h} < \tilde{R}$. From Eq. 2.6, $\partial^3\tilde{h}/\partial\tilde{x}'^3 \simeq 0$. This means that $\tilde{x}'$, the second derivative is finite, which is compatible with the condition (2.2). Eq. 2.6 can be integrated numerically (see Nikolayev et al. (2014) for details). The ending point $(\tilde{x}'_f, \tilde{h}_f)$ of the integration interval is chosen from a condition that $\partial^2\tilde{h}/\partial\tilde{x}'^2$ reaches a plateau (with a required accuracy). Such a calculation results in a numerical value for this plateau

$$\left.\frac{\partial^2 \tilde{h}}{\partial \tilde{x}'^2}\right|_{\tilde{x}'=\tilde{x}'_f} = \alpha \simeq 1.3375 \tag{2.7}$$

Fig. 8a (steady receding) plots the resulting profile $\tilde{h}(\tilde{x}')$. Note that α is equivalent to the numerical value 0.643 originally found by Bretherton (1961); $\alpha \simeq 0.643 \cdot 3^{2/3}$, where the factor appears because of the different scaling. By comparing Eq. 2.2 and Eq. 2.7, we find the expression for the film thickness

$$h_r = \alpha R_m Ca_r^{2/3}. \tag{2.8}$$

The only yet unknown quantity is R_m that can be found by the method proposed by Klaseboer et al. (2014). As mentioned before, near the point $(\tilde{x}'_f, \tilde{h}_f)$ the film shape should

variable	notation	reference values used in problems with	
		infinite liquid film	immobile contact line
axial coordinate	x	$h_\mathrm{r} Ca_\mathrm{r}^{-1/3}$	$\alpha R Ca_0^{1/3}$
film thickness	h	h_r	$\alpha R Ca_0^{2/3}$
time	t	$h_\mathrm{r} Ca_\mathrm{r}^{-1/3} u_\mathrm{r}^{-1}$	$\alpha R Ca_0^{1/3} u_0^{-1}$
velocity	u	u_r	$u_0 = 2\pi A/P$

Table 1: Dimensional reference values that are used to make the governing equations non-dimensional.

satisfy the condition (2.2) which means that at $h \gg h_\mathrm{r}$, it asymptotically approaches a parabola

$$y = (x' - x'_\mathrm{s})^2/(2R_\mathrm{m}) + h_\mathrm{s}, \tag{2.9}$$

where the parameters $(x'_\mathrm{s},\, h_\mathrm{s})$ are yet to be determined. To reveal their meaning, we recall that near its minimum, where its curvature is R_m^{-1}, the parabola approximates the circular meniscus profile

$$(x' - x'_\mathrm{s})^2 + (y - h_\mathrm{s} - R_\mathrm{m})^2 = R_\mathrm{m}^2. \tag{2.10}$$

Evidently, $(x'_\mathrm{s},\, h_\mathrm{s})$ is the circle lowest point. Fitting the film profile $\tilde{h}(\tilde{x}')$ near the point $(\tilde{x}'_\mathrm{f},\, \tilde{h}_\mathrm{f})$ to a parabola results in $(x'_\mathrm{s},\, h_\mathrm{s})$. Klaseboer et al. (2014) report that the dimensionless value of $\tilde{h}_\mathrm{s}$ slightly grows with $\tilde{h}_\mathrm{f}$. Bretherton (1961) gives $\tilde{h}_\mathrm{s} = 2.79$. The asymptotic value $\tilde{h}_\mathrm{s} = 2.90$ is obtained for $\tilde{h}_\mathrm{f} > 10^6$. However, to obtain a continuous overall interface profile, the matching point $(\tilde{x}'_\mathrm{f},\, \tilde{h}_\mathrm{f})$ film–parabola should be lower than the point where the parabola–circle transition occurs. This requires $h_\mathrm{f} < R$. For the value $\tilde{h}_\mathrm{f} \simeq 50$ that satisfies this condition in practical situations, Klaseboer et al. (2014) found $\tilde{h}_\mathrm{s} = 2.5$, which was also the value found from the experimental data fits, as discussed below. In summary, the $\tilde{h}_\mathrm{s}$ variation is weak, and we can consider that the circle is nearly invariant of the specific $\tilde{h}_\mathrm{f}$ choice.

Klaseboer et al. (2014) have proposed the equation

$$R_\mathrm{m} + h_\mathrm{s} = R \tag{2.11}$$

that centers the circle with respect to the tube and thus links R_m to R, cf. Fig. 7. Using Eq. 2.8 in this equation produces finally:

$$R_\mathrm{m} = \frac{R}{1 + \alpha \tilde{h}_\mathrm{s} Ca_\mathrm{r}^{2/3}}. \tag{2.12}$$

Combining Eq. 2.8 and Eq. 2.12, we can now finalize the film thickness expression

$$h_\mathrm{r} = \frac{\alpha R Ca_\mathrm{r}^{2/3}}{1 + \alpha \tilde{h}_\mathrm{s} Ca_\mathrm{r}^{2/3}}. \tag{2.13}$$

The experimental data fits by Aussillous et al. (2000) have determined the value $\tilde{h}_\mathrm{s} \simeq 2.5$, which is very close to the above numerical values. For $Ca_\mathrm{r} \to 0$, $R_\mathrm{m} \simeq R$ and Eq. 2.13 reduces to Bretherton's original expression

$$h_\mathrm{r} = \alpha R Ca_\mathrm{r}^{2/3}. \tag{2.14}$$

Next, consider a meniscus advancing at a constant velocity $u_\mathrm{m} = -u_\mathrm{a}$ (where u_a is the modulus of the advancing velocity) over a pre-existing film of thickness h_r. Such a motion has been understood as well. Bretherton (1961) has shown that the interface demonstrates a wavy shape (ripples) near the meniscus, cf. the solid curve in Fig. 8a (steady advancing). The wavelength of ripples depends on the ratio $u_\mathrm{a}/u_\mathrm{r}$ (Maleki et al., 2011; Nikolayev et al., 2014), where u_r can be deduced (using Eq. 2.14) from h_r. We might regard h_r that is deposited by a meniscus receding at u_r. The meniscus radius for steady advancing cases was determined with Eq. 2.11 by Cherukumudi et al. (2015).

2.2.2 *Film relaxation*

The meniscus oscillation results in a continuous film-shape variation. For this reason, a necessary quantity is the relaxation time t_rel. It is a characteristic time scale of decrease of a film perturbation caused by the meniscus velocity change. On a time scale $\gg t_\mathrm{rel}$, the meniscus is expected to behave as if the velocity were constant at each time moment (i.e., in a quasi-steady way).

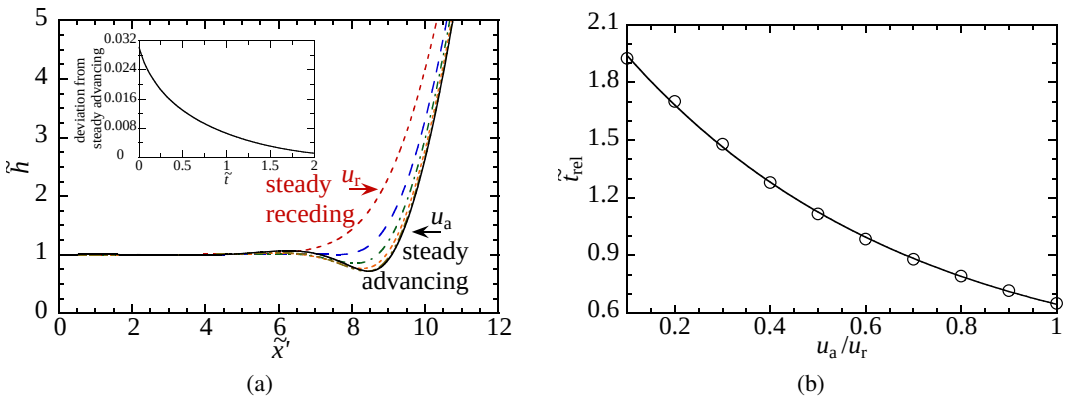

Figure 8: Film relaxation: profile evolution and relaxation time. (a) Film profile evolution (shown in the frame of reference of the meniscus) from steady receding with the velocity u_r to steady advance with the velocity u_a such that $|u_\mathrm{a}| = u_\mathrm{r}$. The time lag between the two curves is $\Delta\tilde{t} = 0.5$. The inset shows the root mean square deviation from the steady advancing profile and (b) relaxation time as a function of $u_\mathrm{a}/u_\mathrm{r}$. The dots are the numerical points. The line is the exponential fit.

Relaxation of the film profile is studied here on an example of a sudden change in the meniscus motion direction, from receding to advancing. The initial profile (monotonic red curve in Fig. 8a) is that of Landau et al. (1942) defined by Eq. 2.6 describing the meniscus receding at a constant velocity u_r. In this calculation, R_m is assumed to remain constant ($= R$) because Ca_r is small. The calculation is performed for $Ca_r = 10^{-3}$ but the results are independent of Ca_r provided it is small enough. The deposited film thickness is given by Eq. 2.14.

At $t = 0$, the meniscus makes a sudden change of its motion direction and for $t > 0$ advances over the liquid film at a constant velocity u_a. The film is infinite so the meniscus frame of reference and thus Eq. 2.3 with $u_\mathrm{m} = -u_\mathrm{a} < 0$ are employed. With the scaling of Tab. 1, the dimensionless governing equation is

$$\frac{\partial \tilde{h}}{\partial \tilde{t}} + \frac{\partial}{\partial \tilde{x}'}\left(\frac{\tilde{h}^3}{3}\frac{\partial^3 \tilde{h}}{\partial \tilde{x}'^3} - \tilde{u}_\mathrm{m}\tilde{h}\right) = 0, \tag{2.15}$$

where $\tilde{u}_\mathrm{m} = -u_\mathrm{a}/u_\mathrm{r}$. The boundary conditions are Eq. 2.4 and Eq. 2.7, where both α and h_r are now known.

Eq. 2.15 is solved numerically, cf. Subsec. 2.3.5 for the details. The time evolution of the interface profile is shown in Fig. 8a. At $\tilde{t} = 0$, the profile is given by the steady receding meniscus of Eq. 2.6. As the time increases, the film relaxes to the steady advancing profile (the solid curve in Fig. 8a), which coincides with the Bretherton profile of the rear meniscus. By fitting the root mean square deviation (shown in the inset) from the steady advancing profile, we introduce the relaxation time $\tilde{t}_{\mathrm{rel}}$; for $u_{\mathrm{a}}/u_{\mathrm{r}} = 1$, $\Delta\tilde{t}_{\mathrm{rel}} \simeq 0.65$.

The calculation shows (Fig. 8b) that the relaxation time t_{rel} decreases with u_{a} and remains smaller than 2. As the exponential vanishes after $\tilde{t} \simeq 5\tilde{t}_{\mathrm{rel}}$, the system is expected to behave independently of a current state after a time lag $\tilde{t} \simeq 10$.

2.3 Forced meniscus oscillation from pinned contact lines

A previous study (Nikolayev et al., 2014) demonstrates the film behavior for the case of an infinite film. There is no physical criterion imposing its thickness, it is thus another input parameter. When the meniscus approaches the leftmost (in the reference of Fig. 7) position observed during oscillations, the ripples created near the advancing meniscus propagate over the film to infinity, so there is no possible periodical regime. This propagation is amplified by the discrepancy between the imposed film thickness and the thickness Eq. 2.8 defined by the receding meniscus velocity, which is zero at the leftmost point. Thus a discrepancy exists for any imposed film thickness. In practical situations of oscillating motion (Fourgeaud et al., 2016; Rao et al., 2017), contact lines appear because of liquid evaporation caused by tube wall heating. Even with small superheating, liquid films will eventually vaporize beyond the leftmost meniscus position. Before addressing heating cases, in this section, we discuss the interface shape in the presence of a contact line without any heating.

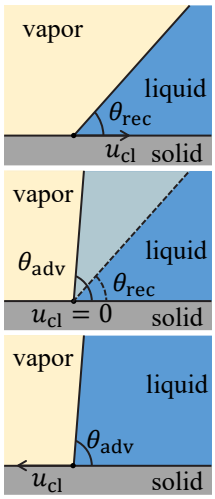

The hydrodynamics of pinned (static) contact lines is simpler than the dynamic case. For this reason, we should understand it first. This is the purpose of this chapter. The contact line pinning often occurs in capillaries (Mohammadi et al., 2015). It is caused by wall heterogeneity (surface defects) that is either chemical or geometrical (surface roughness). The heterogeneity can be modeled as a spatial variation of surface energy. The result of such a theory (Iliev et al., 2014) is that the microscopic contact angle θ_{micro} averaged along the contact line may vary between the static advancing θ_{adv} (above which the contact line advances) and the static receding θ_{rec} (below which the contact line recedes) angles while the contact line remains stationary. In our calculation, $\theta_{\mathrm{adv}} - \theta_{\mathrm{rec}}$ (called wetting hysteresis) is assumed to be sufficiently large, so the contact line always remains immobile, see the marginal illustration. In experiments, the hysteresis can be as large as $50°$ (deGennes, 1985), which is larger than the angle oscillation magnitude considered below.

At oscillations with the fixed contact line, there are no vortices near it (Ting et al., 1987), and the flow is known to be well described by the lubrication approximation, even down to the nanometric scale (Mortagne et al., 2017).

Since we consider the pinned contact line problems, choosing the capillary tube as the frame reference is convenient. Taking the minimal complexity, the governing equation Eq. 1.19 (Nikolayev, 2010) that describes the interface dynamics in the film region is reduced to

$$\frac{\partial h}{\partial t} + \frac{\partial}{\partial x}\left(\frac{h^3}{3\mu}\frac{\partial \Delta p}{\partial x}\right) = -\frac{J}{\rho}, \tag{2.16}$$

where J is zero for isothermal oscillation.

2.3.1 *Relaxing the pressure divergence by the Kelvin effect*

The Stokes problem of the straight wedge with a varying opening angle leads to the logarithmic pressure divergence, cf. Subsec. A.3.1. Such a divergence is integrable and thus does not cause a paradox similar to that of the moving contact line. However, the infinite pressure is non-physical. In addition, the pressure boundary condition at the contact line would be difficult to use in the calculation because it requires prior knowledge of the contact angle and its time derivative (cf. Eq. A.25) that need to be determined themselves during the solution procedure. As we consider volatile fluids, the phase change and the Kelvin effect are introduced. The latter makes the pressure to be finite everywhere, as shown below.

The film is assumed here to be thin with respect to R, so the one-dimensional conduction description applies. The evaporation impact on a film is twofold. First, the film thickness decreases with time everywhere along the film, which is described by the balance of the first and the right-hand side term of Eq. 2.16. Generally, the film thinning is not strong during an oscillation period (Fourgeaud et al., 2017).

We focus here on the second effect that appears because of the evaporation strength in a narrow vicinity of the contact line. If the vapor-liquid interface were at a fixed saturation temperature ($T^{\mathrm{i}} = T_{\mathrm{sat}}$), the mass flux J (1.18) would diverge at the contact line $h = 0$ as $J \sim \Delta T/h$, which is non-physical because total evaporated mass (the integral of J) would be infinite.

The Kelvin effect Eq. 1.24, i. e. the dependence of T^{i} on the interfacial pressure jump Δp can relax the singularity (Janeček et al., 2012), because it allows T^{i} to vary along the interface. Therefore, it can attain the wall temperature T_{w} at the contact line so the mass flux

$$J(x \to 0) = 0. \tag{2.17}$$

From the temperature continuity, we obtain the condition

$$\Delta p(x \to 0) = \Delta p_{\mathrm{cl}}, \tag{2.18}$$

where a constant pressure jump at the contact line is introduced as

$$\Delta p_{\mathrm{cl}} = \frac{\mathcal{L}\rho}{T_{\mathrm{sat}}} \Delta T. \tag{2.19}$$

A solution that satisfies this condition can indeed be found (cf. Subsec. A.3.2). Combining Eq. 1.18 and Eq. 1.24 results in

$$J = \frac{k}{h\mathcal{L}} \left(\Delta T - \Delta p \frac{T_{\mathrm{sat}}}{\mathcal{L}\rho} \right). \tag{2.20}$$

With its substitution into Eq. 2.16, the governing equation becomes

$$\frac{\partial h}{\partial t} + \frac{\partial}{\partial x} \left(\frac{h^3}{3\mu} \frac{\partial \Delta p}{\partial x} \right) = \frac{\Delta p - \Delta p_{\mathrm{cl}}}{h} \frac{k T_{\mathrm{sat}}}{(\mathcal{L}\rho)^2}. \tag{2.21}$$

The problem is now regular (because Δp is not divergent anymore), unlike other microscopic approaches (Savva et al., 2017). As the Kelvin effect alone is capable of relaxing the contact line singularity (Janeček et al., 2012) and the evaporation effect is weak in this chapter, the other microscopic scale effects discussed in Subsec. 1.1.2 are not included in this chapter for the sake of clarity.

In Sec. 2.3, a globally isothermal problem is considered, $T_{\mathrm{w}} = T_{\mathrm{sat}}$, meaning that $\Delta T = 0$ and $\Delta p_{\mathrm{cl}} = 0$. At such conditions, the mass exchange appearing at the macroscopic scale is very weak that it can be safely neglected. This does not mean, however, that the mass

exchange is absent in the microregion where Δp can be large, as mentioned above. The mass flux J scales with Δp according to Eq. 2.20, so phase change occurs. The situation here shares certain similarities with the contact line motion paradox solved by the Kelvin effect (Janeček et al., 2013). Consider e.g. an increase-in-time θ. According to Eq. A.31, $\Delta p > 0$ in the very contact line vicinity, and the condensation occurs there. It is compensated exactly by evaporation farther away from the contact line; therefore, the net mass exchange is zero. It should be noted that the fluid flow associated with the phase change is strongly localized within a nanoscale distance from the contact line comparable to the characteristic length of the Kelvin effect ℓ_{VK}. It is assumed hereafter that the pinning occurs at a length scale smaller than ℓ_{VK}, i.e. there are nanometric defects with sharp borders on which the contact line is pinned.

In conclusion, all results obtained in the present Sec. 2.3, can be seen as obtained with Eq. 2.21 because the microregion details cannot be resolved at the macroscale pictured in the figures below. However, the numerical calculations of the regularized Eq. 2.21 are carried out in reality.

2.3.2 *Oscillation problem statement*

Now consider an oscillating meniscus, and the position x_{m} of its center (which is the experimentally measurable quantity) travels periodically with a period P and an amplitude A. Assuming its harmonic oscillation results in:

$$x_{\mathrm{m}}(t) = x_{\mathrm{i}} + A[1 - \cos(2\pi t/P)], \tag{2.22}$$

where x_{i} is the initial meniscus center position. Alternatively, we can adapt the experimentally measured dependence $x_{\mathrm{m}}(t)$ while comparing the data with the experiment (cf. Subsec. 2.3.6.5 below). The contact line is pinned at position $x = 0$, and the contact angle θ varies. For the harmonic oscillation case, the meniscus velocity is $u(t) = u_0 \sin(2\pi t/P)$, where the velocity amplitude $u_0 = 2\pi A/P$ is convenient to choose as the characteristic velocity to define the capillary number $Ca_0 = \mu u_0/\sigma$ and to make all the quantities dimensionless (cf. Tab. 1).

Because of the fixed contact line, the frame of reference of the tube wall is chosen. Eq. 2.21 (with the substitution of Eq. 2.1) is solved for $x \in [0, x_{\mathrm{f}}]$. The length x_{f} is imposed as explained in Subsec. 2.3.3 and Subsec. 2.3.5 below.

The boundary conditions are defined as

$$h\,(x = 0) = 0, \tag{2.23a}$$

$$\left.\frac{\partial \Delta p}{\partial x}\right|_{x\to 0} = 0, \tag{2.23b}$$

$$\Delta p\,(x = x_{\mathrm{f}}) = R_{\mathrm{m}}^{-1}, \tag{2.23c}$$

$$h\,(x = x_{\mathrm{f}}) = h_{\mathrm{f}}, \tag{2.23d}$$

where R_{m} and h_{f} are discussed in Sec. 2.2. The condition (2.23a) is a geometrical constraint at the contact line. Equation (2.23b) is a weaker form of the condition (2.18) used to provide numerical stability. The boundary conditions (2.23c, 2.23d) impose the liquid film curvature and thickness at the right end of the integration interval for each time moment.

2.3.3 *Determination of the meniscus curvature*

For a small film thickness, the meniscus radius R_{m} is assumed constant and equal to R during oscillation. It is actually a good approximation for a small $Ca_0 \lesssim 10^{-3}$. However, at a larger

Ca_0, the film thickness impacts R_m (see Subsec. 2.3.6.3 below). Since the film thickness depends on the meniscus velocity, so does the meniscus radius R_m, cf. Sec. 2.2. Therefore, R_m varies in time. In this section, we generalize to any meniscus dynamics the method for R_m determination (Klaseboer et al., 2014) discussed above for the steady receding case.

Similarly to the steady case of sec. 2.2, we first match the film shape $h(x)$ to the parabola (2.9), and then the parabola to a circle (2.10). The matching between the film and the parabola means both the continuity and smoothness (equality of the derivatives)

$$h_\mathrm{f} = (x_\mathrm{f} - x_\mathrm{s})^2/(2R_\mathrm{m}) + h_\mathrm{s}, \tag{2.24a}$$

$$\left.\frac{\partial h}{\partial x}\right|_{x=x_\mathrm{f}} = \frac{x_\mathrm{f} - x_\mathrm{s}}{R_\mathrm{m}}, \tag{2.24b}$$

where the left-hand sides come from the film calculation, and all the parabola parameters are time-dependent. As in the approach of Klaseboer et al. (2014), Eq. 2.11 serves to find R_m. We introduce in addition, a relationship of the abscissas of the lowest and rightmost points of a circle that is needed to define x_s (Fig. 7):

$$R_\mathrm{m} + x_\mathrm{s} = x_\mathrm{m}. \tag{2.24c}$$

In the present algorithm, x_f imposed to such a value that the difference $x_\mathrm{m} - x_\mathrm{f}$ does not vary in time and $h_\mathrm{f} = h(x_\mathrm{f})$ remains large with respect to the deposited film thickness. As discussed in sec. 2.2, the solution is nearly independent of the specific choice of h_f (and thus of x_f). The set of Eqs. (2.1), (2.11) and (2.21)–(2.24) is then complete, so the film shape and the unknown parameters (R_m, x_s, h_s, h_f) can be determined for each t.

2.3.4 *Initial conditions and solution periodicity*

One needs to define now the initial film shape $h(x, 0)$ at $t = 0$, which corresponds to the (yet unspecified) leftmost meniscus position x_i according to Eq. 2.22. As an initial film profile, we choose that of equilibrium satisfying the condition $\partial h/\partial t = 0$ that can be used in Eq. 2.21. From the boundary condition Eq. 2.23b, one finds straightforwardly $\partial^3 h/\partial x^3 = 0$, i. e. the parabolic shape

$$h(x, 0) = \frac{x^2}{2R_\mathrm{m,i}} + \theta_\mathrm{i} x, \tag{2.25a}$$

where $\theta_\mathrm{i} \equiv \theta(t = 0)$ is the initial contact angle. It serves as another boundary condition, additional to Eq. 2.23a and Eq. 2.23c. Applying Eq. 2.11 and Eq. 2.24 at $t = 0$ produces,

$$R_\mathrm{m,i} \equiv R_\mathrm{m}(t = 0) = R/(1 - \theta_\mathrm{i}^2/2), \tag{2.25b}$$

$$x_\mathrm{i} = R_\mathrm{m,i}(1 - \theta_\mathrm{i}). \tag{2.25c}$$

These expressions are the small-angle approximations of the expressions $R_\mathrm{m,i} = R/\cos\theta_\mathrm{i}$ and $x_\mathrm{i} = R_\mathrm{m,i}(1 - \sin\theta_\mathrm{i})$ because Eq. 2.25a is an approximation of the initially spherical meniscus.

During oscillation, the liquid is driven by the meniscus motion, and the free interface remains in the state where $\partial h/\partial t$ is always balanced by the curvature gradient, more precisely, by the second term of Eq. 2.16. This occurs because there are no other forces, in particular, no inertia. When the meniscus comes near the leftmost position, u_m decreases, and the system approaches the state (2.25) with no curvature gradient, thus, $|\partial h/\partial t|$ decreases to zero or almost zero. It is not rigorous proof that the state (2.25) belongs to the limit cycle of the system, albeit it should be quite close to it. This is undoubtedly true when the relaxation time is short, $t_\mathrm{rel} \ll P$, which is our case (cf. Subsec. 2.2.2 for t_rel discussion). Indeed, the

numerical simulations show that $h(x, P)$ is indistinguishable from $h(x, 0)$, cf. Fig. 9 below. So do all other parameters (curvature, contact angle, etc.). This finding allows us to simulate a unique period.

2.3.5 *Numerical implementation*

The scales for the main quantities to make them dimensionless are shown in the right column of Tab. 1. With such a "natural" scaling, only three main dimensionless parameters are left: θ_i, $\tilde{P}$ and Ca_0. All quantities will be studied in this parametric space. The dimensionless amplitude is linked to the period

$$\tilde{A} = \tilde{P}/(2\pi), \tag{2.26}$$

where a dimensionless quantity is denoted with a tilde. There is one more dimensionless parameter

$$N = \frac{\mu k T_\mathrm{sat}}{\mathcal{L}\rho\alpha R\, Ca_0} \tag{2.27}$$

that describes the magnitude of the Kelvin effect in the microregion. However, it does not impact the interface shape at the film scale, provided the characteristic microscopic scale (A.29) is chosen to be small enough (cf. Subsec. 2.2.2). The mesh size is exponentially refined near the contact line (as $\tilde{x} \to 0$) to capture the contact angle variation without considerably increasing the total number of nodes (Nikolayev, 2010).

At $\tilde{t} = 0$, a value of $\tilde{x}_\mathrm{f} = 10$, for which $\tilde{h}_\mathrm{f}$ is around 50, cf. the discussion in Sec. 2.2. At $\tilde{t} > 0$, the difference $\tilde{x}_\mathrm{m} - \tilde{x}_\mathrm{f}$ is maintained constant, and equal to that at $\tilde{t} = 0$. To avoid the discretisation error for the contact angle, the initial interface profile is determined numerically by solving the equilibrium version of Eq. 2.21, instead of using the analytical profile (2.25a).

Eq. 2.21 is solved numerically with the finite volume method (FVM), which is more stable numerically (Patankar, 1980) than a more conventional finite difference method. In one dimension, a finite volume is just a segment. The variables such as h and their even-order derivatives are defined at its centre (called a node), while the odd-order derivatives are defined at the segment ends. The FVM has the advantage that the liquid flux is continuous at the segment ends. Nonlinear terms are managed by iteration: they include values from the previous iteration. The numerical algorithm is similar to that used by Nikolayev (2010).

We are interested in amplitudes that are large with respect to the meniscus width $x_\mathrm{m} - x_\mathrm{s}$, which means large dimensionless periods of oscillation, see Eq. 2.26. This signifies that the computational domain size varies considerably during oscillations. The grid thus needs to be adaptive, and the calculation time can be of the order of a day on a regular PC.

2.3.6 *Results and discussion*

2.3.6.1 *Interface profile during oscillation*

Fig. 9 shows the interface profiles at several moments during oscillation. The meniscus motion follows the harmonic law (2.22). The liquid film is deposited until $t = P/2$. For $t > P/2$, the meniscus advances over the deposited film. The ripples near the meniscus appear, like during the steady meniscus advance discussed in Sec. 2.2. The interface profiles $\tilde{h}(\tilde{x}, 0)$ and $\tilde{h}(\tilde{x}, \tilde{P})$ are indistinguishable, which confirms the periodicity of the oscillations.

Fig. 10 shows examples of interface profiles at $t = P/2$ (when the meniscus is at its rightmost position, so the film length attains its maximum) for several values of the initial contact angle θ_i. All the film profiles are presented in the meniscus reference

$$x' = x - 2A - x_\mathrm{i}, \tag{2.28}$$

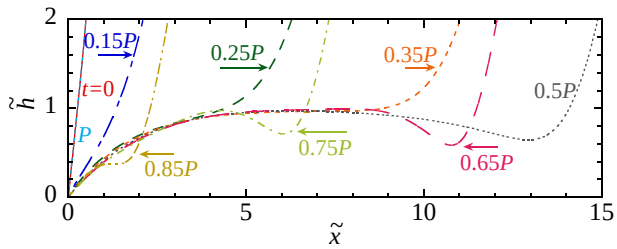

Figure 9: Periodic interface shape variation at oscillation for $\tilde{P} = 50$, $Ca_0 = 1 \times 10^{-3}$ and $\theta_\mathrm{i} = 20°$. The labels give the times corresponding to each profile, and the arrows indicate the meniscus motion direction.

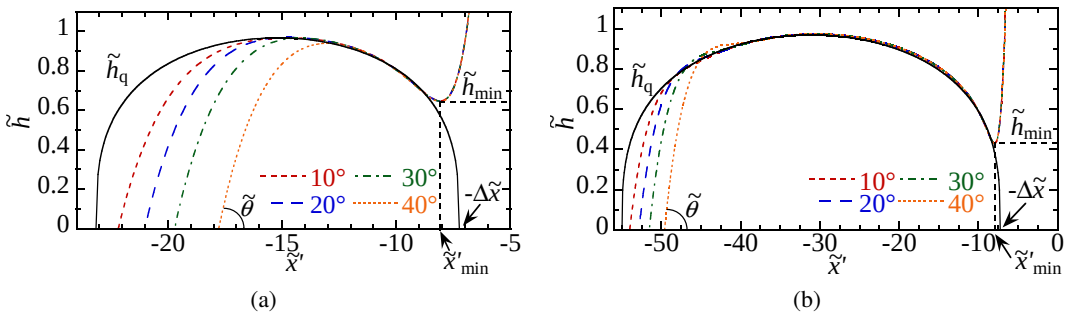

Figure 10: Film shapes in the meniscus center reference at $t = P/2$ for $Ca_0 = 10^{-3}$ and different θ_i and P. The quasi-steady profiles $\tilde{h}_\mathrm{q}$ discussed in Subsec. 2.3.6.4 are shown for comparison. The scaled contact angle $\tilde{\theta}$ defined as $\tan\tilde{\theta} = Ca_0^{-1/3}\tan\theta$ is indicated; (a) $\tilde{P} = 50$ and (b) $\tilde{P} = 150$.

meaning that the meniscus center is at $x' = 0$, cf. Eq. 2.22. Apparently, the interface shapes closer to the meniscus are independent of θ_i; see Fig. 10, because, during the meniscus receding, the film loses information about the contact line. Thereupon, the film shape near the meniscus is controlled exclusively by the meniscus dynamics. This is not surprising as the flow in the film is expected to occur only in the contact line and meniscus vicinities but not in the middle of the film. The film profiles exhibit a local minimum h_min discussed in Subsec. 2.3.6.2 below. It appears because of the meniscus velocity reduction at the end of a half-period.

2.3.6.2 *Contact angle during oscillation*

A typical variation of θ during oscillation is plotted in Fig. 11a. The initial contact angle θ_i is the maximum contact angle achieved during the periodic motion.

At the beginning of a period, capillary forces lead to the fast contact angle reduction until the meniscus recedes far enough. The curvature gradient reduces, and the contact angle becomes nearly constant for a large part of a period. This nearly constant value is quite insensitive to both θ_i and P. A small ridge of constant curvature forms near the contact line. This phenomenon is similar to the dewetting ridge but of a much smaller magnitude because the contact line is pinned. A small ridge can be seen in Fig. 10b in the contact line region for the curve corresponding to $\theta_\mathrm{i} = 40°$.

The ridge width slowly grows so θ slowly decreases until the ripples in the near-meniscus region approach the contact line during the backward stroke (Fig. 11b) at the end of a period. This causes the contact angle oscillations, during which its minimal value θ_min is attained

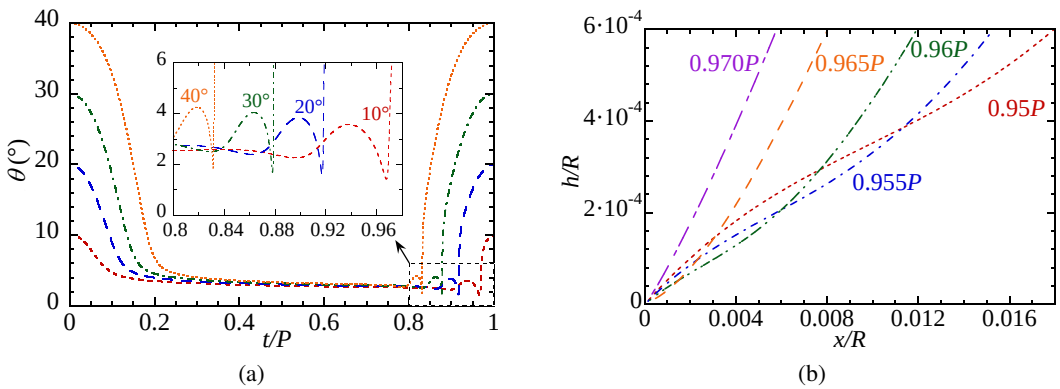

Figure 11: Contact angle variation for $Ca_0 = 10^{-3}$, $\tilde{P} = 50$. (a) Variation of contact angle during an oscillation for different values of θ_i. The inset shows enlarged undulating portions of the curves. (b) The interface shape variation near the contact line around $t = 0.965P$ where θ_min is attained for $\theta_\mathrm{i} = 10°$ (cf. the inset to Fig. 11a).

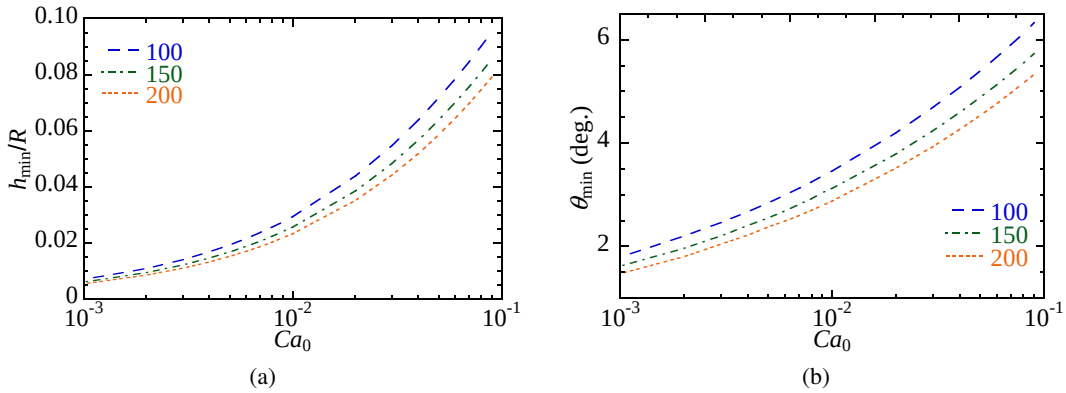

Figure 12: Variations of h_min and θ_min with Ca_0 for $\theta_\mathrm{i} = 20°$ and different $\tilde{P}$; (a) h_min variation with Ca_0 and (b) θ_min variation with Ca_0.

$$\theta(t) \geq \theta_\mathrm{min}. \tag{2.29}$$

It depends quite weakly on θ_i (Fig. 11a). The variation of θ_min with the system parameters follows the variation of h_min (which is a minimum of $h(x, 0.5P)$ observed near the meniscus). This is illustrated in Fig. 12, where the variations of h_min and θ_min with the system parameters are compared. Only the variations with $\tilde{P}$ and Ca_0 are considered (as mentioned above, the dependence on θ_i is quite weak). Evidently, the variations of h_min and θ_min with the system parameters are similar, which shows their intrinsic link. At $Ca_0 \to 0$, the dependence on Ca_0 is weak but becomes stronger at large Ca_0. This minimal contact angle value is important (cf. Sec. 2.4 below). Since the motion is periodic, the contact angle θ_i is attained at $t = P$.

2.3.6.3 *Meniscus curvature during oscillation*

The meniscus curvature (Fig. 13) changes periodically during oscillations. The value of R_m can be compared to the quasi-steady value $R_\mathrm{m,q}$ given by Eq. 2.12 where $\tilde{h}_\mathrm{s} = 2.5$ and Ca_r are calculated with the instantaneous meniscus velocity $u_\mathrm{m} = u_0 \sin(2\pi\tilde{t}/\tilde{P})$ during the liquid receding ($t \leq 0.5P$).

For $t = 0$, R_m is defined with Eq. 2.25b, which differs from the quasi-steady value $R_\mathrm{m,q} = R$ for $U = 0$. This difference occurs because of the contact line presence. In its

absence (pre-wetted tube, the situation equivalent to the limit $\theta_\mathrm{i} \to 0$ in our model), the initial radius would be close to R because the wetting film is much thinner than the film considered here.

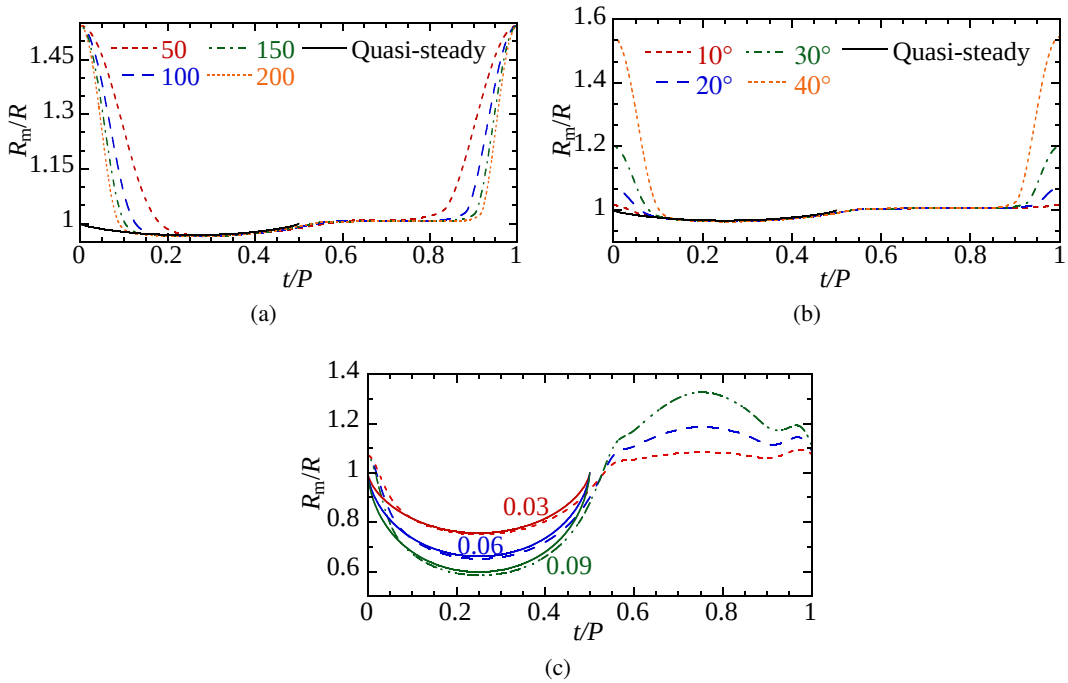

Figure 13: Time evolution of the radius of meniscus curvature during an oscillation. The quasi-steady evolution of $R_\mathrm{m,q}$ at receding ($t \leq 0.5P$) is shown for comparison: (a) R_m evolution for different $\tilde{P}$; $\theta_\mathrm{i} = 40°$ and $Ca_0 = 10^{-3}$ are fixed, (b) R_m evolution for different θ_i; $\tilde{P} = 150$ and $Ca_0 = 10^{-3}$ are fixed and (c) R_m evolution (dashed curves) for different Ca_0; $\tilde{P} = 150$ and $\theta_\mathrm{i} = 20°$ are fixed. The solid curves of the respective color show $R_\mathrm{m,q}(t)$.

Within the time scale $\sim 5t_\mathrm{rel}$ (see Subsec. 2.2.2), R_m relaxes to the quasi-steady value $R_\mathrm{m,q}$. The curvature R_m remains close to $R_\mathrm{m,q}$ until the deceleration that occurs near the rightmost meniscus position (at $t = 0.5P$, where $u = 0$). However, the shape relaxation causes a delay, so the inequality $R_\mathrm{m} < R_\mathrm{m,q}(u = 0) = R$ always holds at the point $t = 0.5P$. During the backstroke, R_m varies, finally attaining the initial value Eq. 2.25b that depends only on θ_i (Fig. 13b). Evidently, the amplitude of R_m oscillation grows with Ca_0 (Fig. 13c), as foreseen by Eq. 2.12. The non-monotonic R_m variation during the backstroke is noteworthy. A local minimum appears around $t \simeq 0.8 - 0.9P$ (Fig. 13c), when the trough of film ripples approaches back the contact line close enough. Thus this minimum is correlated with the minimum in contact angle.

For $\tilde{P} > 100$ considered here, the transient evolution must be considered only at the beginning and the very end of a period where the contact line affects the overall interface shape. A quasi-static approach is expected to be valid for the remaining part of a period.

2.3.6.4 *Quasi-steady approach and average film thickness*

Apparently, the film is thickest in its middle part (Fig. 10), which correlates with the maximum meniscus velocity. It is thus intriguing to compare the film thickness with its quasi-steady value. Within the quasi-steady approach, the term $\partial h/\partial t$ is neglected, and the quasi-steady thickness $h_\mathrm{q}(x)$ can be defined as corresponding to the meniscus receding velocity as if it was constant at each time moment (Fourgeaud et al., 2017; Youn et al., 2018).

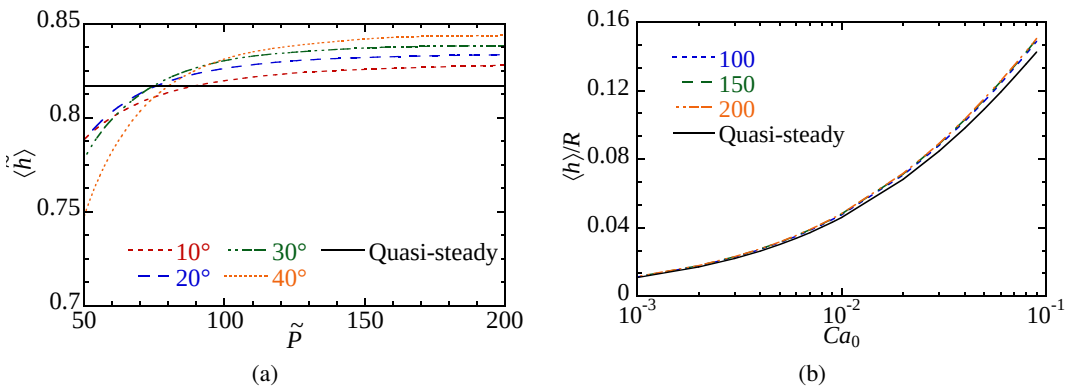

Figure 14: Average thickness of the liquid film at $t = 0.5P$; $\langle h_\mathrm{q}\rangle$ is shown for comparison. (a) Value of $\langle\tilde{h}\rangle$ as a function of oscillation period for different θ_i and for $Ca_0 = 10^{-3}$ and (b) value of $\langle h\rangle$ as a function of Ca_0 for different $\tilde{P}$ and for $\theta_\mathrm{i} = 20°$.

In Subsec. 2.3.6.3 it has been shown that a simple quasi-steady approach predicts well the meniscus curvature for $0 < t < 0.5P$. It is interesting to see if it is efficient in predicting the film profile. In this section, only the profile at $t = 0.5P$ is considered, i.e. that with the longest film.

A difficulty appears because the film thickness $h(x, 0.5P)$ depends on x. It is clear that h depends on the velocity that the meniscus had at the film deposition, but at which time moment? The most obvious first option is a moment t when the meniscus center was at the point x (i.e. $x_\mathrm{m}(t) = x$). A more sophisticated option is a moment $t' > t$ such that

$$x_\mathrm{m}(t') = x + \Delta x \tag{2.30}$$

with $\Delta x > 0$. The first option was used in the previous approaches (Fourgeaud et al., 2017; Youn et al., 2018). Using Eq. 2.22, we easily finds that this assumption defines $u_\mathrm{q}(x)$ for $x \in (x_\mathrm{i}, x_\mathrm{i} + 2A)$. An obvious contradiction occurs at $x = x_\mathrm{i} + 2A$ where $h_\mathrm{q}(x_\mathrm{i} + 2A) = 0$ because $u_\mathrm{q}(x_\mathrm{i} + 2A) = 0$, but the actual film thickness (or rather, the interface height) is R. Therefore, a more realistic $\Delta x > 0$ should be defined. It is reasonable to choose Δx as the meniscus radius, i.e. R_m. However, it varies with time. We propose to use $\Delta x = \langle R_\mathrm{m}\rangle$, the average value of $R_\mathrm{m}(t)$ (defined using Eq. 2.12) over the first half-period.

For the harmonic meniscus oscillation, combining Eq. 2.22 and Eq. 2.30 results in:

$$u_\mathrm{q}(x) = u_0 \left[\frac{x + \Delta x - x_\mathrm{i}}{A}\left(2 - \frac{x + \Delta x - x_\mathrm{i}}{A}\right)\right]^{1/2}. \tag{2.31}$$

This velocity can now be used to calculate Ca_r in Eq. 2.13, thus resulting in the quasi-steady thickness $h_\mathrm{q}(x)$. The $\tilde{h}_\mathrm{q}(\tilde{x}')$ profiles are shown as solid curves in Figs. 10. Note that they are independent of θ_i (cf. Eq. 2.28), so there is a unique curve in each figure. This comparison illustrates the necessity of the Δx introduction: if it were not included, the $\tilde{h}_\mathrm{q}(\tilde{x}')$ curve would be shifted with respect to $\tilde{h}(\tilde{x}')$ curves in Fig. 10. The agreement between the actual and quasi-steady film profiles is good in the central part of the film, which shows that the Δx choice is acceptable.

At the beginning of a period, due to the presence of the contact line, R_m is always larger than $R_\mathrm{m,q}$, which leads to a thinner film: $h < h_\mathrm{q}$, cf. Fig. 10. This difference becomes relatively less important as P increases (compare Fig. 10a and Fig. 10b).

Characterizing the film at oscillation conditions (e.g. to estimate the film evaporation rate) requires knowing the average film thickness $\langle h \rangle$. It is defined as a spatial average over the interval between the contact line and $x_{\min}$ (abscissa of the point where $h_{\min}$ is attained),

$$\langle h \rangle = \frac{1}{x_{\min}} \int_0^{x_{\min}} h(x, t = 0.5P) \mathrm{d}x. \tag{2.32}$$

The dependence of $\langle h \rangle$ on different parameters can be seen in Figs. 14. It is an increasing function of $\tilde{P}$ that saturates for $\tilde{P} \to \infty$. It can be compared to the quasi-steady averaged thickness

$$\langle h_{\mathrm{q}} \rangle = \frac{1}{2A} \int_{x_{\mathrm{i}} - \Delta x}^{2A + x_{\mathrm{i}} - \Delta x} h_{\mathrm{q}}(x) \mathrm{d}x \tag{2.33}$$

which is independent of both A and θ_{i} as follows from Eq. 2.31. It can be easily calculated without doing any complicated simulations. For small $\tilde{P}$ (i.e. for small $\tilde{A}$), $\langle h \rangle < \langle h_{\mathrm{q}} \rangle$, mainly because of the contact line vicinity where $h(x) < h_{\mathrm{q}}(x)$, cf. Fig. 10. It is not surprising that the saturation value of $\langle h \rangle$ increases with θ_{i} (just because of the thicker film near the contact line); however, the increase is weak (Fig. 14a).

In Fig. 14b, one can see the dependence of $\langle h \rangle$ on Ca_0. One can see that the quasi-steady average $\langle h \rangle_{\mathrm{q}}$ Eq. 2.33 gives a globally satisfactory approximation of $\langle h \rangle$. The increase with Ca_0 is mainly due to the $Ca_0^{2/3}$ factor in Eq. 2.8.

2.3.6.5 *Film shape comparison with experiment*

In the experiments of Lips et al. (2010), a capillary tube contains a short liquid plug of pentane in contact with its own vapor at both ends of the tube. One end is connected to a reservoir at constant pressure. The pressure variation at the other end forces the oscillating motion of a liquid plug under isothermal conditions. Such a mode of oscillation leads to the oscillation amplitude increasing in time, which was understood some years later (Signé Mamba et al., 2018). While the amplitude is indeed slightly increasing, the motion is nearly periodic, so the comparison can still be made.

parameter	notation	value
tube inner radius	R	1.2 mm
density	ρ	625.7 kg/m^3
surface tension	σ	0.0152 N/m
shear viscosity	μ	2.37×10^{-4} Pa·s
reference velocity (velocity amplitude)	u_0	0.24 m/s
oscillation frequency		3.7Hz
dimensionless period	$\tilde{P}$	260.1
capillary number	Ca_0	3.74×10^{-3}
Reynolds number	Re_0	1521
Weber number	We_0	5.66

Table 2: Fluid properties (n-pentane) at the experimental conditions (1 bar, 20°C) of Lips et al. (2010), and key dimensionless numbers.

In their experiments, the plug motion is recorded with a high-resolution camera. Both the meniscus velocity and the curvature radius are found in the image analysis. The Weber number $We_0 = 2R\rho u_0^2/\sigma$ is larger than unity (Tab. 2). The Reynolds number $Re_0 =$

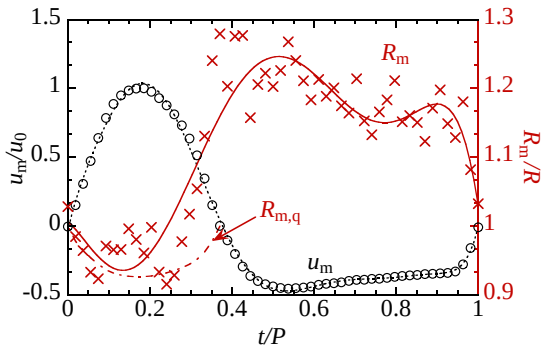

Figure 15: Liquid plug velocity and left meniscus radius variations during one period of the Lips et al. (2010) experiment (markers) and their polynomial fits (lines) used for the calculation. The experimental data have been made available to us by S. Lips. For comparison, the quasi-steady $R_{\mathrm{m,q}}$ variation given by Eq. 2.12 at receding ($t \leq 0.5P$) is also shown.

$2R\rho u_0/\mu$ is quite high too, and the impact of inertia on the shape of the central meniscus part must be taken into consideration. Indeed, the quasi-steady $R_{\mathrm{m}}(t)$ evolution and the experimental measurements of Lips et al. (2010) differ (Fig. 15). One mentions that the measured $R_{\mathrm{m}} \simeq R$ at $t = 0, P$ indicates the complete wetting case. Note the R_{m} local minimum around $t \simeq 0.8P$. A similar minimum appears in the simulation; see Fig. 13c and the associated discussion.

Despite the high We_0 and Re_0 values in the plug mentioned above, the thin film can still be considered as controlled by the viscosity only. In the simulation, instead of using the R_{m} calculation of Subsec. 2.3.3, the experimental plug velocity and the radius variation shown in Fig. 15 are used. Under these conditions, the film ripples in the transition region close to the meniscus can be compared to the calculations.

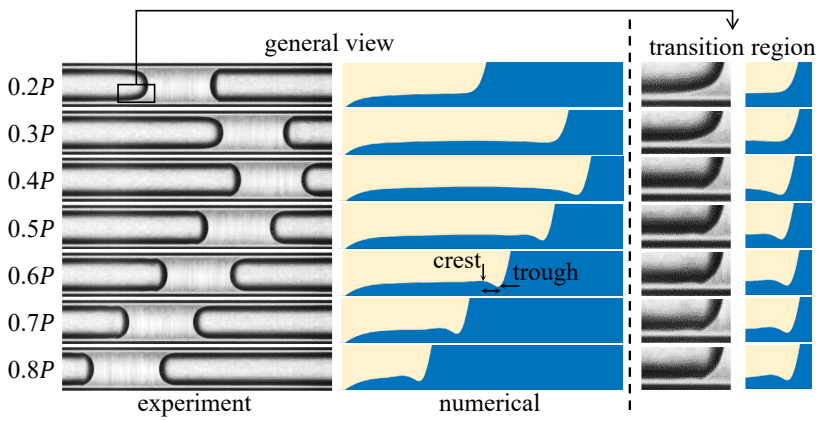

Figure 16: Liquid film shape during meniscus oscillation: comparison with experimental results by Lips et al. (2010) (see the supplementary movie available at https://doi.org/10.1017/jfm.2021.540).

Figure 16 presents several snapshots of plug oscillation. The left column shows the original images of Lips et al. (2010). The liquid film shape in the transition region between the film and the meniscus is enlarged in the middle column. The numerical results are shown in the right column. One can see that the numerical calculation truthfully captures the wavy appearance of the interface.

Unfortunately, the quantitative comparison of the film thickness (i.e. the vertical coordinate) is hardly possible since the refraction by the glass capillary is not corrected and the spatial resolution is insufficient to distinguish the contact line. However, the effect of light

refraction does not impact the axial lengths. The size of one pixel in mm can be obtained from the known outer tube diameter ($4\,\mathrm{mm}$) that is visible in the original images. We can compare the axial distance between the local maximum and the local minimum (Fig. 16) of the interface ripple for the images corresponding to $t \geq 0.5P$ where the ripple is visible. The distance is almost invariable in time. From the experimental images, the axial distance of a local crest and a though (see the arrow in Fig. 16) is 0.50 ± 0.02 mm, while from the simulation, it is 0.51 ± 0.01 mm. Evidently, the agreement is excellent.

2.3.6.6 *Film thickness comparison with experiment*

The experiment of Youn et al. (2018) was carried out under adiabatic conditions. They investigated the deposited film thickness of an oscillating meniscus in a cylindrical capillary tube. Two working fluids are selected for comparison with the present numerical results: water and ethanol. Fluid properties and experimental parameters are summarized in Tab. 3.

In the tests, the capillary tube is partially filled, with a syringe piston in contact with liquid; there is a single meniscus in the tube. The piston is connected to a step motor that imposes the harmonic motion. The other tube end remains open. Initially, the meniscus remains stationary, then, following the piston, starts to oscillate with a constant frequency. Several sensors that measure the film thickness are installed along the tube, within the range of meniscus oscillation. A high-speed camera records the instantaneous velocity of the meniscus when it passes the sensors. Because of the open tube, film evaporation occurs; however, the oscillation period is short for this process to produce any noticeable impact thickness. Once the liquid is deposited, the interface is considered invariable during the oscillation period. Unfortunately, the film shape near the meniscus and the contact line was not studied in their experiments and thus cannot be compared with our results.

The numerical calculation has been completed as described in Sec. 2.3 to get the film profiles at $t = 0.5P$. The experimental film thickness and the numerical results are presented in Fig. 17a and Fig. 17b for ethanol and in Fig. 17c and Fig. 17d for water. The experimental points are plotted with respect to the meniscus position known from the experimental data.

The experiment can also be compared with the quasi-steady film thickness calculated with Eq. 2.13 (with $\tilde{h}_\mathrm{s} \simeq 2.5$) where the instantaneous value of the velocity Eq. 2.31 is used in Ca_r.

Some experimental parameters are summarized in Tab. 3. The numerical results are in excellent agreement with the quasi-steady data for 2 Hz, where both We_0 and Re_0 are moderate. This is not surprising as $\tilde{P}$ is large (see the discussion in Subsec. 2.3.6.4). Generally, there is a good agreement with the experimental data for the same reason. The discrepancy between the experimental and numerical results is larger for the 6 Hz case where both We_0 and Re_0 become large. Both dimensionless numbers are smaller for the ethanol than for the water, and the discrepancy is smaller too. One can conclude that the discrepancy is caused by the inertial effects that become important when Re_0 attains 500 and We_0 attains 10.

An additional discrepancy comes from the non-harmonicity of the meniscus velocity profile. As the experimental $u_\mathrm{m}(t)$ curves are unavailable, we use the harmonic law (2.22) that corresponds to experimental oscillation period P and amplitude A. Because of the film deposition, the experimental $u_\mathrm{m}(t)$ deviates from the harmonic law. This can be observed from Tab. 3. Indeed, the velocity amplitude $2\pi A/P$ calculated from the oscillation amplitude and the frequency differs substantially from the actual maximum velocity, which points out the non-harmonicity of the oscillations. The comparison would be improved if the experimental $u_\mathrm{m}(t)$ were available to us.

parameter [unit]	notation	value			
tube inner radius [mm]	R	0.5			
fluid		water		ethanol	
surface tension [N/m]	σ	7.20×10^{-2}		2.23×10^{-2}	
shear viscosity [Pa·s]	μ	8.88×10^{-4}		1.088×10^{-3}	
liquid density [kg/m^3]	ρ	997		785	
oscillation frequency		2 Hz	6 Hz	2 Hz	6 Hz
oscillation amplitude [mm]	A_0	19.5	22.5	20.69	25.2
u_m amplitude in simulation [m/s]	$2\pi A/P$	0.245	0.848	0.26	0.950
u_m amplitude in experiments [m/s]		0.254	1.025	0.285	1.150
dimensionless period	$\tilde{P}$	1267	966	834	659
Capillary number	Ca_0	0.0030	0.0105	0.0127	0.0463
Reynolds number	Re_0	275.07	952.09	187.59	685.43
Weber number	We_0	0.8312	9.9576	2.3796	31.77

Table 3: Fluid properties at the experimental conditions (1 bar, 25°C) of Youn et al. (2018). A_0 and the experimental u amplitude are not explicitly given by them and are estimated from their graphs.

2.4 Combined effects of oscillation and evaporation

This section shows the implication of the above results for the case of heating condition (i. e. a positive ΔT). According to Eq. 2.20, a net evaporation occurs for $\Delta T > 0$, and the mass flux $J(x) \propto h^{-1}(x)$.

In previous sections of Subsec. 2.3.6, because the isothermal scenario and stationary contact line have been considered, contact angles at different scales are identical, and we did not take special notice of them. They are all denoted by θ. However, in this section, contact angles should be distinguished due to liquid evaporation to facilitate our discussion. The three different length scales introduced in Subsec. 1.1.2.2 are employed. The contact angle variations obtained from the above meniscus oscillation calculation (Fig. 11a and Fig. 12b) are macroscopic results. They are denoted as θ_app here.

2.4.1 *Multiscale approach*

Instead of solving Eq. 2.21 for evaporative cases, we first apply the multiscale reasoning introduced in Subsec. 1.1.2.2. Consider the minimal complexity case, where only the Kelvin effect is included. The characteristic size of the contact line vicinity, where the Kelvin effect is important, is ℓ_VK. It is nanometric and is thus significantly smaller than the characteristic scale of film shape variation that we call macroscopic. For this reason, Eq. 2.21 can be understood within a multiscale paradigm in the spirit of the asymptotic matching techniques.

In the inner region, called the microregion in Subsec. 1.1.2.2, the first (transient) term is negligible with respect to the Kelvin term (Δp-containing term in the r.h.s. of Eq. 2.21). Thus, the problem becomes steady (i.e. with $\partial h/\partial t = 0$). When $\Delta T \neq 0$, a strong interfacial curvature that exists in the microregion causes a difference between the microscopic contact

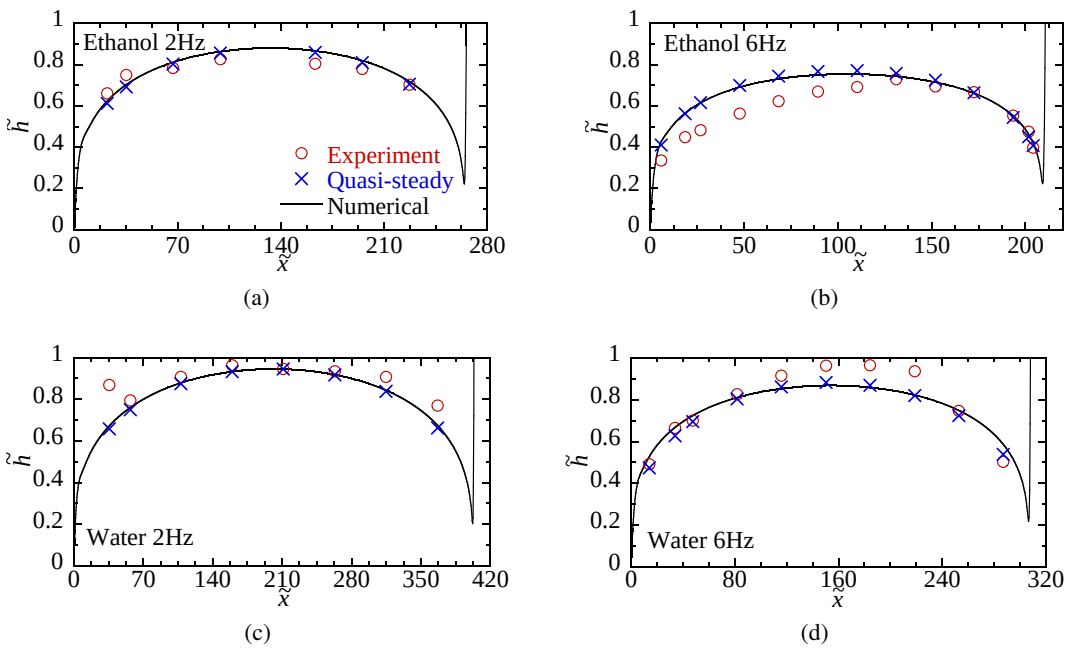

Figure 17: Liquid film thickness: comparison of the experimental data of Youn et al. (2018), quasi-steady estimation with Eq. 2.13 and numerical results for ethanol (a) and (b), for water (c) and (d).

angle θ_{micro} and the interface slope θ_{V} defined at $x \to \infty$ within the microregion. Their relationship can be expressed as

$$\theta_{\text{V}} = \theta_{\text{V}}(\Delta T, \theta_{\text{micro}}), \tag{2.34}$$

The numerical calculation of θ_{V} is based on the steady version of Eq. 2.21, which is solved with the boundary conditions (2.23a, 2.23b). The other two boundary conditions for this fourth-order differential equation are the imposed slope θ_{micro} at the contact line and the condition of zero (on the microregion scale) curvature

$$\left.\frac{\partial h}{\partial x}\right|_{x=0} = \theta_{\text{micro}}, \quad \left.\frac{\partial^2 h}{\partial x^2}\right|_{x\to\infty} = 0. \tag{2.35 a,b}$$

Figure 18 demonstrates an example of θ_{V} as a function of θ_{micro} and ΔT for pentane at 1 bar, cf, Eq. 2.34. It turns out that $\theta_{\text{V}}(\Delta T, \theta_{\text{micro}})$ monotonically grows with both θ_{micro} and intensity of evaporation controlled by ΔT; evidently, $\theta_{\text{V}}(\Delta T = 0) = \theta_{\text{micro}}$.

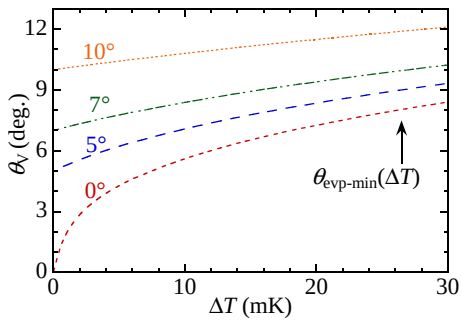

Figure 18: Value of θ_{V} as a function of ΔT for different θ_{micro} computed for pentane at 1 bar. The curve for $\theta_{\text{micro}} = 0$ corresponds to $\theta_{\text{evp-min}}(\Delta T)$.

One now introduces

$$\theta_{\mathrm{evp-min}}(\Delta T) \equiv \theta_{\mathrm{V}}(\Delta T, \theta_{\mathrm{micro}} = 0), \tag{2.36}$$

which is the lower bound of $\theta_{\mathrm{V}}(\Delta T, \theta_{\mathrm{micro}})$, i.e. its value for the complete wetting case (Janeček et al., 2013). Therefore, the $\theta_{\mathrm{micro}} = 0$ curve in Fig. 18 represents $\theta_{\mathrm{evp-min}}(\Delta T)$. For example, for $\Delta T = 30\,\mathrm{mK}$, one finds $\theta_{\mathrm{evp-min}}(\Delta T = 30\,\mathrm{mK}) \simeq 8.4°$, see Fig. 18.

In the outer (macroscopic) region, the Kelvin effect is negligible, so the Δp term on the r.h.s. of Eq. 2.21 vanishes. For $\Delta T = 0$, this equation is that of the isothermal problem Eq. 2.16 with $J = 0$. Both problems can be matched at an intermediate scale $\gg \ell_{\mathrm{VK}}$, but much smaller than the macroscopic scale. Because the contact line is stationary, the apparent contact angle θ_{app} visible on this latter scale is thus equal to θ_{V}.

We consider below a case of a small ΔT, where the evaporation in the film and meniscus regions can be neglected during an oscillation period, and the macroscopic results of Sec. 2.3 still apply.

When the full problem is solved, the micro- and macroregions can be matched for a given ΔT. They are connected through the formula Eq. 2.34, which means that the oscillatory film shape eventually enforces the value of θ_{micro}.

In the sense of the multiscale reasoning, θ_{app} must simultaneously satisfy the conditions:

1. Similarly to the case where $\Delta T = 0$, the dynamic film shape imposes the θ_{app} value because the contact line is fixed (in previous sections, it was denoted as θ). This implies that the inequality (2.29) should also hold for $\Delta T \neq 0$.

2. On the other hand, θ_{app} is defined by Eq. 2.34, because of stationary contact line $\theta_{\mathrm{app}} = \theta_{\mathrm{V}}$. As shown above, it is bounded from below: $\theta_{\mathrm{app}} \geq \theta_{\mathrm{evp-min}}(\Delta T)$.

Condition (ii) means that $\theta_{\mathrm{app}}(t)$ remains larger than $\theta_{\mathrm{evp-min}}(\Delta T)$ throughout oscillation. From the inequality (2.29), one thus obtains

$$\theta_{\mathrm{min}} \geq \theta_{\mathrm{evp-min}}(\Delta T), \tag{2.37}$$

which presents a necessary condition for the matching of two regions. With the equality sign $\theta_{\mathrm{min}} = \theta_{\mathrm{evp-min}}(\Delta T_{\mathrm{max}})$, this equation defines a superheating limit ΔT_{max}. Since $\theta_{\mathrm{evp-min}}(\Delta T)$ is an increasing function (cf. Fig. 18), the superheating limit ΔT_{max} is an upper bound. Thus the inequality (2.37) can hold when $\Delta T < \Delta T_{\mathrm{max}}$. To determine graphically ΔT_{max}, Fig. 19 presents an example where $\theta_{\mathrm{app}}(t)$ (bottom and vertical axes, extracted from Fig. 11a) is plotted together with $\theta_{\mathrm{evp-min}}(\Delta T)$ (top and vertical axes, extracted from Fig. 18). During the oscillation, the minimum value $\theta_{\mathrm{min}} \simeq 1.5°$ is attained. From the dependence $\theta_{\mathrm{evp-min}}(\Delta T)$, one can deduce that $\Delta T_{\mathrm{max}} \simeq 1$ mK. Thereupon, the solution of the oscillation problem with evaporation is nonexistent for $\Delta T > 1$mK.

2.4.2 *Numerical approach*

To support our multiscale discussion, this section shows numerical results of Eq. 2.21. In Fig. 20, variations of θ_{micro} during meniscus oscillation are plotted for small ΔT of $0.2\,\mathrm{mK}, 0.5\,\mathrm{mK}, 0.7\,\mathrm{mK}$ and $0.9\,\mathrm{mK}$. θ_{micro} attains the minimal value near the time moment $t = 0.968P$. The minimum value of θ_{micro} decreases with superheating, which implies that θ_{micro} reaches zero for certain ΔT. The minimal values for $\Delta T = 0.2\,\mathrm{mK}, 0.5\,\mathrm{mK}, 0.7\,\mathrm{mK}$ and $0.9\,\mathrm{mK}$, are about $1.2°, 0.82°, 0.53°$ and $0.2°$ respectively. The simulations confirm that the reasoning of the previous section is correct because the minimal value of θ_{micro} tends to zero when ΔT approaches $\simeq 1\,\mathrm{mK}$.

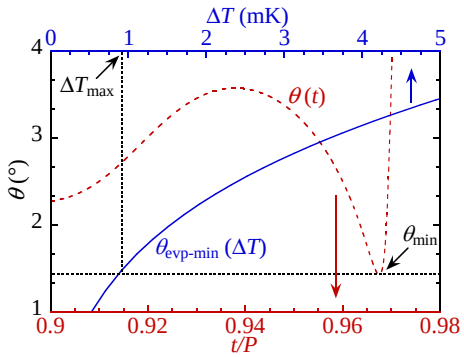

Figure 19: Apparent contact angle θ_{app} calculated for $\theta_{\text{micro}} = 0$ as a function of superheating ΔT (the blue curve, example of pentane at 1 bar, same as in Fig. 18) plotted together with the apparent contact angle variation during meniscus oscillation (the red dashed curve). The latter is a curve for initial value 10°, the same as at the inset of Fig. 11a.

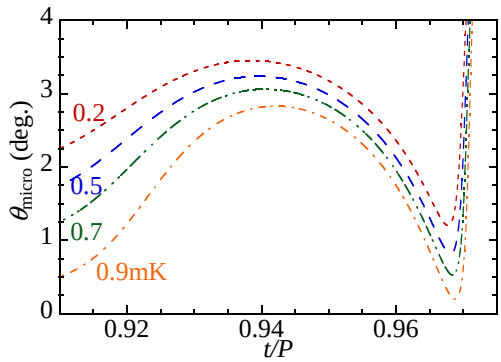

Figure 20: Variations of θ_{micro} from $t = 0.91P$ to $0.97P$, for ΔT of 0.2 mK, 0.5 mK, 0.7 mK and 0.9 mK. $\theta_{\text{i}} = 10°$, $\tilde{P} = 50$.

Moreover, the value of θ_{micro} varies drastically around the minimum. It corresponds to the short time-lapse when the largest ripple formed near the meniscus (cf. Fig. 9) approaches the contact line, cf. Fig. 21a. The interface curvature exhibits rapid and intense changes near this moment, cf. Fig. 21b. After the ripple disappearance (for $t > 0.968P$), the pressure jump quickly relaxes to the steady-state profile, in which Δp saturates towards both the contact line and the meniscus, and decreases monotonically in between, for example, see the curve for $t = 0.974P$. Throughout oscillation, Δp at the contact line remains invariable, which conforms to Eq. 2.19.

2.4.3 *Paradox and its solution*

Both above approaches show that the solution to the oscillation problem is nonexistent when the capillary superheating exceeds a tiny value, much smaller than the realistic superheating.

The reason for this paradox is the pinned contact line: another degree of freedom appears for the receding contact line: the contact angle is no longer constrained. The contact line is necessarily depinned when θ_{app} attains $\theta_{\text{app}}\left(\Delta T, 0\right)$ (actually, a larger value $\theta_{\text{app}}\left(\Delta T, \theta_{\text{rec}}\right)$ but $\theta_{\text{app}}\left(\Delta T, 0\right)$ gives a lower bound).

Note that θ_{min} grows slightly with the meniscus velocity amplitude Ca_0 (Fig. 12b), so does ΔT_{max}. However, the ΔT_{max} value remains of the order of mK. As this maximum superheating is considerably smaller than that encountered in practice (where it is rather of several K, see, e.g., Fourgeaud et al., 2017), one can deduce that the contact line receding at evaporation is inevitable and necessary to be accounted for in PHP modeling.

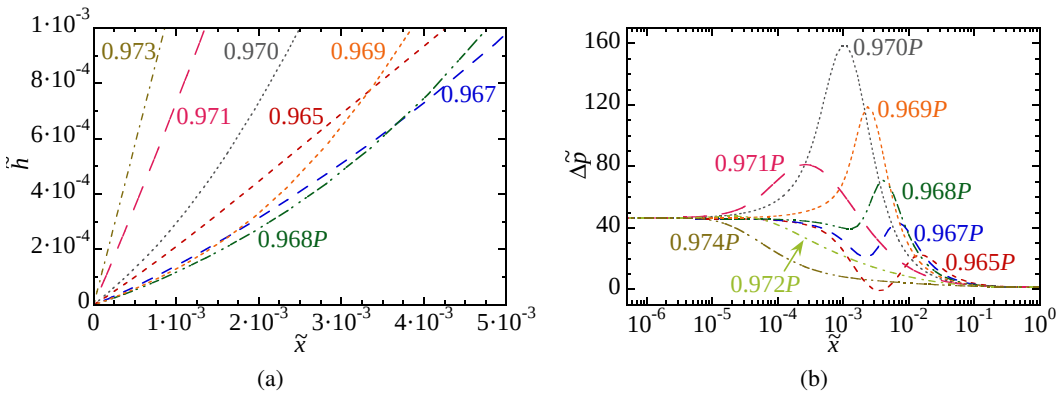

Figure 21: Film thickness (a) and pressure jump profiles (b) in the microregion around the moment $t = 0.968P$ when the minimal θ_{micro} is achieved: $\Delta T = 0.7\,\mathrm{mK}$, $\theta_{\mathrm{i}} = 10°$, $\tilde{P} = 50$.

While the calculation has been completed here only for the pentane case, one can safely state that $\Delta T_{\max}$ is substantially smaller than realistic superheating used in thermal engineering applications for many other fluids.

2.5 Conclusions

This chapter deals with liquid films deposited by oscillating liquid menisci in capillary tubes for the case where contact lines are pinned at the farthest meniscus position. The liquid film thickness is not homogeneous because of the varying meniscus velocity. The periodic solution for such a problem has been identified. The average film thickness is one of the most important quantities. It has been analyzed depending on the main system parameters, which are the initial contact angle (that at the farthest meniscus position), the period of oscillation, and the amplitude of the meniscus velocity represented with the dimensionless capillary number. The average film thickness depends only weakly on the initial contact angle and grows with the oscillation period until saturation. Globally, the average film thickness is well described by the quasi-steady approach.

The meniscus curvature and the contact angle vary in time during such a motion. The contact angle remains nearly constant for a large part of the period. This constant value is independent of the initial contact angle and the oscillation period. The minimal contact angle encountered during oscillation turns out to be a significant quantity. It occurs when the largest film ripple approaches the contact line during the meniscus advance. The minimal contact angle weakly depends on both the oscillation period and the initial contact angle and grows with the capillary number. Its value remains, however, small, of the order of several degrees.

Understanding evaporation that co-occurs with oscillation is essential for modeling PHPs. The most substantial impact of evaporation concerns the contact line vicinity, where the liquid film is the thinnest. It is shown that the minimal contact angle that occurs during oscillation with the pinned contact line sets an upper bound for the tube superheating, for which a solution for such a problem exists. This upper bound is rather small (e.g., it is $\sim 1\,\mathrm{mK}$ for the pentane at 1 bar), much smaller than typical experimental superheating. This shows the necessity of considering the contact line receding during simultaneous oscillation and evaporation, which is the topic of the following chapter.

Chapter 3

Contact line receding at evaporation

Another crucial issue of the liquid film dynamics that has yet to be addressed is the moving edges of liquid films. The edges (contact lines demarcating the wetted and dry areas) spontaneously recede towards the liquid side because of the capillary forces. This phenomenon is called capillary dewetting. A similar phenomenon appears in the dewetting of a liquid film on a partial-wetting solid surface, where the film retracts from the area of a solid substrate originally covered by the liquid. [1]

Previous dewetting studies mainly concern adiabatic conditions. However, thin film flows are used extensively in a myriad of industrial applications where film evaporation/condensation is used as an extremely efficient means of heat transfer, such as falling film chillers and heat pipes. More recently, dewetting was studied in the context of bubble growth in nucleate boiling (Urbano et al., 2018; Bureš et al., 2021). In all these scenarios, phase change co-occurs with dewetting, and liquid films are surrounded by the fluid's vapor.

In this chapter, we continue the line of thought put forward in the previous chapter, where the lubrication approximation is used to describe thin film flows. The objectives of this chapter are threefold. The primary aim is to find the numerical solution to the dewetting problem in the presence of liquid film evaporation created by heated substrates. It is necessary to include the nanoscale effects (Subsec. 1.1.2.1) relevant to the description of the contact line vicinity, where evaporation is extreme. As slopes of liquid-vapor interfaces increase in the presence of evaporation, the conventional lubrication approach becomes insufficient. We thus develop the generalized lubrication theory suitable for larger interface slopes. The numerical results are compared to the experiment in Subsec. 3.3.3. Another objective is to extend the multiscale theory proposed initially by Snoeijer et al. (2010) for adiabatic dewetting (Subsec. 1.1.2.2) to the case of evaporation. The main parameters of the multiscale theory are discussed, and its results are compared to the numerical solution. Finally, we aim to develop a simple model for describing dewetting phenomena in the presence of evaporation and for PHP modeling.

1 This chapter is based on the article (Zhang et al., 2022b) and a manuscript submitted to EPL, formerly Europhysics Letters.

3.1 Problem description

We briefly restate the classic example of dewetting under adiabatic conditions (in the absence of any overall heat and mass transfer between liquid, solid and ambient gas). Consider a smooth solid substrate initially covered by a thick (at least micrometric) liquid film of viscous fluid. Such a film is metastable under partial wetting conditions because once a dry hole is created in the film (the contact line appears), the dry area will grow spontaneously. The capillary forces drive the motion. As the contact line expands outwards, the film collects the liquid situated previously on the dried area. Due to the high viscous friction in the thin film, this liquid cannot flow inside the film. It thus forms a growing ridge that situates along the contact line. One can take the vertical cross-section that passes through the center of a dry hole. The problem is then described in two dimensions, as shown in Fig. 22.

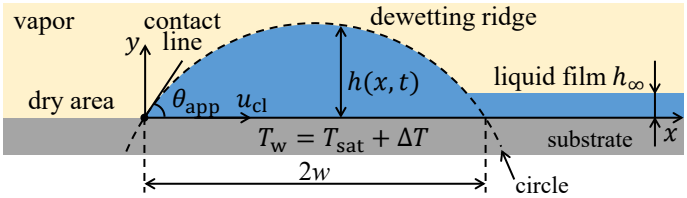

Figure 22: Dewetting ridge receding over a liquid film while the dry area expands.

Experimental studies have shown that the contact line recedes at a constant speed (Brochard-Wyart et al., 1991; deGennes et al., 2004). Conversely, discussed in Subsec. 1.1.2.2, the theoretical analysis by Snoeijer et al. (2010) has refuted that the receding speed $u_{\rm cl}$ should decline very slowly (logarithmically) with time (or with the ridge size w that grows with time). They have used the slip condition to relax the singularity. Though, as argued by Fourgeaud et al. (2016), Eq. 1.29 and Eq. 1.31 should hold for any microregion model (including that accounting for the evaporation) because of the scale separation, one needs to determine the key parameters $\ell_{\rm V}$ and $\theta_{\rm V}$, and verify if the two equations are indeed valid under the conditions of evaporation. To explain their experimental results, Fourgeaud et al. (2016) hypothesized that the liquid mass loss caused by intense evaporation at the contact line could accelerate its receding, in addition to the capillary effect described by Eq. 1.31. This issue needs to be clarified.

3.1.1 *Generalized lubrication theory*

Consider the dewetting problem in the vertical cross-section as shown in Fig. 22, where the liquid film of thickness h_∞ is surrounded by the pure vapor of the same substance. In the 2D description (x, y), the interface is $y = h(x, t)$. The substrate is assumed to be highly conductive and thus isothermal. The temperature of its wall $T_{\rm w} = T_{\rm sat} + \Delta T$ can differ from $T_{\rm sat} = T_{\rm sat}(p_{\rm v})$, thus causing the film evaporation or condensation for positive or negative ΔT, respectively.

Since the vapor density $\rho_{\rm v}$, viscosity and thermal conductivity are all small compared to the liquid, one can apply the "one-sided" formulation, as in Subsec. 1.1.1, where both the vapor-side hydrodynamic stress and the heat flux into the vapor at the interface are neglected in comparison with values on the liquid side. Therefore, the vapor pressure $p_{\rm v}$ is assumed to be spatially homogeneous.

Since we consider large ΔT up to $20\,\mathrm{K}$ in this chapter and moving contact lines, the interface is highly curved, and intense heat and mass transfers occur near the contact line (Janeček et al., 2012; Savva et al., 2017). Instead of the conventional lubrication theory used in Chap. 2, where ΔT is merely $1\,\mathrm{mK}$, the generalized lubrication theory is developed. All

the nanoscale and interfacial effects pertinent to relaxing the singularity are included, cf. Subsec. 1.1.2.1.

When the interface slope ϕ is larger than $\sim 30°$, the conventional lubrication equation Eq. 1.19 valid for small slopes is hardly applicable. In this case, one can take advantage of a more accurate approach suggested initially by Boender et al. (1991) and rediscovered more recently by Snoeijer (2006). Instead of operating with the coordinate x, it uses the parametric interface description in terms of the curvilinear coordinate s that runs along it, $h(s,t)$, with $s = 0$ at the contact line. Therefore, the following geometrical relations hold:

$$\frac{\partial h}{\partial s} = \sin\phi, \tag{3.1a}$$

$$\frac{\partial x}{\partial s} = \cos\phi, \tag{3.1b}$$

where ϕ is the local interface slope.

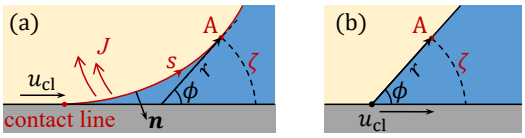

Figure 23: Sketch of (a) a curved interface and (b) the straight liquid wedge, corresponding to the point A.

One of the major advantages of such a parametrization is that instead of the approximation (Eq. 2.1), one uses the rigorous geometrical curvature definition

$$K = \frac{\partial \phi}{\partial s}. \tag{3.2}$$

Consider an example of the curved wedge geometry shown in Fig. 23a. Nevertheless, the approach presented hereafter does not comprise its generality for any liquid film geometry. The approach consists in approximating the tangential pressure gradient $\partial p/\partial s$ at A (an interfacial point with coordinate s, cf. Fig. 23a) by that created by the flow in a straight liquid wedge, the opening angle of which is ϕ; cf. Fig. 23b. In other words, if one introduces the polar radius r of the point A defined within the corresponding straight wedge, then this hypothesis reads

$$\frac{\partial p}{\partial s} \simeq \frac{\partial p}{\partial r}. \tag{3.3}$$

Here, the right-hand side is calculated within the straight wedge problem; the upper ray of the straight wedge (to which A belongs) is tangential to the curved interface, meaning $\partial s = \partial r$.

3.1.1.1 *Generalized moving contact line description*

This theory was developed initially to describe the adiabatic moving contact line problem ($J = 0$); it was used in many works - see e. g. Chan et al. (2013), Chan et al. (2020), and Delon et al. (2008). In this case, the interface motion induces the pressure gradient (in the reference frame where the wedge is immobile). The Stokes problem (Subsec. A.3.3) results in

$$\frac{\partial \Delta p}{\partial s} = \frac{3\mu u_{cl}}{h^2}\bar{F}(\phi). \tag{3.4}$$

where the spatial homogeneity of p_v is assumed and

$$\bar{F}(\phi) = \frac{2}{3}\frac{\sin^3\phi}{\phi - \sin\phi\cos\phi}. \tag{3.5}$$

One mentions that $\bar{F}(\phi \to 0) = 1$, so the generalized theory reduces to the conventional lubrication approach for small slopes as expected.

Another generalization is required to include the hydrodynamic slip in the model. The analytical Stokes problem solution has yet to be discovered for this case. In previous works (Chan et al., 2013; Delon et al., 2008), the slip length was introduced as in the conventional lubrication equation

$$\frac{\partial \Delta p}{\partial s} = \frac{3\mu u_{\text{cl}}}{h(h + cl_{\text{s}})}\bar{F}(\phi) \tag{3.6}$$

with the hypothesis $c = 3$. In a subsequent work (Chan et al., 2020), the c coefficient has been found for the specific problem of adiabatic contact line dynamics as a function of θ_{micro}, $c = 3 - (9/10)\theta_{\text{micro}}^2 + o(\theta_{\text{micro}}^2)$. However, in general, c should depend not on the boundary conditions (θ_{micro} is one of them) but on the local interface slope, so the result of Chan et al. (2020) cannot be used here directly.

We propose the following phenomenological argument that leads to a similar result. The velocity gradient varies linearly along the vertical axis in the conventional lubrication equation. However, in a wedge geometry, where the flow lines are usually convergent (or divergent), one can reasonably assume that the velocity gradient varies linearly along an arc (which is actually the case in the straight wedge Stokes problem of Sec. A.3). The arc center can be defined locally for each interface point A as an intersection of the tangent to the interface with the wall. The arc radius r is the distance from A to the center (Fig. 23a), with r related to h via

$$h = r \sin \phi. \tag{3.7}$$

The arc length is $\zeta = \phi r$ or

$$\zeta = h\phi / \sin \phi. \tag{3.8}$$

Instead of Eq. 3.6, one can thus write

$$\frac{\partial \Delta p}{\partial s} = \frac{3\mu u_{cl}}{\zeta(\zeta + 3l_{\text{s}})}F(\phi), \tag{3.9}$$

where

$$F(\phi) = \frac{2\phi^2}{3}\frac{\sin \phi}{\phi - \sin \phi \cos \phi} \tag{3.10}$$

satisfies $F(\phi \to 0) = 1$.

Note that Eq. 3.9 is equivalent to Eq. 3.6 with $c = 3 \sin \phi / \phi = 3 - (1/2)\phi^2 + o(\phi^2)$. Since $\phi \to \theta_{\text{micro}}$ near the CL, this expression is quite close to the above result of Chan et al. (2020) but has the advantage of being usable universally. On the basis of the above argument, such a "ζ-formulation" will be used hereafter for all other terms.

3.1.1.2 *Generalized description including the phase exchange*

Mathieu (2003) proposed the generalized description of the phase exchange. His approach is based on its strong localization near the contact line. The Stokes problem (Subsec. A.3.4) assumes that the mass exchange is modeled by a point source Φ localized *at* the contact line. Here, Φ is defined as a flux through the arc of the length ζ (Fig. 23):

$$\Phi = \int_0^{\phi} r\, u_r \mathrm{d}\varphi, \tag{3.11}$$

where u_r is the component of the liquid velocity $\boldsymbol{u}$ assumed to be normal to the arc.

From the $\partial p_l / \partial s$ definition, this model assumes that the flow along the interface at a point with the coordinate s (Fig. 23a) is provided by a source located at a smaller s (i.e., closer

to the contact line) (Janeček et al., 2014). Evidently, when the phase exchange is distributed over the interface, $\Phi = \Phi(s)$. This assumption results in

$$\frac{\partial \Delta p}{\partial s} = \frac{3\mu\Phi}{\zeta^2(\zeta + 3l_\mathrm{s})} G(\phi), \tag{3.12}$$

where

$$G(\phi) = \frac{\phi^3}{3} \frac{4}{\sin\phi\cos\phi - \phi\cos 2\phi} \tag{3.13}$$

is the correction factor to the conventional lubrication theory Eq. 1.19, $G(\phi \to 0) = 1$. The slip length is introduced here similarly to Eq. 3.9.

To include both sources of the liquid flow along the wedge, i. e. the contact line motion and the phase exchange, one can take advantage of the linearity of the Stokes equations. The total pressure drop is thus a sum

$$\frac{\partial \Delta p}{\partial s} = \frac{3\mu[\Phi G(\phi) + \zeta u_\mathrm{cl} F(\phi)]}{\zeta^2(\zeta + 3l_\mathrm{s})} \tag{3.14}$$

of the contributions of Eq. 3.9 and Eq. 3.12).

One more assumption concerns the Marangoni term. By using the "ζ-formulation" for it, one can write in an analogy with Eq. 1.19

$$\mu[\Phi G(\phi) + \zeta u_\mathrm{cl} F(\phi)] = \frac{\zeta}{2}(\zeta + 2l_\mathrm{s})\frac{\partial \sigma}{\partial s} + \frac{\zeta^2}{3}(\zeta + 3l_\mathrm{s})\frac{\partial \Delta p}{\partial s}. \tag{3.15}$$

Such an ansatz can be justified by the diverging flow in a wedge and by the fact that the Marangoni term is essential only in the close vicinity of the contact line where the slope remains generally small (of the order of θ_micro) in most cases.

The value of Φ can be expressed via the component $u_\mathrm{n} = \boldsymbol{u} \cdot \boldsymbol{n}$ of the liquid velocity $\boldsymbol{u}$, which is normal to the vapor-liquid interface (with the vector $\boldsymbol{n}$ directed towards the liquid, see Fig. 23a). One can rewrite Eq. 1.14 as

$$u_\mathrm{n} = \frac{\partial \Phi}{\partial s}. \tag{3.16}$$

Instead of the approximation of Eq. 1.16, the interface velocity projection to $\boldsymbol{n}$ is

$$u^\mathrm{i} = -\frac{\partial h}{\partial t}\cos\phi. \tag{3.17}$$

Eliminating Φ in Eq. 3.16 with Eq. 3.15, then substituting the result and Eq. 3.17 into the equation of mass balance at interface Eq. 1.13, one obtains finally the generalized counterpart of Eq. 1.19:

$$\frac{\partial h}{\partial t}\cos\phi + \frac{\partial}{\partial s}\left\{\frac{1}{\mu G(\phi)}\left[\frac{\zeta}{2}(\zeta + 2l_\mathrm{s})\frac{\partial \sigma}{\partial s} + \frac{\zeta^2}{3}(\zeta + 3l_\mathrm{s})\frac{\partial \Delta p}{\partial s}\right] - u_\mathrm{cl}\zeta\frac{F(\phi)}{G(\phi)}\right\} = -\frac{J}{\rho}. \tag{3.18}$$

The pressure jump equation is then written as

$$\frac{\sigma}{\cos\phi}\frac{\partial^2 h}{\partial s^2} - \Delta p = J^2\left(\frac{1}{\rho_\mathrm{v}} - \frac{1}{\rho}\right), \tag{3.19}$$

which is a combination of Eq. 1.26, Eq. 1.25, Eq. 3.1a and Eq. 3.2.

One more equation needs to be written to define J that appears in Eq. 3.18. The temperature distribution is assumed to be linear along the arc length ζ (Fig. 23a) as suggested by the

rigorous thermal analysis of the straight wedge (Anderson et al., 1994). Instead of Eq. 1.18, one then obtains

$$J = \frac{k(T_\mathrm{w} - T^\mathrm{i})}{\zeta \mathcal{L}}, \tag{3.20}$$

where the interface temperature is expressed with Eq. 1.27. Since liquid films are thin, only heat conduction exists in films and is used to vaporize liquid at the interface. A line temperature variation from the solid surface T_w to T^i along ζ is assumed.

Together with Eq. 3.20, Eq. 1.27 and Eq. 3.19, the interface $h(s,t)$ evolution obeys Eq. 3.18.

3.1.2 *Boundary conditions and contact line receding speed*

The problem is numerically solved for $s \in [0, s_\mathrm{f}]$, with s_f a point far from the ridge, where the film can be assumed flat. The film flatness condition (zero spatial derivatives and $\phi = 0$) used in Eq. 3.18 results in

$$h_\infty = h_0 \sqrt{1 - \frac{t}{t_\mathrm{d}}}, \tag{3.21}$$

where h_0 is the initial ($t = 0$) film thickness, and

$$t_\mathrm{d} = \frac{\mathcal{L}\rho h_0^2}{2k\Delta T}$$

is the film drying time. The liquid is assumed at saturation. For the adiabatic problem ($\Delta T = 0$), the thickness, $h(s_\mathrm{f}, t) = h_0$, remains constant.

At the contact line ($s = 0$), the geometry implies

$$h = 0, \tag{3.22a}$$

$$\frac{\partial h}{\partial s} = \sin\theta_\mathrm{micro}, \tag{3.22b}$$

The set of lubrication equations (Eq. 3.18, Eq. 3.19) is of the fourth order, so we need one more boundary condition. It should express the solution regularity at the contact line. To derive this condition for the generalized lubrication approach, one can proceed similarly to Janeček et al. (2012), who obtained it for the conventional case. To provide the temperature continuity, the interface temperature T^i at the contact line should be equal to that of the solid, $T_\mathrm{w} = T_\mathrm{sat} + \Delta T$. From Eq. 1.27, one gets the condition

$$\Delta p = \frac{\mathcal{L}\rho}{T_\mathrm{sat}}(\Delta T - R^\mathrm{i} J \mathcal{L}) - \frac{J^2\rho}{2}\left(\frac{1}{\rho_\mathrm{v}^2} - \frac{1}{\rho^2}\right), \tag{3.23}$$

valid asymptotically as $s \to 0$. To obtain $J(s \to 0)$, Eq. 3.18 is integrated from 0 to s, where s is infinitesimally small, so $\zeta = s\theta_\mathrm{micro}$. This results in

$$-\gamma\frac{\partial T^\mathrm{i}}{\partial s} + \theta_\mathrm{micro} s \frac{\partial \Delta p}{\partial s} = \frac{\mu}{l_\mathrm{s}\theta_\mathrm{micro}}\left[\theta_\mathrm{micro} u_\mathrm{cl} F(\theta_\mathrm{micro}) - \frac{JG(\theta_\mathrm{micro})}{\rho}\right]. \tag{3.24}$$

The T^i derivative can be obtained from Eq. 3.20 by developing T^i into the Taylor series around $s = 0$:

$$\frac{\partial T^\mathrm{i}}{\partial s} = -\frac{\mathcal{L}\theta_\mathrm{micro}}{k} J. \tag{3.25}$$

Its substitution into Eq. 3.24 results in the expression

$$s\frac{\partial \Delta p}{\partial s} = \frac{\mu}{l_\mathrm{s}\theta_\mathrm{micro}}\left[u_\mathrm{cl} F(\theta_\mathrm{micro}) - J\left(\frac{G(\theta_\mathrm{micro})}{\theta_\mathrm{micro}\rho} + \frac{l_\mathrm{s}\mathcal{L}\theta_\mathrm{micro}}{\mu k}\gamma\right)\right]. \tag{3.26}$$

By combining Eq. 3.23 and Eq. 3.26, one obtains a differential equation for Δp that is valid asymptotically. Its solution (Janeček et al., 2012) shows that both Δp and J remain finite at the contact line. The left-hand side of Eq. 3.26 thus tends to zero as $s \to 0$, which results in

$$J(s \to 0) = \frac{u_{\mathrm{cl}} F(\theta_{\mathrm{micro}})}{\dfrac{G(\theta_{\mathrm{micro}})}{\theta_{\mathrm{micro}}\rho} + \dfrac{l_{\mathrm{s}}\mathcal{L}\theta_{\mathrm{micro}}}{\mu k}\gamma}. \tag{3.27}$$

The pressure value at the contact line is easily obtained by substituting Eq. 3.27 into Eq. 3.23. However, a weaker form of the fourth boundary condition

$$\left.\frac{\partial \Delta p}{\partial s}\right|_{s\to 0} = 0 \tag{3.28}$$

is more convenient (Zhang et al., 2021) to provide a better numerical stability.

Another equation is needed to determine the contact line speed (which is a part of the problem); Eq. 3.27 can be used for this purpose.

3.1.3 *Numerical solution*

The problem is solved numerically using the finite volume method (FVM), which provides better stability than the conventional finite difference method. In this one-dimensional case, a finite volume is simply a line segment. The computational algorithm is similar to that used in Subsec. 2.3.5. The variables and their even-order derivatives are defined at the mesh nodes (the centers of segments), while the odd-order derivatives are defined at the segment boundaries. In order to capture the microscopic effects without significantly increasing the total number of nodes, the meshing is exponentially refined near the contact line. The nonlinear terms are managed with iterations. Details of the numerical scheme are in Appendix B.

The numerical approach is first tested for the adiabatic case against the asymptotic theory of Snoeijer et al. (2010). Then we analyze the dewetting dynamics in the presence of liquid film evaporation. The numerical results are finally compared with the experimental data of Fourgeaud et al. (2016).

3.2 Adiabatic dewetting

A typical numerical result demonstrating the growth of the dewetting ridge under classical adiabatic conditions ($\Delta T = 0$) is shown in Fig. 24a for $\theta_{\mathrm{micro}} = 10°$ and for FC-72 (more precisely, n-perfluorohexane) fluid, whose properties are listed in Tab. 4. The flat part of the liquid film has constant thickness h_∞ =50 µm, which is a typical film thickness in pulsating heat pipes (Nikolayev, 2021). The moving contact line has been chosen as the frame of reference, therefore, stays at the origin. The ridge half-width w grows with time (see the supplementary movie), so the evolution is discussed in terms of w rather than time to enable a comparison with the multiscale theory.

The numerically obtained spatial variation of the interface slope ϕ is shown in Fig. 24b for the time moment at which $w/h_\infty = 200$ and $Ca = 4.39 \times 10^{-5}$ (red solid line). All three scales discussed in Subsec. 1.1.2.2 can be recognized.

The intermediate region obeys the governing equation Eq. 3.4. Its solution is known to be well approximated by the Cox-Voinov law Eq. 1.28. Since the equation Eq. 3.4 is of second order with respect to ϕ, its solution contains two integration constants: θ and ℓ_{V}. Obviously, in the absence of contact line motion, the interface is straight, so $\phi(Ca = 0) = \theta_{\mathrm{micro}}$, which results in $\theta = \theta_{\mathrm{micro}}$. From the definition of the Voinov angle, $\theta_{\mathrm{V}} = \theta_{\mathrm{micro}}$ for the adiabatic case, and it remains nearly constant in a region that can be identified with the microregion.

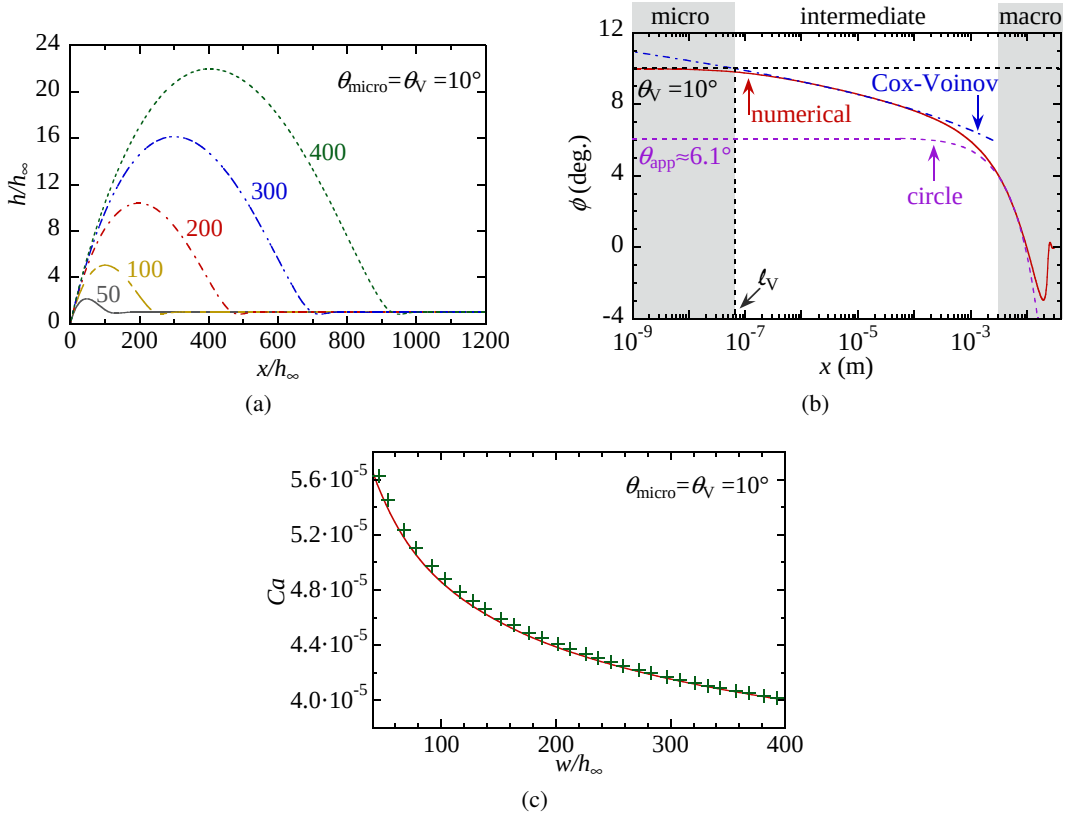

Figure 24: Numerical results concerning the adiabatic dewetting ($\Delta T = 0$) for $\theta_{\text{micro}} = 10°$ and $h_\infty = 50\,\mu\text{m}$. (a) Growth of the liquid ridge (see the supplementary movie available at https://doi.org/10.1017/jfm.2022.725). The curve parameter is w/h_∞. (b) Interface slope for $w/h_\infty = 200$. (c) Contact line receding speed Ca as a function of the ridge width. Line indicates numerical result; crosses come from Eq. 1.31.

The value $\ell_V \simeq 64\,\text{nm}$ is determined from fitting Eq. 1.28 to the numerical curve as an abscissa of the intersection of the fitting curve with the horizontal line $\phi = \theta_{\text{micro}}$. In agreement with the hypothesis of Fourgeaud et al. (2016), the ℓ_V value coincides with that given by the hydrodynamic slip: Eq. 1.30 results in $\ell_{Vsa} \simeq 63\,\text{nm}$. This is not surprising as it exceeds the value provided by the Kelvin effect: $\ell_{VK} \simeq 38\,\text{nm}$ according to Eq. 1.32. This conclusion conforms to the discussion in Subsec. 3.3.2. One needs to note that during the ridge evolution, ℓ_V grows slightly with w/h_∞ (i. e. decreases with Ca), but the variation is below 3%. This means that the Cox-Voinov formula is fairly accurate and is thus suitable for multiscale modeling.

As mentioned above, the interface of liquid ridges is circular in the macroregion. The corresponding fit is also plotted in Fig. 24b (violet dashed line). The angle at which this circle intersects the solid surface (i. e. the intersection of the fitting curve with the ordinate axis) defines the apparent contact angle $\theta_{\text{app}} \simeq 6.1°$. The half-width w of the ridge can be obtained easily from the fit as a distance between the apparent contact line and the ridge summit (Fig. 22).

The receding speed is not rigorously constant but decreases slowly. By using w and ℓ_V, both obtained from the numerical curve as discussed above, one can compare the numerical Ca to the asymptotic result Eq. 1.31 (Fig. 24c). The agreement is excellent, which shows the validity of the approach that we use.

3.3 Dewetting at evaporation

This subsection considers the liquid film evaporation caused by substrate heating. Three different fluids common for heat transfer applications are used in the calculations, whose properties are summarized in Tab. 4. Initially, the liquid film has the thickness h_0 =50 µm typical for the pulsating heat pipe used by Fourgeaud et al. (2016) in their experiments.

notation	T_{sat}	ρ	ρ_{v}	$\mathcal{L}$	k	μ	σ	γ
unit	K	kg/m^3	kg/m^3	kJ/kg	$\frac{\text{W}}{\text{m}\cdot\text{K}}$	μPa·s	10^{-2}N/m	$\frac{10^{-4}\text{N}}{\text{m}\cdot\text{K}}$
FC-72	309.1	1668.5	6.193	89.54	0.0566	559.64	1.035	0.75
Ethanol	318.2	768.04	0.4089	898.8	0.161	752.54	1.926	1.24
Water	373.1	958.37	0.5977	2256.5	0.679	281.66	5.892	1.925

Table 4: Liquid properties at the selected saturation points.

Similarly to the adiabatic case, Fig. 25a demonstrates the dewetting ridge evolution at evaporation. The fluid is FC-72 with $\theta_{\text{micro}} = 5°$, and the substrate superheating is $\Delta T = 5\,\text{K}$. Because of evaporation, liquid film thinning occurs, which is clearly visible in the flat film portion. The receding speed Ca decreases with time. It is shown in Fig. 25b as a function of the ridge half-width w (that increases with time, similarly to the adiabatic case).

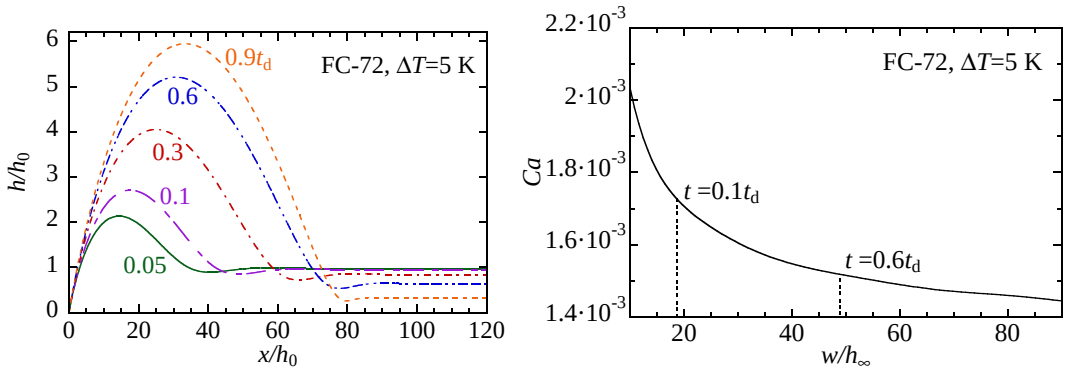

(a) Growth of the liquid ridge. The curve parameter is t/t_{d}.

(b) Evolution of the contact line receding speed Ca.

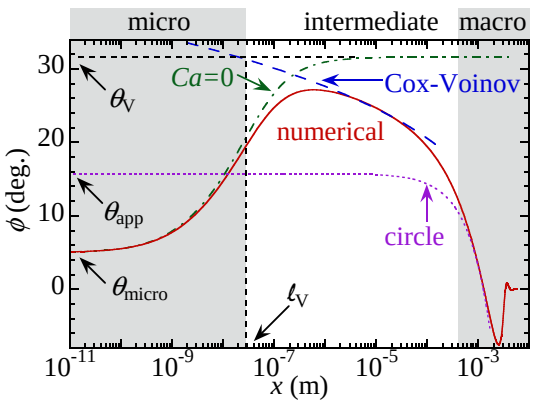

(c) Interface slope variation for $Ca = 1.614 \times 10^{-3}$.

Figure 25: Numerical results showing the formation of a dewetting ridge for FC-72; $\Delta T = 5\,\text{K}$, $\theta_{\text{micro}} = 5°$ and h_∞ =50 µm.

The central question of dewetting theory concerns the contact line dynamics, i. e. Ca as a function of ΔT. However, Ca decreases with time during the film evolution, as shown in Fig. 25b. The PHP modeling desires only an average speed. As the time evolution of Ca is slow, its value can be averaged over a time interval; such an averaging is denoted hereafter with angle brackets. A practical averaging time interval needs to be chosen. Evidently, the averaging makes little sense for times close to t_d, near which the film evaporates completely. We choose the upper averaging limit to be $0.6t_\mathrm{d}$. The averaging needs to be started at a time moment where the influence of the initial conditions fades out; $0.1t_\mathrm{d}$ is selected as the lower averaging limit. For the case of Fig. 25b, $\langle Ca \rangle \simeq 1.60 \times 10^{-3}$. Repeating the process for different ΔT ranging from 0 to 20 K, we plot $\langle Ca \rangle$ as a function of ΔT in Fig. 26 (as markers with bars) for several typical θ_micro values and for selected fluids. The bars represent the variability of Ca: the upper and lower bounds correspond to the numerical Ca at $t = 0.1t_\mathrm{d}$ and $0.6t_\mathrm{d}$, respectively. The bars are narrower for small θ_micro and ΔT, because the speed variation is less drastic.

Note that the dewetting is not only accelerated by the evaporation; it can also be induced by evaporation (Fourgeaud et al., 2016). This is seen clearly in Fig. 26. For small θ_micro (i.e for conditions of almost complete wetting), the adiabatic dewetting speed is extremely low, which means no dewetting in practice. However, it grows considerably with superheating.

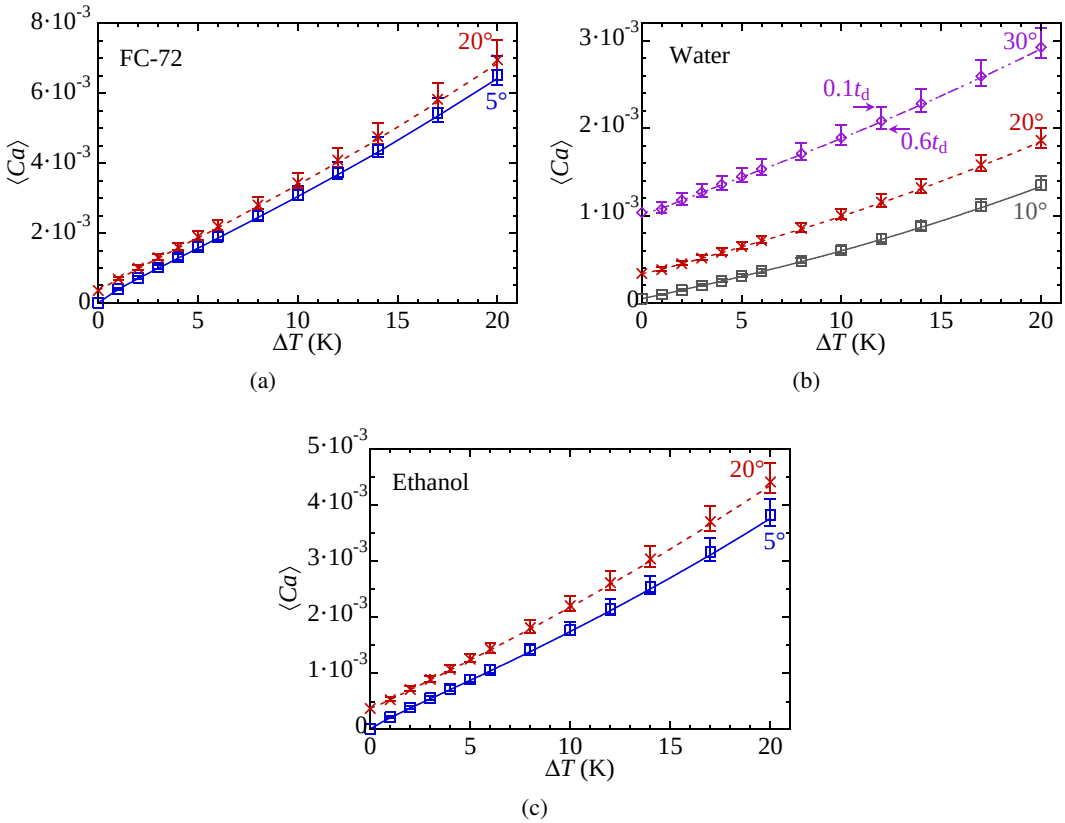

Figure 26: Comparison of numerical (markers with bars) and theoretical (lines) results for $Ca(\Delta T)$ for several θ_micro and different fluids.

3.3.1 *Comparison to multiscale theory*

However, a full numerical solution to the dewetting problem is time- and resource-consuming because of the necessity to resolve several very different length scales on the one hand and to iterate to find the contact-line speed at each time moment, on the other. For this reason,

the multiscale approach to this problem can be a viable alternative. Let us compare the numerical result and the solutions computed in each region within the multiscale approach to determine if it holds.

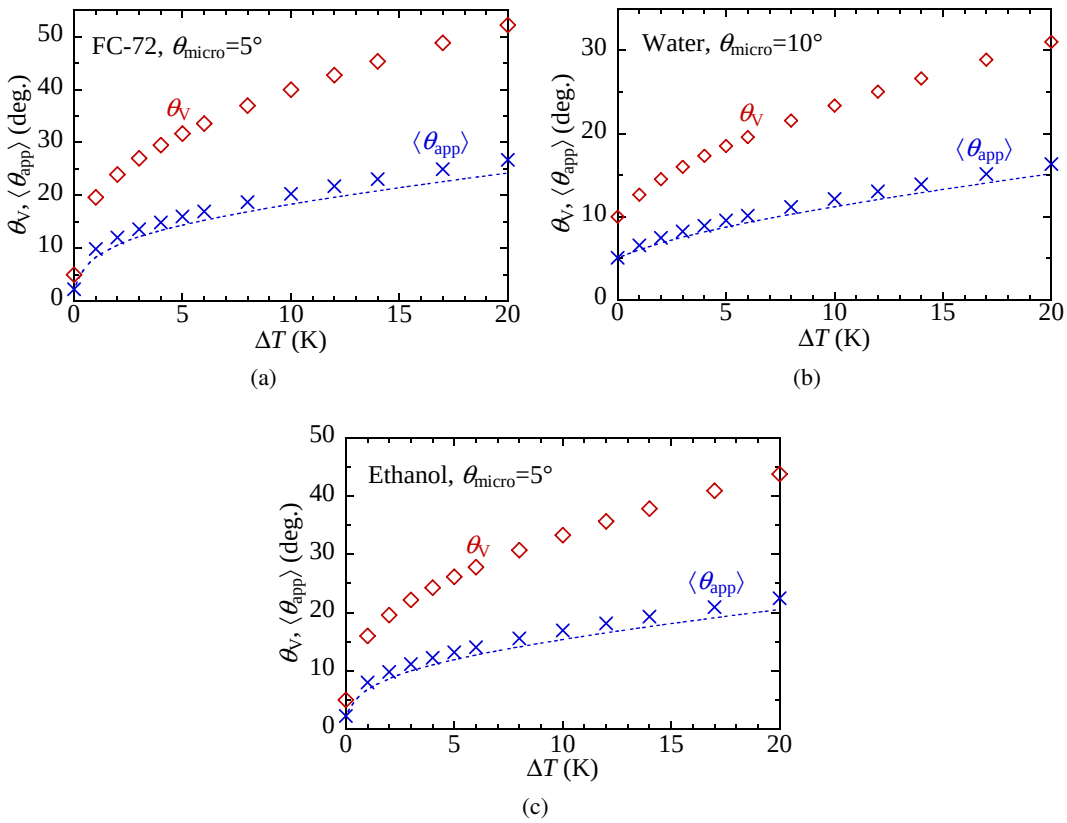

Figure 27: Values of θ_V (red diamonds) and $\langle\theta_{app}\rangle$ (blue crosses) as functions of ΔT for different fluids. The numerical data are shown with markers while the blue dotted line corresponds to the multiscale theory result for $\langle\theta_{app}\rangle$.

Figure 25c shows the spatial variation of the interface slope at the time moment $t = 0.33t_d$. Note the extent of the solution over multiple decades, which was possible to compute thanks to the mesh refinement near the contact line. Similarly to the adiabatic case, three regions can be identified clearly. First, we perform the numerical matching of the microscopic and intermediate regions.

As discussed in Subsec. 1.1.2.2, neglecting both the transient and the u_{cl}-containing terms in Eq. 3.18 results in the equation that governs the microregion (Janeček et al., 2014),

$$\frac{\partial}{\partial s}\left\{\frac{1}{\mu G(\phi)}\left[\frac{\zeta}{2}(\zeta+2l_s)\frac{\partial\sigma}{\partial s}+\frac{\zeta^2}{3}(\zeta+3l_s)\frac{\partial\Delta p}{\partial s}\right]\right\}=-\frac{J}{\rho}. \tag{3.29}$$

This corresponds to the problem of an evaporating immobile liquid wedge sketched in Fig. 3a. In the spirit of the theory of asymptotic matching, the boundary condition $K = 0$ is applied at the right-hand end of the integration interval (which corresponds to the constant slope at infinity) instead of Eq. 3.21. Other three boundary conditions (Eq. 3.22a, Eq. 3.22b and Eq. 3.28) are defined at the CL and thus remain valid.

The slope variation corresponding to the microregion solution is shown in Fig. 25c (green dash-dotted line). It exhibits the ϕ saturation at large x to the value $\theta_V \simeq 31.65°$. The abscissa axis is extended to non-physically small values to show the $x \to 0$ convergence to θ_{micro}.

The treatment of the intermediate and macroscopic regions is similar to the adiabatic case considered in Sec. 3.2. The fit (blue dashed line in Fig. 25c) to the Cox-Voinov law Eq. 1.28 with $\theta = \theta_{\mathrm{V}}$ results in $\ell_{\mathrm{V}} \simeq 20\,\mathrm{nm}$ for this particular case. The fit to a circle in the macroregion (violet dotted line in Fig. 25c) gives $\theta_{\mathrm{app}} \simeq 15.7°$.

Repeating the fitting for different ΔT ranging from 0 to 20K and for three selected fluids, one obtains Fig. 27, which demonstrates θ_{V} and $\langle\theta_{\mathrm{app}}\rangle$ (blue crosses) as functions of ΔT for different fluids. As θ_{app} increases slowly with time as the ridge grows, an average value $\langle\theta_{\mathrm{app}}\rangle$ is taken over the course $(0.1t_{\mathrm{d}}, 0.6t_{\mathrm{d}})$. Here, θ_{V} increases monotonously with ΔT as discussed in numerous works on the microregion (see Nikolayev (2022) for a review); $\theta_{\mathrm{V}}(\Delta T = 0) = \theta_{\mathrm{micro}}$.

The Voinov length ℓ_{V} obtained from the Cox-Voinov fit depends on time but its variation is extremely weak, of the order of the fitting error (less than 2%). We plot ℓ_{V} as a function of ΔT in Fig. 28 for different fluids. As expected for the microregion scale, ℓ_{V} is of the order of 10–100 nm. It shrinks monotonously with ΔT.

One can now use the multiscale theoretical prediction Eq. 1.29 to compare with the numerical data. The averaged values of all parameters obtained from the numerical calculation (such as $\langle w\rangle$ and $\langle Ca\rangle$) can be used on the right-hand side of Eq. 1.29. The resulting $\langle\theta_{\mathrm{app}}\rangle$ is plotted as a function of ΔT as blue dotted lines for different fluids in Fig. 27. A good agreement with the numerical data for all the fluids indicates the success of the multiscale theory.

More importantly, it is possible to compare the numerics to the asymptotic theoretical result Eq. 1.31 for $\langle Ca\rangle$. The averaged values of all the parameters $\langle w\rangle$, $\langle h\rangle$, θ_{V}, and ℓ_{V} obtained from the numerical calculation can be used in the right-hand side of Eq. 1.31. In Fig. 26, the lines show the theoretical results while the markers correspond to the numerical data. Again, the agreement is excellent. One concludes that the multiscale theory is valid for the evaporation case.

3.3.2 *Voinov length approximation*

Two key parameters engendering from the microregion enter Eq. 1.31: θ_{V} and ℓ_{V}. While the first parameter θ_{V} of the multiscale theory is relatively easy to obtain as it requires solving only the microregion problem, the second parameter ℓ_{V} is a more delicate issue. To avoid the laborious numerical calculation of ℓ_{V} for a particular fluid and ΔT, a simpler approach is desirable.

However, because other nanoscale effects have been accounted for in the calculation, Fig. 28 shows that, at least for conventional fluids, this value ℓ_{VK} calculated by Eq. 1.32 remains much smaller than the numerical result and is thus hardly suitable in practice. The slip-controlled value ℓ_{Vsa} calculated by Eq. 1.30 that was used by Fourgeaud et al. (2016) for ℓ_{V} is known only for $\Delta T = 0$. Its value can be somewhat larger than the numerical ℓ_{V} for $\Delta T \neq 0$ (Fig. 28). Therefore, a better general expression is needed.

To determine the value of ℓ_{V}, the relative importance of the nanoscale effects should be examined first. As discussed in Subsec. 1.1.2.2, two main effects that can relax the hydrodynamic singularity of contact lines, are the Kelvin effect and the hydrodynamic slip. For this reason, they should broadly define ℓ_{V}. The other effects considered in our calculation are generally secondary for ℓ_{V}, but impact θ_{V} more or less strongly. The corresponding characteristic length scales can evaluate the contribution of an effect to the overall system dynamics. A length scale is defined as the distance from the contact line along the x axis at which the effect is still significant. An effect overcomes another if its characteristic length is larger. The definitions of these scales presented in Tab. 5 are discussed in Sec. A.4.

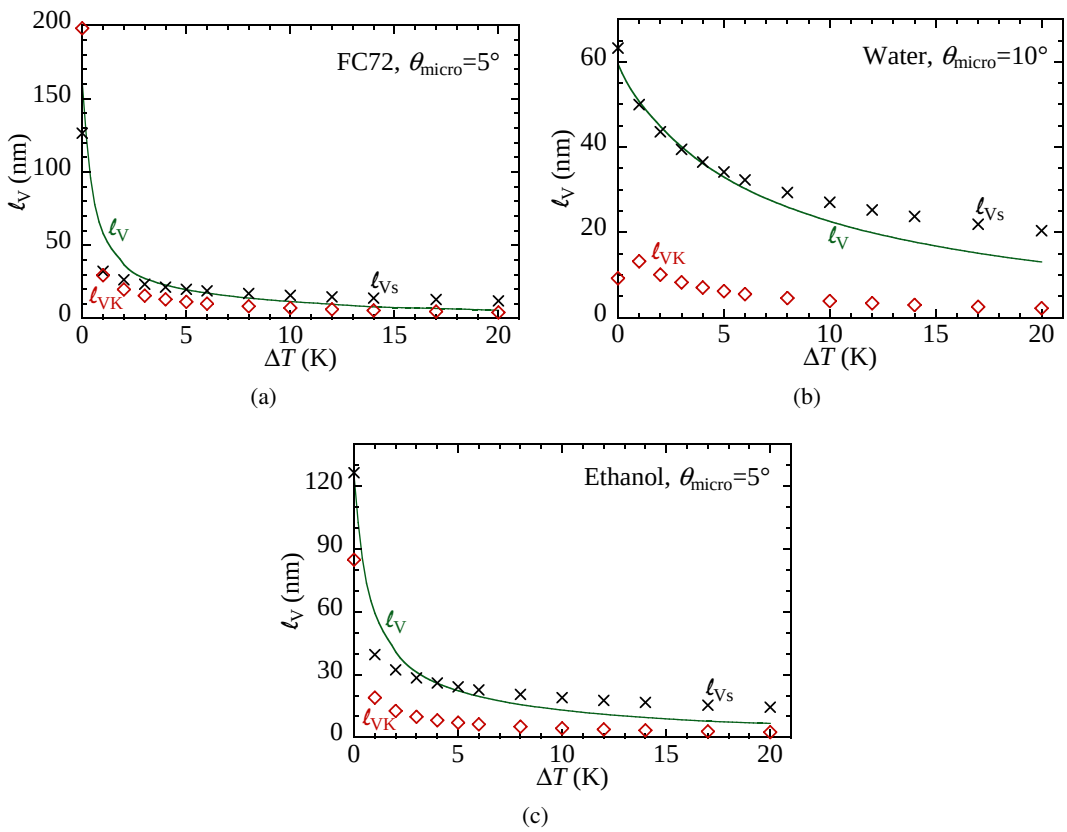

Figure 28: Numerically obtained variation of ℓ_V with ΔT (lines) for different fluids. The variations of ℓ_{VK} (diamonds) and ℓ_{Vs} (crosses) are also shown. The value of ℓ_s corresponds to $\ell_{Vs}(\Delta T = 0)$.

For estimation purposes, one assumes that the liquid forms a straight wedge with the opening angle θ. The above analysis shows, however, that the interface slope grows from θ_{micro} to θ_V in the microregion. Therefore, one can only define the bounds for the characteristic lengths by using these two values for θ.

For all the fluids, the Kelvin length ℓ_K is smaller than the slip characteristic length scale ℓ_s, which means that the slip controls ℓ_V. As the value of ℓ_R is comparable to ℓ_s, the interfacial thermal resistance strongly impacts the Voinov angle. This is valid for all fluids. The vapor recoil is generally weak, which is not surprising, accounting for the low $\Delta T = 5\,\mathrm{K}$ considered in Tab. 5. As its corresponding scale is $\ell_r \sim \Delta T^2$, it exercises a much stronger influence at a higher ΔT. However, this effect is less critical for water than for the other two fluids.

One can see that ℓ_{MR} computed with θ_{micro} can be very large. These large values are, however, only the upper bounds. The impact of the Marangoni effect is extremely strong in close vicinity of the contact line, but drops very quickly as the slope in the microregion increases towards θ_V at the border of the microregion. The analysis shows that, generally, all of the above nanoscale effects impact contact line dynamics, and all of them should be addressed.

On the basis of the scaling discussed above, the slip should have a major impact on ℓ_V. Therefore, we propose to use for ℓ_V the expression

$$\ell_{Vs} = \frac{3l_s}{e\theta_V}. \tag{3.30}$$

	values (nm) for $\Delta T = 5\,\mathrm{K}$					
	FC72		Ethanol		Water	
	$\theta_{\text{micro}} = 5°$		$\theta_{\text{micro}} = 5°$		$\theta_{\text{micro}} = 10°$	
	$\theta_{\text{V}} = 31.6°$		$\theta_{\text{V}} = 26.1°$		$\theta_{\text{V}} = 18.5°$	
effect and length, $\theta =$	θ_{micro}	θ_{V}	θ_{micro}	θ_{V}	θ_{micro}	θ_{V}
Kelvin $\ell_{\text{K}} = \dfrac{\sqrt{3\mu k T_{\text{sat}}}}{\rho \mathcal{L} \theta^2}$	150.7	3.78	64.6	2.36	7.02	2.05
hydrodynamic slip $\ell_{\text{s}} = \dfrac{3 l_{\text{s}}}{\theta}$	344	65.7	344	65.7	172	92.9
interfacial resistance $\ell_{\text{R}} = \dfrac{R^{\text{i}} k}{\theta}$	434	69.6	542	102	248	134
Marangoni $\ell_{\text{MR}} = \dfrac{3\gamma \Delta T R^{\text{i}} k}{2\theta^3 \sigma}$	3138	12.4	3372	23.7	199.5	31.5
vapor recoil $\ell_{\text{r}} = \dfrac{\Delta T^2 k^2}{\theta^3 \mathcal{L}^2 \sigma} \left(\dfrac{\rho - \rho_{\text{v}}}{\rho_{\text{v}} \rho} \right)$	234	0.93	152	1.07	12.1	1.91

Table 5: Characteristic length scales of different nanoscale effects.

Figure 28 shows that the quality of this approximation is satisfactory, especially accounting for the fact that ℓ_{V} always appears under the logarithm in Eq. 1.29 and Eq. 1.31.

3.3.3 *Comparison with experiment*

The only experiment on the dewetting at evaporation, which comprises the data on both θ_{app} and Ca, and with which we can thus compare our modeling, was conducted by Fourgeaud et al. (2016). They observed the dewetting of an ethanol film on a heated sapphire substrate in an airtight chamber filled with saturated ethanol vapor. Initially, an ethanol film of thickness $\sim 60\,\mu\mathrm{m}$ was deposited on the solid surface, whose temperature was above the saturation temperature of the vapor. Both substrate dewetting and liquid film thinning were observed. The time evolution of the interface profile (including the contact line position, w and h_∞) and the vapor pressure were recorded. Hence the receding speed could be derived. Here, T_{sat} was found with the vapor pressure. The value of θ_{app} was obtained by fitting the liquid ridge profile to a circle, whose intersection with the solid surface gave θ_{app}, similarly to our numerical procedure.

The substrate temperature T_{w} could not be measured, but it was clear that it remained nearly constant because of the large thermal inertia of the substrate. The superheating $\Delta T = T_{\text{w}} - T_{\text{sat}}$ varied because of strong T_{sat} variation. According to the assumption of Fourgeaud et al. (2016), $T_{\text{w}} = 48°\mathrm{C}$. In the present work, we propose another approach. Instead of assuming a T_{w} value, we calculate ΔT for each data point from the experimental Ca by using the numerical $Ca(\Delta T)$ curve for ethanol (Fig. 26c). The calculation is done for $\theta_{\text{micro}} = 5°$, which is the value found originally by Fourgeaud et al. (2016).

Figure 29a plots the experimental data for $Ca(t)$ (green squares) and the numerical curve $Ca(\Delta T)$ (solid blue line, the same as in Fig. 26c). By placing the experimental Ca value to the numerical curve, one recovers ΔT for each experimental point. For instance, for the first data point at $t = 0.375\,\mathrm{s}$, given $Ca \simeq 1.57 \times 10^{-3}$, one recovers $\Delta T \simeq 8.9\,\mathrm{K}$.

In the next step, ℓ_{V} can be interpolated from the numerical curve $\ell_{\text{V}}(\Delta T)$ (Fig. 28c). Finally, one can calculate θ_{V} with Eq. 1.29 by using the experimental data for θ_{app} and w and

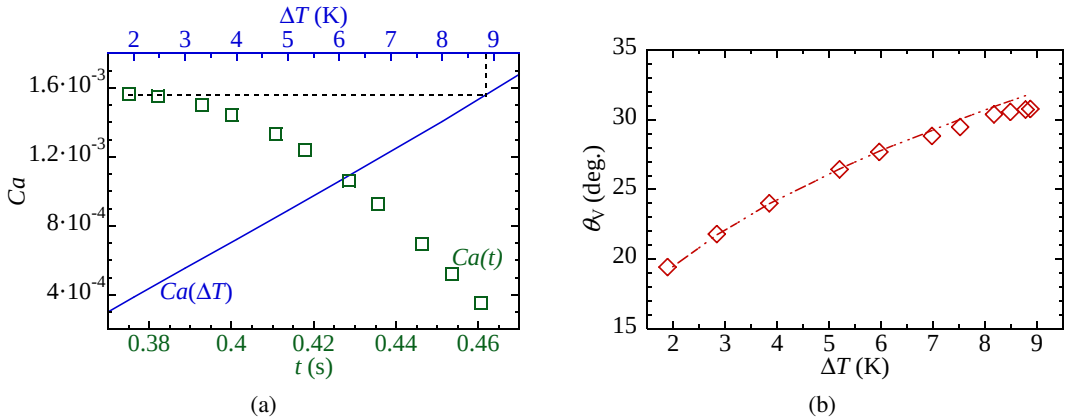

Figure 29: (a) Experimental data of Fourgeaud et al. (2016) for $Ca(t)$ (green squares plotted with respect to the lower abscissa axis) and numerical curve $Ca(\Delta T)$ (blue line plotted with respect to the upper abscissa axis); (b) comparison of $\theta_{\mathrm{V}}(\Delta T)$ functions obtained with the experimental data (Fourgeaud et al., 2016) (red diamonds) and the numerical calculation (line).

the ℓ_{V} found before. We note that the latter only has a small impact on the result as it enters under the logarithm. The points $(\Delta T, \theta_{\mathrm{V}})$ obtained in this way are plotted in Fig. 29b as red diamonds. As demonstrated in Fig. 27, θ_{V} can also be obtained numerically as a function of ΔT. The corresponding dependence is plotted as the red curve in Fig. 29b, the same as the diamonds in Fig. 27c. The numerical line agrees with the experimental estimations, showing our numerical approach's validity.

3.4 Time-averaged approach

Subsec. 3.3.1 has evidenced that the asymptotic multiscale approach developed for conventional adiabatic dewetting cases $\Delta T = 0$ (Snoeijer et al., 2010), can be generalized for evaporation cases $\Delta T > 0$. However, this asymptotic prediction of $\langle Ca \rangle$ (markers in Fig. 26) uses the averaged values of w, h_∞ and ℓ_{V} that result from full numerical calculations. In this subsection, we devise a simple approach that takes time average value over the dewetting process. This approach saves the troubles of numerically solving the governing equations and is universal for various fluids.

First, we replace the quantities in Eq. 1.29 and Eq. 1.31 with time-averaged values for the time interval of $[0.1t_{\mathrm{d}}, 0.6t_{\mathrm{d}}]$, the same interval in Fig. 26.

$$\langle \theta_{\mathrm{app}} \rangle^3 = \theta_V^3 - 9\langle Ca \rangle \ln \frac{2\langle w \rangle}{e\ell_{\mathrm{V}}}, \tag{3.31}$$

$$\langle Ca \rangle = \frac{\theta_V^3}{9} \left[\ln \left(\frac{4a}{e^2} \langle Ca \rangle^{1/3} \frac{\langle w \rangle^2}{\ell_{\mathrm{V}} \langle h_\infty \rangle} \right) \right]^{-1}, \tag{3.32}$$

where ℓ_{V} is calculated by Eq. 3.30 and its time variation is neglected. The value of $\langle h_\infty \rangle$ is computed using Eq. 3.21

$$\langle h_\infty \rangle = \frac{1}{t_2 - t_1} \int_{t_1}^{t_2} h_0 \sqrt{1 - \frac{t}{t_{\mathrm{d}}}} \mathrm{d}t = \beta h_0, \tag{3.33}$$

where t_1 and t_2 are the integral limits; for $t_1 = 0.1t_{\mathrm{d}}$ and $t_2 = 0.6t_{\mathrm{d}}$, $\beta \simeq 0.8$.

Now to calculate $\langle w \rangle$, we follow the simplified theory in the spirit of Brochard-Wyart et al. (1991).

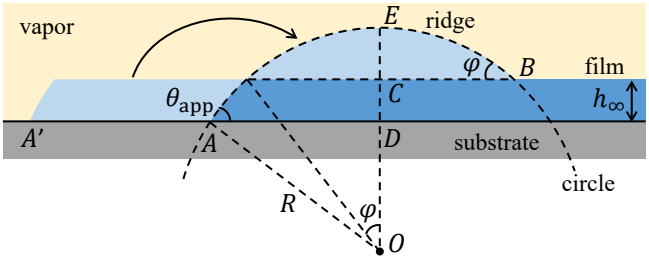

Figure 30: A dewetting ridge is accumulating liquid from the film that previously covers the dry area.

As the contact line recedes, the liquid previously covering the solid surface accumulates in the ridge, shown in Fig. 30. The cross-section of such a liquid ridge is approximately an arc of a circle, with a radius of R, and the center is located at point O. The circle intersects the solid substrate at the point A with the apparent contact angle θ_{app}, and intersects the liquid film at the point B with the angle φ. The point E is the crest of the ridge. The radius R satisfies

$$R \sin \theta_{\text{app}} = w, \tag{3.34}$$

where $w = \overline{AD}$. The angles θ_{app} and φ satisfy the geometrical relation $\overline{OC} - \overline{OD} = \overline{CD}$, meaning that

$$R(\cos \varphi - \cos \theta_{\text{app}}) = h_\infty. \tag{3.35}$$

Substituting Eq. 3.34 into Eq. 3.35 yields,

$$\cos \varphi = \cos \theta_{\text{app}} + \frac{h_\infty}{w} \sin \theta_{\text{app}}. \tag{3.36}$$

The volume of liquid (per unit contact line length) collected during the contact line receding from the point A' (at time $t_1 < t$) to the point A is

$$S = \int_{t_1}^{t} h_\infty(t) u_{\text{cl}}(t) \mathrm{d}t, \tag{3.37}$$

which must be equal to the ridge area

$$S = R^2(\varphi - \sin \varphi \cos \varphi), \tag{3.38}$$

colored in light blue in Fig. 30. Considering the decrease in the contact line velocity is logarithmic, we adopt the approximation that $u_{\text{cl}}(t) \simeq \langle u_{\text{cl}} \rangle$. Eq. 3.37 reduces to $S = \langle u_{\text{cl}} \rangle \langle h_\infty \rangle \Delta t$.

Combining Eq. 3.34, Eq. 3.37 and Eq. 3.38 and averaging Eq. 3.38, results in

$$\beta \langle Ca \rangle \sin^2 \langle \theta_{\text{app}} \rangle \Delta \tilde{t} = N_{\text{d}} \tilde{w}^2 (\langle \varphi \rangle - \sin \langle \varphi \rangle \cos \langle \varphi \rangle). \tag{3.39}$$

where $\tilde{w} = \langle w \rangle / h_0$, and $\Delta \tilde{t} = \Delta t / t_{\text{d}}$. The dimensionless superheating reads

$$N_{\text{d}} = \frac{\mu h_0}{t_{\text{d}} \sigma} = \frac{2k \Delta T \mu}{\mathcal{L} \rho h_0 \sigma}.$$

Replacing the time-dependent quantities with time-averaged quantities in Eq. 3.36, produces

$$\cos \langle \varphi \rangle = \cos \langle \theta_{\text{app}} \rangle + \frac{\beta}{\tilde{w}} \sin \langle \theta_{\text{app}} \rangle. \tag{3.40}$$

The set of equations, Eq. 3.30, Eq. 3.31, Eq. 3.32, Eq. 3.39 and Eq. 3.40, is complete, provided that θ_{V} is known for a given fluid, and for a given set of θ_{micro} and ΔT. One only

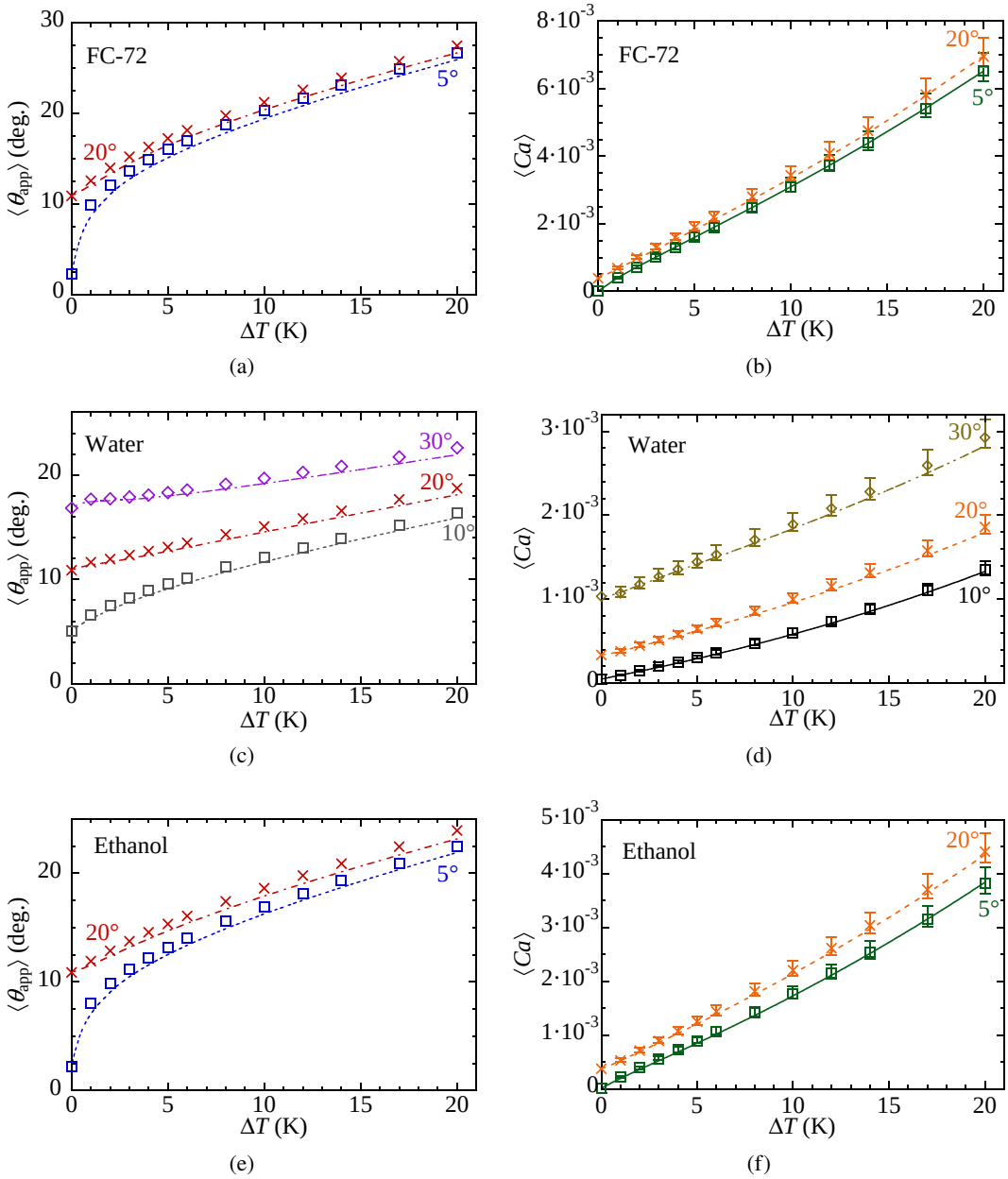

Figure 31: Comparisons of $\langle Ca \rangle$ and $\langle \theta_{\text{app}} \rangle$ between numerical results (markers) and time-averaged approach (lines); θ_{micro} indicated by the curves.

has to solve a set of nonlinear algebraic equations for four variables $\langle \varphi \rangle$, $\tilde{w}$, $\langle \theta_{\text{app}} \rangle$ and $\langle Ca \rangle$, the latter two being of the most interest. The solution depends on the external parameter l_{s} appearing in Eq. 3.30. However, the dependence is feeble, considering that l_{V} enters Eq. 3.31 and Eq. 3.32 under the logarithm.

The dependence of $\langle \theta_{\text{app}} \rangle$ and $\langle Ca \rangle$ on ΔT is plotted in Fig. 31 for FC-72, ethanol and water. A good agreement of the numerical solutions (Sec. 3.3) of the dewetting problem (markers) and time-averaged approach (lines) is achieved.

3.5 Conclusions

The dewetting dynamics in the presence of the liquid film evaporation is analyzed for the case where the liquid film is in contact with the pure vapor of the same fluid. To increase the

precision of numerical results at an interface slope higher than the conventional lubrication theory can handle, we develop the generalized lubrication theory (which uses, however, phenomenological arguments yet to be verified). Several nanoscale effects are included to produce realistic results: hydrodynamic slip, interfacial thermal resistance, Kelvin and Marangoni effects, and vapor recoil. The relative importance of all these effects is analyzed. Our scaling analysis shows that, in general, all of the above nanoscale effects should be addressed while evaluating the evaporation impact. The Kelvin effect, while being less critical in terms of its magnitude, is needed to provide the finiteness of liquid pressure at the contact line. Our theoretical description leads to the contact line receding phenomenon accompanied by spontaneous liquid evaporation in its close vicinity. The evaporation rate at the contact line conforms to its speed. In the presence of forced evaporation caused by substrate heating, the dewetting accelerates. The results show that the dewetting phenomenon is not only accelerated at evaporation; the dewetting can also be induced by evaporation. The dependence of the dewetting speed on the substrate superheating has been computed for three fluids (FC-72, ethanol, and water) for different wetting conditions. Unfortunately, it is difficult at this stage to introduce an analytical theory showing the importance of the boosting effect of evaporation because of the large number of effects that contribute to it.

The model has been validated against the asymptotic multiscale theory of dewetting developed by Snoeijer et al. (2010) for adiabatic conditions. The multiscale theory has been generalized to the evaporation case. It results in a simple analytical expression for the dewetting speed. The main parameters of this expression are the Voinov length and the Voinov angle (the interface slope formed in the microregion), through which the nanoscale effects impact the macroscale physics. While the Voinov angle is relatively easy to compute (it requires only a solution of a stationary microregion model mastered by many research groups), the Voinov length requires a more sophisticated calculation. An approximate analytical formula for the Voinov length is proposed. The results of the generalized multiscale model agree with the numerical calculations. It is shown that the evaporative mass loss at the contact line (hypothesized by Fourgeaud et al., 2016) does not lead to any additional acceleration of its motion controlled entirely by capillarity or by the evaporation-driven modification of the Voinov angle.

The numerical results have been compared to the experiment of Fourgeaud et al. (2016). For this, their experimental data were reanalyzed, and good agreement with our numerics was achieved.

Methods and results in this chapter are of importance for many applications. For instance, in the next chapter, the contact line dynamics will be used to elucidate dry patch expansion of growing bubbles in nucleate boiling. Particularly, in developing a computational model for PHPs, the edges of liquid films recede spontaneously and are accelerated by evaporation. Faithfully reflecting this phenomenon in the model is crucial, as it affects liquid film lengths and, consequently, the rate of overall heat exchange in the device. The simple approach based on the time-average multiscale theory provides a feasible solution to calculate the receding speed of contact lines in numerical models of PHPs.

Chapter 4

Microlayer in nucleate boiling

This chapter presents a case study to which the liquid dynamics theory in the previous two chapters might be applied. [1]

In nucleate boiling, beneath the growing vapor bubble, a thin layer of liquid can often be observed, whose thickness is of a few micrometers (Kim, 2009). Hence, it is called the microlayer. Microlayers stretch from liquid bulk to dry patch on a solid surface, the nucleation site's center, as shown in Fig. 32. Recent numerical (Urbano et al., 2018; Bureš et al., 2021) and experimental (Chen et al., 2017; Tecchio, 2022) evidence suggest that the interface of microlayer is not of a monotonic shape (a wedge), but features a liquid hump that encircles the dry patch. Because of the rapid evaporation over microlayers that contributes significantly to heat transfer (Sharp, 1964; Voutsinos et al., 1975), understanding the formation and evolution of microlayers is of great interest to the nucleate boiling mechanism.

Schweikert et al. (2019) and Bureš et al. (2021) have argued that the dewetting transition could explain the microlayer formation. The DNS simulations by Urbano et al. (2018) suggested that a microlayer is created when the radial velocity of bubble expansion surpasses a threshold value. The theoretical study of Bureš et al. (2021) has proposed a criterion of microlayer formation, which made the analogy with the dewetting phenomenon. This is similar to liquid film entrainment in tubes.

Considering the micrometric thickness that suggests a low Re, the hydrodynamics of liquid in microlayers is controlled by viscous and surface tension forces. Microlayers can be seen as liquid films deposited by the curved outer edge of the bubble interface near the solid substrate. When a bubble expands, its edge is pushed away from the dry nucleation site, which resembles the receding of a meniscus in capillary tubes (presented in Chap. 2). Furthermore, the "hump" formed next to the brim of an enlarging dry patch is similar to the dewetting ridge created by receding contact lines. The liquid in microlayers accumulates as the contact line expands outwards.

Given the similarities demonstrated in these two phenomena, this chapter aims to explain the formation and evolution of a microlayer using the liquid film dynamics presented in Chap. 2 and Chap. 3. The analysis is based on experiments that were elaborately designed

1 This chapter is based on the proceeding Tecchio et al., 2022.

and meticulously conducted by Dr. Cassiano Tecchio at CEA (Tecchio, 2022). Comparison with boiling experiments provides validation for our liquid film theory as well.

4.1 Problem formation

4.1.1 *Experiment setup*

Tecchio (2022) has observed over a hundred nucleation events, and a prodigious amount of data has been collected. Here, their experimental setup is briefly recapitulated.

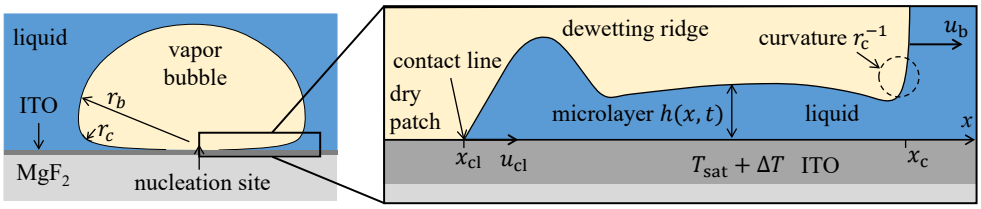

Figure 32: A growing vapor bubble during nucleate boiling and a microlayer beneath it.

A transparent solid substrate (made of MgF_2) is plated with a layer of indium-tin-oxide (ITO) as the boiling surface. It is placed horizontally at the bottom of a container filled with water at atmospheric pressure. MgF_2 is transparent to visible and infrared (IR) light spectrum, whereas ITO is transparent to visible light, albeit opaque to IR light. A beam of IR laser from below is focused on a localized defect fabricated on the ITO surface with great care. This defect is able to lower the nucleation barrier, lessening the laser power required to generate bubbles. A lower laser power also helps prevent surface burnout after nucleation and abates the evaporation rate, slowing down bubble growth and facilitating capturing of this process.

High-speed (4000 frames per second) and high-resolution optical diagnostics are employed to characterize the near-wall phenomena and bubble dynamics. The microlayer thickness $h(x)$, bubble base temperature T_w, and the macroscopic bubble radius r_b are measured simultaneously and synchronously by the white light interferometry (WLI) in the visible spectrum, IR thermography with the 3-5 μm camera and side-wise shadowgraphy, respectively. Time variations of these quantities have been obtained. Technical details of experimental measurements and data processing are out of the scope of this chapter. They can be found in Tecchio (2022).

4.1.2 *Physical model*

Consider an ideal case where nucleation occurs at the surface defect and the bubble growth is radially symmetric. The working fluid is water, whose properties are listed in Tab. 4. Fig. 32 depicts the vapor-liquid interface of the vertical cross-section passing through the bubble center. The generalized lubrication theory, Eq. 3.18, Eq. 3.19 and Eq. 3.20, are used to describe the 2D interface of microlayer $h(x,t)$. The calculation interval ranges from the contact line (the boundary of dry patched, $x = x_{cl}$), up to the outer brim of microlayers ($x = x_c$), which expands and deposits liquid, and it is regarded as the counterpart of menisci in capillary configuration.

At the contact line ($s = s_{cl}$), the boundary conditions of Eq. 3.22a, Eq. 3.22b and Eq. 3.28 used in Sec. 3.3, are employed:

$$h(s = s_{cl}) = 0, \quad \left.\frac{\partial h}{\partial s}\right|_{s=s_{cl}} = \sin\theta_{micro}, \quad \left.\frac{\partial \Delta p}{\partial s}\right|_{s\to s_{cl}} = 0, \tag{4.1 a,b,c}$$

where θ_{micro} is the microscopic contact angle at the ITO surface. The receding speed of contact line u_{cl} is calculated using Eq. 3.27, as a part of the solution.

At the right-hand end s_{c}, the average curvature in this region of the interface (encircled in Fig. 32) is r_{c}^{-1}:

$$\left.\frac{\partial \phi}{\partial s}\right|_{s=s_{\text{c}}} = r_{\text{c}}^{-1}. \tag{4.2}$$

However, the curvature r_{c}^{-1} remains undetermined. Notice that in this region, the nearly-flat microlayer transforms to the hemispherical bubble dome of the curvature r_b^{-1}. We impose r_{c}^{-1} by introducing the ratio $\beta = r_{\text{c}}/r_{\text{b}}$ that is expected to be smaller than unity, and its value will be estimated later using experimental data. This transition region is expected to expand together with the bubble, meaning $x_{\text{c}}(t) = r_{\text{b}}(t)$. The latter has been measured experimentally in Fig. 33a.

4.2 Results and discussion

4.2.1 *Experimental observation*

The bubble radius r_{b} and dry patch boundary x_{cl} measured in the experiment are plotted in Fig. 33a as functions of time. At $t = 0$, nucleation occurs. The values of r_{b} and x_{cl} are read from the surface defect, which is assumed to be the nucleation site and the center of the bubble and of the dry patch. The profiles of interface $h(x)$ at selected moments obtained by WLI are plotted in Fig. 33b. The thickness of the microlayer can be recovered from WLI images in the region, where the interface slope is small (below $\sim 0.1°$), which is the middle part of microlayer: $1.52\,\text{mm} \leq x \leq 1.68\,\text{mm}$.

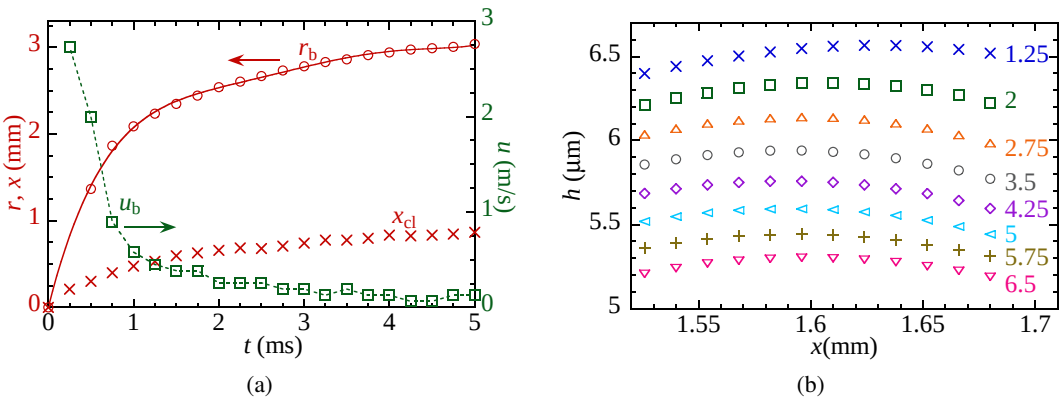

Figure 33: Experimental measurements of Tecchio (2022), (a) time evolution of r_{b} and x_{cl} in markers and the fitting curves, (b) interface profiles of microlayer obtained by WLI at selected time moments in ms.

The bubble experiences rapid inflation during $0 < t \leq 1.25$ ms. The expansion slows down afterward. A similar tendency can be seen in $x_{\text{cl}}(t)$, whereas the dry patch expands much slower. A microlayer forms during this time. Fig. 33b indicates that the middle part of the microlayer is nearly flat, $x-$axis in millimeter and $y-$axis in micrometer. A small bump forms at $x \simeq 1.6$ mm. Due to liquid evaporation, $h(x,t)$ decreases, and the shape of the interface barely changes, which signifies the absence of liquid flow in the radial direction. This behavior resembles the liquid film in capillary tubes. Once deposited on the tube wall, the shape remains essentially the same. One clarifies that this bump is not the dewetting ridge that situates at the left-hand end of microlayers, which is $x_{\text{cl}}(t = 1.25\,\text{ms}) \simeq 0.4\,\text{mm}$.

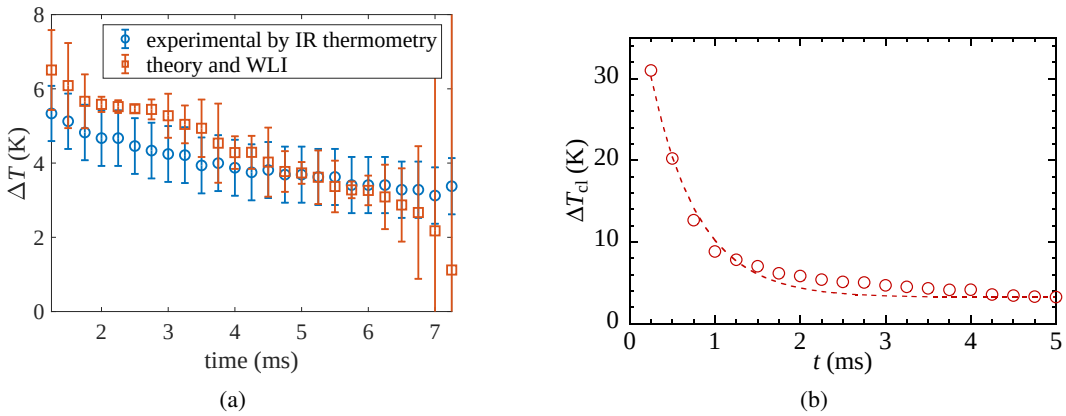

Figure 34: Experimental measurements of superheating condition of ITO surface ΔT, (a) at $x = 1.6$ mm, measured by IR thermometry (orange) and theoretical estimation using WLI measurement (blue). (b) at contact line ΔT_{cl}.

Besides, the dewetting ridge is highly curved, whose interface profile cannot be read by WLI.

The temporal variation of microlayer thickness $h(t)$ can also be used in estimating the local superheating condition ΔT, as expressed in Eq. 3.21. Fig. 34a plots $\Delta T(t)$ at $x = 1.6$ mm obtained by IR thermography (in orange) and calculated by Eq. 3.21 using $h(t)$ data measured by WLI in Fig. 33b. A good agreement between the two data sets indicates that the microlayer thinning result from liquid evaporation. The interfacial relaxation that originates from radial flows in microlayers can be negligible.

With $\Delta T(t)$ and the interface profile $h(x)$ measured by WLI at $t = 1.25$ ms in Fig. 33b, the initial profile $h_0(x)$, after compensating the liquid loss to vapor, can be recovered roughly using:

$$h_0(x) = \sqrt{h(x)^2 + \frac{2k\Delta T}{\mathcal{L}\rho}t}, \tag{4.3}$$

which is obtained by rearranging Eq. 3.21. Assuming an average $\Delta T = 8\,\mathrm{K}$ before $t = 1.25$ ms, the estimated $h_0(x)$ is plotted in Fig. 35.

The temporal evolution of superheating condition at contact line ΔT_{cl} is plotted in Fig. 34b. ΔT_{cl} drops exponentially at the incipient stage of bubble growth because the contact line recedes away from the nucleation site, which is the laser spot center.

4.2.2 *Numerical results*

4.2.2.1 *Quasi-steady estimation*

We first make a simple quasi-steady estimation of the initial thickness $h_0(x)$. Hypothetically, the microlayer is deposited by the outer brim of the bubble interface. Using the quasi-steady approach for liquid film deposition in Subsec. 2.3.6.4, the initial thickness predicted theoretically $h_{0,\mathrm{q}}$ is expressed as

$$h_{0,\mathrm{q}} = 1.34\beta r_{\mathrm{b}} Ca_{\mathrm{c}}(x)^{2/3}, \tag{4.4}$$

where $Ca_{\mathrm{c}} = \mu u_{\mathrm{c}}/\sigma$; u_{c} the receding speed of the outer brim that deposits liquid. It is assumed that u_{c} is equal to the speed of bubble expansion u_{b}, which is obtained by taking the time derivative of $r_{\mathrm{b}}(t)$ that has been experimentally recorded in Fig. 33a. Here, the equivalent radius r_{c} is related to the bubble radius by βr_{b}. The value of β remains unknown,

but it is assumed independent of time. Eq. 4.4 implies that the initial thickness of microlayers is a function of the speed and curvature of the outer brim when it passes by the solid surface.

We may estimate β by plotting $h_{0,\mathrm{q}}(x)$ calculated by Eq. 4.4 and tuning the value of β that the crest of $h_{0,\mathrm{q}}(x)$ has the same maximal value of h_0 profile that was recovered from experimental data in Fig. 33b. $\beta \simeq 0.088$ has been found as a reasonable estimation, as plotted in Fig. 35. As expected, $\beta = 1$ would overrate the initial thickness by order of magnitude. In Fig. 35, both curves obtain the maximum at $x \simeq 1.58$ mm, which is close to the experimental value of $1.6\,\mathrm{mm}$. Tuning β does not alter the shape of $h_0(x)$ predicted by Eq. 4.4 or the position where $h_0(x)$ reaches the maximum. The good agreement implies that the theory of liquid deposition by receding menisci could explain microlayer formation.

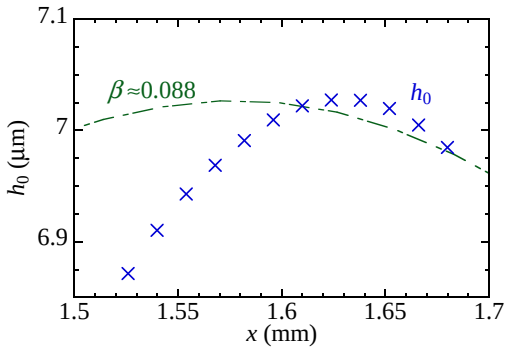

Figure 35: Initial profiles of microlayer predicted by the quasi-steady theory of liquid film deposition with $\beta = 0.088$ (the green curve). The values of h_0 recovered using experimental data are plotted in the blue markers.

4.2.2.2 *Dynamic simulation*

The dynamic simulation used this estimated value of β in the boundary condition, Eq. 4.2. The calculation interval is from $x_{\mathrm{cl}}(t)$ to $x_{\mathrm{c}}(t) = x_{\mathrm{b}}(t)$. The latter is imposed by the experimental data in Fig. 33a. Considering ITO surface is highly smooth in the nanoscale, a tentative value of $10°$ is adopted for θ_{micro}, which is close to the experimental value of about $5°$ (Tecchio, 2022).

A homogeneous profile of superheating over the boiling surface (ITO) $\Delta T(t)$ is assumed, which is imposed by the fitting curve of time variation of $\Delta T_{\mathrm{cl}}(t)$ in Fig. 34b. The value of $\Delta T(t)$ is set to be constant at $31\,\mathrm{K}$ between $0 \leq t \leq 0.25$ ms. Afterwards, it declines exponentially to $3.3\,\mathrm{K}$ at $t = 5$ ms, see Fig. 34b.

The numerical results of a microlayer profile at selected moments are shown in Fig. 36. The microlayer is deposited on a solid surface by the interface of an inflating bubble. The contact line receding (dry patch expansion) leads to the formation of a growing ridge (dewetting ridge), in which liquid previously covering the solid surface accumulates. The liquid ridge that encloses a dry patch has been reported in numerical simulations of nucleate boiling by Bureš et al. (2021) and Urbano et al. (2018) as well. Unfortunately, due to the steep interface of liquid ridges (slope over $10°$), its thickness cannot be obtained by the interferometry methods that are applicable to interfacial slopes not exceeding $\sim 0.1°$.

The middle part of the microlayer is enlarged and shown in Fig. 36 (bottom). The interfacial slope in this region is much smaller than the slope of the dewetting ridge. A small bump that situates at $x \simeq 1.59\,\mathrm{mm}$ has been found, which agrees with experimental observation in Fig. 33b and with the prediction of the quasi-steady in Fig. 35. Because of liquid evaporation, the microlayer thins with time, which is also in good agreement with Fig. 33b.

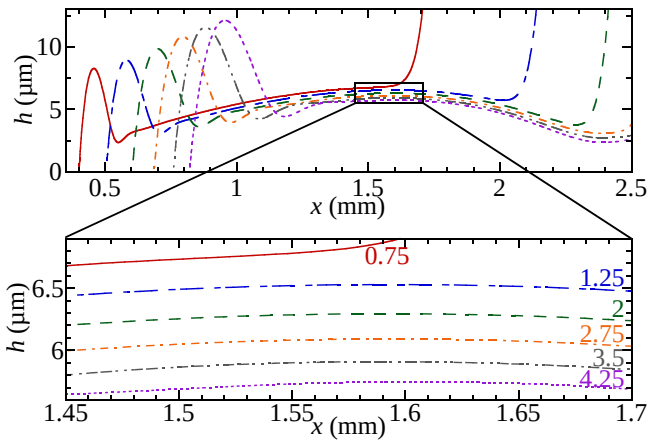

Figure 36: Numerical results showing the temporal evolution of microlayer profile; the corresponding time is labeled in ms; the middle part of microlayer is enlarged in the lower figure.

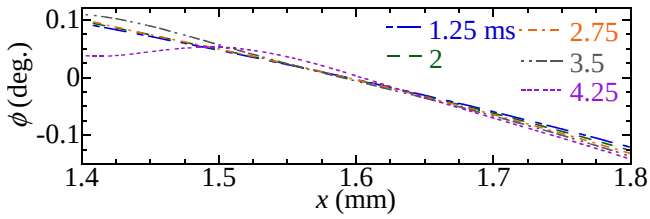

Figure 37: Numerical results of interface slope ϕ in the middle part of microlayer; the corresponding time is labeled in ms.

Numerical results of interface slope ϕ in the middle part of the microlayer are plotted in Fig. 37. The interface slope gradually decreases below the horizontal line $\phi = 0$ at around $x = 1.59$ mm, which indicates a local maximal value of $h(x)$ is attained. Moreover, ϕ is in the range of $[-0.1, 0.1]$ for x in the domain of $[1.45, 1.7]$ approximately. This agrees with the experimental setup that post-process of WLI images could only recover the interface thickness if $|\phi| \lesssim 0.1°$, as shown in Fig. 33b.

4.2.2.3 *Contact line dynamics*

Taking the time derivative of $x_{\text{cl}}(t)$ that is experimental observed in Fig. 33a, we obtain the receding speed of contact line $u_{\text{cl}}(t)$, which is plotted in Fig. 38, and is accompanied by the numerical results.

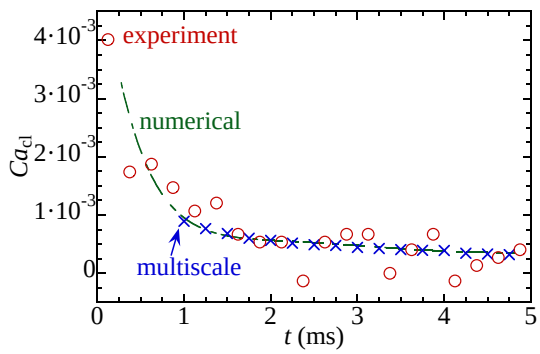

Figure 38: Receding speed (in Ca) of the contact line of microlayer as a function of time (ms): experimental data (red circles), numerical results (greed curve), and multiscale prediction of Eq. 1.31 (blue crosses).

In the beginning, the value of $Ca_{\mathrm{cl}} = u_{\mathrm{cl}}\mu/\sigma$ drops sharply, following the same tendency in $\Delta T_{\mathrm{cl}}(t)$ (Fig. 34b). After about $t = 1$ ms, a liquid film and dewetting ridge have formed, and ΔT_{cl} has also stabilized. Hence, the multiscale expression, Eq. 1.31, can be used to predict the contact-line receding speed and to compare with experimental data, shown in Fig. 38. The values of θ_{V} and ℓ_{V} used in Eq. 1.31 are obtained from Fig. 27 and Fig. 28b for $\theta_{\mathrm{micro}} = 10°$, respectively; h_∞ takes the maximal value of $h(x)$ in the middle part of microlayer from experimental data in Fig. 33b. Due to the changing-in-time ΔT_{cl}, the values of θ_{V}, ℓ_{V} and h_∞ are also functions of time.

The good agreement in Ca_{cl} indicates that the expansion of dry patches conform to the dynamics of dewetting films at evaporation. The receding of the contact line slows down because of the decrease in ΔT_{cl}, which agrees with our conclusion in Chap. 3: larger superheating accelerates the dewetting process.

Since a precise measurement of θ_{micro} is unavailable, the good agreement in Ca_{cl} also indicates that $10°$ could be a tentative value of θ_{micro}.

4.3 Conclusions

Based on experimental data of the growth of a single bubble in nucleation boiling, this chapter makes an attempt to elucidate the microlayer dynamics using the theory of liquid films presented in Chap. 2 and Chap. 3.

Microlayer creation is attributed to the expansion of bubbles, more precisely, the curved interface of outer edges near the solid surface, as in the case of liquid deposition by a receding meniscus. During this process, the curvature and speed of the curved interface vary with time, which results in a non-monotonic initial thickness of the microlayer in agreement with experimental observations. Quantitative prediction of the initial thickness remains unrealized because the curvature of the part of the interface that is believed to deposit microlayers is still being determined. In the current calculations, the equivalent radius of this curvature was assumed proportional to the bubble radius and was chosen by matching the maximal thickness of the microlayer obtained numerically with the value measured experimentally. Due to liquid evaporation, the microlayer thins, whereas its interfacial shape barely deviates from its initial profile, which signifies the absence of radial liquid flows. On the nucleation site, the dry patch enlarges with time and is encircled by a liquid ridge. This phenomenon is similar to the dewetting of a liquid film, in which the receding speed of contact lines can be predicted theoretically. Given the local superheating condition (experimental data) and microscopic contact angle (tentative estimation), the 2D generalized lubrication theory (introduced in Chap. 3) can calculate the receding speed numerically. This result is compared with experimental data. After the rapid inflation of bubbles, the microlayer enters a relatively more stable stage, during which the contact-line receding speed can also be predicted by Eq. 1.31. A good quantitative agreement has been achieved.

In general, the microlayer dynamics is controlled by viscous and surface tension forces; therefore, its behavior can be primarily explained by the theory of thin liquid films. The comparison with microlayer experiments concludes this thesis's theoretical studies of liquid films. In the next part, we shall move on to the application of our theoretical studies on computational model development of PHPs.

Part II

Oscillating Film Thickness (OFT) model

Chapter 5

New liquid film model

Theoretical studies of the liquid film dynamics in capillary tubes presented in Chap. 2 and Chap. 3 provide a solid base, on which a new computational model for liquid films in PHPs can be developed. This chapter presents technical details of the model development [1].

As a practical consideration, the new numerical model adopts one-dimensional lumped geometry, where curved interfaces are simplified, cf. Fig. 39. Compared to the previous numerical models discussed in Sec. 1.2, the salient improvement in liquid film description will be made to better reflect the essential behavior (variations in length and thickness).

Initially, a receding plug deposits a liquid film, whose thickness is mainly a function of the plug receding speed, as discussed in Chap. 2. Even though the interface of a liquid film deposited by an oscillating plug is not perfectly flat, the spatial variation in the initial thickness of the order of $\sim 100\,\mu\mathrm{m}$ is less drastic compared to the film length that is usually of the order of several centimeters. Therefore, liquid films are modeled of uniform thickness: the mass of a liquid film is spread uniformly over its length. Nevertheless, the mass and length evolve and oscillate individually with time. Accordingly, the new model is called the **Oscillating Film Thickness** (OFT) model.

We recall that the positions of two boundaries determine the liquid film length; they can be menisci and free contact lines (not traveling with menisci). The pressure imbalance among vapor bubbles initiates and powers meniscus oscillation. Free contact lines recede spontaneously after liquid film deposition. It is a local phenomenon that is controlled by the local parameters, such as the wetting properties, which can be represented by the microscopic contact angle θ_{micro} at the liquid-solid boundary, and local superheating ΔT_{cl}. Chap. 3 made an analogy between the contact line receding phenomenon in capillary tubes to the dewetting of liquid films. In the absence of net mass exchange (under adiabatic conditions), the receding speed is determined by the wetting properties, the static contact angle θ_{micro}. Liquid evaporation accelerates the receding speed. Chap. 3 established a correlation between the dewetting speed and the combination of ΔT_{cl} and θ_{micro}, which will be used to describe the contact line motion in OFT model.

The main assumptions that are made in OFT model are summarized as follows:

1 This chapter is based on the proceeding (Zhang et al., 2022c) and a manuscript submitted to Physical Review Fluids.

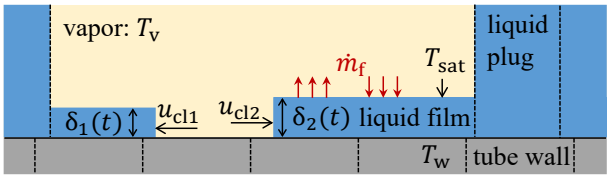

Figure 39: Schematics of Oscillating Film Thickness model.

1. One-dimensional plug/slug flow in round capillary tubes;
2. Physical quantities in a calculation volume are spatially uniform: a bubble or a liquid film is a calculation volume. In contrast, liquid plugs and solid tube are meshed into multiple volumes;
3. Film thickness varies individually with time as a result of the mass and length variations;
4. Vapor phase obeys the ideal gas law, indicating that vapor phase is superheated;
5. Temperature of the free interface in a vapor bubble is equal to the saturation temperature corresponding to the vapor pressure. Since the vapor temperature is higher than the saturation temperature, thin thermal boundary layers exist between vapor bulk and interfaces;
6. Free contact lines recede, conforming to the physics of the dewetting phenomenon.

It is necessary to apply the model first on the simplest PHP configuration, the single branch PHP (see Fig. 40), because comparison with experimental data can be performed in detail, such as the positions of contact line and meniscus, and pressure and temperature of the vapor phase. In addition, this simple configuration only has one meniscus that oscillates between a vapor bubble and a liquid plug, which saves the trouble of considering the coalescence of bubbles and plugs that occurs in multi-branch PHP. At this stage, the model development focuses on fluid behavior; therefore, the liquid-solid thermal coupling is not considered. We designate three calculation volumes for the bubble, film and plug in single branch PHP simulation.

This chapter presents the implementation of OFT model to the configuration shown in Fig. 40. The governing equations are written for three components in the fluid channel: liquid plug, vapor bubble, and liquid film. Simplifications and assumptions will be justified.

5.1 Single branch PHP configuration

Testing numerical models on single branch PHPs (the simplest configuration of PHPs) is a desirable step to evaluate their validity. Thanks to this simple geometry, more general, sometimes even analytical results can be obtained.

Fig. 40 illustrates the typical configuration of a vertical single branch PHP. It consists of a round capillary tube (inner diameter d and cross-section $S = \pi d^2/4$), an evaporator (of length L_e), a condenser (L_c) and an adiabatic section (L_a); the total length $L_t = L_e + L_a + L_c$. One end of the tube is sealed, while the other is open and immersed into a reservoir at constant pressure p_r. Here, L_r denotes the length below the condenser to the open end. A vapor bubble is confined between the sealed end of the tube and the liquid plug. Only one meniscus oscillates in the tube. The contact line and meniscus positions are denoted by x_{cl} and x_m, respectively. This system of a single bubble-plug couple can be deemed as a "unit cell" of multi-branch PHPs.

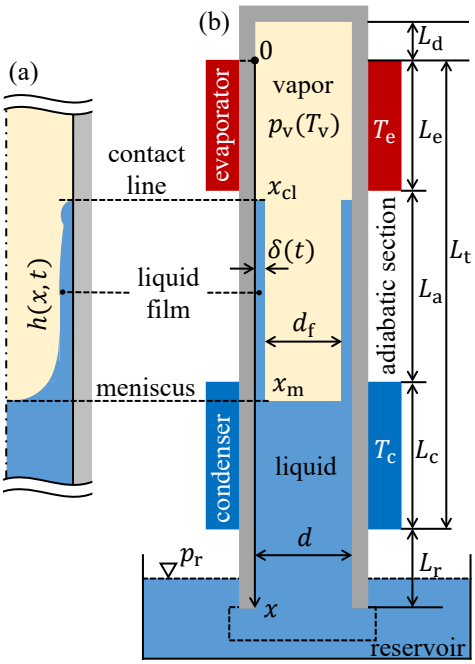

Figure 40: Schematic configuration of a vertical single branch PHP: (a) curved vapor-liquid interface in the fluid channel, and (b) lumped-geometry approach of flat interfaces.

In many experimental setups, additional space between the sealed end of the tube and the evaporator is required for installing pressure and temperature sensors. This space is called the dead volume because the vapor remains stagnant. This volume is represented by an equivalent length L_d. Many simulations neglect the fluid-solid thermal coupling and assume the constant inner wall temperature in the evaporator T_e and in the condenser T_c (Shafii et al., 2001; Dobson, 2004; Das et al., 2010).

Conducting experiments with single branch PHPs is easier than with multi-branch PHPs. Since the bubble is confined between the sealed end of the tube and the plug, the temperature sensors installed in the dead volume are not intermittently drowned by the oscillating liquid plug, which makes it possible to produce reliable data, because only dry sensors can truthfully measure the vapor temperature. The meniscus and contact line displacements with time can be well documented, and the oscillation frequency and amplitude are tunable by adjusting the inner wall temperatures or the reservoir pressure. A large range of available experimental data enables detailed comparisons with numerical results.

5.2 Liquid plug

The liquid in plugs is assumed to be incompressible and of constant density. Since liquid plugs primarily stay in the condenser and the amount of heat exchange is small, the heat transfer phenomenon is not considered here. The plug motion follows the momentum equation (Das et al., 2010),

$$\frac{\mathrm{d}}{\mathrm{d}t}\left[(m_l + m_{l,i})u_l\right] = (p_v - p_r)S - F_l + m_l g, \tag{5.1}$$

where the liquid plug mass is $m_l = \rho(L_t - x_m + L_r)S$; u_l is the plug velocity (the center of mass), which is denoted positive for plug moving downwards. A portion of liquid in the reservoir (the region enclosed by the dashed line in Fig. 40) participates in oscillating motion and impacts the oscillation period. It is designated by an equivalent length L_i. The

corresponding mass $m_{\mathrm{l,i}} = \rho L_{\mathrm{i}} S$. The value of L_{i} depends on the individual case. It is adjusted to agree with the oscillation period observed in experiment (Das et al., 2010).

On the right-hand side of Eq. 5.1, the first term represents the pressure difference between the vapor bubble and the liquid reservoir. The second term is the pressure loss in the plug. It consists of the regular viscous and singular pressure drops, whose signs are opposite to the plug velocity u_{l}: negative for the plug falling downwards and positive for the plug rising upwards,

$$F_{\mathrm{l}} = \left[K\pi d(L_{\mathrm{t}} - x_{\mathrm{m}} + L_{\mathrm{r}} + L_{\mathrm{lf}}) + bS\right] \frac{\rho u_{\mathrm{l}}^2}{2} \mathrm{sign}(u_{\mathrm{l}}). \tag{5.2}$$

The regular friction is calculated by the first term on the right-hand side of Eq. 5.2, in which K is the Fanning friction factor:

$$K = \begin{cases} 0, & \text{if } Re_{\mathrm{l}} = 0 \quad (5.3a) \\ 16/Re_{\mathrm{l}}, & \text{if } 0 < Re_{\mathrm{l}} < 2100, \quad (5.3b) \\ 0.0791 Re_{\mathrm{l}}^{-0.25}, & \text{otherwise .} \quad (5.3c) \end{cases}$$

where the second line is for laminar flows and the last line is the turbulent Blasius correlation applicable for $Re_{\mathrm{l}} \leq 10^5$. In this description, the viscous friction is assumed to be equal to a fully developed single-phase flow in tubes. However, considering the finite plug length in PHPs, Eq. 5.3 underestimates the liquid pressure loss. In addition, the vortexes near menisci and in the reservoir due to the alternation of flow direction increase viscous dissipation (Nikolayev, 2021). To compensate for this effect, the pressure loss term F_{l} introduces an additional length L_{lf}, whose value mainly impacts the amplitude of meniscus oscillation and is tuned to conform to experimental observation.

Near the outlet of the tube in the reservoir, a sudden change in the flow area exerts the singular pressure drop, which is calculated (Rao et al., 2017) as

$$b = \begin{cases} 0.5, & \text{if } u_{\mathrm{l}} > 0 \quad (5.4a) \\ 0.25, & \text{if } u_{\mathrm{l}} \leq 0. \quad (5.4b) \end{cases}$$

The resistance is smaller for liquid in the reservoir entering the tube.

5.3 Vapor phase

Vapor bubbles act as an elastic agent that provides the restoring force responsible for system oscillation. In agreement with Assumption 2, the vapor phase is characterized by its temperature T_{v} and pressure p_{v}; hence any spatial distribution is neglected. The equation of state that describes thermodynamic quantities (T_{v} and p_{v}) shall be established first. Then their variation is investigated, i. e. the energy equation.

5.3.1 *Vapor thermodynamic state*

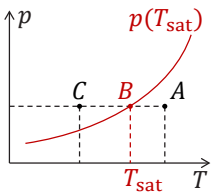

Naïvely, we might suppose that the vapor is at saturation temperature $T_{\mathrm{sat}}(p_{\mathrm{v}})$, corresponding to its pressure p_{v}, as in conventional heat pipes (see the marginal illustration, the point B on the fluid phase diagram). Alternatively, the vapor state is described by the ideal gas law, which signifies that the vapor is superheated with respect to T_{sat}, i. e. vapor temperature $T_{\mathrm{v}} > T_{\mathrm{sat}}(p_{\mathrm{v}})$, the point A. The metastable or supersaturated vapor (the point C) is unlikely to be encountered in PHPs. Because vapor bulks in thin fluid channels are close to free interfaces (films or menisci), even a tiny supersaturation would lead to immediate condensation on interfaces, and the vapor state shifts onto the saturation curve.

Determining whether the vapor is superheated or saturated requires knowing the values of T_{v} and p_{v} at the same time. Gully et al. (2014) measured T_{v} and p_{v} in an operating single

branch PHP. In their experiments, a microscopic thermocouple (μTC, diameter 30 μm) was installed in a vapor bubble. Preventing the thermocouple from being immersed in oscillating liquid plugs is essential. When the μTC is withdrawn out of plugs, it is covered with a layer of liquid, and the μTC would record T_{sat} rather than real T_{v}. The working fluid was oxygen at around 70 K to minimize the parasite heat flows to μTC, particularly the thermal radiation from the inner tube wall. Their measurements revealed several unique features: (i) temperature of the μTC oscillates around the evaporator temperature T_{e}, which confirms the importance of sensible heat exchange; (ii) temperature of the μTC remains above or equal to $T_{\text{sat}}(p_{\text{v}})$, which suggests that the vapor could be deemed as superheated; (iii) due to compression, the vapor occasionally becomes warmer than the tube wall that heats it. Despite substantial efforts to reduce the μTC thermal inertia (by reducing its size and conducting the experiment at the cryogenic temperature where the heat capacity is low), a theoretical analysis suggested that the μTC fail to capture the rapid temperature variations, possibly because of the slow heat exchange between the μTC and vapor.

Rao et al. (2015) also measured T_{v} in a single branch PHP. The working fluid was FC-72, and the experiment was conducted at room temperature. Their results demonstrated a weak fluctuation of T_{v} (probably owing to the radiant heat exchange) around T_{e}, which supports the claim that the vapor is superheated, in agreement with Gully et al. (2014).

Evidently, T_{v} is not perfectly homogeneous in a bubble when it expands or is compressed. Thermal boundary layers develop near the dry wall at T_{w} and near the liquid film at T_{sat}. How thick these boundary layers are is a complex yet unsolved issue. Gully et al. (2014) performed direct numerical simulations of the gas flow in oxygen bubbles during oscillatory compression at the frequency of 1.5 Hz. Their results showed that for oxygen at about 70 K, the thickness of the boundary layer that formed in the tube of $d = 2\,\text{mm}$ is $0.25\,\text{mm}$ approximately. The gaseous flow remained essentially laminar in thermal boundary layers; turbulent mixing was absent near the tube wall. Therefore, in one-dimensional PHP modeling, the vapor can be reasonably described by a unique bulk temperature T_{v}.

The above analysis and experimental results indicate that the vapor phase is mainly superheated, at least in single branch PHPs. Therefore, the thermodynamic state of the vapor phase is well approximated by the ideal gas law (Assumption 4)

$$p_{\text{v}} = \frac{m_{\text{v}} R_{\text{g}} T_{\text{v}}}{\Omega_{\text{v}}}, \tag{5.5}$$

where m_{v} and Ω_{v} are the mass and volume of the vapor bubble, respectively. Moreover, the ideal gas law can provide an elastic response necessary for system oscillation.

5.3.2 *Vapor energy equation*

The temperature of the liquid-vapor interface is assumed to be equal to the saturation temperature T_{sat} corresponding to p_{v}, while T_{v} is determined by the energy balance. Vapor bubbles can exchange energy and mass with the environment,

$$\frac{\mathrm{d}(m_{\text{v}} \boldsymbol{u}_{\text{v}})}{\mathrm{d}t} = \delta Q_{\text{sens}} - p_{\text{v}} \dot{\Omega}_{\text{v}} + \boldsymbol{h}_{\text{v}} \dot{m}_{\text{v}}, \tag{5.6}$$

where $\boldsymbol{u}_{\text{v}}$ and $\boldsymbol{h}_{\text{v}}$ is the internal energy and enthalpy per unit mass. Since the vapor obeys the ideal gas law, $\boldsymbol{u}_{\text{v}} = \boldsymbol{h}_{\text{v}} - R_{\text{g}} T_{\text{v}}$, and the above equation can be rearranged as (Nikolayev, 2011b),

$$m_{\text{v}} c_{\text{vv}} \dot{T}_{\text{v}} = R_{\text{g}} T_{\text{v}} \dot{m}_{\text{v}} - p_{\text{v}} \dot{\Omega}_{\text{v}} + \delta Q_{\text{sens}}. \tag{5.7}$$

Applying the equation to the configuration of single branch PHP (Fig. 40) yields

$$m_{\text{v}} c_{\text{vv}} \dot{T}_{\text{v}} = \dot{m}_{\text{v}} R_{\text{g}} T_{\text{v}} + U_{\text{sens}} \pi d \int_0^{x_{\text{cl}}} \left[T_{\text{w}}(x) - T_{\text{v}} \right] dx - p S u_{\text{l}}. \tag{5.8}$$

On the right-hand side, the second term represents the sensible heat exchange Q_{sens} between vapor and dry tube wall, where U_{sens} is the heat exchange coefficient. It is usually a small value, since U_{sens} is proportional to the vapor heat conductivity k_{v}. The contribution of Q_{sens} to the overall heat transfer is marginal in the stable oscillation regime. However, in certain operation regimes where other heat transfer methods are missing, Q_{sens} becomes significant. For instance, at system start-up, liquid films are absent. Q_{sens} is essential in determining the start-up threshold. Q_{sens} is also not negligible in modeling the intermittent regime where the oscillation ceases and restarts again. Such an operation regime occurs in multi-branch PHPs (Nekrashevych et al., 2019).

Because of the weak heat diffusion in the vapor phase, thermal boundary layers exist, and the bulk temperature T_{v} differs from the free interface temperature T_{sat}, which is usually several degrees lower than T_{v} as discussed above.

5.4 Liquid film

Without the description of curved interfaces, liquid films are characterized by two quantities: the mass m_{f} and the length. Their variations with time are the two key processes emphasized in OFT model.

The length of a liquid film L_{f} in single branch PHPs is determined by the distance between the film edge (contact line) x_{cl} and the meniscus x_{m}: $L_{\text{f}} = x_{\text{m}} - x_{\text{cl}}$.

The liquid film mass is

$$m_{\text{f}} = S_{\text{f}}(x_{\text{m}} - x_{\text{cl}})\rho, \tag{5.9}$$

where $S_{\text{f}} = \pi\delta(d - \delta)$ is the area of film cross-section. Rearranging this equation results in the **effective film thickness** δ,

$$\delta = \frac{d}{2} - \sqrt{\frac{d^2}{4} - \frac{m_{\text{f}}}{\pi\rho(x_{\text{m}} - x_{\text{cl}})}}, \tag{5.10}$$

which is the averaged value of a spatially-varying interface profile $h(x)$, cf. Eq. 5.28 below.

5.4.1 *Length variation*

The film length L_{f} varies because of the meniscus oscillation and the contact line displacement:

$$\dot{L}_{\text{f}} = \dot{x}_{\text{m}} - \dot{x}_{\text{cl}}, \tag{5.11}$$

where $\dot{x}_{\text{m}} = u_{\text{m}}$ and $\dot{x}_{\text{cl}} = u_{\text{cl}}$.

5.4.1.1 *Meniscus motion*

The meniscus is assumed to move at the same velocity as the center of mass of the liquid plug, which is determined by the plug momentum equation, Eq. 5.1,

$$u_{\text{m}} = u_{\text{l}}. \tag{5.12}$$

When a plug is depositing liquid, the meniscus is in fact approaching the center of the plug, due to mass loss. u_{m} is slightly higher than u_{l}. Nevertheless, in the configuration of single branch PHPs, the mass of liquid plugs is considerably larger than the mass deposited to liquid films. The difference between u_{m} and u_{l} can be safely neglected.

5.4.1.2 *Contact line motion*

Because of capillary action, contact lines recede spontaneously after liquid film deposition, which is a local phenomenon controlled by local parameters, such as contact angle and the wall superheating ΔT_{cl} at contact lines, cf. Chap. 3. According to Assumption 6, the contact line motion is modeled by the dewetting of liquid films, which is accelerated in the presence of evaporation. Correlations between the dewetting speed u_{d}, with ΔT_{cl} and θ_{micro}: $u_{\mathrm{d}} = f\left(\Delta T_{\mathrm{cl}}, \theta_{\mathrm{micro}}\right)$, established in Fig. 31, are employed.

Therefore, the contact line dynamics in OFT model is described as

$$u_{\mathrm{cl}} = \begin{cases} u_{\mathrm{m}} & \text{if } x_{\mathrm{m}} = x_{\mathrm{cl}} \text{ and } u_{\mathrm{m}} \leq \epsilon u_{\mathrm{d}}, \quad (5.13a) \\ u_{\mathrm{d}} & \text{otherwise.} \quad (5.13b) \end{cases}$$

The second line indicates that the contact line is the edge of a liquid film, whose dynamics is controlled by the dewetting problem presented in Chap. 3.

The first line indicates that the contact line coincides with the meniscus. It is written for two sub-cases, where (i) the meniscus advances over dry tube $u_{\mathrm{m}} < 0$, naturally $u_{\mathrm{m}} = u_{\mathrm{cl}}$; (ii) the meniscus recedes from dry patch $u_{\mathrm{m}} > 0$ without laying down liquid behind. Sub-case (ii) refers to the dynamic wetting transition, where the liquid film is not deposited until u_{m} surpasses a threshold value ϵu_{d}, where $\epsilon \geq 1$ (Snoeijer et al., 2007); see the marginal illustration. Contact lines are able to recede with menisci at the same speed when u_{m} below the threshold. Gao et al. (2019) performed diffuse-interface simulations to investigate forced dewetting in capillary tubes under adiabatic conditions. They demonstrated that ϵu_{d} increases with the static receding angle θ_{rec}, which corresponds to θ_{micro} in our case. The value of ϵ decreases with θ_{rec} (Gao et al., 2019). For complete wetting cases, $\epsilon = 1$.

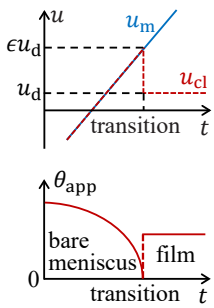

At the onset of the wetting transition, u_{cl} experiences an abrupt drop from u_{m} to u_{d} (see Fig.4 of their paper and the marginal illustration). The contact line then moves slower than the meniscus, and liquid deposition occurs. This plummet in u_{cl} originates from the different mechanisms that control apparent contact angle θ_{app}. Before the transition, the interface is a nearly-spherical meniscus without liquid films, and θ_{app} depends on the values of θ_{V} (when including evaporation, θ_{micro} replaced with θ_{V}) and u_{cl}, which is equal to u_{m}, cf. Eq. 1.28. With increasing u_{m}, θ_{app} dereases: ϵu_{d} corresponds to the value of u_{m} when θ_{app} lessenes to zero. After the transition, separated by a liquid film, the contact line is decoupled from the meniscus, and a dewetting ridge forms (Fig. 3). u_{cl} and θ_{app} become to be determined by the hydrodynamics of dewetting rather than by that of meniscus motion, cf., Subsec. 1.1.2.

In the calculation below, $\epsilon = 2$ is adopted, which conforms to the numerical simulations of Gao et al. (2019).

5.4.2 *Mass variation 1: liquid deposition and collection*

Liquid films exchange mass with plugs and with bubbles:

$$\dot{m}_{\mathrm{f}} = \dot{m}_{\mathrm{dep}} - \dot{m}_{\mathrm{v}}, \quad (5.14)$$

where $\dot{m}_{\mathrm{dep}}$ represents the liquid deposited from and collected by oscillating plugs, and $\dot{m}_{\mathrm{v}}$ is the phase exchange rate, positive for net flux toward vapor phase. Hence, it also can be regarded as the vapor mass growth rate, calculated using Eq. 5.16 below.

The liquid film deposition rate $\dot{m}_{\mathrm{dep}}$ is expressed as

$$\dot{m}_{\mathrm{dep}} = \begin{cases} 0, & x_{\mathrm{cl}} = x_{\mathrm{m}} \text{ and } u_{\mathrm{m}} \leq \epsilon u_{\mathrm{d}}, \quad (5.15a) \\ S_{\mathrm{f}} u_{\mathrm{m}} \rho, & x_{\mathrm{cl}} < x_{\mathrm{m}} \text{ and } u_{\mathrm{m}} < 0, \quad (5.15b) \\ \pi \delta_{\mathrm{dep}} (d - \delta_{\mathrm{dep}}) u_{\mathrm{m}} \rho, & \text{otherwise.} \quad (5.15c) \end{cases}$$

This equation may also be regarded as the mass exchange between the liquid film and the plug.

Condition 5.15a corresponds to the situation where the contact line coincides with the meniscus. This occurs when the meniscus advances over dry tube ($u_\mathrm{m} < 0$), or the meniscus recedes ($u_\mathrm{m} > 0$) but not fast enough to overcome the threshold of dewetting transition. Hence, no film appears, conforming to Eq. 5.13a.

Condition 5.15b corresponds to the situation where the meniscus advances over an existing film ($x_\mathrm{cl} < x_\mathrm{m}$); the plug is collecting liquid from the film. Since $u_\mathrm{m} < 0$, $\dot{m}_\mathrm{dep}$ is negative in this case. Notice that liquid film collection does not change the value of δ.

Condition 5.15c describes two other possible scenarios: (i) $x_\mathrm{cl} = x_\mathrm{m}$ and $u_\mathrm{cl} < u_\mathrm{m}$ (complementary to the clause 5.15b): the contact line coincides with the meniscus, and the meniscus recedes faster than ϵu_d. As a result, a new film is about to be created. (ii) $x_\mathrm{cl} < x_\mathrm{m}$ and $u_\mathrm{m} \geq 0$ (complementary to the clause 5.15a): a liquid film exists, and more liquid is deposited to it. δ_dep is the initial film thickness deposited by receding plugs, as shown in Chap. 2, whose value is a function of the instantaneous velocity of the meniscus u_m and can be well approximated by the quasi-steady correlation, Eq. 1.34, proposed by Aussillous et al. (2000).

5.4.3 *Mass variation 2: phase exchange*

The dynamic wetting transition introduced in Eq. 5.13 also impacts the phase exchange over the interface. Under post-transition conditions, liquid films are present. The following regions of interface that contribute to phase change $\dot{m}_\mathrm{v}$ are distinguished: the contact line vicinity, flat film (J_f), and meniscus center (J_m). Hence,

$$\dot{m}_\mathrm{v} = J_\mathrm{cl} + J_\mathrm{f} + J_\mathrm{m}. \tag{5.16}$$

where J_cl represents the mass flux of the edge of a liquid film (contact line vicinity); see the marginal illustration. When liquid films are absent (pre-transition), $J_\mathrm{f} = 0$, and J_cl now represents mass flux in the liquid layer near the solid surface of the meniscus.

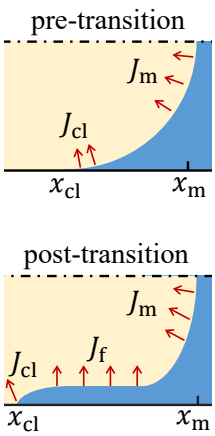

5.4.3.1 *Local mass flux near contact line*

As the liquid thickness approaches zero at contact lines, the local mass flux $j(x)$ proportional to h^{-1} becomes infinite. Relaxing this singularity requires several nanoscale effects discussed in Subsec. 1.1.2. These effects impact heat flux only in the microscopic region. Since the thickness scale pertinent to J_cl is up to 100 µm, the sophisticated description in Chap. 3 can be simplified.

Among all the nanoscale effects, the interfacial thermal resistance R^i, cf. Eq. 1.21, can provide a good estimation $\sim (R^\mathrm{i}k + h)^{-1}$ that relaxes the singularity of mass flux. Retaining only the R^i term in Eq. 3.20 yields the local mass flux $j(s)$ in the 2D cross-section as

$$j(s) = \frac{k}{\mathcal{L}(R^\mathrm{i}k + \zeta)} \Delta T_\mathrm{cl}, \tag{5.17}$$

where ΔT_cl is the local superheating at contact line. Eq. 5.17 assumes a linear temperature gradient along the arc length $\zeta = h\phi/\sin\phi$ from tube wall to interface.The length $R^\mathrm{i}k$ can be deemed as an additional layer of liquid.

To evaluate the approximation of Eq. 5.17, Fig. 41 plots the distributions of $j(x)$ of a dewetting ridge as a function of the horizontal distance from contact line $x - x_\mathrm{cl}$. The fluid is FC-72 with $\theta_\mathrm{micro} = 5°$, and the solid substrate is overheated by 5 K. The red curve results from the hydrodynamic problem of Sec. 3.3, which includes a full range of nanoscale effects;

the green curve is calculated using Eq. 5.17 for the same dewetting ridge. Two distributions differ around the very vicinity of contact lines. Whereas approaching the upper boundary of the microregion, $(x - x_{\mathrm{cl}}) \to 1\,\mu\mathrm{m}$, two curves are almost identical.

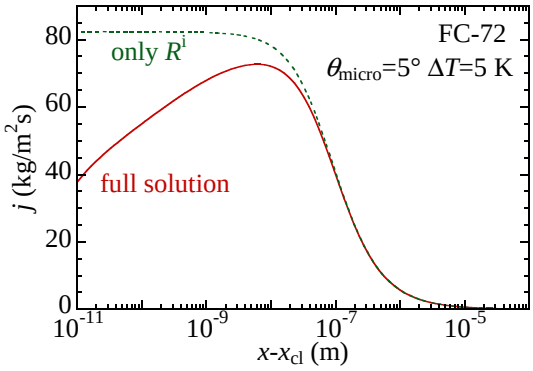

Figure 41: Local interface flux j of a dewetting ridge, plotted as a function of the horizontal distance from contact line $x - x_{\mathrm{cl}}$, fluid: FC-72, $\Delta T = 5\,\mathrm{K}$, $\theta_{\mathrm{micro}} = 5°$.

Though seen in Fig. 41, an intense mass flux is observed as $h \to 0$, albeit it is limited to a short range below the micrometer scale. Modeling PHPs concerns the amount of mass exchange in the microregion and over the entire contact line region that may be up to millimeter scale, i. e. the integrated value of j. For instance, integrating $j(x)$ from $x = 0$ to outside of the microregion, say $x = 0.1\,\mathrm{mm}$, gives the total mass flux of $\sim 4.74 \times 10^{-5}\,\mathrm{kg/(m \cdot s)}$ by the full solution, and of $\sim 4.77 \times 10^{-5}\,\mathrm{kg/(m \cdot s)}$ by the "R^{i}-only" approximation. Two integrals are very close. Therefore, instead of using the full solution, OFT model employs Eq. 5.17 to estimate the phase change rate over the contact line region.

5.4.3.2 *Contact line and meniscus portions, and their relative importance*

We examine the mass fluxes from contact lines and the central part of the menisci by taking the example of a bare meniscus (pre-transition). In this scenario, liquid films are absent, and the liquid-vapor interface is approximately a spherical cap. The 2D cross-section of this interface is an arc of a circle with the radius R_{m} and centers at O with the apparent contact angle θ_{app}; see the marginal illustration. The interface thickness h is related to the local slope ϕ as

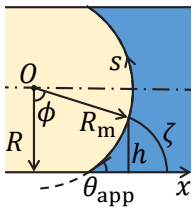

$$h(\phi) = R(1 - \cos\phi / \cos\theta_{\mathrm{app}}),$$

where ϕ ranges from θ_{app} to $\pi/2$, and $R_{\mathrm{m}} = R/\cos\theta_{\mathrm{app}}$. Here $s = R_{\mathrm{m}}(\phi - \theta_{\mathrm{app}})$ which is the curvilinear coordinate that runs along the interface, with $s = 0$ at the contact line, and $s_{\mathrm{m}} = R_{\mathrm{m}}(\pi/2 - \theta_{\mathrm{app}})$ at the tube axis.

Substituting $h(\phi)$ into $\zeta = h\phi/\sin\phi$ (the arc length in the generalized lubrication theory) gives the geometry condition of

$$\zeta(\phi) = R\frac{\phi\,(\cos\theta_{\mathrm{app}} - \cos\phi)}{\sin\phi\cos\theta_{\mathrm{app}}}.$$

Injecting $\zeta(\phi)$ into Eq. 5.17 yields the local mass flux $j(\phi)$ on the circular interface:

$$j(\phi) = \frac{k\Delta T_{\mathrm{cl}}}{\mathcal{L}}\frac{\sin\phi\cos\theta_{\mathrm{app}}}{\alpha\sin\phi\cos\theta_{\mathrm{app}} + \phi\,(\cos\theta_{\mathrm{app}} - \cos\phi)}, \tag{5.18}$$

where $\alpha \equiv R^{\mathrm{i}}k/R$ is constant for a given fluid and a tube.

Integrating Eq. 5.18 from the solid surface (corresponding to $\phi = \theta_{\text{app}}$) to a upper limit $\phi' \leq \pi/2$ produces the mass flux over the 3D spherical interface $J(\phi')$ as a function of ϕ',

$$J(\phi') \equiv \int_0^{s'} j(s) 2\pi (R-h) \mathrm{d}s = \int_{\theta_{\text{app}}}^{\phi'} j(\phi) 2\pi R_{\text{m}} \cos\phi R_{\text{m}} \mathrm{d}\phi, \tag{5.19}$$

where $(R-h) = R_{\text{m}} \cos\phi$, $s' = R_{\text{m}}(\phi' - \theta_{\text{app}})$. Substituting Eq. 5.18 results in,

$$J(\phi') = \frac{2\pi R k \Delta T_{\text{cl}}}{\mathcal{L}} w(\alpha, \theta_{\text{app}}, \phi'), \tag{5.20}$$

and the function w is an integral constant, which is defined as

$$w(\alpha, \theta_{\text{app}}, \phi') = \frac{1}{\cos\theta_{\text{app}}} \int_{\theta_{\text{app}}}^{\phi'} \frac{\sin\phi\cos\phi}{\alpha \sin\phi \cos\theta_{\text{app}} + (\cos\theta_{\text{app}} - \cos\phi)\phi} \mathrm{d}\phi. \tag{5.21}$$

Taking the upper limit to $\phi' = \pi/2$, the integral of Eq. 5.18 gives the total mass flux over the entire spherical interface,

$$J_{\text{cl}} + J_{\text{m}} \equiv J\left(\frac{\pi}{2}\right) = \frac{2\pi R}{\mathcal{L}} Q, \tag{5.22}$$

where Q is the heat transfer power per unit length of the tube circumference and is a function of ΔT_{cl} and θ_{app}.

$$Q = k \Delta T_{\text{cl}} W(\alpha, \theta_{\text{app}}), \tag{5.23}$$

and W is constant,

$$W(\alpha, \theta_{\text{app}}) \equiv w(\alpha, \theta_{\text{app}}, \phi' = \pi/2).$$

We can deem the integral of Eq. 5.19 from solid surface to ϕ' as the mass flux of contact line region and the rest (from ϕ' to $\pi/2$) as the mass flux of the central part of meniscus center. Therefore,

$$J_{\text{cl}} = J(\phi') = \frac{2\pi R k \Delta T_{\text{cl}}}{\mathcal{L}} w, \tag{5.24a}$$

$$J_{\text{m}} = J\left(\frac{\pi}{2}\right) - J(\phi') = \frac{2\pi R k \Delta T_{\text{cl}}}{\mathcal{L}} (W - w). \tag{5.24b}$$

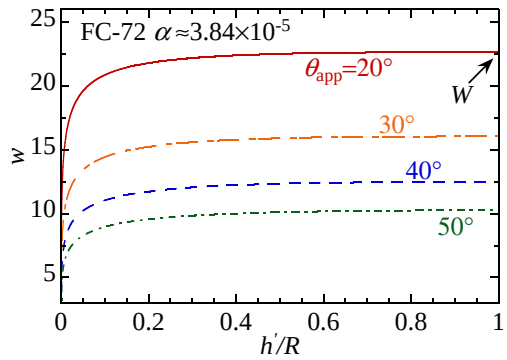

Figure 42: Dependence of the function w on the upper limit of integral h', for FC-72 with $\alpha \simeq 3.84 \times 10^{-5}$, the values of θ_{app} are indicated by the curves.

Examples of $w(h')$ variation for FC-72 with $\alpha \simeq 3.84 \times 10^{-5}$ are plotted in Fig. 42 for various fixed θ_{app} and $R = 1\,\text{mm}$. As the upper limit of integral ϕ' increases from θ_{app} to $\pi/2$, the corresponding $h' = R - R_{\text{m}} \cos\phi'$ monotonously grows from 0 until reaching R at the tube axis. With the enlarging distance h' from the wall, the value of w rapidly saturates

to W, which signifies that evaporation largely occurs in the liquid layer near the wall. For $\theta_{\text{app}} = 20°$ and a liquid layer of $h' = 50\,\mu\text{m}$, we obtain $w \simeq 19.6$ and $W \simeq 22.7$ from Fig. 42. This suggests that most of the phase change over the spherical interface (>80 %) originates from the contact line region J_{cl}. Because the liquid is thick around the tube axis and the interface slope is high, the contribution from meniscus center J_{m} is expected to be small compared to J_{cl}.

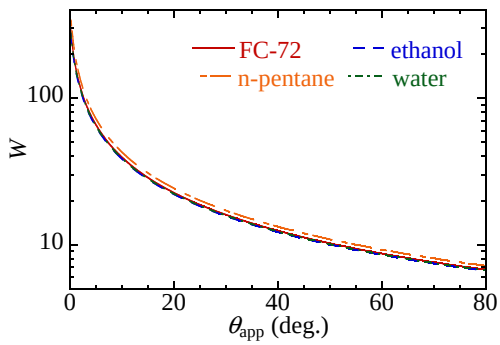

Figure 43: Pre-transition scenario, dependence of the integral constant W on θ_{app} for selected fluids and $R = 1\,\text{mm}$.

For the same $R = 1\,\text{mm}$, dependence of W on θ_{app} is plotted in Fig. 43 for n-pentane with $\alpha \simeq 2.15 \times 10^{-5}$, ethanol with $\alpha \simeq 4.64 \times 10^{-5}$ and water with $\alpha \simeq 4.33 \times 10^{-5}$. The value of W is almost independent of α.

For the pre-transition scenario, θ_{app} is a function of the instantaneous values of u_{m} and ΔT_{cl}. The dependence of $W(\theta_{\text{app}})$ of Fig. 43 can be used to determine the mass exchange rate in this case.

For the post-transition scenario, since J_{m} is minor, to avoid separately calculating the relative contribution of J_{cl} and J_{m} that depends on the time-varying δ, J_{m} is bundled into J_{cl}. Recall the dewetting dynamics in Fig. 31, where θ_{app} is expressed as a function of ΔT_{cl} and θ_{micro} for dewetting ridges. Since the combination of working fluid and tube material determines θ_{micro}, we can build a direct correlation between Q and ΔT_{cl}, using θ_{app} that is calculated in Fig. 31 in Chap. 3. Fig. 44 plots the dependence of Q on ΔT_{cl} for FC-72 with $\theta_{\text{micro}} = 5°$ and for n-pentane with $\theta_{\text{micro}} = 10°$.

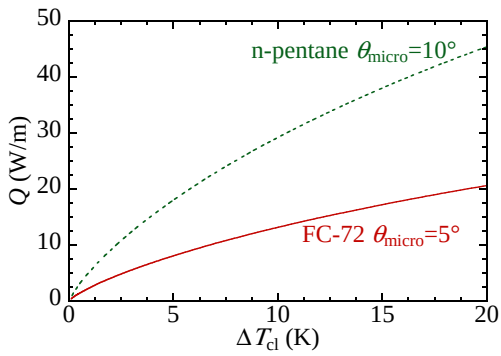

Figure 44: Post-tansition scenario, the value of Q as a function of ΔT_{cl} for FC-72 with $\theta_{\text{micro}} = 5°$ (red solid curve) and for n-pentane with $\theta_{\text{micro}} = 10°$ (green dashed curve).

Therefore, the contributions to phase change from the contactn region and the central part of meniscus are

$$J_{\text{cl}} + J_{\text{m}} = \frac{2\pi R}{\mathcal{L}} Q(\Delta T_{\text{cl}}, \alpha, \theta_{\text{app}}), \tag{5.25}$$

where Q is calculated using Eq. 5.23 and Fig. 43 before the dewetting transition. With liquid film, Q is determined as shown in Fig. 44.

5.4.3.3 *Flat film portion*

Now consider the post-transition case. For pure fluids, the temperature of vapor-liquid interfaces is nearly equal to the saturation temperature. As Assumption 5 states, the mass exchange is characterized by the temperature difference $T_{\mathrm{w}}(x) - T^{\mathrm{i}}$ (which is T_{sat}) and the effective thickness δ. The contribution from flat liquid film J_{f} is

$$J_{\mathrm{f}} = U_{\mathrm{f}} \frac{\pi d_{\mathrm{f}}}{\mathcal{L}} \int_{x_{\mathrm{cl}}}^{x_{\mathrm{m}}} [T_{\mathrm{w}}(x) - T_{\mathrm{sat}}]\, \mathrm{d}x, \tag{5.26}$$

where $U_{\mathrm{f}} = \varsigma k/\delta$ is the heat exchange coefficient of liquid film. Eq. 5.26 reflects the thermal conduction of a thin flat plate of thickness δ, with thermal resistance $\delta/\varsigma k$. Rigorously speaking, the thermal resistance of a liquid film is more like that of a hollow cylinder in the radial direction. Nevertheless, provided δ is small compared to d, the difference in these two values is negligible (Rouaze et al., 2021).

Because the local heat transfer is inversely proportional to local thickness $h(x)$, we need to account for a correction factor ς that originates from the simplification in profiles from curved interfaces in reality (Chap. 2) to the uniform thickness in the model.

Take an example of a spatially varying film with local thickness profile $h(x)$ along the length L_{f} ($x \in [0, L_{\mathrm{f}}]$). The rigorous definition of effective film thickness δ is derived from the film mass expression, Eq. 5.9. Under the assumption $h(x) \ll d$, the liquid mass in the film is

$$m_{\mathrm{f}} = \pi\rho \int_0^{L_{\mathrm{f}}} [d - h(x)]h(x)\mathrm{d}x \simeq \pi d\rho \int_0^{L_{\mathrm{f}}} h(x)\mathrm{d}x = \pi d\rho\delta L_{\mathrm{f}}. \tag{5.27}$$

Therefore, the effective thickness satisfies,

$$\delta \equiv \frac{1}{L_{\mathrm{f}}} \int_0^{L_{\mathrm{f}}} h(x)\mathrm{d}x, \tag{5.28}$$

which can be regarded as the mean of $h(x)$ over L_{f}.

Considering a constant temperature T_{w}, the mass flux of this liquid film is

$$J_{\mathrm{f}} = \frac{k\pi}{\mathcal{L}} \int_0^{L_{\mathrm{f}}} \frac{[d - h(x)](T_{\mathrm{w}} - T_{\mathrm{sat}})}{h(x)} \mathrm{d}x \simeq \frac{k\pi d}{\mathcal{L}} (T_{\mathrm{w}} - T_{\mathrm{sat}}) \int_0^{L_{\mathrm{f}}} \frac{\mathrm{d}x}{h(x)}, \tag{5.29}$$

which is inversely proportional to the harmonic mean of $h(x)$.

Replacing the mean of $h(x)^{-1}$ with the reciprocal of the mean of $h(x)$ requires a correction factor ς,

$$\frac{\varsigma}{\delta} \equiv \frac{1}{L_{\mathrm{f}}} \int_0^{L_{\mathrm{f}}} \frac{\mathrm{d}x}{h(x)}. \tag{5.30}$$

The value of ς depends on $h(x)$. Two simple cases are presented here to illustrate how ς may vary with individual $h(x)$ profiles.

Consider first a linear profile of $h(x) = ax + b$ in the interval of $[0, L_{\mathrm{f}}]$: $h(0) = h_1$ and $h(L_{\mathrm{f}}) = h_2$ are positive. According to Eq. 5.30, ς is found as

$$\varsigma = \frac{\delta}{aL_{\mathrm{f}}} \ln\left(\frac{h_2}{h_1}\right).$$

Replacing h_1 and h_2 with $\delta - \Delta h$ and $\delta + \Delta h$ respectively, we obtain the first approximation,

$$\varsigma \simeq 1 + \frac{1}{3}\left(\frac{\Delta h}{\delta}\right)^2.$$

Since the profile is linear, the ratio of $\Delta h/\delta$ ranges from 0 to 1. Correspondingly, ς ranges from 1 to 1.33.

Move on to a more realistic case, where the film is deposited by an oscillatory liquid plug from an immobile contact line, similarly to the case in Sec. 2.3. The plug oscillates harmonically with the amplitude A and the period P, according to Eq. 2.31, the meniscus receding speed during the first half of the period is

$$u_{\mathrm{m}}(x) = u_{\mathrm{a}}\left[\frac{x}{A}\left(2-\frac{x}{A}\right)\right]^{1/2},$$

where the velocity amplitude $u_{\mathrm{a}} = 2\pi A/P$. Assuming that u_{a} is low, the film thickness $h(x)$ deposited by the meniscus can be approximated by the quasi-steady expression Subsec. 2.3.6.4,

$$h(x) \simeq h_a\left[\frac{x}{A}\left(2-\frac{x}{A}\right)\right]^{1/3}, \tag{5.31}$$

where $h_a = 0.67d\left(\mu u_{\mathrm{a}}/\sigma\right)^{2/3}$ and $\langle h\rangle \simeq 0.84h_a$. Substituting Eq. 5.31 into Eq. 5.30 yields $\varsigma \simeq 2.18$.

Generally speaking, the value of ς is larger than unity. We rearrange Eq. 5.30 as

$$\varsigma \equiv \frac{\dfrac{1}{L_{\mathrm{f}}}\displaystyle\int_0^{L_{\mathrm{f}}} h(x)\mathrm{d}x}{\left[\dfrac{1}{L_{\mathrm{f}}}\displaystyle\int_0^{L_{\mathrm{f}}} \frac{\mathrm{d}x}{h(x)}\right]^{-1}}, \tag{5.32}$$

which represents the ratio of the arithmetic and harmonic means of $h(x)$, which is known in mathematics to be always larger than unity.

Considering the phase change that alters the initial profile of interfaces and non-harmonic oscillation of menisci, the value of ς can hardly be determined precisely and analytically. In single branch PHP simulations, the value of ς is tunable to conform to the oscillation period in experiments. Still, it should have a reasonable value, as the two cases demonstrated. $\varsigma \approx 1.5$ is set.

5.4.3.4 *Relative importance of three portions*

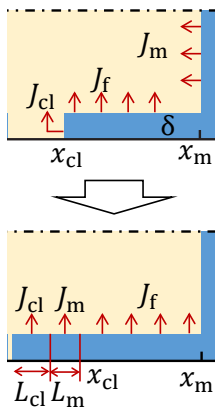

Consider a liquid film of effective thickness δ attached to a meniscus. Integrating the local interface flux Eq. 5.17 from solid surface to δ results in the total mass flux from the contact line region J_{cl}. In this case, ζ in Eq. 5.17 corresponds to the interfacial profile of a dewetting ridge. However, given that δ is small, the calculation of J_{cl} in Eq. 5.24a that uses the spherical profile of ζ can be used as an approximation to this case, where the contact line region is a dewetting ridge.

To compare the relative importance of J_{cl} and J_{f}, we assume a uniform superheating ΔT, and introduce an equivalent length L_{cl}. The phase change of liquid film over the length L_{cl} (which is calculated by Eq. 5.26) is equal to J_{cl}; see the marginal illustration.

$$\frac{\varsigma k}{\delta}\frac{\pi d_{\mathrm{f}}}{\mathcal{L}}\Delta T L_{\mathrm{cl}} = \frac{2\pi R k \Delta T}{\mathcal{L}} w.$$

Therefore,

$$L_{\mathrm{cl}} = \frac{Rw(\delta)\delta}{\varsigma(R-\delta)}.$$

Similarly, we introduce the equivalent length L_m to the liquid film that produces the same amount of phase change as J_m,

$$L_\mathrm{m} = \frac{R[W - w(\delta)]\delta}{\varsigma(R-\delta)}.$$

Fig. 45 plots the equivalent lengths L_cl (the left y-axis) and L_m (the right y-axis) for FC-72, $R = 1\,\mathrm{mm}$ and δ ranging from 10 to 200 µm. For $\theta_\mathrm{app} = 20°$, we obtain $L_\mathrm{cl} \simeq 0.70\,\mathrm{mm}$ and $L_\mathrm{m} \simeq 0.11\,\mathrm{mm}$ which generally are much shorter than film length. This suggests that J_cl contribute several times more than J_m, whereas both are of little importance compared to J_f, for the film length is as long as several centimeters. Nevertheless, J_cl and J_m are not trivial for system start-up, where liquid films are absent. For instance, liquid films have dried out in fluid channels after a stop-over in the intermittent regime.

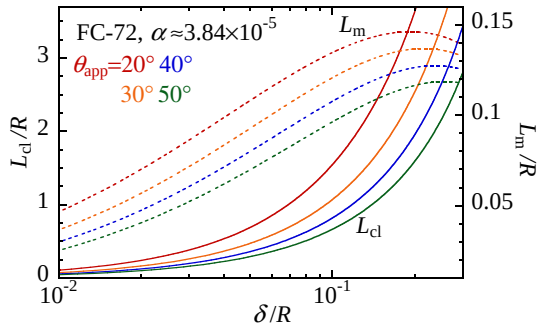

Figure 45: Equivalent film lengths corresponding to the contact line region contribution L_cl (solid lines) and to that of the central meniscus part L_m (dashed lines); the values of θ_app are indicated by the color.

Using Eq. 5.25, we calculate the total phase change over the interface as,

$$\dot{m}_\mathrm{v} = \frac{2\pi R}{\mathcal{L}} Q(\Delta T_\mathrm{cl}, \alpha, \theta_\mathrm{app}) + U_\mathrm{f} \frac{\pi d_\mathrm{f}}{\mathcal{L}} \int_{x_\mathrm{cl}}^{x_\mathrm{m}} [T_\mathrm{w}(x) - T_\mathrm{sat}]\,\mathrm{d}x. \tag{5.33}$$

5.5 Singularity analysis

Singularities appear in Eq. 5.10 when the film length is short, $x_\mathrm{m} - x_\mathrm{cl} \to 0$, which takes place: (i) at the beginning of film deposition, where $(u_\mathrm{m} - u_\mathrm{cl}) > 0$; (ii) near the ending moment of film collection by the plug, where $(u_\mathrm{m} - u_\mathrm{cl}) < 0$.

5.5.1 *Onset of film deposition*

Notably, at the starting moment of film deposition, the effective thickness δ does not necessarily coincide with δ_dep, despite the enforced Eq. 5.15c. Consider the time-lapse Δt at the onset of film deposition. According to Eq. 5.12, $u_\mathrm{m} = \epsilon u_\mathrm{d}$ and $u_\mathrm{cl} = u_\mathrm{d} > 0$. Since the film is short, $\dot{m}_\mathrm{v}$ contribution to $\dot{m}_\mathrm{f}$ is negligible, and $\dot{m}_\mathrm{f} \simeq \dot{m}_\mathrm{dep}$ according to Eq. 5.15c. The liquid film mass at this instant is approximated as,

$$m_\mathrm{f} \simeq \pi\delta_\mathrm{dep}(d - \delta_\mathrm{dep})\epsilon u_\mathrm{d}\rho\Delta t.$$

On the other hand, from Eq. 5.9 and Eq. 5.10,

$$m_\mathrm{f} \simeq \pi\delta(d-\delta)(x_\mathrm{m} - x_\mathrm{cl})\rho = \pi\delta(d-\delta)(\epsilon - 1)u_\mathrm{d}\rho\Delta t.$$

Under the assumption $\delta, \delta_\mathrm{dep} \ll d$, equalizing the two above expressions produces the effective film thickness at this instant,

$$\delta \simeq \frac{\epsilon}{\epsilon - 1}\delta_\mathrm{dep}, \tag{5.34}$$

which in fact deviates from δ_{dep}. This apparent paradox originates from the fact that $u_{\mathrm{cl}} > 0$ at the onset of liquid film deposition. If the contact line were immobile, δ would follow the variation of δ_{dep}, and this singularity would not appear.

A receding meniscus without laying down liquid film rarely occurs in PHPs, given that u_{m} is usually large enough and the tube surface is wettable, which lessens ϵ. The choice of ϵ affects the very initial stage of film evolution and barely impacts the overall heat exchange. However, if without the plummet in u_{cl}, meaning $\epsilon = 1$, δ would be infinite according to Eq. 5.34.

5.5.2 *End of film collection*

Taking the time derivative of both sides of Eq. 5.10, one obtains the δ variation as

$$\dot{\delta} = \frac{\dot{m}_{\mathrm{f}} - \rho S_{\mathrm{f}}(u_{\mathrm{m}} - u_{\mathrm{cl}})}{\pi(d - 2\delta)(x_{\mathrm{m}} - x_{\mathrm{cl}})\rho}. \tag{5.35}$$

Similar to the previous case, it is possible to neglect the phase change near the ending moment of liquid collection, when a meniscus draws back to the contact line, $u_{\mathrm{cl}} > 0$ and $u_{\mathrm{m}} < 0$. Therefore, $\dot{m}_{\mathrm{f}} = \dot{m}_{\mathrm{dep}}$ and Eq. 5.15b is satisfied. Under the assumption $\delta \ll d$, Eq. 5.35 reduces to

$$\dot{\delta} = \frac{\delta u_{\mathrm{cl}}}{x_{\mathrm{m}} - x_{\mathrm{cl}}}. \tag{5.36}$$

A constant relative velocity $(u_{\mathrm{cl}} - u_{\mathrm{m}}) = u_{\mathrm{c}} > 0$ is assumed close to the instant t_{d} of film disappearance: for $t < t_{\mathrm{d}}$, the film length, $x_{\mathrm{m}} - x_{\mathrm{cl}} \simeq u_{\mathrm{c}}(t_{\mathrm{d}} - t)$. Hence $\dot{\delta}$ is expressed as

$$\dot{\delta} = \frac{u_{\mathrm{cl}}}{u_{\mathrm{c}}} \frac{\delta}{t_{\mathrm{d}} - t}, \tag{5.37}$$

which results in $\delta(t) = C(t_{\mathrm{d}} - t)^{-u_{\mathrm{cl}}/u_{\mathrm{c}}}$, where C is the integration constant. As $t \to t_{\mathrm{d}}$, $\delta(t)$ diverges. Typically $u_c \gg u_{\mathrm{cl}}$, i. e. this divergence is weak. This singularity arises from $u_{\mathrm{cl}} > 0$. If the contact line were stationary as the meniscus closes in, without phase change, δ would remain constant. In reality, when a meniscus approaches the contact line, capillary action takes over interface evolution, where the short liquid film promptly coalesces into the plug and the interface rapidly restores to a smooth spherical meniscus, cf. Fig. 21a. This rapid evolution is also seen in the variation of contact angle in Fig. 11a. The contact angle soars back to the initial value near the end of the film's disappearance. To avoid this singularity, a film removal condition is introduced: when the film length $|x_{\mathrm{m}} - x_{\mathrm{cl}}| < \delta$ and $u_{\mathrm{m}} < u_{\mathrm{cl}}$, the liquid film is removed from the system, and its mass is reassigned to the adjacent liquid plug. In Fig. 48b, the condition is satisfied when menisci withdraw to contact lines.

5.6 Boundary conditions

In the current calculations, the inner wall temperatures in the evaporator section T_{e} and in the condenser section T_{c} are assumed to be uniform and invariable with time. It is close to the reality in many experiments where heat conduction in the solid tube can be efficient enough to impose constant temperatures on the tube (Das et al., 2010; Rao et al., 2015, 2017). In the adiabatic section, a linear transition from T_{e} to T_{c} is assumed.

A set of six ordinary differential equations: Eq. 5.1, Eq. 5.8, Eq. 5.12, Eq. 5.13, Eq. 5.14 and Eq. 5.16, defines the behavior of three components (a bubble, film, and plug) in single branch PHPs. As an analytical solution is impossible to be found, the equations are solved numerically using the standard 4th-order Runge-Kutta method to find the temporal evolution of the system.

5.7 Results and discussion

5.7.1 *Comparison with FEC model*

To evaluate OFT model performance, it is first compared to FEC model on simulating a single branch PHP: a capillary tube of $d = 2\,\mathrm{mm}$ is horizontally oriented, and n-pentane is chosen as the working fluid. Tuning the lengths and temperatures of the evaporator and the condenser can produce different oscillation patterns. Major parameters used in the calculation are summarized in row (i) of Tab. 6.

	configuration										simulation			
			d	L_e	L_a	L_c	T_e	T_c	p_r	k	L_{lf}	L_i	ς	W
	orientation	fluid	mm	cm	cm	cm	°C	°C	kPa	W/(m·K)	cm	cm	-	-
(i)	horizontal	n-pentane	2	20	1	20	40	10	90	0.109	10	10	1.5	20
(ii)	vertical	FC-72	2	20	1	20	44	16	50	0.057	30	6	1.5	20
(iii)	horizontal	n-pentane	2	15	1	25	45	10	90	0.109	8	3	1.1	15

Table 6: Major parameters used in simulations of single branch PHP for comparisons with: (i) FEC model; (ii) experiment of Rao et al. (2015); (iii) experiment of Das et al. (2010).

Fig. 46 displays the temporal variations of selected system parameters calculated by OFT and FEC models. In this figure, $T_e = 40°\mathrm{C}$, $T_c = 10°\mathrm{C}$, $L_e = 20\,\mathrm{cm}$, $L_c = 20\,\mathrm{cm}$ and $L_a = 1\,\mathrm{cm}$. The red and blue bars by the vertical axis represent the evaporator and condenser sections, respectively. Both models produce very similar periodic oscillations (periods: $0.68\,\mathrm{s}$ for OFT and $0.65\,\mathrm{s}$ for FEC).

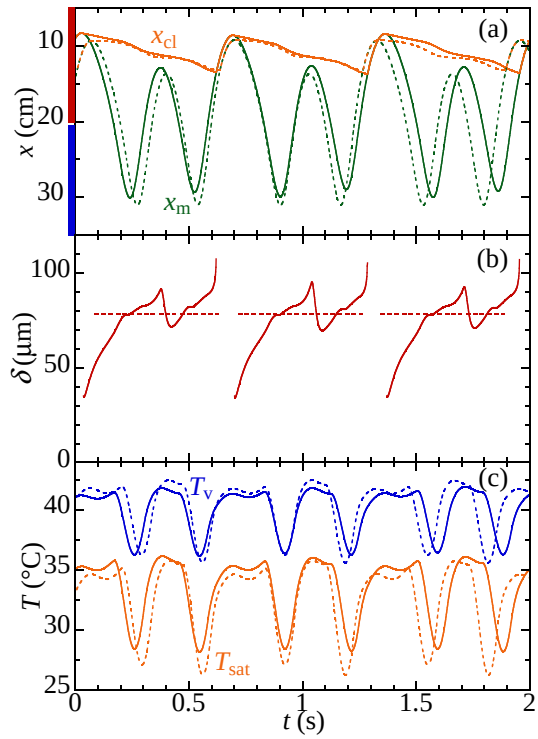

Figure 46: Comparisons between OFT (solid curves) and FEC (dashed curves) models.

Unlike the OFT model, the FEC model requires the value of δ as an input parameter. It is determined with an iteration algorithm proposed by Nekrashevych et al. (2017). The

first iteration of the simulation adopts a practical δ value as its input, $\sim 100\,\mu\mathrm{m}$. Then the output results are used to find the root mean square of the plug velocity $u_{\mathrm{m,RMS}}$ throughout oscillation. The next round of simulation uses a new value for the film thickness δ' that is predicted by Eq. 1.34 corresponding to $u_{\mathrm{m,RMS}}$. This process is repeated until convergence between δ and δ' is achieved. The constant value $\delta \simeq 78.5\,\mu\mathrm{m}$ plotted in Fig. 46b as a dashed horizontal line is a result of such an iteration scheme; it corresponds to the meniscus velocity $u_{\mathrm{m,RMS}} \simeq 1.37\,\mathrm{m/s}$. Fig. 46b plots variation of the effective thickness in OFT model. At the onset of liquid deposition, δ starts growing from $\simeq 35.1\,\mu\mathrm{m}$, which corresponds to the value predicted by Eq. 5.34 with the meniscus velocity around $0.118\,\mathrm{m/s}$ that is observed at this moment. Over a period, $\delta(t)$ has an average value of $\sim 75.1\,\mu\mathrm{m}$, which is very close to the constant film thickness in the FEC model.

OFT model determines the film thickness as a part of the solution. This is a significant advantage and is expected to be especially desirable for simulations of multi-branch PHPs, where numerous liquid films exist with *a priori* different thicknesses.

5.7.2 *Comparison with vertically orientated PHP*

Rao et al. (2015) conducted experiments of single branch PHP using a vertical capillary tube and FC-72 as the working fluid. Their experiment setup is similar to that illustrated in Fig. 40 with a transparent glass circular capillary tube of $d = 2\,\mathrm{mm}$. Two heat exchangers acting as the evaporator and condenser provide constant temperatures (overall accuracy of $\pm 1°$C) to the external tube wall. The lengths of evaporator, condenser and adiabatic sections are $L_{\mathrm{e}} = 20\,\mathrm{cm}$, $L_{\mathrm{c}} = 20\,\mathrm{cm}$ and $L_{\mathrm{a}} = 1\,\mathrm{cm}$, respectively. The reservoir is maintained at the constant pressure $p_{\mathrm{r}} = 0.5$ bar. Their measurements include the vapor pressure, vapor temperature, and displacements of the meniscus and the contact line. In the calculation, $L_{\mathrm{i}} = 6\,\mathrm{cm}$ in Eq. 5.1 and $L_{\mathrm{lf}} = 30\,\mathrm{cm}$ in Eq. 5.2 are used.

In the original experiments (Rao et al., 2015), the thermal regulation targeted the evaporator temperature at $46°$C, whereas in their later analysis (Rao et al., 2017), considering heat conduction through the glass tube, the temperature of the inner tube wall was estimated to be lower. Gully et al. (2014) demonstrated that in single branch PHPs, the vapor temperature oscillates around T_{e} (which is the inner wall temperature). Therefore, our calculations adopted the vapor temperature $\simeq 44°$C, which was measured by Rao et al. (2015), as the imposed value of T_{e}. The inner wall temperatures in the condenser $T_{\mathrm{c}} = 16°$C. Major parameters used in the simulation are summarized in Tab. 6. Since the solid surface wettability is not available, the value of W is assumed constant.

Several snapshots of meniscus oscillation resulting from OFT simulation are displayed in Fig. 47. The images demonstrate the displacement of the meniscus and the variation of liquid film thickness over an oscillation period. The liquid film edge (free contact line) receding is noticeable from $0.54\,\mathrm{s}$ to $1.22\,\mathrm{s}$.

Figure 48a displays the temporal variations of x_{m} and x_{cl} over three oscillation periods, with a period around $1.5\,\mathrm{s}$. The solid and dashed curves are experimental measurements and simulation results, respectively. Contact line receding is observed, whose speed in simulation is in good agreement with the experimental data.

The corresponding variation of liquid film mass m_{f} and the effective thickness δ are plotted in Fig. 48b. Since the experimental measurement of δ is not available, only the numerical result is plotted.

The meniscus oscillates over three sections of the tube, while the contact line always stays in the evaporator. The film deposition takes place at $t_0 \simeq 0.23\,\mathrm{s}$, with the initial thickness $\delta_0 \simeq 71\,\mu\mathrm{m}$. Between t_0 and $t_1 \simeq 0.67\,\mathrm{s}$, the meniscus keeps falling downwards and depositing liquid, leading to increases in m_{f} and δ. At t_1, the meniscus hits the trough

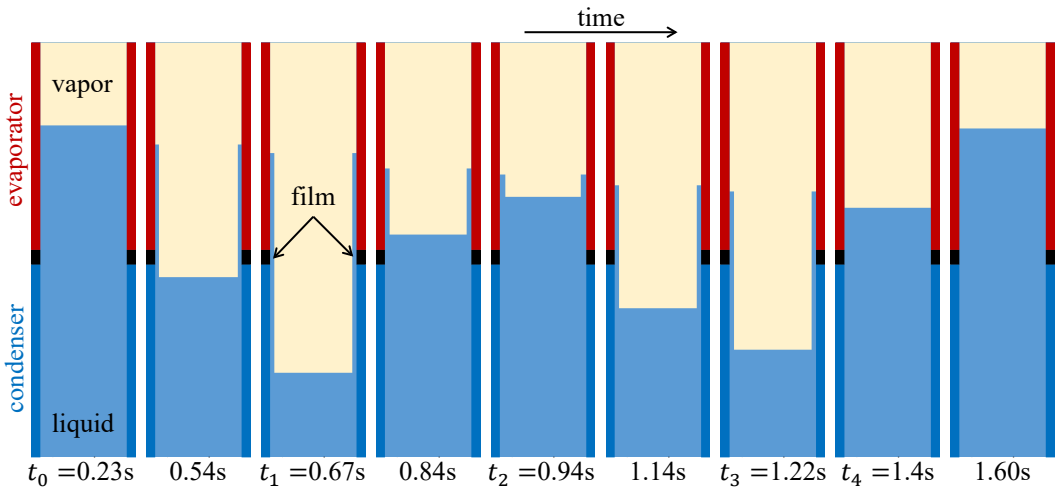

Figure 47: Simulation results showing the meniscus displacement and liquid film variation during an oscillation period, corresponding to experimental setup of Rao et al. (2015). A supplementary movie is available.

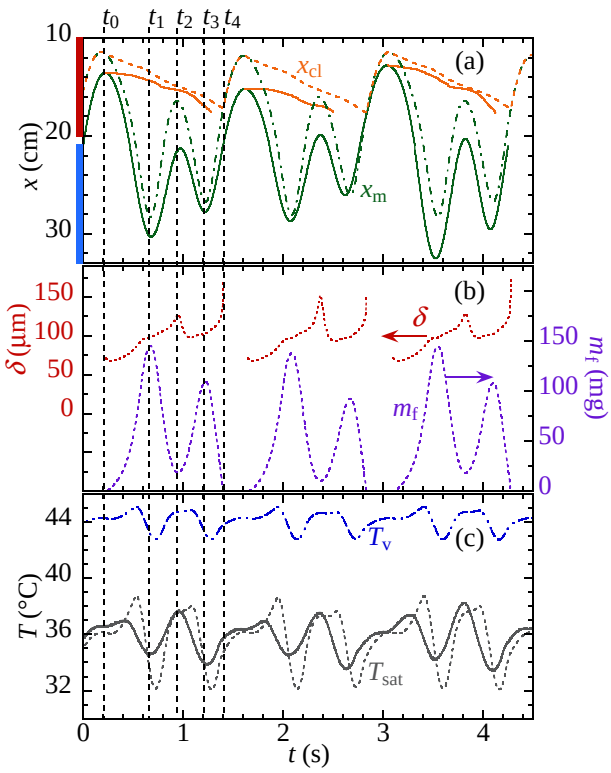

Figure 48: Comparison of the numerical results (dashed curves) and the experimental data (solid curves) by Rao et al. (2015) on x_m and x_{cl} (a); L_e and L_c are indicated with red and blue bars, respectively. Numerical results of δ and m_f, (b); T_v and T_{sat}, (c).

and rises afterward until $t_2 \simeq 0.94\,\mathrm{s}$. The plug collects liquid from the film; therefore, m_f declines. Notably, such an absorption does not lead to a δ variation, cf. Eq. 5.10 and Eq. 5.15b. However, between t_1 and t_2, δ increases because of the contact line receding, the same amount of liquid being averaged over shorter film length. This effect outperforms evaporation, which tends to lessen δ. Immediately before the meniscus draws back at $1.4\,\mathrm{s}$, the value of δ soars up again, as explained in Subsec. 5.5.2, which triggers the film removal condition. The average value of δ is about $\sim 97\,\mu\mathrm{m}$ over a period.

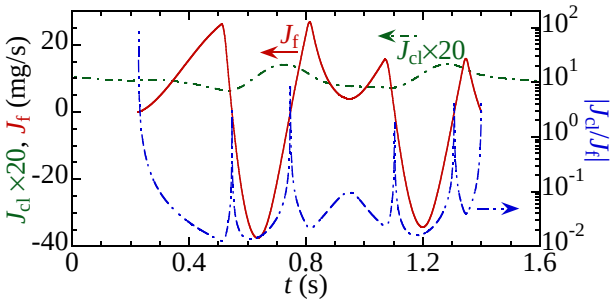

Figure 49: Phase change from the liquid film J_f and from the contact line J_{cl}, positive for net evaporation, and a comparison showing as $|J_{cl}/J_f|$

Simulation results of T_v and T_{sat} are plotted in Fig. 48c. The saturation temperature deduced from the experimentally measured vapor pressure is also plotted. Notably, T_v oscillates around T_e and stays well above T_{sat}. This supports the assumption that the vapor phase remains superheated.

Generally, a very good agreement between the experimental and simulation results is observed. The model reproduces the behavior of major system parameters, including the oscillation period doubling and the rate receding of film edges. Remarkably, a very good agreement is observed for the speed receding of contact lines without accounting for adjustable parameters in the film modeling. Unfortunately, the film thickness variation could not be measured experimentally and thus cannot be compared.

Phase changes from the liquid film J_f and the contact line region J_{cl} (calculated using Eq. 5.25) are plotted in Fig. 49, positive for net evaporation to vapor phase. The relative contribution is plotted on the right vertical axis in the log scale. Throughout a period, J_f is significantly larger than J_{cl}, except near the onset of film deposition, around $t = 0.23\,\mathrm{s}$ and near the instants when J_f flips the sign. In both cases, the ratio of $|J_{cl}/J_f|$ quickly plunges. Notice that J_{cl} can be 10 times larger than J_f immediately after liquid film deposition, supporting our hypothesis in Subsec. 5.4.3 that J_{cl} is non-negligible for the device start-up.

5.7.3 *Comparison with horizontally oriented PHP*

In the experiments conducted by Das et al. (2010), a capillary tube ($d = 2\,\mathrm{mm}$) was horizontally oriented, and n-pentane was chosen as the working fluid. The evaporator was made of a cylindrical copper block ($L_e = 15\,\mathrm{cm}$), which was regulated at a constant temperature $T_e = 45°\mathrm{C}$. The condenser section ($L_c = 25\,\mathrm{cm}$) was made of a transparent glass, whose temperature was regulated by a heat exchanger at the constant value $T_c = 10°\mathrm{C}$. A short connection of $1\,\mathrm{cm}$ long was thermally insulated, which acted as the adiabatic section. Their experiments recorded the meniscus position x_m in the condenser and the vapor pressure p_v. Major parameters used in the simulation are summarized in row (iii) of Tab. 6.

Fig. 50a plots the temporal variations of x_m and p_v over several oscillation periods (solid curves: experimental data, dashed curves: numerical results). Because the evaporator is not transparent, the meniscus position is not displayed for $x_m \leq 15\,\mathrm{cm}$. The vapor pressure oscillates with the amplitude of about $15\,\mathrm{kPa}$, and the period is about $0.28\,\mathrm{s}$. The corresponding variation of liquid film thickness is plotted in Fig. 50b, with the average value about $76.9\,\mu\mathrm{m}$ over a period.

Values of T_v and T_{sat} are plotted in Fig. 50c: T_v remains well above T_{sat}. Hence, the vapor phase is mainly superheated, and the ideal gas equation Eq. 5.5 is suitable to describe p_v in single branch PHPs. The comparisons in Fig. 50 deliver a good qualitative agreement

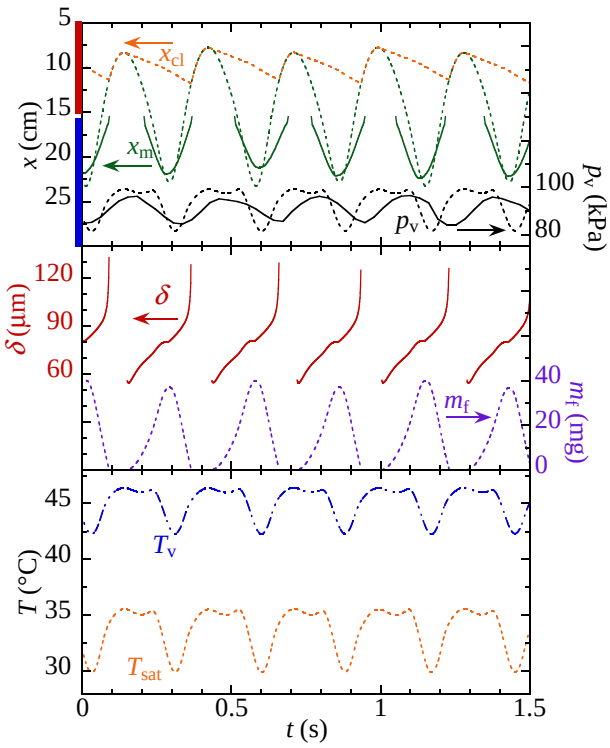

Figure 50: Temporal variations of the vapor pressure p_v, the meniscus position x_m, liquid film thickness δ, vapor T_v and saturation T_{sat} temperatures: (a) comparison between the numerical results (dashed curves) and the experimental data (solid curves) by Das et al. (2010); (b) and (c) numerical results.

between the numerical results and the experimental data, and the plug oscillation with a large amplitude is captured.

5.8 Conclusions

This chapter details the model development of a new one-dimensional numerical model for liquid films in PHPs. It is named the Oscillating Film Thickness (OFT) model. Choosing the one-dimensional approach is a trade-off between result accuracy and efficiency, as it can substantially reduce computational time and resources compared to multi-dimensional approaches. Because the new model employs our theoretical studies of liquid film dynamics in capillary tubes presented in Part I, OFT model can better reflect the essential phenomena of liquid films in real fluid channels than existing models. Three aspects of liquid film behavior are emphasized, the film deposition by receding liquid plugs, the time variation of film thickness due to phase change, and the contact line dynamics that shortens film length.

The model has been validated against experimental data of single branch PHPs. Features and differences between the OFT and previous numerical models are summarized in Tab. 7.

The current calculations focus on the hydrodynamic behavior of working fluid in single branch PHPs. The thermal coupling between the liquid and the solid tube will be accounted for when extending the model to multi-branch PHP simulations.

<table>
<tr><th></th><th>Superheated Vapor</th><th>FEC</th><th>OFT</th></tr>
<tr><td>publications</td><td>Shafii et al., 2001</td><td>Das et al., 2010</td><td>Zhang et al., 2022a</td></tr>
<tr><td>vapor state</td><td colspan="3">superheated, described by the ideal gas law</td></tr>
<tr><td rowspan="2">free interface</td><td>vapor temperature</td><td colspan="2">saturation temperature</td></tr>
<tr><td rowspan="2">liquid film thickness</td><td colspan="2" rowspan="2">uniform and invariable with time</td><td>uniform, varies individually with time</td></tr>
<tr><td>contact line dynamics</td><td>dry areas not included</td><td>follows evaporation rate of liquid film</td><td>conforms to dewetting phenomenon</td></tr>
</table>

Table 7: Major features and differences of selected one-dimensional PHP models.

Chapter 6

Extension to multi-branch PHPs

This chapter proposes an extension of OFT model to simulations of multi-branch PHPs. Since the numerical models for the other components, such as vapor bubbles, liquid plugs, thermal coupling with solid tubes, and heat conduction in tube walls, have been well established, the chapter presents only the module of liquid films that supersedes FEC model used in CASCO (Nikolayev, 2011a, Nekrashevych et al., 2017 and Nikolayev et al., 2018a). This extension inherits the general numerical implementation and data structure from CASCO code. The salient difference from simulations of single-branch PHPs is the management of multiple films and dry patches in vapor bubbles.

Several main assumptions concerning OFT model for multi-branch PHPs are summarized below:

1. Two-phase flow in the fluid channel stays in the plug-slug region (no dispersed flow). Vapor bubbles containing liquid films are tube size, separated from liquid plugs by the tube cross-section size menisci.

2. Liquid films are spatially uniform, but the thickness varies with time individually.

3. Liquid (in films and plugs) is assumed incompressible and of constant density.

4. Vapor can be at the superheated state (in which vapor obeys the ideal gas law), or at saturation (in which vapor is characterized by saturation pressure p_{sat}).

6.1 General configuration

One-dimensional modeling of multi-branch PHPs usually unrolls the meandering fluid channel and projects the channel onto a straight line. The periodic boundary conditions are applied from a starting point. Fig. 51(a) illustrates a 8-branch PHP that chooses the starting point $x = 0$ at the boundary of the first evaporator. The evaporator, adiabatic section, and condenser are projected on the x-axis as periodic sequences of the corresponding domains, see Fig. 51(b). The number of these sequences is equal to the number of U-turns in the evaporator N_{p}, which is a main geometrical parameter of multi-branch PHPs. The length of a periodic sequence in x-axis $L_{\text{p}} = L_{\text{e}} + 2L_{\text{a}} + L_{\text{c}}$. Therefore, the total length of the fluid

channel is $L_t = N_p L_p + L_{fb}$, where L_{fb} represents the length of the feedback section in the condenser. Gravitational force can also be applied along the x-axis.

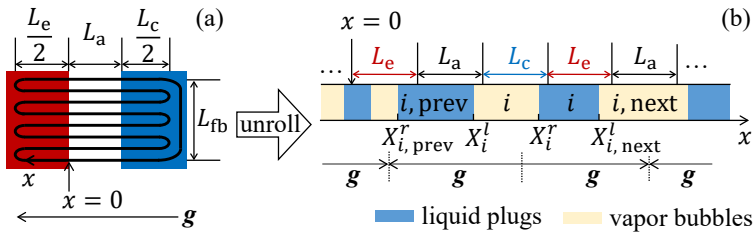

Figure 51: Unrolling a multi-branch PHP ($N_p = 4$) from a starting point $x = 0$ and projecting the meandering fluid channel onto x-axis with periodic boundary conditions.

The vapor bubble and the liquid plug on the right-hand side of the bubble are denoted by the same index $i = 0, ..., M-1$. The total number of bubble-plug pairs, M, varies in time because of bubble and plug coalescence. Nucleation in liquid plugs generates new bubbles. Vapor bubbles are bounded by two menisci represented by the 2D cross-section of fluid channels. For the bubble i, its left and right menisci situate at X_i^l and X_i^r, respectively. Notice that X_i^r also represents the left-hand boundary of the plug i, whose right-hand boundary is $X_{i,\text{next}}^l$, where $X_{i,\text{next}}^l = X_{i+1}^l$, except $i = M-1$, for which $X_{i,\text{next}}^l = X_0^l + L_t$.

6.1.1 *Numbering system of liquid films*

At the time moment t, within the bubble i, the number of dry patches (that are called "**holes**" of liquid film, for brevity) on the tube wall is denoted by $N_{h,i}$. Dry holes of zero length can also be created within a film wherever the film rupture condition is satisfied. The rupture condition creates new dry holes on continuous liquid films; an example is shown in Fig. 52: the hole $j+1$. Therefore, $N_{h,i}$ is the total number of dry holes and rupture points on films in the bubble i. Positions of two edges of the hole j (two triple contact lines) are denoted as $X_{h,i}^{l,j}$ and $X_{h,i}^{r,j}$, respectively. Here, the index $j = 1, ..., N_{hv,i}$, where

$$N_{hv,i} = \begin{cases} N_{h,i}, & \text{if } N_{h,i} \geq 1, \\ 1, & \text{if } N_{h,i} = 0. \end{cases} \tag{6.1}$$

The number of contact lines is $2N_{hv,i}$. The second line of Eq. 6.1 reflects the case when the bubble i is wrapped completely by a film ($N_{h,i} = 0$), a virtual hole of zero length is assigned at the right meniscus X_i^r, and $N_{hv,i} = 1$. The quantity $N_{hv,i}$ is introduced in CASCO out of programming consideration: $N_{hv,i} \geq 1$ can avert the frequent allocation and reallocation of vectors for $X_{h,i}^{l,j}$ and $X_{h,i}^{r,j}$ in algorithm.

From such a definition, the following inequalities always hold:

$$X_i^l \leq X_{h,i}^{l,1} \leq X_{h,i}^{r,1} \leq \cdots \leq X_{h,i}^{l,N_{hv,i}} \leq X_{h,i}^{r,N_{hv,i}} \leq X_i^r.$$

Their satisfaction is enforced in CASCO.

Liquid **films** (index n) are given the index of the dry hole on the right-hand of it. The rightmost film is always attached to a plug (which can be of zero length). Therefore, $n = 1, ..., N_{f,i}$; $N_{f,i} \equiv N_{hv,i} + 1$ is the total number of liquid films in the bubble i. Accordingly, the length of film n is determined as

$$L_{f,i}^n = \begin{cases} X_{h,i}^{l,n} - X_i^l, & \text{if } n = 1, \\ X_i^r - X_{h,i}^{r,n-1}, & \text{if } n = N_{f,i}, \\ X_{h,i}^{l,n} - X_{h,i}^{r,n-1}, & \text{otherwise}. \end{cases} \tag{6.2}$$

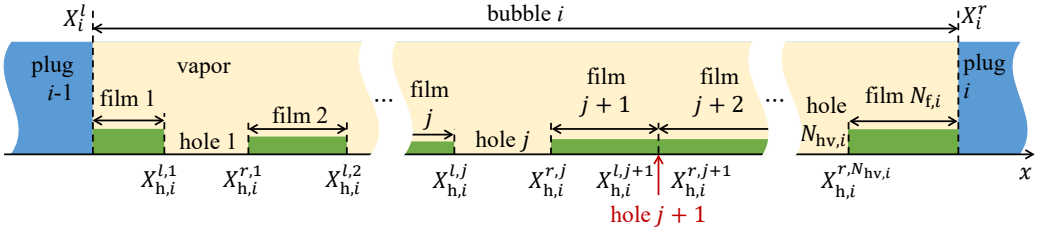

Figure 52: Numbering system for liquid films and dry holes in the bubble i; the hole $j+1$ is of zero length.

Fig. 53 draws two particular scenarios worth examining. (a) a continuous film wraps the bubble without dry holes. A hole of zero length is assigned at $X_{\mathrm{h},i}^{l,1} = X_{\mathrm{h},i}^{r,1} = X_i^r$. In this case, $N_{\mathrm{h},i} = 0$, $N_{\mathrm{hv},i} = 1$ and $N_{\mathrm{f},i} = 2$. Film 2 of zero length is attached to the left meniscus. According to Eq. 6.2, $L_{\mathrm{f},i}^1 = X_{\mathrm{h},i}^{l,1} - X_i^l$, and $L_{\mathrm{f},i}^2 = 0$. Notice that Fig. 53a could also represent the scenario where a film rupture occurs at X_i^r. where $N_{\mathrm{h},i} = N_{\mathrm{hv},i} = 1$, and $N_{\mathrm{f},i} = 2$. (b) liquid dries out completely in the bubble: $N_{\mathrm{h},i} = N_{\mathrm{hv},i} = 1$, and $N_{\mathrm{f},i} = 2$; $X_i^l = X_{\mathrm{h},i}^{l,1}$ and $X_{\mathrm{h},i}^{r,1} = X_i^r$. Eq. 6.2 gives two films of zero length.

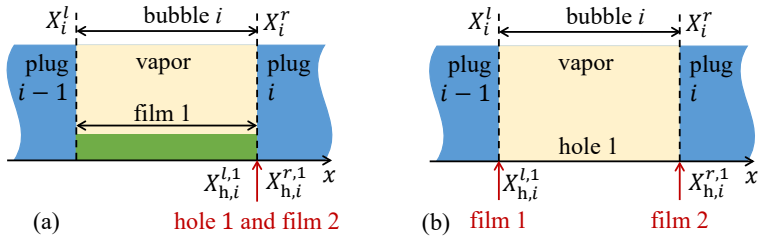

Figure 53: Two special scenarios that may encounter in calculations.

6.2 Liquid films

6.2.1 *Effective film thickness*

Take the example of the liquid film n in the bubble i. OFT model characterizes this film using the liquid mass $m_{\mathrm{f},i}^n$ and length $L_{\mathrm{f},i}^n$. The effective thickness δ_i^n is deduced from the equation,

$$m_{\mathrm{f},i}^n = \pi \delta_{\mathrm{f},i}^n (2R - \delta_{\mathrm{f},i}^n) L_{\mathrm{f},i}^n \rho, \tag{6.3}$$

which yields

$$\delta_i^n = \begin{cases} 0, & \text{if } m_{\mathrm{f},i}^n = 0, \\ R - \sqrt{R^2 - \dfrac{m_{\mathrm{f},i}^n}{\pi \rho L_{\mathrm{f},i}^n}}, & \text{otherwise.} \end{cases} \tag{6.4}$$

where R is the inner radius of the tube. Variations in $m_{\mathrm{f},i}^n$ and length $L_{\mathrm{f},i}^n$ lead to the variation in δ_i^n with time. The effective thickness reflects the average film thickness value that varies in real fluid channels.

6.2.2 *Length variation*

Length variation of liquid films obeys the same mechanism in Eq. 5.11, which results from displacement of two boundaries, i. e. menisci or free contact lines. The plug momentum equation determines the displacement of menisci, cf. Eq. 6.31 and Eq. 6.30. The description of receding contact lines is based on the dewetting phenomenon at evaporation (Chap. 3).

6.2.2.1 *Contact line dynamics*

Consider the left edge of the hole j in the bubble i, whose velocity $\dot{X}^{l,j}_{\mathrm{h},i}$ is

$$\dot{X}^{l,j}_{\mathrm{h},i} = \begin{cases} \dot{X}^l_i, & \text{if } j = 1 \ \& \ \mathcal{C}^{l,j}_{1,i}, \\ \dot{X}^r_i, & \text{if } j = N_{\mathrm{hv},i} \ \& \ \mathcal{C}^{l,j}_{2,i} \\ -u_\mathrm{d}\left[\Delta T(X^{l,j}_{\mathrm{h},i})\right], & \text{otherwise,} \end{cases} \tag{6.5}$$

where the clauses (i. e. conditions) are

$$\mathcal{C}^{l,j}_{1,i} = X^{l,1}_{\mathrm{h},i} \leq X^l_i \quad \text{and} \quad \dot{X}^l_i \geq -\epsilon u_\mathrm{d}\left[\Delta T(X^l_i)\right], \tag{6.6a}$$

$$\mathcal{C}^{l,j}_{2,i} = X^{l,N_{\mathrm{hv},i}}_{\mathrm{h},i} \geq X^r_i \quad \text{and} \quad \dot{X}^r_i \leq -u_\mathrm{d}\left[\Delta T(X^r_i)\right], \tag{6.6b}$$

where $\Delta T(x) = T_\mathrm{w}(x) - T_{\mathrm{sat},i}$ is the local superheating condition at x, and $T_{\mathrm{sat},i}$ is the saturation temperature corresponding to the vapor pressure in the bubble i. The quantity $u_\mathrm{d} \geq 0$ is the dewetting speed of contact lines, which has been studied in Chap. 3, and has been successfully employed in simulations of single branch PHPs in Chap. 5. Originally, u_d is a function of ΔT and the microscopic contact angle θ_{micro}. The value of θ_{micro} is imposed constant for a given fluid and a solid surface. Therefore, the second argument of u_d is omitted in the above equations. Note that for $\Delta T \geq 0$, $u_\mathrm{d}(\Delta T)$ is an increasing function, i. e. evaporation accelerates the dewetting. For $\Delta T < 0$, $u_\mathrm{d}(\Delta T) = u_\mathrm{d}(0)$.

The quantity ϵ reflects the wetting transition. A liquid film starts to be deposited after the meniscus speed exceeds a threshold ϵu_d with $\epsilon > 1$. Once the film begins to be deposited, the contact line speed suddenly drops to u_d. In the present model, $\epsilon = 2$ in agreement with the model validation for the single branch PHPs in the previous chapter.

The clauses in Eq. 6.5 are tested consecutively starting from Eq. 6.6a: the clause Eq. 6.6b is tested if Eq. 6.6a is invalid, and the 3rd option is employed if the first two are both invalid.

The clause (6.6a) corresponds to the absence of the leftmost film (see Fig. 54), i. e. the hole edge $X^{l,1}_{\mathrm{h},i}$ coincides with the left meniscus of the bubble i: $X^{l,1}_{\mathrm{h},i} = X^l_i$ (the sign $\leq$ manages a possible overlap that may appear because of the finite time step). The contact line having the velocity of the left meniscus indicates two possible evolutions: (i) the left meniscus advances to the right $\dot{X}^l_i > 0$; (ii) the left meniscus recedes at speed below the threshold speed $\epsilon u_\mathrm{d}\left[\Delta T(X^l_i)\right]$ for liquid deposition. In both evolution, $X^{l,1}_{\mathrm{h},i}$ moves together with X^l_i.

The clause (6.6b) indicates that the left edge of the rightmost dry hole coincides with the right meniscus of bubble i: $X^{l,N_{\mathrm{hv},i}}_{\mathrm{h},i} = X^r_i$. This condition implies that the length of the hole $N_{\mathrm{hv},i}$ is zero: $X^{l,N_{\mathrm{hv},i}}_{\mathrm{hv},i} = X^{r,1}_{\mathrm{hv},i}$. According to the numbering system, the film $N_{\mathrm{hv},i} + 1$ of zero length situates at the right of the dry hole $N_{\mathrm{hv},i}$, whose edges collapse at $x = X^r_i$, see Fig. 55(ii). This situation persists as long as the right meniscus advances faster than the contact line could recede: $\dot{X}^r_i \leq -u_\mathrm{d}\left[\Delta T(X^r_i)\right]$.

The 3rd option of Eq. 6.5 reflects the receding of free contact lines.

Similar equations are written for the right edges of dry holes,

$$\dot{X}^{r,j}_{\mathrm{h},i} = \begin{cases} \dot{X}^r_i, & \text{if } j = N_{\mathrm{hv},i} \ \& \ \mathcal{C}^{r,j}_{1,i}, \\ \dot{X}^l_i, & \text{if } j = 1 \ \& \ \mathcal{C}^{r,j}_{2,i} \\ u_\mathrm{d}\left[\Delta T(X^{r,j}_{\mathrm{h},i})\right], & \text{otherwise,} \end{cases} \tag{6.7}$$

where the clauses are

$$\mathcal{C}^r_{1,i} = X^{r,j}_{\mathrm{h},i} \geq X^r_i \text{ and } \dot{X}^r_i \leq \epsilon u_\mathrm{d} \left[\Delta T(X^r_i)\right], \tag{6.8a}$$

$$\mathcal{C}^r_{2,i} = X^{r,j}_{\mathrm{h},i} \leq X^l_i \text{ and } \dot{X}^l_i \geq u_\mathrm{d} \left[\Delta T(X^l_i)\right]. \tag{6.8b}$$

Eq. 6.5 and Eq. 6.7 state that when contact lines do not move with menisci, they can only recede towards the liquid film side, and dry holes can only expend.

6.2.3 *Mass variation*

Liquid film mass variation consists of two parts, the exchange with plugs and the phase change with vapor.

6.2.3.1 *Phase change*

According to the assumption that the interface has the saturation temperature, the phase change rate (evaporation and condensation) of liquid film n in the bubble i, $J^n_{\mathrm{f},i}$ is an integration over the film length given by Eq. 6.2, similar to Eq. 1.43,

$$J^n_{\mathrm{f},i} = \frac{2\pi U^n_i r^n_i}{\mathcal{L}} \begin{cases} \int\limits_{X^l_i}^{X^{l,n}_{\mathrm{h},i}} [T_\mathrm{w}(x) - T_{\mathrm{sat},i}]\mathrm{d}x, & \text{if } n = 1 \\ \int\limits_{X^{r,n-1}_{\mathrm{h},i}}^{X^{l,n}_{\mathrm{h},i}} [T_\mathrm{w}(x) - T_{\mathrm{sat},i}]\mathrm{d}x, & \text{if } 1 < n \leq N_{\mathrm{f},i} - 1 \\ \int\limits_{X^{r,n-1}_{\mathrm{h},i}}^{X^r_i} [T_\mathrm{w}(x) - T_{\mathrm{sat},i}]\mathrm{d}x, & \text{if } n = N_{\mathrm{f},i} \end{cases} \tag{6.9}$$

where $T_{\mathrm{sat},i} = T_\mathrm{sat}(p_i)$; $r^n_i = R - \delta^n_i$, and $U^n_i = \varsigma k/\delta^n_i$, where $\varsigma \gtrsim 1$ is the correction of interface shape, discussed in Subsec. 5.4.3.

The mass exchange rates at contact lines (two ends of holes) are calculated using the heat transfer rate Q, which is a function of local superheating, cf. Eq. 5.23. We denote the mass flux of two ends of the dry hole j as $J^{\xi,j}_{\mathrm{h},i}$, where $\xi \in \{l, r\}$ indicates the left and right ends, respectively,

$$J^{\xi,j}_{\mathrm{h},i} = \begin{cases} \dfrac{2\pi R}{\mathcal{L}} Q\left[\Delta T(X^{\xi,j}_{\mathrm{h},i})\right], & \text{if } X^{l,j}_{\mathrm{h},i} \neq X^{r,j}_{\mathrm{h},i} \\ 0. & \text{otherwise} \end{cases} \tag{6.10}$$

6.2.3.2 *Liquid collection and deposition by liquid plugs*

Liquid could be deposited to and collected from films by moving menisci. These two process are collectively denoted as $\dot{m}^\xi_{\mathrm{dep},i}$, where $\xi \in \{l, r\}$. Here, $\dot{m}^\xi_{\mathrm{dep},i}$ can be regarded as the mass exchange rate between menisci and films, positive for films obtaining liquid (deposition from menisci), and negative for films losing liquid (collection by menisci).

We start from the left meniscus of the bubble i. $\dot{m}^l_{\mathrm{dep},i}$ is calculated as

$$\dot{m}^l_{\mathrm{dep},i} = -\rho S^l_{\mathrm{f},i} \dot{X}^l_i, \tag{6.11}$$

where

$$S^l_{\mathrm{f},i} = \begin{cases} 0 & \text{if } \mathcal{A}^l_i, \\ S^1_{\mathrm{f},i} & \text{if } X^l_i < X^{l,1}_{\mathrm{h},i} \;\&\; \dot{X}^l_i > 0, \\ S^2_{\mathrm{f},i} & \text{if } \mathcal{C}^{r,1}_{2,i}, \\ S^l_{\mathrm{dep},i} & \text{otherwise} \end{cases} \tag{6.12}$$

is the cross-section of liquid film that exchanges liquid with the plug. Similar to Eq. 5.15, the above expression reflects three scenarios: no mass exchange between the film and the left meniscus (the clause $\mathcal{A}^l_i$ is true), liquid collection (the second and 3rd clauses) and liquid deposition (the last clause). Fig. 54 demonstrates all possible position configurations of the left meniscus. For each configuration, the velocity conditions determine how the mass is exchanged, as listed in the tables next to the illustrations.

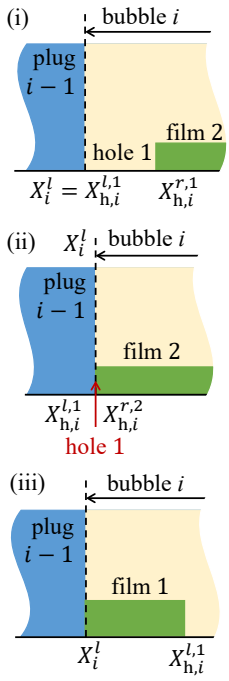

velocity \ position	$\mathcal{D}^l_i$
$\dot{X}^l_i \geq -\epsilon u_{\mathrm{d}}[\Delta T(X^l_i)]$	**(a)** $\dot{m}^l_{\mathrm{dep},i} = 0$
$\dot{X}^l_i < -\epsilon u_{\mathrm{d}}[\Delta T(X^l_i)]$	**(e)** deposition

velocity \ position	$X^l_i \geq X^{r,1}_{\mathrm{h},i}$
$-\epsilon u_{\mathrm{d}}[\Delta T(X^l_i)] \leq \dot{X}^l_i \leq u_{\mathrm{d}}[\Delta T(X^l_i)]$	**(b)** $\dot{m}^l_{\mathrm{dep},i} = 0$
$\dot{X}^l_i > u_{\mathrm{d}}[\Delta T(X^l_i)]$	**(c)** collection
$\dot{X}^l_i < -\epsilon u_{\mathrm{d}}[\Delta T(X^l_i)]$	**(f)** deposition

velocity \ position	$X^l_i < X^{l,1}_{\mathrm{h},i}$
$\dot{X}^l_i > 0$	**(d)** collection
$\dot{X}^l_i \leq 0$	**(g)** deposition

Figure 54: Configurations of the left meniscus and the corresponding velocity conditions: (i) the first dry hole is of non-zero length, (ii) absence of the first film and the dry hole, (iii) the first film of non-zero length.

The configuration (i) corresponds to the leftmost dry hole of non-zero length adjacent to the left meniscus, which corresponds to the clause $\mathcal{D}^l_i$. $\mathcal{D}^\xi_i$ is true when no film is attached to the meniscus ξ,

$$\begin{aligned} \mathcal{D}^l_i &= N_{\mathrm{h},i} > 0 \,\&\, X^l_i \geq X^{l,1}_{\mathrm{h},i} \;\&\; X^{r,1}_{\mathrm{h},i} > X^l_i; \\ \mathcal{D}^r_i &= N_{\mathrm{h},i} > 0 \,\&\, X^r_i \leq X^{r,N_{\mathrm{hv},i}}_{\mathrm{h},i} \;\&\; X^r_i > X^{l,N_{\mathrm{hv},i}}_{\mathrm{h},i}. \end{aligned} \tag{6.13}$$

Two velocity conditions are given: **(a)** the left meniscus advances, or recedes at speed lower than the film deposition threshold, $\dot{X}^l_i \geq -\epsilon u_{\mathrm{d}}\left[\Delta T(X^l_i)\right]$, therefore, $S^l_{\mathrm{f},i} = 0$; In the opposite case **(e)** corresponding to $\dot{X}^l_i < -\epsilon u_{\mathrm{d}}\left[\Delta T(X^l_i)\right]$, a liquid film is about to be deposited, and $S^l_{\mathrm{f},i} = S^l_{\mathrm{dep},i}$. Note that the cross-section of the deposited film by the meniscus ξ is

$$S^\xi_{\mathrm{dep},i} = \pi[R^2 - (R - \delta^\xi_{\mathrm{dep},i})^2] = \pi\delta^\xi_{\mathrm{dep},i}(2R - \delta^\xi_{\mathrm{dep},i}), \tag{6.14}$$

where the deposited film thickness

$$\delta^{\xi}_{\text{dep},i} = \frac{1.34\, R(Ca^{\xi}_i)^{2/3}}{1 + 3.35\,(Ca^{\xi}_i)^{2/3}}, \tag{6.15}$$

is determined by the meniscus velocity (cf. Eq. 1.34) that appears in the capillary number $Ca^{\xi}_i = \mu|\dot{X}^{\xi}_i|/\sigma$. In the case **(e)**, $\dot{X}^l_i < 0$ and $\dot{m}^l_{\text{dep},i}$ is positive as given by Eq. 6.11.

Configuration (ii) occurs when the second film is attached to the left meniscus, i.e. $X^l_i \geq X^{r,1}_{\text{h},i}$ holds. Three velocity conditions can occur. Case **(b)**: while instantly touching the contact line $X^{r,1}_{\text{h},i}$, the left meniscus advances slower than $X^{r,1}_{\text{h},i}$ could recede, or the left meniscus recedes slower than the liquid deposition threshold ϵu_{d}. The first dry hole will expand at the next time step and $S^l_{\text{f},i} = 0$. Case **(c)**: the left meniscus collects liquid from the second film when the meniscus overruns the contact line: $\dot{X}^l_i > u_{\text{d}}\left[\Delta T(X^l_i)\right]$, therefore, $S^l_{\text{f},i} = S^2_{\text{f},i}$. This is equivalent to $\mathcal{C}^{r,1}_{2,i}$, cf. Eq. 6.8b. Case **(f)**: the receding left meniscus deposits liquid to the first film: $\dot{X}^l_i < -\epsilon u_{\text{d}}\left[\Delta T(X^l_i)\right]$, and $S^l_{\text{f},i} = S^l_{\text{dep},i}$.

Configuration (iii) indicates that the first liquid film is of non-zero length, i.e. $X^l_i < X^{l,1}_{\text{h},i}$ holds. Two velocity-based cases exist. Either the left meniscus collects liquid while advancing (case **(d)**), which results in $S^l_{\text{f},i} = S^1_{\text{f},i}$, or it keeps depositing the film (case **(g)**), and $S^l_{\text{f},i} = S^l_{\text{dep},i}$.

Therefore, the clause $\mathcal{A}^l_i$ of Eq. 6.12 combining the cases **(a)** and **(b)** reads

$$\begin{aligned}\mathcal{A}^l_i =& \{\mathcal{D}^l_i \;\&\; \dot{X}^l_i \geq -\epsilon u_{\text{d}}\left[\Delta T(X^l_i)\right]\} \\ &\vee \{X^l_i \geq X^{r,1}_{\text{h},i} \;\&\; -\epsilon u_{\text{d}}\left[\Delta T(X^l_i)\right] \leq \dot{X}^l_i \leq u_{\text{d}}\left[\Delta T(X^l_i)\right]\},\end{aligned} \tag{6.16}$$

which can be rearranged as,

$$\mathcal{A}^l_i = \{\dot{X}^l_i \geq -\epsilon u_{\text{d}}\left[\Delta T(X^l_i)\right]\}\&\{\mathcal{D}^l_i \vee \{X^l_i \geq X^{r,1}_{\text{h},i} \;\&\; \dot{X}^l_i \leq u_{\text{d}}\left[\Delta T(X^l_i)\right]\}\}. \tag{6.17}$$

A similar equation is written for the right meniscus of the bubble i. $\dot{m}^r_{\text{dep},i}$ is calculated as

$$\dot{m}^r_{\text{dep},i} = \rho S^r_{\text{f},i}\dot{X}^r_i, \tag{6.18}$$

where $S^r_{\text{f},i} \geqslant 0$ is the liquid film cross-section area that is determined as

$$S^r_{\text{f},i} = \begin{cases} 0 & \text{if } \mathcal{A}^r_i, \\ S^{N_{\text{f},i}}_{\text{f},i} & \text{if } X^{r,N_{\text{hv},i}}_{\text{h},i} < X^r_i \;\&\; \dot{X}^r_i < 0, \\ S^{N_{\text{hv},i}}_{\text{f},i} & \text{if } \mathcal{C}^{l,N_{\text{hv},i}}_{2,i}, \\ S^r_{\text{dep},i} & \text{otherwise.} \end{cases} \tag{6.19}$$

Here, the clause $\mathcal{A}^r_i$ signifies the absence of liquid deposition or collection, which can only occur when the last film is also absent, see Fig. 55: **(a)** the hole $N_{\text{hv},i}$ is non-zero; **(b)** the hole $N_{\text{hv},i}$ is zero.

$$\begin{aligned}\mathcal{A}^r_i =& \{\mathcal{D}^r_i \;\&\; \dot{X}^r_i \leq \epsilon u_{\text{d}}\left[\Delta T(X^r_i)\right]\} \\ &\vee \{X^{l,N_{\text{hv},i}}_{\text{h},i} \geq X^r_i \;\&\; -u_{\text{d}}\left[\Delta T(X^r_i)\right] \leq \dot{X}^r_i \leq \epsilon u_{\text{d}}\left[\Delta T(X^r_i)\right]\},\end{aligned} \tag{6.20}$$

where $\mathcal{D}^r_i$ is defined in Eq. 6.13. It can be rearranged as:

$$\mathcal{A}^r_i = \{\dot{X}^r_i \leq \epsilon u_{\text{d}}\left[\Delta T(X^r_i)\right]\} \;\&\; \{\mathcal{D}^r_i \vee \{X^{l,N_{\text{hv},i}}_{\text{h},i} \geq X^r_i \;\&\; -u_{\text{d}}\left[\Delta T(X^r_i)\right] \leq \dot{X}^r_i\}\}, \tag{6.21}$$

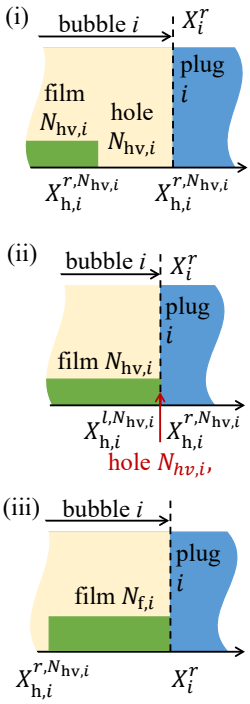

velocity \ position	$\mathcal{D}_i^r$
$\dot{X}_i^r \le \epsilon u_{\mathrm{d}}[\Delta T(X_i^r)]$	**(a)** $\dot{m}_{\mathrm{dep},i}^r = 0$
$\dot{X}_i^r > \epsilon u_{\mathrm{d}}[\Delta T(X_i^r)]$	**(e)** deposition

velocity \ position	$X_{\mathrm{h},i}^{l,N_{\mathrm{hv},i}} \ge X_i^r$
$-u_{\mathrm{d}}[\Delta T(X_i^r)] \le \dot{X}_i^r \le \epsilon u_{\mathrm{d}}[\Delta T(X_i^r)]$	**(b)** $\dot{m}_{\mathrm{dep},i}^r = 0$
$\dot{X}_i^r < -u_{\mathrm{d}}[\Delta T(X_i^r)]$	**(c)** collection
$\dot{X}_i^r > \epsilon u_{\mathrm{d}}[\Delta T(X_i^r)]$	**(f)** deposition

velocity \ position	$X_{\mathrm{h},i}^{r,N_{\mathrm{hv},i}} < X_i^r$
$\dot{X}_i^r < 0$	**(d)** collection
$\dot{X}_i^r \ge 0$	**(g)** deposition

Figure 55: Configuration of the right meniscus and corresponding velocity conditions: (i) absence of the last film; the hole $N_{\mathrm{hv},i}$ is of non-zero length, (ii) absence of the last film and hole, (iii) the last film of non-zero length.

The second and third options in Eq. 6.19 signify the liquid collection from the last film **(d)**, or the second last film **(c)**, when the last is of zero length and the second last is attached to the right meniscus, which is equivalent to $\mathcal{C}_{2,i}^{l,N_{\mathrm{hv},i}}$ defined in Eq. 6.6b. The last option of Eq. 6.19 covers the cases **(e)**, **(f)** and **(g)** in Fig. 55, where the film deposition takes place.

6.2.3.3 *Film mass variation*

The liquid deposition rates by plugs, $\dot{m}_{\mathrm{dep},i}^l$ and $\dot{m}_{\mathrm{dep},i}^r$, are assigned to the corresponding liquid films. For $N_{\mathrm{h},i} = 0$,

$$\dot{m}_{\mathrm{f},i}^n = -J_{\mathrm{f},i}^n + \dot{m}_{\mathrm{dep},i}^l + \dot{m}_{\mathrm{dep},i}^r. \tag{6.22}$$

where $J_{\mathrm{f},i}^n$ is the film evaporation rate calculated with Eq. 6.9, and $\dot{m}_{\mathrm{dep},i}^\xi$ is the film deposition rate by the ξ-th meniscus; $\dot{m}_{\mathrm{dep},i}^\xi > 0$ when the film mass grows.

For $N_{\mathrm{h},i} \neq 0$, there are at least 2 liquid films in the bubble. The mass variation rate of the film n is

$$\begin{aligned}\dot{m}_{\mathrm{f},i}^n = -J_{\mathrm{f},i}^n - &\left\{\begin{array}{ll} 0, & \text{if } \{L_{\mathrm{f},i}^n = 0\} \vee \{n = N_{\mathrm{f},i}\} \\ J_{\mathrm{h},i}^{l,n} & \text{otherwise} \end{array}\right\} - \left\{\begin{array}{ll} 0 & \text{if } \{L_{\mathrm{f},i}^n = 0\} \vee \{n = 1\} \\ J_{\mathrm{h},i}^{r,n-1}, & \text{otherwise} \end{array}\right\} + \\ &\left\{\begin{array}{ll} \dot{m}_{\mathrm{dep},i}^l, & \text{if } \{n = 1 \,\&\, \bar{\mathcal{C}}_{2,i}^{r,1}\} \vee \{n = 2 \,\&\, \mathcal{C}_{2,i}^{r,1}\} \\ 0 & \text{otherwise} \end{array}\right\} + \\ &\left\{\begin{array}{ll} \dot{m}_{\mathrm{dep},i}^r, & \text{if } \{n = N_{\mathrm{f},i} \,\&\, \bar{\mathcal{C}}_{2,i}^{l,N_{\mathrm{hv},i}}\} \vee \{n = N_{\mathrm{hv},i} \,\&\, \mathcal{C}_{2,i}^{l,N_{\mathrm{hv},i}}\} \\ 0 & \text{otherwise} \end{array}\right\}.\end{aligned} \tag{6.23}$$

On the right-hand side, the first term represents liquid evaporation from the flat film part, which is calculated by Eq. 6.9. The second term is the mass flux of the right end of the film n (the left edge of the dry hole n), which is calculated with Eq. 6.10. This term is zero for liquid films of zero length and for the rightmost film $n = N_{\mathrm{f},i}$, which is attached to the right meniscus. When the film $n = 1$ is of zero length and $J_{\mathrm{h},i}^{l,1}$ should be subtracted from the left meniscus, cf. Eq. 6.28. Correspondingly, the third term is the mass flux of the left end of the film n (the right edge of the dry hole $n-1$), which is calculated with Eq. 6.10. This term is zero for the leftmost film $n = 1$, and for the first film $n = N_{\mathrm{f},i}$ if its length is zero and no liquid is deposited. The second scenario indicates that the film $n = N_{\mathrm{f},i}$ would remain of zero length and $J_{\mathrm{h},i}^{r,N_{\mathrm{hv},i}}$ should be subtracted from the right meniscus, cf. Eq. 6.27. The 4th term indicates that $\dot{m}_{\mathrm{dep},i}^{l}$ is assigned to the first film when the case **(c)** in Fig. 54 is excluded, or to the second film, then the clause $\mathcal{C}_{2,i}^{r,1}$ is satisfied. Similarly, $\dot{m}_{\mathrm{dep},i}^{r}$ is added to the last ($N_{\mathrm{f},i}$-th) film in all the cases except **(c)** in Fig. 55 or to the second last (number $N_{\mathrm{hv},i} = N_{\mathrm{f},i} - 1$) in the case **(c)**. The rest of the liquid films do not exchange mass with menisci.

6.2.4 *Meniscus velocity*

In simulations of single branch PHPs, Eq. 5.12 assumes that two menisci of a liquid plug move at the same speed with the center of mass of the plug. This is a reasonable approximation considering the small amount of collected or deposited liquid compared to the liquid in plugs. However, in multi-branch PHPs, liquid plugs can be short that depositing liquid causes a noticeable further shortening in length and two menisci gathering towards each other. This indicates a difference in velocity between the two menisci and the center of mass. More importantly, the mass balance of liquid plugs is essential for conserving the total mass in multi-branch PHP systems. $m_{\mathrm{dep},i}$ should be addressed.

Taking the example of the liquid plug i, the liquid mass of this plug is calculated as,

$$m_{\mathrm{l},i} = \rho S(X_{i,\mathrm{next}}^{l} - X_{i}^{r}). \tag{6.24}$$

where $\dot{X}_{i}^{r}$ and $\dot{X}_{i,\mathrm{next}}^{l}$ are the left and right boundaries, respectively, see Fig. 51. The velocity of the center of mass V_i satisfies:

$$V_i = \frac{1}{2}(\dot{X}_{i}^{r} + \dot{X}_{i,\mathrm{next}}^{l}), \tag{6.25}$$

where the momentum equation determines V_i.

Since the liquid is assumed constant in density, the variation in $m_{\mathrm{l},i}$ leads to a non-zero relative displacement between the center of mass and the boundaries. Two processes can cause a change in $m_{\mathrm{l},i}$: (i) phase change at menisci and (ii) mass exchange with films (liquid deposition or conversely collection), which yields the following mass balance of the plug i:

$$\dot{m}_{\mathrm{l},i} = -J_{\mathrm{m},i}^{r} - J_{\mathrm{m},i,\mathrm{next}}^{l} - \dot{m}_{\mathrm{dep},i}, \tag{6.26}$$

where the first two terms are the amount of liquid evaporation at menisci that are not subtracted from liquid films in Eq. 6.23. They are determined as,

$$J_{\mathrm{m},i}^{r} = \begin{cases} J_{\mathrm{h},i}^{r,N_{\mathrm{hv},i}} & \text{if } L_{\mathrm{f},i}^{N_{\mathrm{f},i}} = 0 \\ 0 & \text{otherwise} \end{cases} \tag{6.27}$$

and

$$J_{\mathrm{m},i,\mathrm{next}}^{l} = \begin{cases} J_{h,i,\mathrm{next}}^{l,1}, & \text{if } L_{f,i,\mathrm{next}}^{1} = 0 \\ 0, & \text{otherwise} \end{cases} \tag{6.28}$$

The film deposition rate $\dot{m}_{\text{dep},i}$ the a sum of two meniscus contributions,

$$\dot{m}_{\text{dep},i} = \dot{m}^r_{\text{dep},i} + \dot{m}^l_{\text{dep},i,\,\text{next}} = \rho S^r_{\text{f},i}\dot{X}^r_i - \rho S^l_{\text{f},i,\,\text{next}}\dot{X}^l_{i,\text{next}}, \tag{6.29}$$

where Eq. 6.11 and Eq. 6.18 are employed.

The equations for $\dot{X}^r_i, \dot{X}^l_{i,\text{next}}$ are obtained from a set of two equations: Eq. 6.25 and differentiated Eq. 6.24 with substitution of Eq. 6.26 and Eq. 6.29. Its solution is

$$\dot{X}^r_i = \frac{\left(1 - \dfrac{S^l_{\text{f},i,\text{next}}}{S}\right) V_i + \dfrac{J^r_{\text{m},i} + J^l_{\text{m},i,\text{next}}}{2\rho S}}{1 - \dfrac{S^l_{\text{f},i,\text{next}} + S^r_{\text{f},i}}{2S}}, \tag{6.30}$$

and

$$\dot{X}^l_{i,\text{next}} = \frac{\left(1 - \dfrac{S^r_{\text{f},i}}{S}\right) V_i - \dfrac{J^r_{\text{m},i} + J^l_{\text{m},i,\text{next}}}{2\rho S}}{1 - \dfrac{S^l_{\text{f},i,\text{next}} + S^r_{\text{f},i}}{2S}}. \tag{6.31}$$

Velocities of the plug ends relative to the center of mass are thus non-zero and are defined by the change in plug volume.

6.3 Conclusions

This chapter presents an extended version of OFT model that is applicable for simulations of multi-branch PHPs. The extension employs the same method of modeling liquid films in Chap. 5, which reflects three physical processes, phase change, length variation, and mass exchange with plugs. The difficulty of extending the numerical model is managing the multiple liquid films and dry patches that appear in vapor bubbles. Compared to Chap. 5 where only a film and a meniscus exist in the system, multiple liquid films engender various situations that demand different calculation equations. Properly handling all the possibilities requires the extended model, including more conditional judgments; consequently, expressions are more complex.

In describing liquid films, the OFT model differs significantly from the FEC model in many aspects. Liquid films are characterized by two quantities (the length and mass) in the OFT model. In contrast, the FEC model only needs the length because of the constant thickness assumption that automatically gives the film mass once its length is determined. OFT model reflects the contact line receding using the dewetting phenomenon. Therefore OFT model precludes the necessity of introducing effective evaporators, which are used in FEC model to determine the rate of liquid film shortening. Moreover, the difference in velocity of plugs can be enormous in multi-branch PHPs. The thickness of deposited films, which depends on the plug receding speed, also differs greatly. The pre-determined constant δ FEC model is less justified in simulating multi-branch PHPs. Due to these disparities, replacing the current film model in CASCO with the new film model requires substantial changes to the code structure. Therefore, the numerical implementation is still in progress and, unfortunately, could not be accomplished before the end of my doctoral studies.

Conclusions

Recall our objectives that were set at the beginning of the thesis, to propose a new one-dimensional computational model of liquid films for the simulation of pulsating heat pipes. Even being one-dimensional, our new model reflects real physical processes in fluid channels of PHPs, better than existing numerical models. Naturally, a theoretical study of liquid film dynamics in capillary tubes is the starting point of the thesis.

Liquid film dynamics during meniscus oscillation was investigated first. Since contact lines generally move much slower than menisci and the large-scale behavior of liquid films is concerned, this study adopts a less complex scenario where the contact line is pinned on a surface defect, and the oscillation is harmonic. The system parameters include the initial contact angle (macroscopic), the period and amplitude of oscillation. A periodic solution of this problem has been identified. Our results show that the liquid film that is deposited by an oscillatory meniscus is non-uniform, because the thickness depends on the speed and curvature of the meniscus, which vary during oscillation. The average film thickness depends weakly on the initial contact angle, whereas it grows with the period and amplitude of oscillation. As the meniscus departs from the pinned contact line, the contact angle sharply drops to a small value of merely several degrees, regardless of the initial value, and hardly fluctuates until the end of the period when the meniscus draws back. During this time, because the interface ripples that were created by the advancing meniscus are compressed to the contact line, the contact angle oscillates strongly and attains a global minimum. The initial contact angle and the oscillation period have a low impact on this minimal contact angle. The velocity amplitude can augment this minimum, albeit its value remains small, of the order of several degrees. Finally, the problem of the combined effects of meniscus oscillation and tube heating is considered. The minimal contact angle during oscillation sets an upper bound for tube superheating. This upper bound is considerably low–of merely several mK, which is much smaller than typical superheating in experiments. This signifies that considering the receding of contact lines is essential for analyzing liquid film behavior in PHPs where meniscus oscillation and evaporation occur simultaneously.

Contact line receding has been studied in the case of liquid film dewetting at evaporation. To obtain more precise results, our theory includes several nanoscale effects that are known to have non-negligible impacts on describing physical phenomena near the microscopic scale of contact lines. The conventional lubrication theory is generalized to account for large interfacial slopes, over 30°, which are encountered in high superheating. Our theoretical description attributes the contact line receding phenomenon to spontaneous liquid evaporation in its close vicinity. The evaporation rate at the contact line is correlated with its speed. Our results demonstrate that forced evaporation not only accelerates contact line receding speed, but also induces dewetting. We generalize the asymptotic multiscale theory of dewetting, which was initially developed for adiabatic conditions, to evaporation cases. This results in a simple analytical expression for dewetting speed. The main parameters of this expression are the Voinov length and the Voinov angle (the interface slope formed in the microregion), through which the nanoscale effects impact the macroscale physics. While the Voinov angle

is relatively easy to compute (it requires only a solution of a stationary microregion model mastered by many research groups), the Voinov length requires a more sophisticated calculation. An approximate analytical formula for the Voinov length is proposed. The results of our generalized multiscale model agree with the numerical calculations. It is shown that the evaporative mass loss at contact lines does not lead to any additional acceleration of its motion, which is controlled entirely by capillarity and by the evaporation-driven modification of the Voinov angle. Apart from being used in PHP modeling, this simple expression is invaluable for a great number of applications that deal with the phase change phenomena of thin liquid films.

The above theory of liquid films is applied to explain the formation and evolution of microlayers beneath vapor bubbles in nucleate boiling. Comparison with experimental observations has evidenced that the creation of microlayers can be regarded as a result of liquid film deposition from the expanding bubble edge near solid surfaces. A local maximal thickness in the middle part of microlayers, which has been observed in the experiments, is ascribed to the interplay of two opposing forces: the deceleration of expansion that decreases the thickness, and the growing bubble radius, which tends to increase the thickness. Our theory predicts the position of this local maximum on solid substrates and is in good agreement with experimental data. Expansion of the dry patch under bubbles highly resembles the geometry of liquid film dewetting at evaporation. Theoretical prediction of contact-line receding speed conforms to experimental observations.

Developing a computational model of liquid films in PHPs is a trade-off between simplicity (efficiency) and result reliability. Our new liquid film model, the Oscillating Film Thickness OFT model, follows this principle. Though our model simplifies the vapor-liquid interface shape, it can truthfully reflect key features of liquid film evolution in fluid channels of PHPs. Thanks to the studies of dewetting at evaporation, OFT model expresses the receding speed of contact lines as a function of local superheating and wettability. Together with meniscus oscillation, receding contact lines determine the length variation of liquid films. The initial thickness of deposited films follows the quasi-steady equation, which depends on the instantaneous speed of receding menisci. Our theoretical study has verified that the quasi-steady equation can be an acceptable approximation even under oscillatory conditions. Simulation results of single branch PHPs have shown a good agreement with experimental data. An extension of the new film model to simulate multiple bubbles and films is proposed. This extension can be incorporated into CASCO code that can simulate PHPs of complex configurations: multi-branch and multiple evaporators and condensers.

Future Work

Replacing FEC model in CASCO with the new OFT model is still in process. Due to the significant differences in describing liquid film dynamics between the two models, numerous modifications will have to be made in CASCO, and code debugging and verification of results can take months. Considering the success of OFT model on single-branch PHP simulations, we are confident that the extension to multi-branch PHPs will yield good results.

In the study of oscillatory menisci, though curvature in the central part of a meniscus varies with time, the interface was considered here as spherical. This ignores inertial effects from liquid flows inside plugs that might originate from rapid changes in the flow direction and distort the spherical shape of the interface. Consequently, the liquid deposited from the meniscus should account for inertial effects.

The dewetting problem considered here is limited to the ideal scenario where the gaseous phase is the pure vapor of evaporating liquid. In reality, non-condensible (inert) gases always

exist. In an atmosphere of inert gases, liquid evaporation is controlled largely by the diffusion of vapor molecules from gas-liquid interfaces to the gas bulk. Natural or forced convection in the gaseous phase strongly impacts diffusion. However, for pure vapor cases, the physics in the gas domain can be neglected, and the phase change rate is determined completely by the heat transfer in liquid. Different mechanisms that control evaporation in two cases require a re-examination of the dewetting problem.

At the onset of liquid deposition, OFT model employs the wetting transition that was established under adiabatic conditions. However, evaporation is known to accelerate the dewetting process, suggesting that the transition criterion might also be altered. Ideally, the wetting transition criterion should depend on local superheating and wettabilities, similar to determining contact line receding speeds.

OFT model assumes an axially-symmetrical vapor-liquid interface, which is acceptable for circular capillary tubes. For most of Flat-Plate PHPs, the cross-section of fluid channels is rectangular, where liquid fingers develop at the corners and stretch out away from the almost-spherical bulk meniscus in the tube center. Similar to liquid films in round tubes, the liquid fingers have the potential to transfer a tremendous amount of energy via phase change. A numerical model for this type of PHP must reflect the unique liquid fingers. This calls for new efforts to quantify the differences from better-understood round tubes.

Part III

Appendices

Appendix A

Nanoscale effects

A.1 Kelvin effect

Kelvin effect provides the dependence of the local interface temperature T^{i} on the local interface curvature that is notable on the microscopic scale, where the interface can be strongly curved.

In the simplest situation, as demonstrated in Fig. 56a, a liquid-vapor system of a single substance is at saturation, and the global equilibrium is established. Since the interface is flat, the pressures in the two phases are equal to the saturation pressure $p_{\mathrm{sat}}(T^{\mathrm{i}})$, corresponding to the interface temperature T^{i}. Gibbs free energy in the two phases is expressed as,

$$\boldsymbol{u}_{\mathrm{v}} + \frac{p_{\mathrm{sat}}}{\rho_{\mathrm{v}}} - T^{\mathrm{i}}\mathscr{s}_{\mathrm{v}} = \boldsymbol{u} + \frac{p_{\mathrm{sat}}}{\rho} - T^{\mathrm{i}}\mathscr{s}, \tag{A.1}$$

where, $\boldsymbol{u}$ is the internal energy per unit mass; $\mathscr{s}$ is the specific entropy.

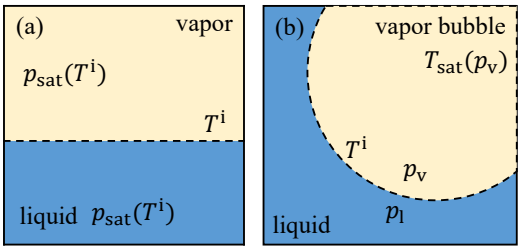

Figure 56: Liquid-vapor system of the same substance at thermodynamic equilibrium separated: (a) by a flat interface; (b) by a curved interface.

When the interface is not flat, (for instant Fig. 56b depicting a vapor bubble in liquid), a pressure difference (jump) across the interface exists: $\Delta p \equiv p_{\mathrm{v}} - p$, whose value can be predicted by the Laplace-Young equation (Ishii et al., 2006)

$$\Delta p = \sigma\kappa_{\mathrm{vl}} = -\sigma\kappa_{\mathrm{lv}}, \tag{A.2}$$

where κ_{vl} is the curvature taken from vapor to liquid phase, positive for the case in Fig. 56b; σ is the surface tension. The vapor is at saturation state, whose temperature corresponds to $T_{\mathrm{sat}}(p_{\mathrm{v}})$.

Because the curved interface changes the surface energy, the interface temperature T^{i} deviates away from the regular saturation state, where the interface is flat. To evaluate this impact on T^{i}, consider now the two-phase system in Fig. 56b, where a *local* equilibrium is achieved near the interface. Similar to Eq. A.1, the chemical potentials in Fig. 56b can be expressed as

$$\boldsymbol{u}_{\mathrm{v}} + \frac{p_{\mathrm{v}}}{\rho_{\mathrm{v}}} - T^{\mathrm{i}}\boldsymbol{s}_{\mathrm{v}} = \boldsymbol{u} + \frac{p}{\rho} - T^{\mathrm{i}}\boldsymbol{s}. \tag{A.3}$$

Subtracting Eq. A.1 from Eq. A.3 and using the pressure jump definition yields

$$p_{\mathrm{sat}} - p_{\mathrm{v}} = \Delta p \frac{\rho_{\mathrm{v}}}{\rho - \rho_{\mathrm{v}}}. \tag{A.4}$$

For pure vapor, small changes in saturation state satisfy the *Clausius–Clapeyron* equation (Landau et al., 1980)

$$\left.\frac{dp}{dT}\right|_{\mathrm{sat}} = \frac{\mathcal{L}\rho_{\mathrm{v}}\rho}{(\rho - \rho_{\mathrm{v}})T_{\mathrm{sat}}}. \tag{A.5}$$

Assuming $|p_{\mathrm{sat}} - p_{\mathrm{v}}| \ll p_{\mathrm{v}}$ in Eq. A.4, which is easily satisfied because of $\rho_{\mathrm{v}} \ll \rho$, one can make use of Eq. A.5 to approximate its value as,

$$p_{\mathrm{sat}} - p_{\mathrm{v}} = \frac{(T^{\mathrm{i}} - T_{\mathrm{sat}})\mathcal{L}\rho_{\mathrm{v}}\rho}{(\rho - \rho_{\mathrm{v}})T_{\mathrm{sat}}}. \tag{A.6}$$

Consequently equating Eq. A.4 and Eq. A.6, T^{i} variation due to the curved interface is expressed in Eq. 1.24.

If the bubble interface is a sphere of radius R, one obtains $\Delta p = 2\sigma/R$ and $T^{\mathrm{i}} > T_{\mathrm{sat}}$.

In the microscopic description of contact lines, we assume a homogeneous distribution of vapor pressure, p_{v}. However, the liquid pressure is allowed to vary near the interface, responding to its local curvature, which also causes a temperature variation.

A.2 Interfacial thermal resistance

Interfacial thermal resistance is observed when interfaces are out of thermodynamic equilibrium, and phase exchanges occur on them.

Consider the situation, where the liquid evaporates into the pure vapor of the same substance. Following Schrage's molecular-kinetic theory of evaporation (Carey, 1992; Schrage, 1953), the vapor is treated as the ideal gas, and the molecule speeds are predicted by the Maxwell-Boltzmann distribution. The mass flux traversing a plane in a given direction, for instance, the rate of molecules striking the container wall, is equal to

$$J = p_{\mathrm{v}}\sqrt{\frac{M}{2\pi R_{\mathrm{g}} T_{\mathrm{v}}}}. \tag{A.7}$$

Image a plane in the vapor phase, situating immediately above the interface, as shown in Fig. 57. The mass flux escaping the liquid phase is denoted by J_{e}; similarly, the mass flux that strikes the interface and becomes part of the liquid is denoted by J_{c}. The net mass flux across the imaginary plane is

$$J_{\mathrm{net}} = J_{\mathrm{e}} - J_{\mathrm{c}}. \tag{A.8}$$

When a thermodynamic equilibrium is established, for example in Fig. 57a, J_{e} is balanced by J_{c} and $J_{\mathrm{net}} = 0$.

If the balance is broken, as a result of phase changes, the vapor must have a bulk velocity u_{0z} in the z direction, cf. Fig. 57b. The value of u_{0z} is positive for evaporation. Using

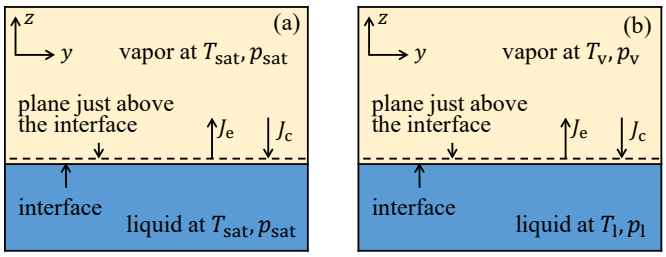

Figure 57: Mass exchanges between two phases at a liquid-vapor interface: (a) a saturation system in equilibrium, (b) a net mass transfer occurs.

Eq. A.7, one might approximate the mass flux through a plane in the vapor bulk, in and opposite to the z direction

$$J_{z+} = \Gamma(a) p_\mathrm{v} \sqrt{\frac{M}{2\pi R_\mathrm{g} T_\mathrm{v}}}; \quad J_{z-} = \Gamma(-a) p_\mathrm{v} \sqrt{\frac{M}{2\pi R_\mathrm{g} T_\mathrm{v}}}, \tag{A.9}$$

where,

$$a = \frac{u_{0z}}{\sqrt{2RT_\mathrm{v}/M}}, \tag{A.10}$$

and the factor $\Gamma(a)$ reflects the impact of the vapor bulk motion,

$$\Gamma(a) = \exp(a^2) + a\sqrt{\pi}[1 + \mathrm{erf}(a)]. \tag{A.11}$$

It is worth mentioning that J_c is not equal to J_{z-}, because a portion of the vapor molecules that strike the interface would bounce back to the vapor, without entering the liquid phase. The actual mass flux due to condensation is smaller than J_{z-},

$$J_\mathrm{c} = f J_{z-} = f\Gamma(-a) p_\mathrm{v} \sqrt{\frac{M}{2\pi R_\mathrm{g} T_\mathrm{v}}}, \tag{A.12}$$

where f is the evaporation (or condensation) coefficient, whose value obtained from experiments is close to 1 (Marek et al., 2001).

To evaluate J_e, it is assumed that the mass flux, due to the molecules escaping from the liquid phase, is characterized by the temperature and pressure of the interface,

$$J_\mathrm{e} = f p^\mathrm{i} \sqrt{\frac{M}{2\pi R_\mathrm{g} T^\mathrm{i}}}. \tag{A.13}$$

Thus, the net mass flux traversing the imaginary plane is

$$J_\mathrm{net} = f \sqrt{\frac{M}{2\pi R_\mathrm{g}}} \left[\frac{p^\mathrm{i}}{\sqrt{T^\mathrm{i}}} - \Gamma(-a) \frac{p_\mathrm{v}}{\sqrt{T_\mathrm{v}}} \right] \tag{A.14}$$

For small $|a|$, one employs $\Gamma(-a) \sim 1 + a\sqrt{\pi}$ and substitutes Eq. A.7 and Eq. A.10 into the equation above, which yields

$$J_\mathrm{net} = \frac{2f}{2-f} \sqrt{\frac{M}{2\pi R_\mathrm{g}}} \left(\frac{p^\mathrm{i}}{\sqrt{T^\mathrm{i}}} - \frac{p_\mathrm{v}}{\sqrt{T_\mathrm{v}}} \right). \tag{A.15}$$

Assuming that p^i is equal to the saturation pressure corresponding to T^i and the temperature in vapor near the interface is continuous, i. e. $T^\mathrm{i} = T_\mathrm{v}$. The derivation of Fig. 57b from

the saturation state Fig. 57a in the liquid phase is small, thus, Eq. A.5 is applicable, which yields

$$p^{\mathrm{i}} - p_{\mathrm{v}} = \frac{\mathcal{L}\rho_{\mathrm{v}}\rho}{(\rho-\rho_{\mathrm{v}})T_{\mathrm{sat}}}\left[T^{\mathrm{i}} - T_{\mathrm{sat}}(p_{\mathrm{v}})\right]. \tag{A.16}$$

Substituting the equation above into Eq. A.15 results in the net mass flux as a function of the difference between the interface temperature and the saturation temperature corresponding to the vapor pressure

$$J_{\mathrm{net}} = \frac{2f}{2-f}\sqrt{\frac{M}{2\pi R_{\mathrm{g}}T_{\mathrm{sat}}}}\frac{\mathcal{L}\rho_{\mathrm{v}}\rho}{(\rho-\rho_{\mathrm{v}})T_{\mathrm{sat}}}\left[T^{\mathrm{i}} - T_{\mathrm{sat}}(p_{\mathrm{v}})\right]. \tag{A.17}$$

Defining the interfacial thermal resistance R^{i} as

$$R^{\mathrm{i}} = \frac{2-f}{2f}\frac{T_{\mathrm{sat}}\sqrt{2\pi R_{\mathrm{g}}T_{\mathrm{sat}}/M}(\rho-\rho_{\mathrm{v}})}{\mathcal{L}^2\rho_{\mathrm{v}}\rho}. \tag{A.18}$$

Taking $f = 1$ results in Eq. 1.21.

A.3 Stokes problem of the straight wedge

In the polar reference (r, φ), the components of the liquid velocity $\boldsymbol{u} = (u_r, u_\varphi)$ can be expressed as

$$u_r = \frac{1}{r}\frac{\partial\Psi}{\partial\varphi}, \tag{A.19a}$$

$$u_\varphi = -\frac{\partial\Psi}{\partial r}. \tag{A.19b}$$

with the stream function Ψ that satisfies the equation

$$\nabla^4\Psi = 0. \tag{A.20}$$

Because of the mass conservation along the wedge in both problems considered below, The liquid flux Φ defined by Eq. 3.11 is independent of r.

A.3.1 *Pinned contact line and varying angle*

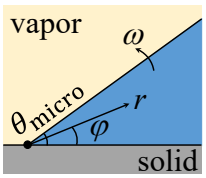

We search for a solution to the Stokes problem inside a straight two-dimensional liquid wedge (see the sketch of a straight liquid wedge with a varying angle) where the opening angle ϕ varies with the angular velocity ω. In polar coordinates (r, φ), the Stokes equations for the liquid velocity $\boldsymbol{u} = (u_r,\ u_\varphi)$ read

$$\frac{\partial p}{\partial r} = \mu\left\{\frac{\partial}{\partial r}\left[\frac{1}{r}\frac{\partial(ru_r)}{\partial r}\right] + \frac{1}{r^2}\frac{\partial^2 u_r}{\partial\varphi^2} - \frac{2}{r^2}\frac{\partial u_\varphi}{\partial\varphi}\right\}, \tag{A.21a}$$

$$\frac{\partial p}{\partial \varphi} = r\mu\left\{\frac{\partial}{\partial r}\left[\frac{1}{r}\frac{\partial(ru_\varphi)}{\partial r}\right] + \frac{1}{r^2}\frac{\partial^2 u_\varphi}{\partial\varphi^2} + \frac{2}{r^2}\frac{\partial u_r}{\partial\varphi}\right\}, \tag{A.21b}$$

$$\boldsymbol{\nabla}\cdot\boldsymbol{u} = 0. \tag{A.21c}$$

Equation (A.20) admits a solution $\Psi \propto r^\lambda f(\varphi)$, where λ is a constant (Moffatt, 1964). On the one hand, Ψ should scale with ω because it causes the flow. On the other, from Eq. A.19b, its dimension should be length^2/time. The only choice is thus

$$\Psi = \omega r^2 f(\varphi). \tag{A.22}$$

The corresponding function f is $f(\varphi) = A\cos 2\varphi + B\sin 2\varphi + C\varphi + D$ (Moffatt, 1964), where A, B, C, D are constants. They can be determined with the boundary conditions. A zero velocity ($u_r = u_\varphi = 0$) is imposed at the liquid-solid surface $\varphi = 0$. A radial velocity $u_\varphi = \omega r$ is imposed at the liquid-vapor boundary $\varphi = \phi$, which is also stress-free ($\partial u_r/\partial\varphi = 0$). The result is

$$\Psi = \omega r^2 \frac{\tan 2\phi(\cos 2\varphi - 1) + 2\varphi - \sin 2\varphi}{2(\tan 2\phi - 2\phi)}. \tag{A.23}$$

Substituting Eq. A.23 into Eq. A.21 gives

$$\begin{aligned} \frac{\partial p}{\partial r} &= \frac{4\mu\omega}{r(\tan 2\phi - 2\phi)}, \\ \frac{\partial p}{\partial \varphi} &= 0, \end{aligned} \tag{A.24}$$

thus, $p \sim \log r$. Note that for a small ϕ, Eq. A.24 reduces to

$$\frac{\partial p}{\partial r} = \frac{3\mu\omega}{2r\phi^3}. \tag{A.25}$$

A.3.2 *Conventional lubrication approach to straight wedge flow*

Consider the case with no phase change. It is described by Eq. 2.16, where $J = 0$. As in the above Stokes problem, one can consider asymptotically (near the contact line) the straight wedge $h = \theta x$ with the angular velocity $\partial\theta/\partial t = \omega$. The governing equation

$$\mu\omega x + \frac{\partial}{\partial x}\left(\frac{\theta^3 x^3}{3}\frac{\partial \Delta p}{\partial x}\right) = 0$$

results in

$$\frac{\partial \Delta p}{\partial x} = -\frac{3\mu\omega}{2x\theta^3}. \tag{A.26}$$

With no surprise, this expression agrees with the small θ asymptotics Eq. A.25 of the Stokes approach and leads to the logarithmic pressure divergence at the contact line.

Consider now the lubrication theory for the volatile liquids that accounts for the Kelvin effect, Eq. 2.21. For the straight wedge with the varying contact angle, it becomes

$$\mu\omega x + \frac{\partial}{\partial x}\left(\frac{\theta^3 x^3}{3}\frac{\partial \Delta p}{\partial x}\right) = \frac{\Delta p - \Delta p_{\mathrm{cl}}}{\theta x}\frac{\mu k T_{\mathrm{sat}}}{(\mathcal{L}\rho)^2}. \tag{A.27}$$

For the fixed contact angle case ($\omega = 0$), this equation admits an analytical solution (Janeček et al., 2012) that satisfies the condition (2.18):

$$\Delta p = \Delta p_{\mathrm{cl}}\left[1 - \frac{\ell_{\mathrm{K}}}{x}K_1\left(\frac{\ell_{\mathrm{K}}}{x}\right)\right], \tag{A.28}$$

where $K_1(\cdot)$ is the modified Bessel function of the first order and

$$\ell_{\mathrm{K}} = \frac{\sqrt{3\mu k T_{\mathrm{sat}}}}{\mathcal{L}\rho\theta^2} \tag{A.29}$$

is a characteristic length of the Kelvin effect. At $x \ll \ell_{\mathrm{K}}$,

$$\Delta p = \Delta p_{\mathrm{cl}}\left\{1 - \exp\left(-\frac{\ell_{\mathrm{K}}}{x}\right)\left[\sqrt{\frac{\pi}{2}\frac{\ell_{\mathrm{K}}}{x}} + \mathcal{O}(x^{1/2})\right]\right\}. \tag{A.30}$$

For the case of varying contact angle $\omega \neq 0$, a solution that satisfies the condition (2.18) can be found as an asymptotic expansion

$$\Delta p = \Delta p_{\mathrm{cl}} + \frac{3\mu\omega}{\theta^3\ell_{\mathrm{K}}^2}x^2 + \mathcal{O}(x^4). \tag{A.31}$$

A.3.3 *Moving Contact line*

Consider the substrate moving at speed u_{cl} to the left in Fig. 23b, which is equivalent to the contact line receding. The conventional non-slip condition at the solid surface and non-tangential stress condition at the interface to (A.20) are

$$\begin{aligned} &\frac{\partial \Psi}{\partial \varphi} = -r u_{\mathrm{cl}} \text{ and } \frac{\partial \Psi}{\partial r} = 0 \text{ at } \varphi = 0, \\ &\frac{\partial \Psi}{\partial r} = 0 \text{ and } \frac{\partial^2 \Psi}{\partial \varphi^2} = 0 \text{ at } \varphi = \phi. \end{aligned} \tag{A.32}$$

The solution to this problem is (Moffatt, 1964)

$$\Psi(r, \varphi) = -r u_{\mathrm{cl}} \frac{(2\phi - \varphi)\sin\varphi - \varphi \sin(2\phi - \varphi)}{2\phi - \sin(2\phi)}, \tag{A.33}$$

and the pressure gradient at the interface reads

$$\frac{\partial p}{\partial r} = u_{\mathrm{cl}} \frac{\mu}{r^2} \frac{4\sin\phi}{\sin(2\phi) - 2\phi}. \tag{A.34}$$

Note that $\Phi = 0$ for this case as it is zero in the apex. Many authors pointed out the non-integrable pressure divergence $p \sim r^{-2}$. It means the infinite viscous dissipation, so such a problem statement is, in fact, non-physical, and other microscale phenomena like the hydrodynamic slip and/or the Kelvin effect need to be accounted for to relax the singularity.

A.3.4 *Localized evaporation*

Consider the flow induced by the localized evaporation modeled by a point source Φ placed at the wedge apex (Fig. 23b). The boundary conditions to (A.20) are

$$\begin{aligned} &\frac{\partial \Psi}{\partial \varphi} = 0 \text{ and } \frac{\partial \Psi}{\partial r} = 0 \text{ at } \varphi = 0, \\ &\frac{\partial \Psi}{\partial r} = 0 \text{ and } \frac{\partial^2 \Psi}{\partial \varphi^2} = 0 \text{ at } \varphi = \phi. \end{aligned} \tag{A.35}$$

They signify (i) the impermeability and no-slip conditions at the solid surface $\varphi = 0$, (ii) the impermeability and zero tangential stress at the liquid-vapor interface $\varphi = \phi$. The velocity should satisfy (3.11), where Φ is constant. One mentions that for this, $\Psi(r, \varphi)$ should be independent of r.

The solution found by Mathieu (2003) is

$$\Psi(r, \varphi) = \Phi \frac{\sin(2\phi - 2\varphi) + 2\varphi\cos(2\phi)}{2\phi\cos(2\phi) - \sin(2\phi)}. \tag{A.36}$$

The corresponding pressure field is

$$p(r, \varphi) = \Phi \frac{\mu}{r^2} \frac{4\cos(2\phi - 2\varphi)}{\sin(2\phi) - 2\phi\cos(2\phi)},$$

and the pressure gradient at the interface $\varphi = \phi$ reads

$$\frac{\partial p}{\partial r} = \Phi \frac{\mu}{r^3} \frac{4}{\phi\cos(2\phi) - \cos\phi\sin\phi}. \tag{A.37}$$

A.4 Characteristic length scales of nanoscale effects

The characteristic lengths shown in Tab. 5 can be obtained from Eq. 1.26, Eq. 1.27 and Eq. 3.29 describing the microregion. For these estimations, small slopes are assumed, thus $G \simeq 1$ and $\zeta \simeq h$. One assumes for the estimation the wedge liquid shape with the opening angle θ. Therefore, if the x scale is denoted as ℓ (to be defined for each effect), then the h scale is $\theta\ell$. Eq. 3.2 yields $K \sim \theta/\ell$, consequently $\Delta p \sim \sigma K \sim \sigma\theta/\ell$. The mass flux scales as $J \sim k\Delta T/(\mathcal{L}\theta\ell)$.

From Eq. 1.23, the interfacial resistance scale $\ell_{\mathrm{R}} = R^{\mathrm{i}}k/\theta$. The vapor recoil scale ℓ_{r} is found using Eq. 1.26. It reflects the vapor recoil on the Voinov angle. The slip length scale ℓ_{s} is easily obtained from Eq. 3.29. The Kelvin length scale ℓ_{K} is derived by Janeček et al. (2013).

The Marangoni effect is more delicate because the T^{i} spatial variation does not appear without either Kelvin or interface resistance terms; cf. Eq. 1.22. After having left aside the slip, Eq. 3.29 reduces to

$$\frac{1}{\mu}\frac{\partial}{\partial x}\left[-\frac{\gamma h^2}{2}R^{\mathrm{i}}\mathcal{L}\frac{\partial J}{\partial x}+\left(\frac{h^3}{3}-\frac{\gamma h^2}{2}\frac{T_{\mathrm{sat}}}{\mathcal{L}\rho}\right)\frac{\partial \Delta p}{\partial x}\right]=-\frac{J}{\rho}. \tag{A.38}$$

By comparing the two terms in the round brackets (the second of which comes from the Kelvin effect), one obtains the Marangoni-Kelvin scale

$$\ell_{\mathrm{MK}} = \frac{3\gamma T_{\mathrm{sat}}}{2\theta\mathcal{L}\rho}.$$

It appears to be below $1\,\mathrm{nm}$ for all the cases under consideration, so the corresponding effect is negligible. Conversely, the Marangoni effect appearing due to the interfacial thermal resistance with respect to the capillary action is characterized by the balance of the terms

$$\frac{\gamma h^2}{2}R^{\mathrm{i}}\mathcal{L}\frac{\partial J}{\partial x} \quad \text{and} \quad \frac{h^3}{3}\frac{\partial \Delta p}{\partial x} \tag{A.39}$$

which results in the characteristic scale

$$\ell_{\mathrm{MR}} = \frac{3\gamma\Delta T R^{\mathrm{i}}k}{2\theta^3\sigma} = \frac{3\gamma\Delta T}{2\theta^2\sigma}\ell_{\mathrm{R}}$$

displayed in Tab. 5.

Since the interfacial resistance should be present to provide the Marangoni effect, one should check if a range of x exists such that $\ell_{\mathrm{R}} < x < \ell_{\mathrm{MR}}$ (i. e. where the Marangoni effect created by the interfacial resistance is more important than the effect of the interfacial resistance alone). This interval exists if

$$\ell_{\mathrm{R}} < \ell_{\mathrm{MR}}, \tag{A.40}$$

equivalent to

$$\gamma\Delta T > \frac{2}{3}\theta^2\sigma. \tag{A.41}$$

This means that ℓ_{MR} is relevant if the product $\gamma\Delta T$ is large enough.

Appendix B

Numerical scheme

This appendix deals with the numerical scheme used in solving governing equations in the generalized lubrication theory in Chap. 3. Three equations are considered:

(i) interface dynamic equation $h(s,t)$: taking derivative on both sides of Eq. 1.27 yields:

$$\frac{\partial T^{\mathrm{i}}}{\partial s} = \frac{T_{\mathrm{sat}}}{\mathcal{L}\rho}\frac{\partial \Delta p}{\partial s} + \frac{T_{\mathrm{sat}}}{\mathcal{L}}\left(\frac{1}{\rho_{\mathrm{v}}^2} - \frac{1}{\rho^2}\right) J\frac{\partial J}{\partial s} + R^{\mathrm{i}}\mathcal{L}\frac{\partial J}{\partial s}. \tag{B.1}$$

The Marangoni effect is written as

$$\frac{\partial \sigma}{\partial s} = -\gamma\frac{\partial T^{\mathrm{i}}}{\partial s}. \tag{B.2}$$

Substituting the Marangoni effect and Eq. B.1 into Eq. 3.18, the interface dynamic equation in full expansion is:

$$\frac{\partial h}{\partial t}\cos\phi + \frac{\partial}{\partial s}\left[\frac{1}{\mu G(\phi)}\left(A\frac{\partial J}{\partial s} + B\frac{\partial \Delta p}{\partial s}\right) - u_{\mathrm{cl}}\zeta\frac{F(\phi)}{G(\phi)}\right] = -\frac{J}{\rho}, \tag{B.3}$$

where

$$\begin{aligned} A &= -\gamma\left[R^{\mathrm{i}}\mathcal{L} + \frac{T_{\mathrm{sat}}}{\mathcal{L}}\left(\frac{1}{\rho_{\mathrm{v}}^2} - \frac{1}{\rho^2}\right)J\right]\left(\frac{\zeta^2}{2} + \zeta l_{\mathrm{s}}\right), \\ B &= \frac{\zeta^3}{3} + \zeta^2 l_{\mathrm{s}} - \frac{\gamma T_{\mathrm{sat}}}{\mathcal{L}\rho}\left(\frac{\zeta^2}{2} + \zeta l_{\mathrm{s}}\right). \end{aligned} \tag{B.4}$$

(ii) evaporation flux J: substituting Eq. 1.27 into Eq. 3.20 and replacing T_{w} with $T_{\mathrm{sat}} + \Delta T$, one obtains,

$$J = \frac{k}{\mathcal{L}\left(R^{\mathrm{i}}k + h\dfrac{\phi}{\sin\phi}\right)}\left[\Delta T - \frac{\Delta p T_{\mathrm{sat}}}{\mathcal{L}\rho} - \frac{T_{\mathrm{sat}}}{2\mathcal{L}}\left(\frac{1}{\rho_{\mathrm{v}}^2} - \frac{1}{\rho^2}\right)J^2\right]. \tag{B.5}$$

(iii) pressure jump equation, Eq. 3.19.

	length	pressure	temperature	mass flux	time
notation	h, ζ, s	Δp	T	J	t
unit	m	Pa	K	kg/m^{2}s	s
reference value	l_{ref}	σ / l_{ref}	T_{sat}	$kT_{\text{sat}} / \mathcal{L} l_{\text{ref}}$	$\mu l_{\text{ref}} / \sigma$

Table 8: Reference values used in equation non-dimensionalization.

B.1 Non-dimensionalization

The reference values that make the equations dimensionless are listed in Tab. 8. The dimensionless quantities are denoted with $\sim$.

The interface dynamic equation $\tilde{h}(\tilde{s}, \tilde{t})$ in dimensionless form is

$$\frac{\partial \tilde{h}}{\partial \tilde{t}} \cos\phi + \frac{\partial}{\partial \tilde{s}} \left(-\tilde{A} \frac{\partial \tilde{J}}{\partial \tilde{s}} + \tilde{B} \frac{\partial \Delta \tilde{p}}{\partial \tilde{s}} - \tilde{D} Ca_{\text{cl}} \right) = -N_{\text{e}} \tilde{J}, \tag{B.6}$$

where

$$\begin{aligned} \tilde{A} &= \frac{1}{G} N_{\text{M}} \left(N_{\text{R}} + N_{\text{A}} \tilde{J} \right) \left(\frac{\tilde{\zeta}^2}{2} + \tilde{\zeta} \tilde{l}_{\text{s}} \right), \\ \tilde{B} &= \frac{1}{G} \left[\frac{\tilde{\zeta}^2}{3} + \tilde{\zeta} \tilde{l}_{\text{s}} - N_{\text{M}} N_{\text{p}} \left(\frac{\tilde{\zeta}}{2} + \tilde{l}_{\text{s}} \right) \right] \tilde{\zeta}, \\ \tilde{D} &= \frac{F}{G} \tilde{\zeta}. \end{aligned} \tag{B.7}$$

Evaporation flux $\tilde{J}$:

$$\tilde{J} = \frac{\Delta \tilde{T} - N_{\text{p}} \Delta \tilde{p} - \frac{N_{\text{A}}}{2} \tilde{J}^2}{N_{\text{R}} + \tilde{h} \frac{\phi}{\sin\phi}}. \tag{B.8}$$

Pressure jump $\Delta \tilde{p}$:

$$\frac{\partial^2 \tilde{h}}{\partial \tilde{s}^2} = \cos\phi \Delta \tilde{p} + \cos\phi N_{\text{r}} \tilde{J}^2. \tag{B.9}$$

Dimensionless numbers appearing in the equations above are

$$\begin{aligned} N_{\text{M}} &= \frac{\gamma T_{\text{sat}}}{\sigma}, \; N_{\text{R}} = \frac{R^{\text{i}} k}{l_{\text{ref}}}, \; N_{\text{A}} = \frac{T_{\text{sat}}^2 k^2}{\mathcal{L}^3 l_{\text{ref}}^2} \left(\frac{1}{\rho_{\text{v}}^2} - \frac{1}{\rho^2} \right) \\ N_{\text{p}} &= \frac{\sigma}{l_{\text{ref}} \mathcal{L} \rho}, \; N_{\text{e}} = \frac{\mu k T_{\text{sat}}}{\sigma \rho \mathcal{L} l_{\text{ref}}}, \; N_{\text{r}} = \frac{T_{\text{sat}}^2 k^2}{\sigma l_{\text{ref}} \mathcal{L}^2} \left(\frac{1}{\rho_{\text{v}}} - \frac{1}{\rho} \right) \end{aligned}$$

B.2 Discretized equations

The dimensionless equations are solved numerically using the finite volume method. In this 1D scenario, a finite volume is simply a line segment. The computational mesh grid is shown in Fig. 58. The quantities, such as h, p, T, and J, and their even-order derivatives are defined at the mesh nodes (the centers of segments), while the odd-order derivatives are defined at the segment boundaries denoted with *.

We first create the heterogeneous grid for the microregion. The node number counts from 1 to nmic. Node 0 is reserved for the contact line $s_0 = 0$. We designate the size of the first half-segment as d_0 and the growth rate r. The segments grow gradually $d_i = d_0 r^i$.

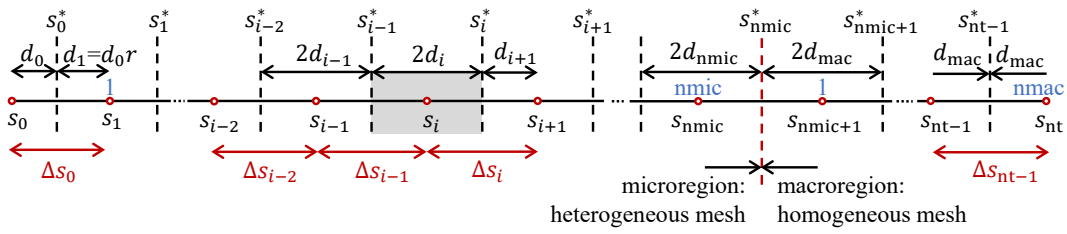

Figure 58: One-dimensional computational mesh grid.

The mesh grid is homogeneous in the macroregion, and the node number counts from 1 to nmac. To ensure a smooth transition, the segment size d_{mac} is equal to the last segment in the microregion $d_{\mathrm{mac}} = d_0 r^{\mathrm{nmic}}$. The total number of nodes in the grid is nt+1=nmic+nmac+1.

In discretized form, given $\Delta\tilde{t}$ as the time step, Eq. B.6 is written for nodes 1 to nt-1:

$$\frac{2d_i}{\Delta\tilde{t}}\tilde{h}_i\cos\phi_i + \frac{B_{i-1}^*}{\Delta\tilde{s}_{i-1}}\Delta\tilde{p}_{i-1} - \left(\frac{B_{i-1}^*}{\Delta\tilde{s}_{i-1}} + \frac{B_i^*}{\Delta\tilde{s}_i}\right)\Delta\tilde{p}_i + \frac{B_i^*}{\Delta\tilde{s}_i}\Delta\tilde{p}_{i+1}$$
$$- \frac{A_{i-1}^*}{\Delta\tilde{s}_{i-1}}\tilde{J}_{i-1} + \left(\frac{A_{i-1}^*}{\Delta\tilde{s}_{i-1}} + \frac{A_i^*}{\Delta\tilde{s}_i} + 2d_iN_{\mathrm{e}}\right)\tilde{J}_i - \frac{A_i^*}{\Delta\tilde{s}_i}\tilde{J}_{i+1} + \left(D_{i-1}^* - D_i^*\right)Ca_{\mathrm{cl}}$$
$$= \frac{2d_i}{\Delta\tilde{t}}\tilde{h}_i^{F-1}\cos\phi_i \quad \text{(B.10)}$$

where on the r.h.s, the superscript $^{F-1}$ indicates the previous time step, and the coefficients at node i are

$$\tilde{A}_i = \frac{1}{G_i}N_{\mathrm{M}}\left(N_{\mathrm{R}} + N_{\mathrm{A}}\tilde{J}_i\right)\left(\frac{\tilde{\zeta}_i^2}{2} + \tilde{\zeta}_i\tilde{l}_{\mathrm{s}}\right),$$
$$\tilde{B}_i = \frac{1}{G_i}\left[\frac{\tilde{\zeta}_i^2}{3} + \tilde{\zeta}_i\tilde{l}_{\mathrm{s}} - N_{\mathrm{M}}N_{\mathrm{p}}\left(\frac{\tilde{\zeta}_i}{2} + \tilde{l}_{\mathrm{s}}\right)\right]\tilde{\zeta}_i, \quad \text{(B.11)}$$
$$\tilde{D}_i = \frac{F_i}{G_i}\tilde{\zeta}_i,$$

whose values are updated after each iteration.

The evaporation flux equation is written from node 0 to nt as:

$$N_{\mathrm{p}}\Delta\tilde{p}_i + \left(N_{\mathrm{R}} + \frac{\phi_i}{\sin\phi_i}\tilde{h}_i + \frac{N_{\mathrm{A}}}{2}\tilde{J}_i^{\mathrm{prev}}\right)\tilde{J}_i = \Delta\tilde{T}, \quad \text{(B.12)}$$

where J_i^{prev} is value from the previous iteration.

The pressure jump equation is written from node 1 to nt-1:

$$\frac{\tilde{h}_{i-1}}{\Delta\tilde{s}_{i-1}} - \left(\frac{1}{\Delta\tilde{s}_{i-1}} + \frac{1}{\Delta\tilde{s}_i}\right)\tilde{h}_i + \frac{\tilde{h}_{i+1}}{\Delta\tilde{s}_i} - 2d_i\cos\phi_i\Delta\tilde{p}_i - 2d_iN_{\mathrm{r}}\tilde{J}_i^{\mathrm{prev}}\cos\phi_i\tilde{J}_i = 0. \quad \text{(B.13)}$$

The total number of discretized equations is 3nt-1. With 4 boundary conditions, the problem is complete.

One more equation at node 0 is required for solving Ca_{cl}:

$$\left(G_0N_{\mathrm{e}} + \tilde{l}_{\mathrm{s}}N_{\mathrm{M}}\theta_{\mathrm{micro}}^2\right)\tilde{J}_0 - F_0\theta_{\mathrm{micro}}Ca_{\mathrm{cl}} = 0. \quad \text{(B.14)}$$

Appendix C

Résumé substantiel en français

C.1 Introduction

Au début des années 1990, le caloduc oscillant (en anglais, Pulsating Heat Pipe PHP, également connu sous le nom de Oscillating Heat Pipe OHP), a été conçu par Hisateru Akachi (Akachi, 1993), et est rapidement devenu une alternative prometteuse aux caloducs conventionnels. En tant que dispositif de transfert de chaleur émergent, les PHPs combinent les principes de conductivité thermique et de transition de phase. Ni les structures internes capillaires ni la force gravitationnelle ne sont nécessaires à son fonctionnement.

Conceptuellement, le transfert d'énergie dans les PHPs est réalisé dans un canal fluide, qui relie les sections de réception (appelées **évaporateurs**) et de dissipation (appelées **condenseurs**) de l'énergie. Des sections adiabatiques facultatives peuvent séparer les évaporateurs des condenseurs. Ce canal de fluide est généralement disposé en serpentin formant un faisceau. Le canal doit être suffisamment étroit pour être capillaire. Il ne doit pas y avoir de stratification du fluide. Des bouchons liquides et des bulles de vapeur se forment naturellement à l'intérieur, lorsque le canal est chargé d'un fluide pure diphasique. Pour la plupart, ces bulles et bouchons sont sensiblement plus longues que le diamètre du canal.

Fig. 1 illustre l'une des conceptions PHP les plus populaires, où le canal de fluide est bouclé dans le condenseur. Ce type de conception est appelé PHP à boucle fermée, qui est reconnu par de nombreux chercheurs comme le plus efficace (Nikolayev, 2021).

Dans un PHP fonctionnel, l'évaporation persistante du liquide et la condensation de la vapeur génèrent un champ de pression hors équilibre qui pompe le système bulle-bouchon. Le mouvement des bouchons liquides dans une branche déplace les bulles et les bouchons dans des branches adjacentes, ce qui entraîne un écoulement à oscillations auto-entretenues.

Lorsque les ménisques liquides se retirent, ils déposent des films liquides d'une épaisseur d'environ 10-100 μm sur la paroi des canaux. Bien que ces films n'occupent qu'une infime partie de section des canaux, le taux d'échange de chaleur latente pourrait être substantielle, en raison de la faible résistance thermique. L'évaporation du liquide peut entraîner la rupture du film. Des taches sèches et des lignes de contact triple apparaissent sur la paroi du tube. Sous l'effet de l'action capillaire, les lignes de contact reculent vers le côté liquide, formant des bourrelets liquides, illustrées dans Fig. 1.

Un autre mécanisme de transfert de chaleur par changement de phase est la création de nouvelles bulles dans les bouchons liquides, lorsque la surchauffe locale, par rapport à la température de saturation, dépasse une certaine limite (barrière de nucléation). Le transfert de chaleur sensible dans les bulles et les bouchons jouent également un rôle, bien que moins important. Cette dernière peut être renforcée par le mouvement oscillatoire. Néanmoins, le transfert de chaleur latente via les films liquides reste le principal mécanisme responsable du fonctionnement de PHP (Nikolayev, 2021).

C.2 Motivations

Bien que les principes de fonctionnement aient été étudiés par de nombreux chercheurs, en raison de la complexité des phénomènes de transport interne de chaleur et de masse, une théorie complète du fonctionnement du PHP et de la prédiction des performances reste en développement (Ma, 2015 ; Marengo et al., 2018 ; Nikolayev et al., 2018b). L'absence d'un outil de conception fiable entrave l'application industrielles de ce dispositif. Son mécanisme interne unique demande une nouvelle perspective de recherche. Des dizaines d'articles scientifiques sont publiés chaque année ; la modélisation de PHP est un domaine de recherche très actif.

Les chercheurs ont tenté d'établir des corrélations empiriques pour prédire les performances thermiques du dispositif. Cependant, la description de la configuration d'un dispositif spécifique nécessite un grand nombre de paramètres. Pour ne citer que quelques exemples, les quantités physiques, notamment les propriétés du fluide de travail et du matériau solide ; la conception du dispositif : topologie du PHP (boucle ouverte ou fermée), taille (longueurs et rayons) et section transversale du canal de fluide (ronde ou rectangulaire), le nombre de branches et le nombre de sources de chaleur et de froid. De plus, les conditions de fonctionnement ont un impact sur les performances : le positionnement du dispositif (vertical ou horizontal), la méthode et la puissance de chauffage, efficacité de refroidissement , le taux de remplissage du liquide. Inévitablement, certaines études ont omis certains paramètres difficiles à quantifier, ce qui a limité les corrélations empiriques à la seule gamme de paramètres qu'elles ont examinés. En raison de la compréhension insuffisante des mécanismes de fonctionnement, il est difficile de justifier quels paramètres sont indispensables et lesquels peuvent être exclus sans risque. Ce problème apparaît également dans les approches utilisant l'ANN.

La modélisation thermo-hydrodynamique semble être le moyen le plus prometteur de disposer d'un outil de calcul pour la conception et l'optimisation des PHP. Le comportement physique de ses composants (bulles de vapeur, bouchons et films liquides, paroi solide du canal) doit être étudié.

DNS est l'une des techniques largement employées dans laquelle les équations de Navier-Stokes sont résolues numériquement. Les simulations utilisant le DNS, généralement en deux et trois dimensions, peuvent sans aucun doute illustrer le comportement des fluides de manière très détaillée. Cependant, d'énormes efforts de programmation et des ressources de calcul sont nécessaires pour suivre les interfaces liquide-vapeur libres. Les modèles de changement de phase interfaciale impliquent souvent des paramètres artificiels qui induisent une incertitude dans les résultats. Les films liquides qui sont essentiels pour révéler correctement le fonctionnement du PHPs, ne sont souvent pas résolus dans les calculs du DNS.

Pour ces difficultés, la modélisation unidimensionnelle (en supposant l'axisymétrie dans les canaux de fluide circulaires) est considérée comme l'approche la plus pragmatique. Cette approche est capable de reproduire globalement les phénomènes physiques sans en compro-

mettre largement la précision. Des études de simulation (Nikolayev, 2011a) et expérimentales (Kamijima et al., 2020; Francom et al., 2021) ont confirmé que les films liquides représentent jusqu'à 70-80% du transfert total d'énergie dans ce dispositif. Une modélisation adéquate des films liquides devient donc une priorité absolue.

Le CASCO a été développé au CEA. Il s'agit d'un code de simulation 1D, basé sur le modèle FEC (détaillé dans Subsec. 1.2.2). La géométrie des films liquides est simplifiée. Tous les films liquides sont représentés par une épaisseur constante et uniforme, mais leurs longueurs varient individuellement en fonction du changement de phase sur les films. Grâce à la géométrie 1D simple, CASCO est capable de réduire prodigieusement le temps de calcul. Par exemple, la simulation 2D d'une topologie PHP importante sur le plan industriel peut prendre jusqu'à 4 à 6 semaines par exécution (Mucci et al., 2021), alors que la simulation de la même configuration par CASCO peut être réalisée en une heure (Nikolayev, 2021). Cette simple approche 1D peut produire la performance thermique et le comportement d'oscillation qui sont en accord avec les observations expérimentales (Bae et al., 2017 ; Abela et al., 2022).

Néanmoins, en termes de représentation réaliste du comportement du film liquide pendant les oscillations, le modèle FEC peut encore être amélioré. L'hypothèse d'une épaisseur de film imposée doit être abandonnée. La dynamique de la ligne de contact, à savoir le phénomène de démouillage lors de l'échange de phase, n'a pas été modélisée de manière adéquate. Un nouveau modèle numérique avancé qui ne dépend pas de l'entrée externe pour le calcul de l'épaisseur du film et qui peut refléter le recul de la ligne de contact est souhaité pour la prochaine version du code CASCO. C'est la motivation et l'objectif général de cette thèse. Le développement d'un tel modèle nécessite des études approfondies de la dynamique des films liquides, c'est pourquoi le comportement de ces derniers doit être compris comme point de départ de la thèse.

C.3 Structure de la thèse

Le corps principal de cette thèse se compose de deux parties: les études théoriques et le développement du modèle de PHP.

Après une courte introduction, Chap. 1 récapitule les théories sur la dynamique du film liquide dans les tubes capillaires circulaires et compare plusieurs modèles numériques existants de PHPs. Chap. 2 détaille une analyse théorique de la dynamique du film liquide pendant l'oscillation d'un ménisque. En utilisant la théorie des bulles de Taylor, le profil dynamique du film liquide déposé est décrit dans le cadre de l'approximation de lubrification tenant compte de la présence d'une ligne de contact. Cette dernière est supposée être accrochée par un défaut de surface et donc immobile ; l'angle de contact est autorisé à varier. L'effet de l'écoulement du liquide dans le bouchon sur la courbure dans la partie centrale du ménisque est négligé. Cette courbure varie dans le temps et est déterminée en même temps que le profil du film. Tout d'abord, l'oscillation dans des conditions adiabatiques est considérée. Ensuite, l'effet combiné de l'oscillation et de l'évaporation sur le comportement du film liquide est examiné.

Chap. 3 poursuit les études et traite du phénomène qui n'est pas mentionné dans Chap. 2 : le recul de la ligne de contact en présence d'un changement de phase dans les tubes capillaires. L'objectif principal est de trouver une approche simple et utilisable dans les modèles de PHP pour décrire la dynamique de la ligne de contact. Notre analyse prend l'analogie suivante : la dynamique de la ligne de contact peut être comprise en résolvant le problème de démouillage en présence de l'évaporation causée par la surchauffe du substrat.

La théorie du film liquide développée précédemment est appliquée pour élucider la formation de la microcouche sous les bulles de vapeur lors de l'ébullition nucléée dans Chap. 4.

L'expansion de la tache sèche sous la bulle ressemble fortement au démouillage du film liquide lors de l'évaporation. Une comparaison avec une expérience est faite.

La deuxième partie est consacrée au développement d'un nouveau modèle numérique 1D de films liquides dans les simulations PHP, appelé modèle OFT. L'objectif est, d'une part, de maintenir l'avantage du modèle 1D d'être efficace en termes de calcul et, d'autre part, d'incorporer les études théoriques précédentes afin de mieux refléter les processus physiques des films liquides. Trois phénomènes clés sont mis en avant : (1) le dépôt du film par des bouchons liquides oscillants (détaillé dans Chap. 3) ; (2) l'évolution temporelle de l'épaisseur du film qui s'ensuit en raison de l'échange de masse sur les films ; (3) la dynamique de la ligne de contact (discutée dans Chap. 3) qui raccourcit la longueur du film. Pour évaluer le nouveau modèle, il est employé dans Chap. 5 pour simuler le PHP le plus simple, à branche unique, pour lequel des données expérimentales détaillées sont disponibles. La comparaison entre les résultats de la simulation et l'observation expérimentale peut être effectuée de manière approfondie. Finalement, une extension du nouveau modèle de film liquide pour simuler les PHPs à branches multiples est proposée dans Chap. 6. Cette extension sera intégrée dans la prochaine version de CASCO et devrait améliorer la fiabilité de la simulation.

Les détails mathématiques, le schéma numérique, et les résumés de la thèse en français et en chinois sont regroupés dans la partie III, les annexes. En résumé, la thèse étudie la dynamique du film liquide dans les tubes capillaires, sur laquelle un modèle de calcul 1D est développé.

C.4 Conclusions

La dynamique du film liquide pendant l'oscillation du ménisque a d'abord été étudiée. Étant donné que les lignes de contact se déplacent généralement beaucoup plus lentement que les ménisques et qu'uniquement le comportement à grande échelle des films liquides est considéré, cette étude adopte un scénario moins complexe où la ligne de contact est coincée sur un défaut de surface, et l'oscillation est harmonique. Les paramètres du système comprennent l'angle de contact initial (macroscopique), la période et l'amplitude de l'oscillation. Une solution périodique de ce problème a été identifiée. Nos résultats montrent que le film liquide qui est déposé par un ménisque oscillant est non-uniforme, car l'épaisseur dépend de la vitesse et de la courbure du ménisque, qui varient pendant l'oscillation. L'épaisseur moyenne du film dépend faiblement de l'angle de contact initial, alors qu'elle croît avec la période et l'amplitude de l'oscillation. Lorsque le ménisque s'éloigne de la ligne de contact épinglée, l'angle de contact chute brusquement à une faible valeur de quelques degrés seulement, quelle que soit la valeur initiale, et fluctue à peine jusqu'à la fin de la période où le ménisque recule. Pendant ce temps, comme les ondulations de l'interface créées par l'avancée du ménisque sont comprimées sur la ligne de contact, l'angle de contact oscille fortement et atteint un minimum global. L'angle de contact initial et la période d'oscillation ont un faible impact sur cet angle de contact minimal. L'amplitude de la vitesse peut augmenter ce minimum, bien que sa valeur reste faible, de l'ordre de quelques degrés. Enfin, le problème des effets combinés de l'oscillation du ménisque et du chauffage du tube est considéré. L'angle de contact minimal pendant l'oscillation fixe une limite supérieure pour la surchauffe du tube. Cette limite supérieure est considérablement basse - de seulement quelques mK, ce qui est très inférieur à la surchauffe typique dans les expériences. Cela signifie que la prise en compte du recul des lignes de contact est essentielle pour analyser le comportement du film liquide dans les PHPs où l'oscillation du ménisque et l'évaporation se produisent simultanément.

Le recul des lignes de contact a été étudié dans le cas de démouillage du film liquide lors de l'évaporation. Pour obtenir des résultats plus précis, notre théorie inclut plusieurs effets à l'échelle nanométrique qui sont connus pour avoir des impacts non négligeables sur la description des phénomènes physiques à l'échelle microscopique des lignes de contact. La théorie conventionnelle de la lubrification est généralisée pour tenir compte des grandes pentes interfaciales, supérieures à $30°$, qui sont rencontrées en cas de surchauffe élevée. Notre description théorique attribue le phénomène de recul de la ligne de contact à l'évaporation spontanée du liquide dans son voisinage immédiat. Le taux d'évaporation au niveau de la ligne de contact est corrélé à sa vitesse. Nos résultats démontrent que l'évaporation forcée accélère non seulement la vitesse de retrait de la ligne de contact, mais peut également induire le démouillage. Nous généralisons la théorie multi-échelle asymptotique de démouillage, qui a été initialement développée pour des conditions adiabatiques, aux cas d'évaporation. Il en résulte une expression analytique simple pour la vitesse de démouillage. Les principaux paramètres de cette expression sont la longueur de Voinov et l'angle de Voinov (la pente de l'interface formée dans la microrégion), par lesquels les effets à l'échelle nanométrique ont un impact sur la physique à grande échelle. Alors que l'angle de Voinov est relativement facile à calculer (il ne nécessite que la solution d'un modèle de microrégion stationnaire maîtrisé par de nombreux groupes de recherche), la longueur de Voinov nécessite un calcul plus sophistiqué. Une formule analytique approximative pour cette dernière est proposée. Les résultats de notre modèle multi-échelle généralisé sont en accord avec les calculs numériques. Il est démontré que la perte de masse par évaporation au niveau des lignes de contact n'entraîne pas d'accélération supplémentaire de leur mouvement. Ce dernier est entièrement contrôlé par la capillarité et par la modification de l'angle de Voinov induite par l'évaporation. Outre son utilisation dans la modélisation du PHP, cette expression simple est précieuse pour un grand nombre d'applications qui traitent des phénomènes de changement de phase des films liquides minces.

La théorie des films liquides développée ci-dessus est appliquée pour expliquer la formation et l'évolution de la microcouche se formant sous les bulles de vapeur lors de l'ébullition nucléée. La comparaison avec les observations expérimentales montre que la création de microcouche peut être considérée comme le résultat du dépôt d'un film liquide par le bord de la bulle en expansion. Une épaisseur maximale observée expérimentalement dans la partie centrale de microcouche est attribuée à l'interaction de deux tendances opposées : la décélération de l'expansion qui diminue l'épaisseur, et la décroissance de courbure de la bulle qui tend à augmenter l'épaisseur. Notre théorie prédit la position de ce maximum local sur les substrats solides et est en bon accord avec les données expérimentales. L'expansion de la tache sèche sous les bulles est analogique au démouillage d'un film liquide lors de l'évaporation. Notre prédiction théorique de la vitesse de recul de la ligne de contact est conforme aux observations expérimentales.

Appendix D

Abstract in Chinese

The author hopes a terse summary in Chinese would give this thesis greater visibility among researchers working on relevant topics in China.

题目：脉动热管模拟（Modeling of Pulsating Heat Pipes）

作者：张晓龙；论文导师：瓦季姆·尼古拉耶夫（Vadim S. NIKOLAYEV）

论文单位：法国原子能与替代能源委员会巴黎-萨克雷中心（CEA Paris-Saclay Center），巴黎萨克雷大学（Université Paris-Saclay）

关键词：脉动热管（Pulsating Heat Pipes），毛细管液膜（liquid films in capillaries），接触线动力学（contact line dynamics），毛细管传热（heat transfer in capillaries）

摘要：脉动热管（PHP）是一种结构简单、传输效率高、有着广泛应用前景的换热系统。从原理上说，脉动热管是封闭的毛细管，其中充满了两相流体。流体蒸发和冷凝将能量从加热部分（蒸发器, evaporators）转移到冷却部分（冷凝器, condensers）。毛细管内部光滑, 不具备任何机械结构。管子内径足够窄，以便在内部形成交替的液塞和汽泡。当冷凝器和蒸发器之间的温差超过一个阈值时，气泡和液塞开始可持续得振荡。这种振荡和由它引起的对流传热使脉动热管与其他类型的热管相比效率更高。然而，其物理过程是非稳态的，这使得理解和开发一个计算模型具有挑战性。在其振荡过程中，后退的半月板沉积液膜，液膜相变传热是整个设备的主要热传导模式。因此，本论文先集中于对毛细管中液膜的理论研究。首先研究了在三重接触线静止以及半月板间简谐荡条件下的液膜动力学。之后研究了在毛细作用以及蒸发效应下，接触线后退现象。此外，这部分研究被用于解释泡核沸腾中形成于汽泡下方的微观液膜（microlayer）行为。基于液膜理论研究，论文的第二部分建立了一个一维计算模型，并应用于单管脉动热管模拟。在每个阶段，理论结果都与现有的实验进行了比较。

更多讨论请引用相关论文：Zhang et al., 2021; Zhang et al., 2022b; Tecchio et al., 2022; Zhang et al., 2022c.

Nomenclature

*Unless otherwise indicated, all quantities mentioned refer to the liquid phase.
Latin symbols

Ca		Capillary number $Ca = \mu u/\sigma$
d	[m]	diameter
F	[N]	Friction in liquid plugs
f		Evaporation (or condensation) coefficient
g	[m/s^2]	Gravitational acceleration
h	[m]	liquid-vapor interface thickness
$\boldsymbol{\hbar}$	[J/kg]	specific enthalpy
J	[kg/s]	mass flux
j	[kg/(m^2·s)]	local mass flux
K		Fanning friction factor
k	[W/(m·K)]	thermal conductivity
L	[m]	Film length
l_{s}	[m]	Slip length
ℓ	[m]	characteristic length
$\mathcal{L}$	[J/kg]	latent heat
m	[kg]	mass
$\boldsymbol{n}$		unit normal vector
p	[Pa]	pressure
R	[m]	radius
R_{g}	[J/(K·mol)]	molar gas constant $\simeq$ 8.314 J/(K·mol)
R^{i}	[(m^2·sK)/W]	Interfacial thermal resistance
Re		Reynolds number $Re = \rho u d/\mu$
s	[m]	curvilinear coordinate
$\mathscr{s}$	[J/(kg·K)]	specific entropy
$\boldsymbol{T}$		stress tensor
T	[K]	temperature
$\boldsymbol{t}$		unit tangent vector
t	[s]	time
U	[m/s]	heat transfer coefficient
u	[m/s]	velocity
$\boldsymbol{u}$	[J/kg]	specific internal energy

v	[m^3/kg]	specific volume
w	[m]	width of dewetting ridges

Greek symbols

α		constant defined as $R^{\mathrm{i}}k/R$
β		coefficient in time-averaged thickness of evaporating films
γ	[N/(m·K)]	surface tension gradient $\gamma = -\mathrm{d}\sigma/\mathrm{d}T$
δ	[m]	effective film thickness
ϵ		coefficient in wetting transition
ζ	[m]	arc length
θ	rad	contact angle
κ	[m^{-1}]	interface curvature
μ	[Pa·s]	dynamic viscosity
ρ	[kg/m^3]	density
σ	[N/m]	surface tension
ϕ		interface slope
Ω	[m^3]	volume of vapor phase in bubbles

Subscripts

a	adiabatic (section)
app	apparent (contact angle)
c	condenser
cl	contact line
d	dry out; dewetting
dep	deposition
e	evaporator
f	(liquid) film
fb	feedback section
h	dry hole
hv	dry hole vector
i	bubble-plug pair index
l	liquid plug
m	meniscus
micro	microscopic scale
p	periodic sequences of multi-branch PHPs
s	slip length
sat	saturation
sens	sensible heat
V	Voinov
Vsa	Voinov length evaluated by l_{s} and θ_{micro}

VK	Voinov length evaluated by the Kelvin effect
Vs	Voinov length evaluated by l_{s} and θ_{V}
v	vapor
w	solid wall
0	initial
∞	long flat liquid film

Superscripts

l	left (meniscus)
r	right (meniscus)
i	interface
ξ	$\xi = \{r, l\}$ left or right (meniscus)

Bibliography

Abela, Mauro et al. (Sept. 2019). "Comparison of experiments and simulations on large diameter PHP in microgravity environment." In: *Proc. Int. Symp. Oscillating/Pulsating Heat Pipes (ISOPHP)*. Daejeon, Korea.

Abela, Mauro et al. (2022). "Experimental analysis and transient numerical simulation of a large diameter pulsating heat pipe in microgravity conditions." In: *Int. J. Heat Mass Transfer* 187, p. 122532. DOI: 10.1016/j.ijheatmasstransfer.2022.122532.

Akachi, H. (1993). *Structure of micro-heat pipe*. US Patent 5219020. URL: https://www.lens.org/lens/patent/053-368-069-338-252.

Anderson, D. M. and S. H. Davis (1994). "Local fluid and heat flow near contact lines." In: *J. Fluid Mech.* 268, pp. 231 –265. DOI: 10.1017/S0022112094001333.

Anderson, Daniel M. et al. (2007). "General dynamical sharp-interface conditions for phase transformations in viscous heat-conducting fluids." In: *J. Fluid Mech.* 581, pp. 323 –370. DOI: 10.1017/S0022112007005587.

Angeli, P. and A. Gavriilidis (2008). "Hydrodynamics of Taylor flow in small channels: a review." In: *Proc. Inst. Mech. Eng. Part C J. Mech. Eng. Sci.* 222.5, pp. 737 –751. DOI: 10.1243/09544062JMES776.

Aubin, P. et al. (2019). "Numerical Simulations of Pulsating Heat Pipes, Part 1: Modeling." In: *2019 18th IEEE Intersociety Conf. on Thermal and Thermomechanical Phenomena in Electronic Systems (ITherm)*. Las Vegas, USA, pp. 232 –242. DOI: 10.1109/ITHERM.2019.8757388.

Aussillous, P. and D. Quéré (2000). "Quick deposition of a fluid on the wall of a tube." In: *Phys. Fluids* 12.10, pp. 2367 –2371. DOI: 10.1063/1.1289396.

Bae, Joohan, Sang Yong Lee, and Sung Jin Kim (2017). "Numerical investigation of effect of film dynamics on fluid motion and thermal performance in pulsating heat pipes." In: *Energy Convers. Manage.* 151, pp. 296 –310. DOI: 10.1016/j.enconman.2017.08.086.

Baudoin, Michael et al. (2013). "Airway reopening through catastrophic events in a hierarchical network." In: *Proc. Natl. Acad. Sci. USA* 110.3, pp. 859 –864. DOI: 10.1073/pnas.1211706110.

Boender, W., A. K. Chesters, and A. J. J. van der Zanden (1991). "An approximate analytical solution of the hydrodynamic problem associated with an advancing liquid-gas contact line." In: *Int. J. Multiphase Flow* 17, pp. 661 –676. DOI: 10.1016/0301-9322(91)90031-W.

Bretherton, F. P. (1961). "The motion of long bubbles in tubes." In: *J. Fluid Mech.* 10, pp. 166 –188. DOI: 10.1017/S0022112061000160.

Brochard-Wyart, F. et al. (1991). "Spreading of nonvolatile liquids in a continuum picture." In: *Langmuir* 7.2, pp. 335 –338. DOI: 10.1021/la00050a023.

Burelbach, J. P., S. G. Bankoff, and S. H. Davis (1988). "Nonlinear stability of evaporating/condensing liquid films." In: *J. Fluid Mech.* 195, pp. 463 –494. DOI: 10.1017/S0022112088002484.

Bureš, Lubomír and Yohei Sato (2021). "Direct numerical simulation of evaporation and condensation with the geometric VOF method and a sharp-interface phase-change model." In: *Int. J. Heat Mass Transfer* 173, p. 121233. DOI: 10.1016/j.ijheatmasstransfer.2021.121233.

Carey, V. P. (1992). *Liquid-Vapor Phase Change Phenomena*. Washington D.C.: Hemisphere. DOI: 10.1201/9780429082221.

Chan, T. S. et al. (2013). "Hydrodynamics of air entrainment by moving contact lines." In: *Phys. Fluids* 25.7, p. 074105. DOI: 10.1063/1.4814466.

Chan, Tak Shing et al. (2020). "Cox-Voinov theory with slip." In: *J. Fluid Mech.* 900, A8. DOI: 10.1017/jfm.2020.499.

Chen, Zhihao, Atsushi Haginiwa, and Yoshio Utaka (2017). "Detailed structure of microlayer in nucleate pool boiling for water measured by laser interferometric method." In: *Int. J. Heat Mass Transfer* 108, pp. 1285 –1291. DOI: 10.1016/j.ijheatmasstransfer.2017.01.003.

Cheng, Hao et al. (2020). "Experimental study on the oscillation characteristics of thin liquid film in a microchannel." In: *Exp. Therm Fluid Sci.* 115, p. 110089. DOI: 10.1016/j.expthermflusci.2020.110089.

Cherukumudi, Aditya et al. (2015). "Prediction of the shape and pressure drop of Taylor bubbles in circular tubes." In: *Microfluid. Nanofluid.* 19.5, pp. 1221 –1233. DOI: 10.1007/s10404-015-1641-x.

Cox, R. G. (1986). "The dynamics of the spreading of liquids on a solid surface. Part 1. Viscous flow." In: *J. Fluid Mech.* 168, pp. 169 –194. DOI: 10.1017/S0022112086000332.

Das, S. P. et al. (2010). "Thermally induced two-phase oscillating flow inside a capillary tube." In: *Int. J. Heat Mass Transfer* 53.19-20, pp. 3905 –3913. DOI: 10.1016/j.ijheatmasstransfer.2010.05.009.

Delhaye, J.-M. (1974). "Jump conditions and entropy sources in two-phase systems. Local instant formulation." In: *Int. J. Multiphase Flow* 1, pp. 395 –409. DOI: 10.1016/0301-9322(74)90012-3.

Delon, G. et al. (2008). "Relaxation of a dewetting contact line. Part 2: Experiments." In: *J. Fluid Mech.* 604, pp. 55 –75. DOI: 10.1017/S0022112008000979.

Dobson, R. T. (2004). "Theoretical and experimental modelling of an open oscillatory heat pipe including gravity." In: *Int. J. Therm. Sci.* 43.2, pp. 113 –119. DOI: 10.1016/j.ijthermalsci.2003.05.003.

Fourgeaud, L. et al. (2016). "Evaporation-driven dewetting of a liquid film." In: *Phys. Rev. Fluids* 1.4, 041901(R). DOI: 10.1103/PhysRevFluids.1.041901.

Fourgeaud, Laura (Sept. 2016). "Analysis of the liquid film dynamics in a Pulsating Heat Pipe." PhD thesis. Université Grenoble-Alpes. URL: https://tel.archives-ouvertes.fr/tel-01409530.

Fourgeaud, Laura et al. (2017). "In situ investigation of liquid films in pulsating heat pipe." In: *Appl. Therm. Eng.* 126, pp. 1023 –1028. DOI: 10.1016/j.applthermaleng.2017.01.064.

Francom, Matthew and Jungho Kim (2021). "Experimental investigation into the heat transfer mechanism of oscillating heat pipes using temperature sensitive paint." In: *J. Heat Transfer* 143.4, p. 041901. DOI: 10.1115/1.4049512.

Gao, Peng et al. (2019). "Forced dewetting in a capillary tube." In: *J. Fluid Mech.* 859, pp. 308 –320. DOI: 10.1017/jfm.2018.834.

Gully, P. et al. (2014). "Evaluation of the vapor thermodynamic state in PHP." In: *Heat Pipe Sci. Technol.* 5.1-4, pp. 369 –376. DOI: 10.1615/HeatPipeScieTech.v5.i1-4.410.

Han, Youngbae and Naoki Shikazono (2010). "The effect of bubble acceleration on the liquid film thickness in micro tubes." In: *Int. J. Heat Fluid Flow* 31.4, pp. 630 –639. DOI: 10.1016/j.ijheatfluidflow.2010.02.002.

Hocking, L. M. (1983). "The spreading of a thin drop by gravity and capillarity." In: *Q. J. Mechanics Appl. Math.* 36.1, pp. 55 –69. DOI: 10.1093/qjmam/36.1.55.

Holley, Brian and Amir Faghri (2005). "Analysis of pulsating heat pipe with capillary wick and varying channel diameter." In: *Int. J. Heat Mass Transfer* 48.13, pp. 2635 –2651. DOI: 10.1016/j.ijheatmasstransfer.2005.01.013.

Iliev, Stanimir, Nina Pesheva, and Vadim S. Nikolayev (2014). "Contact angle hysteresis and pinning at periodic defects in statics." In: *Phys. Rev. E* 90 (1), p. 012406. DOI: 10.1103/PhysRevE.90.012406.

Ishii, M. and T. Hibiki (2006). *Thermo-fluid Dynamics of Two-Phase Flow*. Springer.

Janeček, V. (2012). "Evaporation at microscopic scale and at high heat flux." PhD thesis. Université Pierre et Marie Curie Paris 6. URL: http://tel.archives-ouvertes.fr/tel-00782517.

Janeček, V. and V. S. Nikolayev (2012). "Contact line singularity at partial wetting during evaporation driven by substrate heating." In: *Europhys. Lett.* 100.1, p. 14003. DOI: 10.1209/0295-5075/100/14003.

Janeček, V. and V. S. Nikolayev (2014). "Triggering the boiling crisis: a study of the dry spot spreading mechanism." In: *Interfacial Phenom. Heat Transf.* 2.4, pp. 363 –383. DOI: 10.1615/InterfacPhenomHeatTransfer.2015012273.

Janeček, V. et al. (2013). "Moving contact line of a volatile fluid." In: *Phys. Rev. E* 88.6, 060404(R). DOI: 10.1103/PhysRevE.88.060404.

Janeček, Vladislav and Dan M. Anderson (2016). "Microregion model of a contact line including evaporation, kinetics and slip length." In: *Interfacial Phenom. Heat Transf.* 4.2-3, pp. 93 –107. DOI: 10.1615/InterfacPhenomHeatTransfer.2017017202.

Jo, Jaeyeong, Jungho Kim, and Sung Jin Kim (2019). "Experimental investigations of heat transfer mechanisms of a pulsating heat pipe." In: *Energy Convers. Manage.* 181, pp. 331 –341. DOI: 10.1016/j.enconman.2018.12.027.

Kamijima, Chihiro et al. (2020). "Relating the thermal properties of a micro pulsating heat pipe to the internal flow characteristics via experiments, image recognition of flow patterns and heat transfer simulations." In: *Int. J. Heat Mass Transfer* 163, p. 120415. DOI: 10.1016/j.ijheatmasstransfer.2020.120415.

Kim, Jungho (2009). "Review of nucleate pool boiling bubble heat transfer mechanisms." In: *Int. J. Multiphase Flow* 35.12, pp. 1067 –1076. DOI: 10.1016/j.ijmultiphaseflow.2009.07.008.

Klaseboer, Evert, Raghvendra Gupta, and Rogerio Manica (2014). "An extended Bretherton model for long Taylor bubbles at moderate capillary numbers." In: *Phys. Fluids* 26.3, p. 032107. DOI: 10.1063/1.4868257.

Landau, L. D. and B. V. Levich (1942). "Dragging of a liquid by a moving plate." In: *Acta physico-chimica USSR* 17, pp. 42 –54. DOI: 10.1016/B978-0-08-092523-3.50016-2.

Landau, L. D. and E. M. Lifshitz (1980). *Statistical physics*. Oxford: Pergamon Press.

Lauga, E., M. P. Brenner, and H. A. Stone (2007). "Microfluidics: the no-slip boundary condition." In: *Springer Handbook of Experimental Fluid Dynamics*. Ed. by C. Tropea, A. Yarin, and J. Foss. New York: Springer. Chap. 19, pp. 1217 –1240. DOI: 10.1007/978-3-540-30299-5_19. URL: https://arxiv.org/pdf/cond-mat/0501557.pdf.

Launay, Stéphane et al. (2007). "Transient modeling of loop heat pipes for the oscillating behavior study." In: *J. Thermophys. Heat Transfer* 21.3, pp. 487 –495. DOI: 10.2514/1.26854.

Lips, S. et al. (2010). "Experimental evidences of distinct heat transfer regimes in pulsating heat pipes (PHP)." In: *Appl. Therm. Eng.* 30.8-9, pp. 900 –907. DOI: 10.1016/j.applthermaleng.2009.12.020.

Ma, Hongbin (2015). *Oscillating Heat Pipes*. New York: Springer. ISBN: 978-1-4939-2504-9. DOI: 10.1007/978-1-4939-2504-9.

Maleki, M. et al. (2011). "Landau-Levich menisci." In: *J. Colloid Interface Sci.* 354.1, pp. 359 –363. DOI: 10.1016/j.jcis.2010.07.069.

Mameli, M., M. Marengo, and S. Zinna (2012). "Numerical model of a multi-turn closed loop pulsating heat pipe: effects of the local pressure losses due to meanderings." In: *Int. J. Heat Mass Transfer* 55.4, pp. 1036 –1047. DOI: 10.1016/j.ijheatmasstransfer.2011.10.006.

Marek, R. and J. Straub (2001). "The origin of thermocapillary convection in subcooled nucleate pool boiling." In: *Int. J. Heat Mass Transfer* 44, pp. 619 –632. DOI: 10.1016/S0017-9310(00)00124-1.

Marengo, Marco and Vadim Nikolayev (2018). "Pulsating Heat Pipes: Experimental Analysis, Design and Applications." In: *Encyclopedia of Two-Phase Heat Transfer and Flow IV*. Ed. by J. R. Thome. Vol. 1: Modeling of Two-Phase Flows and Heat Transfer. World Scientific, pp. 1 –62. ISBN: 978-981-3234-39-0. DOI: 10.1142/9789813234406_0001.

Mathieu, B. (2003). "Etudes physiques, expérimentale et numérique des mécanismes de base intervenant dans les écoulements diphasiques." PhD thesis. Polytech Marseille, Université de Provence. URL: https://triocfd.cea.fr/Documents/DOCS%20THESES/these_Mathieu_2003.pdf.

Moffatt, H. K. (1964). "Viscous and resistive eddies near a sharp corner." In: *J. Fluid Mech.* 18.1, pp. 1 –18. DOI: 10.1017/S0022112064000015.

Mohammadi, Mahshid and Kendra V. Sharp (2015). "The role of contact line (pinning) forces on bubble blockage in microchannels." In: *J. Fluids Eng.* 137.3, p. 031208. DOI: 10.1115/1.4029033.

Mortagne, Caroline et al. (2017). "Dynamics of anchored oscillating nanomenisci." In: *Phys. Rev. Fluids* 2.10, p. 102201. DOI: 10.1103/PhysRevFluids.2.102201.

Mucci, Alberto et al. (2021). "Numerical investigation of flow instability and heat transfer characteristics inside pulsating heat pipes with different numbers of turns." In: *Int. J. Heat Mass Transfer* 169, p. 120934. DOI: 10.1016/j.ijheatmasstransfer.2021.120934.

Nekrashevych, Iaroslav and Vadim S. Nikolayev (2017). "Effect of tube heat conduction on the pulsating heat pipe start-up." In: *Appl. Therm. Eng.* 117, pp. 24 –29. DOI: 10.1016/j.applthermaleng.2017.02.013.

Nekrashevych, Iaroslav and Vadim S. Nikolayev (2019). "Pulsating heat pipe simulations: impact of PHP orientation." In: *Microgravity Sci. Technol.* 31.3, pp. 241 –248. DOI: 10.1007/s12217-019-9684-3.

Nikolayev, V. S. (2010). "Dynamics of the triple contact line on a nonisothermal heater at partial wetting." In: *Phys. Fluids* 22.8, p. 082105. DOI: 10.1063/1.3483558.

Nikolayev, V. S. (2011a). "A dynamic film model of the pulsating heat pipe." In: *J. Heat Transfer* 133.8, p. 081504. DOI: 10.1115/1.4003759.

Nikolayev, V. S. (2011b). "Comment on "Flow and heat transfer of liquid plug and neighboring vapor slugs in a pulsating heat pipe" by Yuan, Qu, & Ma." In: *Int. J. Heat Mass Transfer* 54.9-10, pp. 2226 –2227. DOI: 10.1016/j.ijheatmasstransfer.2011.01.007.

Nikolayev, V. S. (2013). "Oscillatory instability of the gas-liquid meniscus in a capillary under the imposed temperature difference." In: *Int. J. Heat Mass Transfer* 64, pp. 313 –321. DOI: 10.1016/j.ijheatmasstransfer.2013.04.043.

Nikolayev, V. S. (2016). "Effect of tube heat conduction on the single branch pulsating heat pipe start-up." In: *Int. J. Heat Mass Transfer* 95, pp. 477 –487. DOI: 10.1016/j.ijheatmasstransfer.2015.12.016.

Nikolayev, V. S. and D. A. Beysens (1999). "Boiling crisis and non-equilibrium drying transition." In: *Europhys. Lett.* 47.3, pp. 345 –351. DOI: 10.1209/epl/i1999-00395-x.

Nikolayev, V. S. and I. Nekrashevych (2018a). "Vapor thermodynamics and fluid merit for pulsating heat pipe." In: *Proc. 19th Int. Heat Pipe Conf. and 13th Int. Heat Pipe Symp.* Pisa, Italy.

Nikolayev, Vadim S. (2021). "Physical principles and state-of-the-art of modeling of the pulsating heat pipe: A review." In: *Appl. Therm. Eng.* 195, p. 117111. DOI: 10.1016/j.applthermaleng.2021.117111.

Nikolayev, Vadim S. (2022). "Evaporation effect on the contact angle and contact line dynamics." In: *The Surface Wettability Effect on Phase Change*. Ed. by Marco Marengo and Joel De Coninck. Springer. Chap. 6, pp. 133 –187. DOI: 10.1007/978-3-030-82992-6_6.

Nikolayev, Vadim S. and Senthilkumar Sundararaj (2014). "Oscillating menisci and liquid films at evaporation/condensation." In: *Heat Pipe Sci. Technol.* 5.1-4, pp. 59 –67. DOI: 10.1615/HeatPipeScieTech.v5.i1-4.30.

Nikolayev, Vadim and Marco Marengo (2018b). "Pulsating Heat Pipes: Basics of Functioning and Numerical Modeling." In: *Encyclopedia of Two-Phase Heat Transfer and Flow IV*. Ed. by J. R. Thome. Vol. 1: Modeling of Two-Phase Flows and Heat Transfer. World Scientific, pp. 63 –139. ISBN: 978-981-3234-39-0. DOI: 10.1142/9789813234406_0002. URL: https://hal-cea.archives-ouvertes.fr/cea-03261340v1.

Noh, Hyung Yun and Sung Jin Kim (2020). "Numerical simulation of pulsating heat pipes: parametric investigation and thermal optimization." In: *Energy Convers. Manage.* 203, p. 112237. DOI: 10.1016/j.enconman.2019.112237.

Oron, A., S. H. Davis, and S. G. Bankoff (1997). "Long-scale evolution of thin liquid films." In: *Rev. Mod. Phys.* 69.3, pp. 931 –980. DOI: 10.1103/RevModPhys.69.931.

Palmer, H. J. (1976). "The hydrodynamic stability of rapidly evaporating liquids at reduced pressure." In: *J. Fluid Mech.* 75.part 3, pp. 487 –511. DOI: 10.1017/s0022112076000347.

Patankar, S. V. (1980). *Numerical heat transfer and fluid flow*. Washington: Hemisphere.

Potash, M. and P. C. Wayner (1972). "Evaporation from a two-dimensional extended meniscus." In: *Int. J. Heat Mass Transfer* 15.10, pp. 1851 –1863. DOI: 10.1016/0017-9310(72)90058-0.

Rao, M. et al. (2015). "Heat and mass transfer mechanisms of a self-sustained thermally driven oscillating liquid-vapour meniscus." In: *Int. J. Heat Mass Transfer* 86, pp. 519 –530. DOI: 10.1016/j.ijheatmasstransfer.2015.03.015.

Rao, M. et al. (2017). "Numerical and experimental investigations of thermally induced oscillating flow inside a capillary tube." In: *Int. J. Therm. Sci.* 115, pp. 29 –42. DOI: 10.1016/j.ijthermalsci.2017.01.009.

Recklin, Viktor, Arvind Pattamatta, and Peter Stephan (2015). "Experimental investigation on the thermo-hydrodynamics of oscillatory meniscus in a capillary tube using FC-

72 as working fluid." In: *Int. J. Multiphase Flow* 75, pp. 82 –87. DOI: 10.1016/j.ijmultiphaseflow.2015.05.011.

Rednikov, A. Ye. and P. Colinet (2011). "Truncated versus extended microfilms at a vapor-liquid contact line on a heated substrate." In: *Langmuir* 27.5, pp. 1758 –1769. DOI: 10.1021/la102065c.

Rednikov, A. and P. Colinet (2013). "Singularity-free description of moving contact lines for volatile liquids." In: *Phys. Rev. E* 87.1, p. 010401. DOI: 10.1103/PhysRevE.87.010401.

Rouaze, Gautier et al. (2021). "Simulation and experimental validation of pulsating heat pipes." In: *Appl. Therm. Eng.* 196, p. 117271. DOI: 10.1016/j.applthermaleng.2021.117271.

Sakulchangsatjatai, P. et al. (2004). "Operation modeling of closed-end and closed-loop oscillating heat pipes at normal operating condition." In: *Appl. Therm. Eng.* 24.7, pp. 995 –1008. DOI: 10.1016/j.applthermaleng.2003.11.006.

Savva, Nikos, Alexey Rednikov, and Pierre Colinet (2017). "Asymptotic analysis of the evaporation dynamics of partially wetting droplets." In: *J. Fluid Mech.* 824, pp. 574 –623. DOI: 10.1017/jfm.2017.330.

Schrage, R. W. (1953). *A Theoretical study of interphase mass transfer*. Columbia University Press.

Schweikert, K., A. Sielaff, and P. Stephan (2019). "On the transition between contact line evaporation and microlayer evaporation during the dewetting of a superheated wall." In: *Int. J. Therm. Sci.* 145, p. 106025. DOI: 10.1016/j.ijthermalsci.2019.106025.

Senjaya, Raffles and Takayoshi Inoue (2013). "Bubble generation in oscillating heat pipe." In: *Appl. Therm. Eng.* 60.1-2, pp. 251 –255. DOI: 10.1016/j.applthermaleng.2013.06.041.

Senjaya, Raffles and Takayoshi Inoue (2014). "Oscillating heat pipe simulation considering dryout phenomena." In: *Heat Mass Transfer* 50.10, pp. 1429 –1441. DOI: 10.1007/s00231-014-1354-9.

Shafii, M. B., A. Faghri, and Y. Zhang (2001). "Thermal modeling of unlooped and looped pulsating heat pipes." In: *J. Heat Transfer* 123.6, pp. 1159 –1172. DOI: 10.1115/1.1409266.

Shao, Wei and Yuwen Zhang (2011). "Effects of film evaporation and condensation on oscillatory flow and heat transfer in an oscillating heat pipe." In: *J. Heat Transfer* 133.4, p. 042901. DOI: 10.1115/1.4002780.

Sharp, Robert R (1964). *The nature of liquid film evaporation during nucleate boiling*. National Aeronautics and Space Administration.

Signé Mamba, S. et al. (2018). "Dynamics of a liquid plug in a capillary tube under cyclic forcing: memory effects and airway reopening." In: *J. Fluid Mech.* 838, pp. 165 –191. DOI: 10.1017/jfm.2017.828.

Snoeijer, J. H. (2006). "Free-surface flows with large slopes: Beyond lubrication theory." In: *Phys. Fluids* 18, p. 021701. DOI: 10.1063/1.2171190.

Snoeijer, J. H. and B. Andreotti (2013). "Moving contact lines: scales, regimes, and dynamical transitions." In: *Annu. Rev. Fluid Mech.* 45.1, pp. 269 –292. DOI: 10.1146/annurev-fluid-011212-140734.

Snoeijer, J. H. and J. Eggers (2010). "Asymptotic analysis of the dewetting rim." In: *Phys. Rev. E* 82.5, p. 056314. DOI: 10.1103/PhysRevE.82.056314.

Snoeijer, J. et al. (2007). "Relaxation of a dewetting contact line. Part 1. A full-scale hydrodynamic calculation." In: *J. Fluid Mech.* 579, pp. 63 –83. DOI: 10.1017/S0022112007005216.

Talimi, V., Y. S. Muzychka, and S. Kocabiyik (2012). "A review on numerical studies of slug flow hydrodynamics and heat transfer in microtubes and microchannels." In: *Int. J. Multiphase Flow* 39, pp. 88 –104. DOI: 10.1016/j.ijmultiphaseflow.2011.10.005.

Taylor, G. I. (1961). "Deposition of a viscous fluid on the wall of a tube." In: *J. Fluid Mech.* 10.2, pp. 161 –165. DOI: 10.1017/S0022112061000159.

Tecchio, C. (2022). "Experimental study of boiling: characterization of near-wall phenomena and bubble dynamics." PhD thesis. Paris-Saclay University.

Tecchio, C. et al. (2022). "Microlayer dynamics at bubble growth in boiling." In: *Proc. 16th Int. Conf. Heat Transfer Fluid Mech. Thermodynamics (HEFAT-ATE 2022)*, pp. 624 –629.

Tessier-Poirier, Albert et al. (2019). "How evaporation and condensation lead to self-oscillations in the single-branch pulsating heat pipe." In: *Phys. Rev. Fluids* 4.10, p. 103901. DOI: 10.1103/PhysRevFluids.4.103901.

Thome, J. R., V. Dupont, and A. M. Jacobi (2004). "Heat transfer model for evaporation in microchannels. Part I: presentation of the model." In: *Int. J. Heat Mass Transfer* 47.14-16, pp. 3375 –3385. DOI: 10.1016/j.ijheatmasstransfer.2004.01.006.

Ting, C.-L. and M. Perlin (1987). "Boundary conditions in the vicinity of the contact line at a vertically oscillating upright plate: an experimental investigation." In: *J. Fluid Mech.* 179, pp. 253 –266. DOI: 10.1017/s0022112095001960.

Urbano, A. et al. (2018). "Direct numerical simulation of nucleate boiling in micro-layer regime." In: *Int. J. Heat Mass Transfer* 123, pp. 1128 –1137. DOI: 10.1016/j.ijheatmasstransfer.2018.02.104.

Voinov, O.V. (1976). "Hydrodynamics of wetting." In: *Fluid Dyn.* 11.5, pp. 714 –721. DOI: 10.1007/BF01012963.

Voutsinos, CM and RL Judd (1975). "Laser interferometric investigation of the microlayer evaporation phenomenon." In.

Wayner, Peter C. (1993). "Spreading of a liquid film with a finite contact angle by the evaporation/condensation process." In: *Langmuir* 9.1, pp. 294 –299. DOI: 10.1021/la00025a056.

Yoon, Aejung and Sung Jin Kim (2017). "Characteristics of oscillating flow in a micro pulsating heat pipe: Fundamental-mode oscillation." In: *Int. J. Heat Mass Transfer* 109, pp. 242 –253. DOI: 10.1016/j.ijheatmasstransfer.2017.02.003.

Youn, Young Jik, Youngbae Han, and Naoki Shikazono (2018). "Liquid film thicknesses of oscillating slug flows in a capillary tube." In: *Int. J. Heat Mass Transfer* 124, pp. 543 –551. DOI: 10.1016/j.ijheatmasstransfer.2018.03.102.

Youn, Young Jik et al. (2016). "The effect of bubble deceleration on the liquid film thickness in microtubes." In: *Int. J. Heat Fluid Flow* 58, pp. 84 –92. DOI: 10.1016/j.ijheatfluidflow.2016.01.002.

Zhang, Jiaxun, Zengqi Hou, and Chenghui Sun (1998). "Theoretical analysis of the pressure oscillation phenomena in capillary pumped loop." In: *J. Therm. Sci.* 7.2, pp. 89 –96. DOI: 10.1007/s11630-998-0004-2.

Zhang, Xiaolong and Vadim S. Nikolayev (2021). "Liquid film dynamics with immobile contact line during meniscus oscillation." In: *J. Fluid Mech.* 923, A4. DOI: 10.1017/jfm.2021.540.

Zhang, Xiaolong and Vadim S. Nikolayev (2022a). "Dewetting accelerated by evaporation." In: *Proc. 16th Int. Conf. Heat Transfer Fluid Mech. Thermodynamics (HEFAT-ATE 2022)*, pp. 311 –316.

Zhang, Xiaolong and Vadim S. Nikolayev (2022b). "Dewetting acceleration by evaporation." In: *J. Fluid Mech.* 948, A49. DOI: 10.1017/jfm.2022.725.

Zhang, Xiaolong and Vadim S. Nikolayev (2022c). "Liquid film model for pulsating heat pipes." In: *Proc. 16th Int. Conf. Heat Transfer Fluid Mech. Thermodynamics (HEFAT-ATE 2022)*, pp. 612 –617.

Zhang, Y. and A. Faghri (2002). "Heat transfer in a pulsating heat pipe with open end." In: *Int. J. Heat Mass Transfer* 45.4, pp. 755 –764. DOI: 10.1016/S0017-9310(01)00203-4.

d'Entremont, Brian P. and John R. Thome (2015). "A numerical study of pulsating heat pipe performance." In: *Proc. InterPACKICNMM 2015*, V003T10A025. DOI: 10.1115/ipack2015-48350.

deGennes, P.-G. (1985). "Wetting: statics and dynamics." In: *Rev. Mod. Phys.* 57, pp. 827 –863. DOI: 10.1142/9789812564849_0041.

deGennes, P.-G., F. Brochard-Wyart, and D. Quéré (2004). *Capillarity and Wetting Phenomena: Drops, Bubbles, Pearls, Waves*. New York: Springer. DOI: 10.1007/978-0-387-21656-0.

Declaration

I declare that this thesis was composed by myself, that the work contained herein is my own except where explicitly stated otherwise in the text, and that has not been previously included in a thesis or dissertation submitted to this or any other institution for a degree, diploma, or other qualifications.

This doctoral project has been co-financed by the French National Center for Space Studies (abbreviated from the French *Centre national d'études spatiales*) (CNES) and the CEA NUMERICS program, which has received funding from the *European Union's Horizon 2020 research and innovation programme* under grant agreement No 800945 — NUMERICS — H2020-MSCA-COFUND-2017. It is also supported by the project TOPDESS, financed through the Microgravity Application Program by the European Space Agency. Additional financial support of CNES awarded through GdR MFA is acknowledged.

CEA Paris-Saclay Center, France, October 2022

Xiaolong ZHANG